THE DEFORMATION OF POLYCRYSTALLINE GRAPHITE UNDER PRESSURE

A thesis submitted in accordance with the requorements of the University of Liverpool for the degree of Doctor in Philosophy by

Siek Yeng BOEY

Department of Metallurgy and Materials Science

University of Liverpool

January, 1984.

ABSTRACT

A study of the deformation behaviour of polycrystalline graphite subjected to pressures up to 600 psi (4.14 MPa) is reported. Four graphites are investigated: two are Gilsocarbon materials and are isotropic in nature, the other two have anisotropic properties. Strain measurements are made in the longitudinal and circumferential directions of cylindrical specimens using resistance strain gauges. Specimens are coated to study the effect of closed porosity upon the hydrostatic deformation. Porosity measurements are made to determine the open and closed pore volumes and investigate their contribution towards the dilatation of graphite under pressure.The effect of compressive pre-stressing and raising the test temperatures from 20 to 300°C are investigated. Other work includes uniaxial compression tests, 4-point bend tests under pressure and hydrostatic testing of neutron irradiated sleeve graphites.

All the graphites investigated here exhibit linear pressure-strain behaviour in both the circumferential and longitudinal directions. Small residual strains or permanent sets are produced during pressure unloading to atmospheric condition. The strains at 600 psi (e_m) are generally small and range from $130x10^{-6}$ for the isotropic graphite to $280x10^{-6}$ for the anisotropic graphite. The open porosity is envisaged to have little effect in the hydrostatic deformation of graphite since internal pressure in the open porosity can restrict the shear deformation of coke grains into the open voidage. The closed porosity, however, contributes significantly in both uniaxial and hydrostatic deformation for it provides free surfaces to accommodate the shear deformation of individual coke grains.The hydrostatic strain, at low pressure, is a combination of shear and compression of individual crystallites within the grains.The coated specimens produce substantial increases in deformation in both directions over the uncoated ones due to the increase of

closed porosity. The values of e_m for the coated specimens range from $200x10^{-6}$ for the isotropic graphite to over $600x10^{-6}$ for the anisotropic graphite. Since the total porosity of coated specimens becomes closed, the compressibility increases as the network of grains and pores can be compressed as a whole. The results of the specimens with known porosity values indicate that the increase in dilatation of the coated specimens is proportional to the increase in closed porosity. The porosity expression due to Hasselman [27] gives a fairly accurate relationship between the closed porosity and the bulk modulus for the graphites employed here. Compressive pre-stressing dose not affect the linear deformation of graphite with pressure. The decrease in the bulk modulus following pre-stressing is found to be small. This is attributed to an increase in dislocation density in the pre-compressed specimens. The increase in crack density has little effect since the cracks resemble open pores already present in the material. Raising the test temperature to 300°C is found to have a small effect on the bulk modulus of graphite. The slight fall in the bulk modulus at 300°C is probably due to a dislocation unpinning mechanism which is thermally activated. For the neutron irradiated sleeve materials, it is found that the bulk modulus increases with increasing neutron dose, a dislocation pinning effect due to the presence of irradiation-induced defects in the graphite crystallites. The 4-point bend tests show that the mean bend strength and strain to failure of graphite drop when the tests are performed under a pressure of 600 psi. This behaviour is explained by the presence of internal pressure in the bend specimens which can penetrate and open up the pores and cracks in the coke grains. Consequently crack propagation will be enhanced under the influence of pressure. The internal pressure can also restrict the bending deformation of the bend specimens and results in the stiffer behaviour observed.

CONTENTS

ACKNOWLEDGEMENTS

I would like to thank Dr. D.J. Bacon for his invaluable advice, guidance and overall supervision of this project.

The work was supported by the United Kingdom Atomic Energy Authority and an Oversea Research Student Award from the committee of Vice-Chancellors and Principals of the Universities of the United Kingdom. I would like to thank also Mr.B.T. Kelly, Mr.J. Brocklehurst and Dr.M. Birch for helpful discussions carried out at Springfields Nuclear Power Development Laboratories.

Thanks are also due to:

Mr.P Schofield for specimens and equipment preparations.

Mr.R.G. Brown for the porosity measurements of graphite specimens.

Finally, members of my family for their continuous support and encouragement.

Glossary of principal symbols

C_{ij} = single crystal elastic stiffness

S_{ij} = single crystal elastic compliance

$\bar{C}_{ij}$ = aggregrate elastic stiffness

$\bar{S}_{ij}$ = aggregrate elastic compliance

E = Young's modulus

μ = shear modulus

ν = Poisson's ratio

V = volume fraction of total porosity

U = volume fraction of closed porosity

K = bulk modulus

p = pressure

F = compressive load

s = stress

s_f = fracture stress

e = strain

e_m = strain at 600 psi

e_f = strain to failure

γ = surface energy

c = crack length

d = density

S = probability of fracture

T = temperature

CHAPTER 1

INTRODUCTION

With the use of graphite in the nuclear and other high technology industries, there has been a rapid increase in the number of research publications regarding the properties of this material. The vast amount of technical information available on graphite today signifies the enormous efforts scientists and engineers have contributed towards the understanding and exploitation of graphite for service.

In natural form graphite exists as single crystals of often quite remarkable perfection. It shows a planar morphology and a brilliant silvery surface. The ideal crystal density is 2.265 g/cm^3 (1 g/cm^3 = 1 t/m^3). In polycrystalline form, graphite is dark grey in colour. It is rather porous with a density considerably lower than that of the single crystals. Artificial graphites are well-graphitised polycrystalline materials manufactured from filler particles, usually formed with a binder and impregnated to increase density. Typical densities of the manufactured products range from 1.7 to 1.9 g/cm^3 with some 20 - 30% total porosity. The material contains a wide spectrum of pores, from microcracks to large voids, which arise mainly from the manufacturing processes or are inherent from the raw materials.

Graphite has a wide range of applications. Besides its original use as electrodes and brushes, its stability at high temperatures and chemical inertness has led to widespread use in crucibles and various resistance furnaces. Its low surface friction makes it an ideal material for bearings in the engineering industry. There are also more specialised uses such as rocket nozzles and guide vanes, nose-cones and high temperature heat exchangers. Apart from these the major use of graphite is in the nuclear power industry. It is used extensively as neutron moderator and fuel sleeve material in nuclear fission reactors because of its low neutron absorption cross-section

and its remarkable refractory properties.

In the United Kingdom the Advanced Gas-cooled Reactors (A.G.R.) operate at a coolant pressure of 600 psi (4.14 MPa). Polycrystalline graphite used as moderator material in the reactors has a density less than ideal with the presence of closed and open porosity. These will affect its bulk compressibility under pressure. Apart from the problems of irradiation damage, the effective compliance of graphite [1-3] is known to contribute to the radiation-induced creep strain. This could lead to a volumetric creep in reactor graphites under a neutron flux which should be added to the usual dimensional changes which are obtained essentially under irradiation at ambient pressure.

The purpose of the work reported here is to investigate the deformation of four types of graphites under pressures up to 600 psi. Cylindrical graphite specimens are subjected to a few pressure cycles of loading-unloading and dimensional changes are measured using resistance strain gauges. The effect of increasing the closed porosity of graphite specimens on the hydrostatic deformation is investigated. This is achieved by coating the specimens with a flexible rubber layer which prevents the pressure fluid from penetrating the open pores during the pressure tests. The porosity values of each graphite are determined using the Beckman air comparison pycnometer. The effect of compressive pre-stressing on the hydrostatic deformation of graphite is also investigated in this work. Elevated temperature test is carried out in which the specimen is subjected to a pressure of 600 psi while the test temperature is raised from 20°C to 300°C. Uniaxial compression tests are included to provide useful data such as Young's modulus, Poisson's ratio and fracture stress. Neutron irradiated sleeve graphites of three different doses are also employed for the hydrostatic tests. Annealing of some of the irradiated specimens is conducted at 2350°C to investigate the effect of annealing on the pressure-

strain curve. Finally 4-point bend testing of graphite is carried out under a pressure of 600 psi to study the effect of pressure on the bend strength. The bend test is performed on a stainless steel pressure vessel which is specially designed to enable 4-point bend testing of graphite beams at atmospheric pressure and at 600 psi.

A description of the structure and manufacture of graphite is given in chapter 2 while chapter 3 is a brief review on the physical and mechanical properties of graphite. Since strain gauges are used extensively in this work chapter 4 deals with the basic instrumentation of strain gauges. Chapter 5 gives an account of the test materials, experimental equipments and methods. The results are presented in chapter 6 while the analysis and interpretation of the results are discussed in chapter 7. The concluding remarks are summarised in chapter 8.

CHAPTER 2

MANUFACTURE OF GRAPHITE

Graphite is an allotropic form of the element carbon consisting of layers of hexagonally arranged carbon atoms in a planar condensed ring system. The layers are stacked parallel to each other. There are two allotropic forms with different stacking arrangements, hexagonal and rhombohedral. The chemical bonds within the layers are covalent while the bonds between the layers are of van der Waals type. Hexagonal graphite is the thermodynamically stable form of graphite with an ABAB stacking sequence of the hexagonal layers where alternate layers repeat exactly, while adjacent layers are displaced so that half the carbon atoms lie above the centres of the hexagons in the adjacent layers (fig. 2.1). The interlayer spacing or "c" spacing is 0.335 nm, whilst the atomic separation within layers is 0.142 nm. The crystal density is 2.265 g/cm^3. Rhombohedral graphite is a thermodynamically unstable form of graphite with an ABCABC stacking sequence of the layers. The structure of rhombohedral graphite can be best considered as an extended stacking fault repeated in the hexagonal form. The rhombohedral form is produced by shear derformation of hexagonal graphite and will transform to the hexagonal form upon heat treatment.

Graphite for commercial usage is produced artificially. There are several methods of manufacture and a common one is the Acheson process [4]. The flow diagram in fig.2.2 shows the different stages of manufacture of pure graphite for the nuclear industry. The starting materials consist of carbonaceous filler particles and a binder. The filler material can either be raw petroleum coke or pitch coke or coke from other sources. The binder is usually coal tar pitch which has a softening point of around 100°C. The coke product is broken up and then calcined at 1300°C to remove volatile hydrocarbon content and prevent excessive shrinkage of the coke particles in

later heat-treatments. The calcined coke is then crushed into small particles of size ranging from 0.4 mm to 10 mm. The structure and properties of the crushed coke particles depend on the coke sources and they are important in determining the properties of the final manufactured article. Particles of different sizes are mixed together according to manufacturing specifications and then blended with coal tar pitch to produce a plastic mix where the pitch is able to flow freely around the coke particles. The plastic mixture is then formed into shape by either extrusion or moulding. The forming process affects the properties of the manufactured artefact as particles with a long axis tend to lie parallel to the extrusion direction or perpendicular to the pressing direction. The formed body or the "green article" is ba ked to coke the pitch binder at about 1000°C for a period of 30 to 70 days during which time the pitch changes from thermoplastic material to infusible solid. The baking cycle volatilises about one-third of the pitch content. The resulting baked article shows a loss in density which can then be increased by impregnating with additional pitch and reba king to pyrolise the impregnant carbon in the pores. Useful increases in density and other physical properties are obtained with up to six impregnations but two to three impregnations are more common. Graphtisation of the baked article is then carried out at about 2800°C in an Acheson furnace where crystallite growth occurs and the material is converted into an ordered polycrystalline structure. The whole process lasts approximately 15 days and results in a marked increase in the dimensions of the crystallites and also in an improvement of the structural perfection of these crystallites in the graphitised materials.

The microstructures of the final graphite body can be seen in fig.2.3 where the elongated coke particles or grains (for example,needle coke) align themselves parallel to the extrusion direction. The two constituents, coke grains and binder, are clearly distinguishable in that the coke grains are discrete and striated while the binder forms a more or less continuous matrix

with random structure. The majority of the large pores appear in the binder since this gives off volatiles in heat treatment during manufacture

The coke grains are made up of individual crystallites which are themselves preferentially oriented within the coke grains [5-7]. As a result the bulk material will show anisotropic properties when tested in different directions. On the other hand if the grains are spherical and the crystallites have no preferred orientation (for example, the gilsonite coke), the resultant graphite is isotropic in nature. The carbon atoms within the crystallites themselves are built up in a layer pattern. The structural perfection and dimensions of these crystallites vary from graphite to graphite. Crystallite size, Lc, of up to 150 nm and crystallite diameters of the order 300 nm have been dertermined [8]. The voids between the crystallites are known as micropores while larger voids between the grains are known as macropores. Micropores are formed due to the differential thermal contraction of the crystallites when cooled from graphitisation temperature [9]. Macropores are produced from the release of gases during manufacture or simply the mismatch of the coke grains. These voids or pores have size ranged from 1 nm to many μm and they affect the physical and mechanical properties of the bulk graphite.

Another important development in graphite production has been the pyrolysis of industrial hydrocarbons to produce pyrolytic graphite. In this process, a stream of gas is passed over a heated substrate where pure carbon may be deposited in different structural forms depending on the deposition conditions. The pyrolysis conditions can be suitably adjusted such that the deposit takes the form of highly oriented layers and large slabs of quite pure and perfect single crystals can be produced with density approaching that of an ideal crystal.

CHAPTER 3

PROPERTIES OF POLYCRYSTALLINE GRAPHITE

3.1 Mechanical properties

Commercial polycrystalline graphite is generally a weak and brittle solid. Its strength is commonly measured in tension, flexure and compression with values increasing in that order. The tensile strengths at room temperature are typically in the range 10 to 30 MPa [10] while the tensile strains to failure are in the range 0.1 to 0.3%. However some high strength graphites have values considerably higher than those quoted above. Compressive strengths are typically higher than the tensile strengths by a factor of 3 to 4 and the bend strengths are normally 1.3 to 1.5 times higher than the tensile strengths. The strength of graphites is known to increase with temperature and reaches about twice the room temperature strength at about 2000 - 2500°C [11-13]. This makes graphite a prime candidate for structural components operating at high temperatures.

The stress-strain behaviour of graphite is well-known for its non-linearity with stress, with hysteresis loops formed under cyclic stressing and permanent deformation (set) on removal of the applied stress. Many investigations on this area have been reported in the past. For instance Losty and Orchard [14] obtained non-linear stress-strain curves of the form shown in fig.3.1. Under uniaxial tension the loading curves are always convex with respect to the strain axis while the unloading curves are always concave with permanenet sets produced at zero stress. The permanent set increases when the previous maximum stress reached in loading increases. The stress-strain curves obtained after a range of pre-stressing up to the fracture stress are all parallel at low stress and Young's modulus is obtained from these slopes. Similar effects occur in compression but the hysteresis loops are larger since the maximum applied stress before fracture is much higher. The series of

hysteresis loops obtained in the stress-strain curves is a direct indication of the damping characteristics of graphite when subjected to cyclic stressing [15]. The damping is associated with the strain energy lost during a stress cycle of loading and unloading.

Seldin [16] conducted a series of investigations on both the longitudinal and transverse stress-strain properties of several graphites in tension and compression as well as a combination of both tests alternately. Under uniaxial tension he demonstrated that the longitudinal and transverse data, when taken together, showed an overall increase in volume after the tensile test due to the positive permanent sets in both directions. These permanent sets would be relieved by a high temperature anneal such that there was an excellent correlation between the original stress-strain curves and those obtained after the first anneal. The recovery of permanent sets of graphite by annealing was also observed by Andrew et al. [17] and Davidson et al. [18]. Greenstreet et al. [19] investigated the size effects and stress gradient upon the material behaviour of EGGR-type Agot graphite in flexural and uniaxial tests. Size effects such as volume and cross-sectional area were reported to be small or non-existent within the size range investigated.

In the past a number of attempts [20-24] have been made to describe the stress-strain curves of graphite based on phenomenological models or simple theories of deformation. Marion Birch [8] in her thesis investigated the applicability of these models to the stress-strain results she obtained and showed that the equation of the form proposed by Wooley [22] was the best fit for both the unirradiated and irradiated Gilsocarbon graphite under compression (see fig.3.2 and 3.3).

Conventional graphite contains a wide spectrum of pores which may be accessible or inacessible to a gas and give rise to the so-called open and closed porosity. Since some 20% of the total volume is occupied by pores, the properties of the polycrystalline materials are affected by the existence

of such pores. Hutcheon et al. [25] investigated the dependence of the properties of graphite on porosity. The starting material was a large block of amorphous carbon which was cut into specimens and then impregnated at various stages. All the impregnated specimens were then graphitised at 2700°C in argon. Their results showed that sucessive impregnations increased the bulk density from 1.62 to 1.87 g/cm^3. Other properties such as thermal conductvity, thermal expasion, Young's modulus and bend strengths also increased after impregnations. They interpreted their results following the arguments of Mackenzie [26] and obtained a simple relation (for Young's modulus, E) of the form

$$E = Eo (1 - kV)$$

where V is the total voidage, k is a constant and Eo is the values of E at zero voidage. They found a linear relationship of E with voidage (see fig.3.4) and obtained a value of 2.8 for k and Eo of 1.22×10^6 psi. A similar expression was also obtained for thermal conductivity which again showed a linear relationship with total voidage. Bulk thermal expansion was found to increase approximately linearly with closed voidage whereas strength varied as a power function of voidage. Other investigations on the relationship between elastic modulus, E and voidage (porosity), V, had been conducted by Hasselman [27] and Spriggs [28] and the expressions obtained were as follows:

1) $E = Eo\ (1-V)/(1-bV)$ due to Hasselman, and

2) $E = Eo \exp(-cV)$ due to Spriggs

where b and c are constants and Eo is the value of E at zero porosity.

In graphite moderated reactors cooled by CO_2, some degree of oxidation will occur due to the absorption of radiation energy in the gas contained in the open pores of the material. This causes the CO_2 to break down into active spechies which attack the graphite resulting in a weight loss of the material. Brocklehurst et al. [29] investigated the effect of this radiolytic oxidation on the properties of PGA (Pile Grade A) and isotropic

reactor graphites for weight loss of up to 35%. The effects of the oxidation are separated from the effects due to radiation damage by careful thermal annealing of the latter. Properties such as thermal conductivity, Young's modulus and strength were reported to decrease with increasing weight loss associated with increasing porosity.

Jenkins et al. [30] reported the existence of thermal cycling creep in graphite. They subjected specimens of PGA graphite to torsional dead-weight loading and temperature cycles of 50-350-50°C and 350-50-350°C. It was found that all the creep strain occurs in the first cycle. The strain is dependent on the temperature difference in a cycle but independent of the direction of the cycle. They explained the creep strain in terms of the internal strain generation due to the large differential thermal expansion of the graphite crystallites as the graphite is thermally cycled under an external load. This strain is sufficient to bring a fraction of the crystallites to the yield point and these deform under the external load.

Visual observations of micro-crack formation prior to ultimate failure have been reported in several investigations [31-34]. Jenkins [31] monitored controlled crack growth of reactor grade graphite by bending thin strip specimens bonded to a brass strip, and observing under a microscope the sequence of events in the plane of maximum stress subjected to increasing uniform strain. He observed that fracture proceeds preferentially along striations within the highly oriented structure of grist particles and that cracks travel between pores and isolated cracks appear before major fracture. Slagle [32] used a controlled brittle ring test on graphite specimens loaded in compression across its diameter. He observed the sequential propagation of cracks under increasing load and reported that cracks appear to initiate preferentially at the boundaries of existing pores. There is evidence for a build-up in crack density as original cracks stabilised at pores and new ones formed. From observation of the microphotographs on the

sucessive growth of cracks in nuclear grade graphites subjected to increasing compressive stress, Oku and Eto [34] concluded that crack growth becomes noticeable above a stress level of about 60% of the compressive failure stress.

Associated with the formation of micro-cracks prior to ultimate failure, other studies [14,35-37] on the effect of pre-stressing have shown a decrease in Young's modulus with pre-stressing. Jenkins [31] concluded from his investigation that localised cracking occurs prior to fracture and the effect of the pre-stressing is such that the nearer the stress approaches a critical value, the greater the probability of localised cracking and the greater the decrease in modulus. Hall [36] pre-compressed reactor grade graphite specimens to 6.9 MPa and 20.7 MPa. After measuring the dynamic Young's modulus, he annealed them in vacuum in increasing temperatures up to 2000°C. The Young's modulus was found to increase with annealing temperature. After annealing at 1500°C, the modulus of the specimens pre-compressed to 6.9 MPa had reached the original unstressed values while the other specimens (20.7 MPa) had increased their moduli by about 20% of the stressed values (see fig.3.5). From these results he concluded that at low pre-stress level the fall in modulus is due entirely to an increase in dislocation density which would recover completely following thermal annealing. However, at higher pre-stress level micro-cracking occurs and the fall in modulus due to this would not be recoverable.

3.2 Hydrostatic deformation

The behaviour of polycrystalline graphite under high pressures of up to 15 kbars (1 kbar = 100.5 MPa) was reported by Kmetko et al. [38]. Specimens of AUC graphite were tested in two conditions:

1) when encased in a thin copper jacket sealed with solder to prevent the pressure transmitting fluid (pentane) from penetrating the pores of the

graphite; and

2) when not jacketed to allow the pentane to penetrate the pores.

Dimensional changes were measured using a dilatometer located inside the pressure vessel. Their results showed a marked difference in behaviour for the two conditions of test specimens. The displacement observed for the jacketed specimen was very non-linear and very much greater that that of the unjacketed one (see fig.3.6). Initially, the jacketed graphite was highly compressible under pressure with an average linear compressibility of about 42.4×10^{-6} per bar. From 5 kbars (500 MPa) onwards the displacement was not so large and had become quite linear and the linear compressibility had decreased to about 0.82×10^{-6} per bar (fig.3.6). The displacement for the unjacketed specimen was very small and quite linear over the entire range with an average linear compressibility of about 0.28×10^{-6} per bar. The authors attributed this difference in behaviour to be due to the effects of porosity of the AUC graphite. For the unjacketed specimen the pressure fluid is able to penetrate the pores and compress the individual crystallites comprising the rigid cross-linked network in the material. On the other hand, when the pressure fluid is excluded from the pores (as in the case of the jacketed specimen) the pressure is only applied to the outer boundary of the material and the entire network of crystallites including porosity is compressed as a whole. The large deformation of the jacketed specimen under pressure showed a large reduction in porosity. It was reported that at pressure above 6 kbars, virtually all the porosity has been eliminated and the average volume compressibility is about 3.03×10^{-6} per bar. This value is very close to Bridgeman's value [39] of 2.96×10^{-6} per bar for natural ceylon graphite.

Paterson and Edmon [40] observed the effects of high confining pressures on the compressive stress-strain response of a porous polycrystalline graphite. Specimens of 10 mm diameter and 20 mm length

were obtained from EY9 electrographite. The apparatus consisted of a pressure vessel containing a fluid medium to which a piston was introduced to apply a superposed axial load on the specimen. The confining pressures (from 1 to 8 kbars) were independently controlled and measured. The specimen was sealed in a copper jacket 0.25 mm thick, closed with steel end pieces and forced fitted sealing rings. The stress was expressed as differential stress which was the difference between the axial stress and the confining pressures. Their results showed that the compressive stress-strain curves are very much dependent on the confining pressures (see fig.3.7). Considerable volume changes are observed during the axial straining as well as during the application of pressure. There is a volume decrease during straining under pressure and this is additional to the initial decrease due to the confining pressure. The decrease in volume during straining becomes much less at higher pressures (see fig.3.8). The four stages of volume changes at each confining pressure are shown in fig.3.9 where stage 1 is the application of the confining pressure, stage 2 the axial load, stage 3 the removal of the axial load and stage 4 the removal of the confining pressure. There is almost complete recovery of both length and volume during the release of confining pressure after strains of up to 20%. The authors attributed the remarkable recovery effects to the presence of internal stresses introduced during the high pressure experiment and these stresses give rise to internal strain when the pressure is released. The internal stresses are possibly due to the bending of graphite platlets or the elastic back-stress present in the ligaments which have deformed into the porosity during the initial deformation under pressure. Frictional forces would inhibit the release of elastic stresses remaining in the bent platelets while the confining pressure is maintained but this inhibition would be removed as the pressure is released. It was concluded that, in addition to basal slip, frictional sliding on internal surfaces is an important mechanism of deformation and that the deformation is

accompanied by some process such as flexure of graphite platelets which introduces the internal stresses responsible for the recovery effects.

Jortner [41] also reported behaviour of polycrystalline graphite under hydrostatic pressures of up to 20000 psi (138 MPa). ATJ-S graphite specimens were coated with a flexible rubber layer known commercially as M-coat C. Strains were measured in the with-grain direction as well as the across-grain direction using resistance strain gauges. The high pressure experiments were also carried out for the uncoated specimens of the same material. He reported a very non-linear pressure-strain response for the coated specimen during pressure loading up to 20000 psi. On unloading, the pressure-strain curve follows a different path showing significant hysteresis effects. A permanent compressive strain is produced at zero pressure (atmospheric pressure) after unloading from pressure levels higher than 1000 psi (6.9 MPa). Repressurisation to the same pressure level would produce strains which follow a resonable extrapolation of the pressure trend (see fig 3.10). These features show that the behaviour of the coated material under hydrostatic deformation is quite similar to the stress-strain response observed in uniaxial compression tests. However the strains measured on the coated specimens are smaller than those measured in the uniaxial compression test. Generally, the strains in the with-grain direction are less than those in the across-grain direction (see fig.3.11). The pressure-strain behaviour for the uncoated specimens is entirely different. At pressures higher than about 2000 psi (13.8 MPa), the uncoated material shows much smaller strains and the strain response appears to stiffen as pressure is increased further. At pressures higher than about 20 000 psi the strains are only about one-tenth of those observed in the coated material (see fig.3.12). Jortner explained the marked difference in deformation between the coated and uncoated specimens to be due to the porosity of the ATJ-S graphite. The results for both types of specimens are different from the behaviour of a non-

porous body. In a non-porous body shear stresses are not produced by hydrostatic pressurisation and only elastic behaviour would be observed. For the coated material with no forces exerting on the surface of the pores, localised shear stresses will be established and plastic deformation due to dislocation glide can occur. When all the pores are filled with the pressure fluid the stress state through the uncoated material would be triaxial with no shear stresses to produce plastic flow and with no tendency for the pores to collapse. Under such conditions the pressure-strain behaviour should correspond to the elastic behaviour of an "ideal" polycrystalline graphite which is stiffer than that measured in uniaxial tests. Measurements of the open porosity of ATJ-S graphite by the mercury intrusion technique, as reported by Jortner, indicated that at mercury pressure above 2000 psi the open pore volume increased rapidly so that at 14000 psi, the open pore volume was greater than that measured in helium. This was attributed to the mechanical action of the mercury pressure which could fracture walls enclosing closed pores or enlarge any pre-existing passage between closed pores. The rapid increase in the open pore volume occurred at 2000 psi which was the critical pressure necessary to cause previously closed pores to become accessible. This critical pressure also corresponded approximately to the pressure at which the strain responses to hydrostatic pressurisation diverge from the simple elastic prediction.

3.3 Effects of fast neutron irradiation

One of the major uses of graphite is as neutron moderator in nuclear reactors. Its low atomic mass and low neutron absorption cross-section enable it to slow down fast neutrons without much loss of neutron density. Due to the large amount of kinetic energy which has to be disposed of many carbon atoms will be displaced from the proper sites and come to rest in metastable states. This can cause changes in dimensions and lattice

parameters. Neutrons emitted from the fission process have an average energy of 2 MeV. These neutrons move freely through the graphite lattice until they collide with a particular atom, which is ejected from its lattice site. This carbon atom, known as a primary "knock-on", has considerable kinetic energy which it loses either by electron excitation or by displacing more carbon atoms which themselves displace further atoms until there is no longer sufficient energy for further atomic displacement. The displaced atoms can combine to form lattice defects such as sub-microscopic clusters of a few atoms (2 - 6) or interstitial loops which grow by collecting diffusing interstitial atoms (see fig.3.13). In addition vacancy and small group of vacant lattice sites are also produced [42-44].

In the United Kingdom the irradiations of PGA graphite provided a vast amount of data on dimensional changes needed for the Magnox reactors. The irradiation behaviour of PGA graphite [44] is shown in fig.3.14 and 3.15. The results showed a complex pattern of behaviour with growth in the direction perpendicular to extrusion for temperature below 300°C and shrinkage in the same direction at higher temperatures. The parallel to extrusion direction shrunk at all of the temperatures investigated. The early PGA graphite used in the Magnox reactors could not be used to the doses proposed for the AGR reactors due to the large shrinkages in the direction parallel to extrusion at high neutron doses. The considerations (based on thermal expansion coefficients and the crystal dimensional changes) were applied to develop a graphite of adequate dimensional stability. By restricting the modera tor temperature to the range 270 - 550°C, it was found possible to produce high thermal expansion isotropic graphites of adequate dimensional stability on a large scale. Very high flux irradiations were undertaken to obtain the necessary high dose data on these graphites. The results are shown in fig.3.16. The graphites all tend to contract up to 2-3% linearly and then change to growth. The growth occurred earlier at higher

temperatures. However, up to doses of $2x10^{22}$ n/cm^2 (EDN) this behaviour was satisfactory for reactor design. Measurements of the porosity by helium density and mercury porosimetry showed that the high dose growth was due to the generation of pores.

Other studies on the irradiation behaviour of nuclear graphites [45-47] also confirmed the following points. The initial contraction in the direction that is predominantly influenced by the c-axis properties of the crystallites is followed by expansion at high fluences. In the direction predominantly influenced by the a-axis properties of the crystallites the initial contraction continued to higher fluences before expansion again. Volumetric changes were similar: initial densification followed by a rapid expansion. The initial contraction occurred because the c-axis expansion was partially accommodated in the available porosity while a-axis shrinkage of the crystallites was transmitted more directly to the bulk material. This densification process continued as the neutron flux increased until all the pores were exhausted and the c-axis expansion of the crystallites was able to be transmitted to the bulk material. This marked the on-set of the expansion phase where large pores were formed between the filler particles at high doses and accounted for the large volume expansion of the graphites.

The initial effect of fast neutron irradiation on polycrystalline graphite is to increase the mean strength and Young's modulus. This has been attributed to dislocation pinning by small irradiation-induced defects within the graphite crystals. The increases are initially rapid and tend to saturate at a level which decreases with increasing irradiation temperature. The amount of increase in the Young's modulus varies between different types of graphites, the amount for a poorly graphitized type being lower than the more highly graphitized type. For some graphites, there is a difference between directions parallel and perpendicular to extrusion; a greater increase in E being observed in the perpendicular direction for a given dose and

temperature [48-50]. Kelly et al. [51] irradiated PGA graphite up to a dose of 6.3×10^{20} n.v.t. The Young's modulus measured in both parallel and perpendicular directions showed a tendency to saturate at a level of E/Eo of 1.5 where Eo is the original unirradiated modulus. Upon annealing, the modulus decreased as the annealing temperature increased. However, their results showed that for annealing temperatures above 1500°C in the control samples and a little higher in the irradiated samples, the modulus fell below that of the virgin material, the decrease continuing steadily right up to the highest annealing temperature (see fig.3.17). Birch and Bacon [52] conducted a study on the effects of fast neutron irradiation on the mechanical properties of a Gilsocarbon nuclear grade graphite. The maximum neutron dose reached was 1.14×10^{19} n/cm². It was found that the dynamic Young's modulus increased with neutron dose reaching saturation at a value 2.4 times the unirradiated value (see fig. 3.18). The static Young's modulus also reached 2.5 times the unirradiated value after a dose of 6×10^{18} n/cm². The linearity of the compressive stress-strain curve increased and the hysteresis losses decreased. The fracture stress was found to double while the fracture strain decreased by 24%. Upon subsequent thermal annealing the Young's modulus decreased and had almost reached its unirradiated value by 400°C. The fracture stress also decreased toward its unirradiated value and the hysteresis losses increased.

CHAPTER 4

STRAIN GAUGE INSTRUMENTATION

Strain gauges were used extensively in this work to measure the dimensional changes of polycrystalline graphite under pressure. This chapter describes the selection, installation, accuracy and temperature effects of strain gauges employed in strain measurements.

4.1 Strain gauge selection

The conventional resistance strain gauge is produced from a photo-etched metal foil which has a grid pattern mounted on a plastic backing. The gauge length is the strain-sensitive length of the grid. The plastic backing provides a means for handling the foil pattern during installation. It also presents a readily bondable surface for cementing the metal foil to the test piece and provides electrical insulation between them. A wide range of strain gauges are available in the market offering strain analysts different choices of strain-sensing alloys, backing materials, gauge pattern and resistance as well as other configuration options. The strain gauges selected for use in this work were the WK series from Welwyn Strain Measurements Ltd. The WK gauges are a family of fully encapsulated nikel-chromium alloy (a modified karma or k-alloy in self-temperature compensated form) strain gauges used in both experimental stress analysis and transducer applications. These gauges are characterized by good fatigue life and excellent stability and are recommended for accurate static strain measurements over long period. They also have an operating temperature range of -269°C to 290°C (or 400°C over short periods) for continuous use in static strain measurements. In addition k-alloy offers a much flatter apparent strain curve (see later) which permits more accurate correction for apparent strain errors at temperature extremes. The S.T.C. (self-temperature-compensation) numbers in k-alloy

also match the thermal expansion coefficients of various graphites used in this work. The WK gauges are supplied with high endurance lead wires which eliminate delicate soldering work on the gauges. Strain gauges with lengths of 3 mm and 6mm were selected with a gauge resistance of 350 ohms and a gauge factor from 2.01 to 2.05.

4.2 Strain gauge installation

In this work strain measurements were required in the longitudinal and circumferential directions of cylindrical specimens. Hence two WK gauges were needed for every graphite specimen under test. The adhesive used was M-Bond 200 and catalyst. The bonding area on the specimen was first prepared by degreasing and polishing it with 400-grit silicon-carbide paper followed by cleaning with M-prep neutralizer. A gauge was placed on a clean flat surface (e.g. on top of the gauge box) with the bond side of the gauge facing downward. Solder terminals were positioned adjacent to the gauge with the lead wires at the far side (see fig.4.1). A piece of cellophane tape was slowly brought into contact with the gauge and solder terminals and was then lifted at a shallow angle. The gauge/tape assembly (fig.4.1) was positioned on the bonding surface of the specimen. A drop of the adhesive was applied on the bonding surface of the specimen while the catalyst was applied on the back of the gauge and solder terminals. The gauge/tape assembly was eventually brought into contact with the bonding surface of the specimen and was held there firmly for about two minutes. The tape was then removed from the the gauge installation. The wiring was carried out by bending the lead wires backward and soldering them onto the solder terminals. The external connection was made by soldering appropriate wires onto the same terminals. The gauge installation was then protected by coating over it with M-coat C which is a siliconerubber layer. For elevated temperature operation the adhesive used was M-bond 610 which is a high

performance epoxy resin. A thin layer of this adhesive was applied to the back of the gauge and the bonding area of the specimen. After air-drying for 30 minutes the gauge/tape assembly was positioned on the specimen. This was covered by a thin sheet of teflon tape followed by a thick silicone gum pad. A back-up aluminium plate was used to wrap round the specimen while pressure was applied on the plate through three equally spaced wires. The whole assembly was then put in a furnace where temperature was slowly raised to about 200°C and held there for about one hour to cure the adhesive. Upon completion of the curing cycle the temperature in the furnace was allowed to cool slowly to 50°C before the specimen was removed from the furnace. The wiring procedure was carried out as described earier.

4.3 Strain measurements

Strain measurements were made using the BAM bridge amplifier and meter (referred to later as the bridge meter) manufactured by Vishay Instruments Inc. This bridge meter is a battery operated instrument supplying bridge excitation up to 12 V d.c. Static strain outputs can be read directly on the self-contained deflection meter or through an external recorder. The bridge meter could be calibrated to give full-scale deflection corresponding to the maximum strain expected in a test. A quarter bridge circuitry was employed where the external wires of the strain gauge were connected to one active arm of the wheastone bridge. For a more stable operation, a 3-wire configuration was used for connecting the strain gauge to the bridge meter to eliminate drift due to temperature difference on the lead wires (see fig.4.2).

4.4 Accuracy considerations

The absolute accuracy of strain measurements by means of strain gauges is limited in the sense that individual gauges cannot be calibrated prior to use. Once a gauge is installed it cannot be removed without damage.

Hence strain gauge users have to rely on the gauge factor (a factor relating the fractional change in resistance to the fractional change in length) supplied by the gauge manufacturers which have been obtained by destructive calibration of a certain number of gauges per batch. For the WK gauges there is a variation of ±1% in the gauge factor and ±0.3% in the gauge resistance. Considering also the accuracy of the internal shunt calibration (±1%) and the linearity of the deflection meter (±0.5% full-scale) of the bridge meter, an overall accuracy of at least ±3% could be achieved by carefully executed strain measurements.

Since most of the work described here involved the application of pressure on the test specimens, it is essential to discuss the effects of pressure on the performance of strain gauges. These pressure effects have been the subject of many investigations. Milligan [53-55] obtained linear pressure-strain curves for strain gauges mounted on flat surfaces as well as concave and convex surfaces subjected to pressure up to 140000 psi (966 MPa). The linear strains due to pressure were compared with the compressibility constant (1 - 2v)/ Eo where Eo and v were de termined experimentally from uniaxial tests. The slight deviation between the two constants could be corrected due to the linear response from strain gauges. Gerdeen [56] also obtained calibration curves of pressure effects for flat and curved surfaces and reported that curvature correction factors were not necessary for convex radii of curvature greater than 0.25 inches and for concave radii greater than 0.80 inches. Brace [57] developed a simple theory to explain the pressure effects on strain gauges and predicted a value of 0.07×10^{-6} per bar as opposed to 0.06 to 0.12×10^{-6} per bar observed by Milligan and Gerdeen. A separate investigation [58] showed success with strain gauges up to 20000 psi (138 MPa) with a pressure effect of 0.5 to 3.5 microstrains per 1000 psi. Since the maximum pressure used in this work was only 600 psi (4.14 MPa), the pressure effect was negligible and quite accurate

strain measurements could be obtained by using resistance strain gauges. Other strain measurements of polycrystalline graphite have also been made using strain gauges. Both Greenstreet et al. [19] and Seldin [16] employed strain gauges in the uniaxial testing of graphite and obtained stress-strain curves in different directions. Jortner [41] also reported success in using strain gauges on the hydrostatic deformation of ATJ-S graphite up to a pressure of 20 000 psi.

4.5 Strain gauge temperature effects

When there is a change in temperature in the test environment the gauge installation will register an "apparent strain" due to the change in gauge resistance. For strain measurements at elevated temperatures the apparent strains have to be accounted for to give the actual strain due to the applied stress. The WK gauges have much smaller apparent strains over a wide temperature range when they are bonded to materials with thermal expansion coefficients for which they are intended. The apparent strains are then corrected using the data sheet supplied with the gauges. Since the apparent strain curve (see fig.4.3) provided by the manufacturers represents an average and there is some variation from gauge to gauge within a batch, the most accurate method is to obtain the apparent strain curve for each strain gauge installation on the actual test specimen. For the hydrostatic testing of graphite at elevated temperatures, individual apparent strain curves were obtained for all the test specimens. This involved raising the temperature of the specimen and recording the strain outputs while keeping the pressure at atmospheric condition. An apparent strain versus temperature curve was thus obtained which represented the correction data for that particular specimen. A detailed investigation on the apparent strain behaviour for graphite specimens is discussed in section 5.3.

CHAPTER 5

EXPERIMENTATION

5.1 Materials

Four different types of polycrystalline graphites were employed in this work. Two were isotropic in nature and they were designated Graphite A and B while the other two were anisotropic in nature and were designated C and D. All the graphites were supplied by UKAEA Springfields Nuclear Power Development Laboratories (SNPDL). The isotropic graphites are essentially the Gilsocarbon nuclear grade graphites. The raw material for this type of graphite is the Gilsonite coke which is made up of approximately spherical particles. After impregnations and graphitisation at 2700°C, the isotropic graphites have a density of around 1.8 g/cm^3. Graphite A is a nuclear grade Gilsocarbon material while graphite B is a moderator graphite used in the AGR reactors in the United Kingdom. Graphite C is a fuel sleeve material also used in the AGR reactors. Graphite D is essentially the Pile Grade A (PGA) graphite originally developed for use in the Magnox reactors. This graphite is made up of long dimension coke particles which have a preferential direction of alignment during manufacture. The coke particles are quite large in dimensions ($\sim$mm) and are quite clearly distinguishable from the binder (see fig.5.1). Specimens for uniaxial and hydrostatic testing were machined in the form of cylinders 25 mm in length and 20 mm in diameter.

Neutron irradiated sleeve graphite of the type similar to graphite C was also investigated. This graphite was obtained from the fuel sleeve material of the Hunterston reactor and the material had been subjected to a neutron flux of 0.7×10^{20} n/cm^2. A total of twelve specimens were received from SNPDL and they were machined in the form of cylinders 20 mm in length and 14 mm in diameter. Neutron irradiated graphites similar to type C

but of higher doses were also employed in the later stage of this work. Two samples of six specimens each were received from SNPDL for hydrostatic testing. Specimens from one sample were machined in the circumferential direction from a fuel sleeve and the irradiation burn-up was 9.5 GWd/te (equivalent dose of 11.0×10^{20} n/cm^2). Specimens from the other sample were machined in the axial direction from a fuel sleeve and the irradiation burn-up was 14.7 GWd/te (equivalent dose of 17.0×10^{20} n/cm^2). All specimens were cylinders of 25 mm length and 8 mm diameter.

Three graphites were employed for the bend tests under pressure. One was AGR moderator graphite (block S12,IJ) and the other two were fuel sleeve material (block 392 and 398). The bend specimens were graphite beams of 50 mm in length and a cross-section of 5 mm by 5 mm.

5.2 Experimental equipment and procedures

5.2.1 Compression tests

The compression equipment used was the floor model Instron (TT-CM-L) which has a maximum capacity of 5000 kg. This machine incorporates a highly-sensitive electronic weighing system with load cells which use bonded-wire strain gauges for detecting and recording the load applied to the specimen. The accuracy of the overall load weighing system is 0.5% of indicated load.

Uniaxial compression was performed on graphite specimens to obtain useful data such as static Young's modulus and Poisson's ratio. The outputs from the strain gauges mounted on the specimen were connected to two BAM bridge meters and the amplified strain signals were then connected to two separate y-inputs of a xy-recorder. The load signal was taken from the Instron and connected to the common x-input of the recorder. In this way, both the load and strain signals could be fed directly to the xy-recorder to produce compressive stress-strain curves in the longitudinal and

circumferential directions. The maximum compressive load reached was about 140 kg (which produces a stress of approximately 4.14 MPa on the specimen) and both the loading and unloading curves were simultaneously plotted on the chart paper of the xy-recorder.

Although the specimen was only subjected to a small compressive load, slight bending of the specimen during the initial application of load was observed due to the fact that the two anvils of the Instron were not truly parallel. This was overcome by placing a half-steel ball (one inch diameter) on top of the specimen during the compression test. As the upper anvil of the Instron pressed against the curvature of this half steel ball, the load was evenly applied to the end faces of the specimen. This eliminated the initial bending on the specimen and enables true stress-strain curves to be plotted.

Besides obtaining the stress-strain properties of various graphites used in this work, their compressive strengths were also obtained by compressing the specimens under the Instron until fracture occurred. Four specimens of each graphite were employed and the failure loads and strains were obtained from the chart recorder on the Instron.

5.2.2 Hydrostatic tests

Hydrostatic testing was performed in a stainless steel pressure vessel supplied by the UKAEA at Springfields. The pressure vessel is three and a half feet long with an inner diameter of about an inch. It was connected to an instrument panel which received external pressure from a cylinder of nitrogen gas. The instrument panel consists of a pressure gauge which was set to read zero at atmospheric pressure, a 750 p.s.i. bursting disc (safety valve) with a vent pipe and control valve for regulating the gas flow (see fig.5.2). External wires from the strain gauges were taken from the pressure vessel and connected to two bridge meters where the amplified strain signals were monitored to the y-inputs of a xy-recorder. The common x-input was

employed as the pressure input and was set manually.

For the hydrostatic testing, each cylindrical graphite specimen was subjected to pressures up to 600 psi (4.14 MPa) in increments of 100 psi. The longitudinal and circumferential strains at each pressure increment were recorded on the chart paper of the xy-recorder. When a pressure of 600 psi was reached, the pressure was slowly released to atmospheric condition (zero gauge pressure) in decrements of 100 psi. The two strains at each pressure decrement were also recorded. The loading and unloading pressure-strain cueves were plotted by joining all the data points and together they represented the deformation behaviour of graphite subjected to a complete pressure cycle. The whole test was repeated to investigate the effect of pressure cyclings on the deformation of graphite under pressure.

Coated specimens

Because of the porous nature of polycrystalline graphite the effect of porosity on the hydrostatic deformation was investigated. This was achieved by coating graphite specimens with a flexible layer which prevented the pressure fluid from penetrating the open pores. As a result pressure was only applied to the external surface of the coated specimens and a bulk deformation of graphite under pressure was achieved.

The coating used is known commercially as M-coat C which is a flexible silicone rubber layer used to protect strain gauge installations against moisture. Previously tested specimens were employed. Having checked that the strain gauge installations on the specimen were in good condition, a layer of M-coat C was applied on the specimen covering the entire surface, including part of the external wires that were in contact with the gauge terminals. The coating was then allowed to dry in air. This was followed by further coatings on the specimen to achieve a thick layer. Usually three or four successive coatings were necessary to give a flexible layer of sufficient thickness to withstand the pressure during the hydrostatic tests. The coated

specimen was put in a plastic bag for easy handling inside the pressure vessel. Hydrostatic testing of the coated specimen was carried out as described earlier.

Effect of gauge cement

Two specimens were taken to the laboratories at Springfields to investigate whether the application of gauge cement to part of a specimen surface affected the open porosity. The open and closed pore volumes were determined using a pyncometer (see later) before and after the gauge installations. The change in porosity values due to the applied cement were then evaluated.

5.2.3 Compressive pre-stressing

Compressive pre-stressing of graphite is known to affect its mechanical and physical properties [47-50]. For instance the Young's modulus is known to decrease as the level of pre-stressing increases. The effect of compressive pre-stressing on the hydrostatic deformation of polycrystalline graphite was also investigated in the present work.

Initially graphite A was tested in two methods as described below.

Test (1): Two specimens were employed. Strain gauges were mounted in the longitudinal and circumferential directions respectively. The specimens were then compressed in an Instron by uniaxial loading of magnitude F applied longitudinally. Values of F of 0, 300, 600, 900, 1200 and 1500 kg were uesd (100 kg produces a uniaxial stress of 3.02 MPa on the specimen). After each step of loading the specimens were hydrostatically tested to a pressure of 600 psi. The pressure loading and unloading curves were obtained for the pre-stressed specimens.

Test (2): Three different specimens were employed. They were subjected to a compressive load of 1500 kg. Strain gauges were then installed in the longitudinal, transverse and circumferential directions. The specimens were

then tested in pressures up to 600 psi. The results were compared with the earlier ones to determine if the compressive pre-stressing of specimens would affect the gauge installations as well as the performance of strain gauges in test (1).

Compressive pre-stressing was also performed on other graphites used in this work. Graphites A, B and C were subjected to a compressive load of 2000 kg (as in test (2)) while graphite D was only subjected to a load of 750 kg due to the low fracture load of this material. Hydrostatic testing was performed on the pre-stressed specimens and strains were measured in both the longitudinal and circumferential directions.

5.2.4 Irradiated specimens

Irradiated sleeve graphite from the Hunterston reactor was employed. The sleeve graphite had been previously subjected to a neutron dose of 0.7×10^{20} n/cm^2 and specimens of diameter 14 mm and length 20 mm were machined from it. Uniaxial compression was performed to obtain data such as Young's modulus and Poisson's ratio. Hydrostatic tests were carried out and strains were measured in the longitudinal and circumferential directions. The irradiated specimens were also coated with M-coat C and tested under pressure. Irradiated graphites also similar to graphite C but of higher doses were also investigated in the later work. Two types of specimens were employed with neutron doses of 11.0 and 17.0×10^{20} n/cm^2 respectively (see 5.1 for details). The specimens were cylinders of diameter 8 mm and length 20 mm. Due to the small size of the specimens, strain gauges were cemented in the longitudinal and circumferential directions on separate specimens which were then subjected to pressures up to 600 psi. They were also coated with M-coat C and tested under pressure.

Annealed specimens

Three neutron irradiated graphite specimens (specimen 106, 109

and 110) were sent to the UKAEA laboratories at Springfields to be annealed at 2350°C for one hour in an argon atmosphere to investigate the effect of annealing on the pressure-strain curves. One specimen (106) was previously tested while the other two (109 and 110) were untested. After the annealing, the specimens showed an average weight loss of about 0.4% which was due to the loss of volatile matter. Hydrostatic testing was carried out on the annealed specimens as described earlier.

5.2.5 Porosity measurements

The open and closed porosity of graphite specimens were measured using the Beckman Air Comparison Pycnometer which had been adapted to use helium and the reproducibility of volume measurement had been improved to 0.002 cm^3 (P.Schofield, private communication). The pycnometer consists of two chambers of equal volume and two pistons as illustra ted in fig.5.3. When there is no specimen in either chamber and with the coupling valve closed, any change in position of one piston must be duplicated by an identical stroke in the other in order to maintain the same pressure on each side of the differential pressure indicator. When both pistons are advanced to position 1 with a specimen of volume Vx in chamber B (see fig. 5.3), the pressures will not remain the same. However the pressures in the two chambers can be made equal by withdrawing piston B from position 2 to position 3, an amount equivalent in volume to Vx. The distance between positions 2 and 3 (dx) can be calibrated and made to read volume directly in terms of cubic centimeters via a digital counter. The open and closed pore volumes of a porous solid such as graphite can be measured by first measuring the bulk volume (Vb) and weight of a specimen to determine the bulk density. The solid plus closed pore volume (Vscp) of the specimen was then determined using the pycnometer. Knowing the crystal density (d_c) of graphite, the crystal volume (Vc) was then calculated from W/d_c where W is

the weight of the specimen. The open and closed pore volumes were then calculated as shown below:

$$\text{open pore volume (vol. \%)} = (Vb - Vscp)/Vb \times 100$$

$$\text{closed pore volume (vol. \%)} = (Vscp - Vc)/Vb \times 100$$

$$\text{total porosity (vol. \%)} = (Vb - Vc)/Vb \times 100$$

The porosity values of two specimens of each graphite were measured. The specimens of known porosity values were then tested under pressure in two conditions: uncoated and coated with M-coat C.

5.2.6 Elevated temperature tests

In the elevated temperature tests, graphite specimens were subjected to a constant pressure of 600 psi and the test temperature was raised from ambient condition (20°C) to an upper limit. The effect of raising the temperature on the deformation of graphite under pressure was investigated. The equipment used was the tubular pressure vessel (see 5.2.2), a Mayes furnace, a 3-zone temperature controller model TR 122-2Y and a Comark electronic thermometer. The constant temperature zone of the furnace was investigated by altering the three heating zones of the furnace through the controller and determining the temperature at various positions of the furnace after a fixed heating time. Fig.5.4 shows the temperature at different positions from the centre of the furnace tube. A constant temperature zone of seven inches was established in the centre of the furnace.

Strain gauges were used to measure the dimensional changes of graphite in the elevated temperature tests, the highest temperature reached in the tests was 300°C which is the limit specified by the gauge manufacturer for satisfactory operation for extended periods. Strain gauges of the correct S.T.C. numbers were selected to match the thermal expansion coefficients of the graphites under investigation. To obtain the most accurate apparent

strain data, it was essential that the individual strain gauge installation on the test specimen was examined. The procedure was carried out as follows. The test specimen was put inside the pressure vessel which rested on the furnace tube with both ends plugged with insulation material. With no pressure applied to the vessel the temperature of the furnace was raised while the temperature on the test specimen was closely monitored by a thermo-couple whose tip was placed 5 mm inside the specimen. The outputs of the thermo-couple were connected to the Comark thermometer where temperature could be read directly. With the pressure in the vessel maintained at atmospheric condition, the temperature of the specimen was raised from 20°C to 300°C and the corresponding strains as registered by the gauge installation were recorded on the chart paper of the xy-recorder. In this way a curve of temperature versus apparent strain could be plotted for the temperature range under investigation. The whole procedure was repeated until a reproducible apparent strain curve was obtained which represented a correction curve for that particular gauge installation. Other parameters such as the rate of heat input and the effects of heating and cooling on the apparent strain behaviour were also investigated and the results are reported in section 5.3.

Having obtained a consistent apparent strain curve for the test specimen, the elevated temperature test was then conducted by applying a constant pressure of 600 psi to the pressure vessel while the temperature of the specimen was raised from 20°C to 300°C. The temperature and the indicated strain (apparent strain + pressure induced strain) from 20°C to 300°C were recorded on the chart paper of the xy-recorder. A curve of temperature versus total strain was plotted. With the help of the apparent strain correction curve obtained earlier, the effect of varying the temperature on the deformation of graphite under constant pressure was observed. The results are presented in chapter 6.

5.2.7 Four-point bend test under pressure

The bend test rig is basicaly a stainless steel pressure vessel which contains special features to enable 4-point bend testing of graphite specimens under pressure. It was designed and made by SNPDL with minor modification being made subsequently at Liverpool. The vessel is in two parts (see fig.5.5). The lower part is a cylindrical can attached to a base plate for bench mounting. The top part (referred to here as the load column assembly) has a groove and O ring to be fitted tightly onto the lower vessel can to which it is locked securely by means of a "screw cap" (see fig.5.5). The load column assembly (see fig.5.6), besides being used as a closure for the vessel can, is an assembly of various parts that provide the loading mechanism. It contains two central shafts (shown as A and B in fig.5.7) coupled together, a cup-shaped load-cell holder with two inner knife edges, a round gear at the top of shaft A and a worm gear driven by a handle. A central pin is used to hold the load-cell holder, shaft B and the load column together. This pin also prevents shaft B from twisting and turning. Movement of the load-cell holder relative to the load column is made possible by sliding along two vertical slots on the cylindrical part of the load column (see fig.5.6 and 5.7). The handle is used to turn the worm gear which drives the round gear. This causes shaft A to rotate in a fixed position and shaft B to move vertically, thereby providing a driving mechanism for loading the load-cell and the inner knife edges. A pair of outer knife edges can be put in position in a specimen holder which sits at the bottom centre of the vessel can. There is only one orientation for the load column to be fitted in the vessel can to ensure that both pairs of knife edges are in the same plane. This is achieved by means of a location pin on the load column and a slot on the rim of the vessel can. The bend test rig can be connected to the instrument panel (see section 5.2.2) to receive external pressure from a cylinder of nitrogen gas. The load signal is taken from a cable of the load-cell and passes through the top of the load

column and is connected to a digital indicator. The indicator had been calibrated to read load in pounds to an accuracy of $\pm$ 0.1 lbs.

Initial testing and modification

When the equipment was delivered to the University and tested with a few trial specimens at atmospheric pressure, it was found that the loads recorded prior to specimen fracture were far too low and small residual loads were displayed on the indicator showing a frictional force existing in the moving parts of the load column assembly. On other occasions, no load was displayed during loading up to fracture indicating that the frictional force was quite substantial and could lead to erronous results. After many trials, this frictional force was eventually overcome by grinding and lubricating the moving parts as well as the central pin in the load column assembly. When tested with a few specimens the digital indicator would display steadily increasing loads until specimen fracture where the loads suddenly dropped to zero. This showed a satisfactory operation for the bend test rig at atmospheric pressure. When the equipment was tested at 600 psi. it was found that turning the round gear would not rotate shaft A due to the pressure acting on the seal being too high for the grub screw that held the round gear to the shaft. This was overcome by driving two grub screws through to the center of shaft A to hold firmly onto the gear. The cir-clip on the shaft that held the worm gear in position was also replaced by a pin through the shaft to withstand the load from the round gear. With further grinding and lubrication on the moving parts of the load column assembly, the bend test rig was finally in a satisfactory condition for operation at both atmospheric pressure and 600 psi. Later the equipment was modified to accommodate a circular protractor on top of the round gear to measure the angle through which the gear moved before the specimen was broken. The angular movement of the gear could then be calibrated to give the downward

displacement of the inner knife edges which in turn gives the deflection of the graphite beams.

The aim of the bend test was to investigate the effect of pressure on the bend strength of graphite. Initially the bend strength of graphite specimens at atmospheric pressure was determined. This was carried out by placing a specimen to rest on the outer knife edges on the specimen holder. Care was taken to ensure that the specimen was properly aligned with both ends well cleared of the specimen holder. The load column was then then slid onto the vessel can and locked in position with the screw cap. After fitting the protractor, the handle was turned anticlockwise to apply a load on the specimen. When the load-cell began to display a small load (0.1 lb) the angle on the protractor was noted. A slowly increasing load was then applied onto the bend specimen until fracture occurred. The fracture load was noted visually from the digital display unit together with the angle at fracture. These could then be evaluated to give the fracture stress and strain for a particular bend specimen. For bend test under pressure the procedure was similar except that a constant pressure was applied to the rig before applying a load to the bend specimen. The fracture load and angle would then give the fracture stress and strain under pressure. A total of 30 bend tests were performed on each of the three graphites supplied, 15 at atmospheric pressure and 15 at 600 psi. The results were analysed statistically.

5.3 Apparent strain investigation

Apparent strain is the strain registered by strain gauge installations due to a change of temperature in the test environment. Since this is different from the strain on the test piece due to the applied pressure, it must be correctly accounted for to avoid misleading results. As strain gauges are used in the present work, this section describes the lengthy work involved in the investigation of the apparent strain behaviour of strain gauges

installed on polycrystalline graphite.

5.3.1 Apparent strain behaviour of graphite A

The early investigation on graphite A was not satisfactory. The apparent strain curve was not of the same form as that supplied by the manufacturer (see fig.4.3). The apparent strains were very large and negative and increased rapidly with temperature (see fig.5.8). The apparent strain curve from the manufacturer was, on the other hand, rather flat for the temperature range under investigation. Hence it was suspected that the initial apparent strain curve was inaccurate and that the temperature recorded by the thermo-couple might not be the true temperature of the test specimen. Since the thermo-couple was close to the specimen but not in contact with the vessel wall, the specimen could be at a higher temperature than that measured by the thermo-couple. As a result the apparent strains obtained were larger than expected. In order to measure the true temperature of the specimen a small hole of 5 mm depth was drilled in the centre of a specimen face to accommodate the tip of the thermo-couple. This gave a much smaller apparent strain behaviour. After many tests which gave negative apparent strains, it was found that the apparent strain behaviour was very sensitive to the mis-match between the thermal expansion coefficients of the foil gauge and the graphite specimen. However, when a gauge which matched closely the thermal expansion of graphite A was used, the apparent strain curve (from 20°C to 250°) was found to be parabolic (see fig.5.9) and the strains were positive and also smaller. In another test the temperature was allowed to rise steadily and continuously to 250°C and then drop back to 20°C in continuous cooling. Two sets of apparent strain data were taken during the heating and cooling processes. It was found that the apparent strain curves from both sets of data were slightly different with a maximum variation of 16×10^{-6} (see fig.5.10). At first it was thought that this

slight discrepancy was due to the material properties of graphite rather than the performance of the gauge. A piece of molybdenum was employed with a strain gauge cemented on it. The apparent strain behaviour was investigated from 20°C to 200°C and the curves were plotted using data obtained from the continuous heating and cooling processes. It was found that the two curves were also slightly different as shown in fig.5.11. Since both materials exhibited this behaviour, a simple explanation is that the continuous heating and cooling processes only gave the instantaneous temperatures which were only slightly different from the actual temperatures. As a result, a slight difference in the apparent strain curves was observed.

In the following test, a different test procedure was carried out such that the temperature of the test specimen was slowly increased in several steps to the upper limit and held constant at each step before the temperature and the apparent strain were recorded. The cooling process was also carried out in the same way. An apparent strain curve was plotted using both sets of data obtained and is shown in fig.5.12. The two sets of data fitted quite nicely on a single curve. This implied that if the test temperature was allowed to stabilise at every temperature increment the apparent strain at that temperature would be reproducible during the heating or cooling part of the test. Since it was easier to obtain the apparent strain data from slow heating rather than slow cooling, the former method was employed. Usually two or there tests were performed to make sure that the apparent strain data were consistent and reproducible.

5.3.2 Preliminary results

Having obtained a reliable apparent strain curve, the specimen was then ready for the elevated temperature test. The procedure was the same as that for determining the apparent strain data except that the specimen was subjected to a constant pressure of 600 psi (4.14 MPa). The temperature

versus total strain curve (pressure induced strain + apparent strain) was obtained which, when subtracted away the apparent strains were, would give the pressure deformation of graphite under the effect of changing temperature. A few tests were carried out on a specimen of graphite A and the results obtained were irregular as shown in fig.5.13. Test (1) was incomplete due to the break down of wire insulation above 250°C. A different type of wire capable of operating above 300°C was subsequently used. Test (2) and (3) produced rather similar results with an initial drop in strain followed by a slow increase at temperature above 100°C. Before drawing any conclusion, a new apparent strain curve was determined after these tests and was found to be different from the original one (shifted in position) as shown in fig.5.14. It was not known exactly why the apparent strain calibration changed after the elevated temperature tests. An explanation could be that the thermal properties such as thermal expansion coefficient changes slightly after the tests which would then affect the later apparent strain behaviour. The fact that test (2) and test (3) were similar to each other implied that subjecting the specimen to a few tests under the same conditions should produce no further change in the thermal properties and the apparent strain data should then be reproducible. The same specimen was subjected to two more test (4 and 5) and the new apparent strain curve was used as the correction data. Both the tests produced a similar trend of behaviour which showed a slight increase in deformation with temperature as shown in fig.5.15.

5.3.3 Apparent strain behaviour of other graphites

For specimens of other graphites used in this work, a series of repetitive experiments were carried out on the apparent strain calibration. The procedure is described as follows. For every specimen under test, a reproducible apparent strain curve was first obtained at atmospheric pressure followed by an elevated temperature test at 600 psi. Then a second apparent

strain curve was determined for the same specimen followed by a second elevated temperature test. The whole process was repeated a few times and the successive apparent strain curves were compared with each other. For graphites B, C and D it was observed that the second apparent strain curves for all the specimens tested were different from the initial ones but were very similar to the third ones. This showed that the original apparent strain curves changed after the initial elevated temperature tests and that consistent results were only possible after the initial tests. All the graphites showed this behaviour in both the longitudinal and circumferential directions (see fig.5.16 to 5.18) and the results for the elevated temperature tests were taken from the third tests and are discussed in chapter 6.

CHAPTER 6

EXPERIMENTAL RESULTS

6.1 Uniaxial testing

6.1.1 Compressive stress-strain properties

Uniaxial compression of a graphite specimen subjected to a relatively small load of up to about 140 kg was prone to effects due to any non-parallelism between the compression anvils of the Instron as well as the end faces of the specimen. As a result, spurious effects due to initial bending on the specimen could be observed. In order to eliminate this phenomenon, great care was exercised in positioning the specimen between the compression anvils. This eliminated the initial bending and enabled smooth stress-strain curves to be plotted on the xy-recorder during loading and unloading. Typical stress strain curves are shown in fig.6.1 to 6.4. At a load of 140 kg (4.14 MPa) the longitudinal strains were over 500×10^{-6} for graphites A, B and D and 350×10^{-6} for graphite C. Young's moduli, as determined from the stress-strain curves, varied from 12.6 GPa for graphite C to 7.6 GPa for graphites B and D. Poisson's ratios ranged from 0.10 for graphite D to 0.15 for graphite C. The results for all the graphites tested are summarised in table 6.1.

6.1.2 Fracture strength under compression

Four specimens of each graphite were compressed to failure in the Instron. Two modes of failure were observed: multiple fracture where specimens broke into a few fragments and single fracture where specimens broke into halves along the diagonal.

Graphite B showed the highest fracture strength of 91.4 MPa (average over 4 values) and a fracture strain of 3.28%. Graphite C showed an average fracture strength of 88.3 MPa and a fracture strain of 2.83%.

Graphite A produced an average fracture strength of 79.3 MPa with a fracture strain of 2.85%. Graphite D which is essentially PGA material showed the lowest strength of only 27.4 MPa with a strain of only 1.7%. All specimens of graphite A, B and C showed multiple fracture with a loud explosive sound. Graphite D only showed single fracture with no sound as the specimens slowly broke into halves along the diagonal. The results for all the specimens tested are shown in table 6.2.

6.2 Hydrostatic testing

6.2.1 Uncoated specimen

Generally all the graphites employed in this work showed a linear relation between deformation in the longitudinal direction and pressure when subjected to hydrostatic pressures up to 600 psi (4.14 MPA). The strain at 600 psi (e_m) varied significantly from graphite to graphite and there were also variations in different specimens of the same graphite (see later). During unloading the deformation was again found to be linearly dependent on pressure. However, the pressure-strain curve during unloading did not follow that of loading and a small residual strain or permanent set was produced when the pressure was released to atmospheric condition (zero gauge pressure). This implied that after a pressure cycle the specimen was slightly shortened (see fig.6.5). The permanent set obtained under hydrostatic testing is in a way similar to that observed in a uniaxial test. However, uniaxial compression produces a bigger plastic strain and a larger permanent set due to the non-linearity of the compressive stress-strain curve. The compressive strains were also larger than those observed under hydrostatic pressures for all the graphites investigated. Upon reloading to 600 psi the pressure-strain curve followed quite closely the first unloading curve and e_m increased only slightly. The permanent set following the second pressure unloading curve also changed slightly. Further pressure cycling tests on the same specimen

produced little or no changes in e_m and permanent set. This behaviour is also similar to that observed under cyclic loading and unloading of polycrystalline graphite under uniaxial testing [14]. The response in the circumferential direction was similar to that of the longitudinal direction with linear pressure-strain curves in loading and unloading and small permanent set at zero gauge pressure. However, there are large differences in the circumferential strains for the different graphites tested and the anisotropic ones generally showed a larger deformation in the circumferential direction than the isotropic ones, which produced roughly equal strains in both directions (see later).

Graphite A : a nuclear grade Gilsocarbon material

Strain measurements were made in the longitudinal, circumferential and transverse directions. The strains at 600 psi (e_m) obtained for the first specimen were 135×10^{-6} in the longitudinal and transverse directions and 140×10^{-6} in the circumferential direction. Since the difference in strains was very small the dimensional changes of graphite A under pressure can be considered to be equal in all three directions. This indicates the isotropic nature of this graphite which is manufactured from approximately spherical coke particles with random orientation. For four specimens tested the longitudinal strains (e_m) ranged from 130 to 135×10^{-6} while the circumferential ones varied from 120 to 140×10^{-6}. These hydrostatic strains were very much smaller than those obtained in uniaxial compression tests where strains of around 500×10^{-6} were observed at a load of 140 kg which produced a stress on the specimen equivalent to 600 psi (4.14 MPa). The experimental bulk modulus for uncoated specimen, K_{expt}(uncoat) was determined from the ratio of pressure over dilatation and a mean value of 10.0 GPa was obtained for graphite A. Typical pressure-strain curves are shown in fig.6.6.

Graphite B : moderator graphite

This graphite also revealed its isotropic nature when tested under hydrostatic pressures up to 600 psi. For four specimens investigated, the longitudinal strains (e_m) varied from 132 to 138×10^{-6} while the circumferential strains were 140×10^{-6}. Since this is also a nuclear grade Gilsocarbon graphite, the values of e_m are quite close to those obtained for graphite A and are also smaller than the compressive strains of about 520×10^{-6} under a uniaxial stress of 4.14 MPa (see fig.6.2). The bulk modulus was found to be 10.0 GPa. Typical pressure-strain curves for this graphite are shown in fig.6.7.

Graphite C : sleeve graphite

This graphite showed a slight anisotropic nature when tested under hydrostatic pressures in which the circumferential strains were found to be larger than the longitudinal ones. The variations in e_m were quite significant for different specimens in a batch in both directions. For a sample of four specimens investigated, the longitudinal strains varied from 102 to 126×10^{-6} with a mean value of 115×10^{-6}. The circumferential strains varied from 155 to 180×10^{-6} with a mean value of 165×10^{-6}. The longitudinal strains under pressure were also smaller than the compressive strains by a factor of three (see fig.6.3). The mean bulk modulus was found to be 9.3 GPa. Typical pressure-strain curves for the sleeve graphite are shown in fig.6.8.

Graphite D : PGA moderator graphite

This graphite was extremely anisotropic when tested under hydrostatic pressures up to 600 psi. The circumferential strains were larger than the longitudinal ones by a factor of over 2. This is in accordance with the nature of the long dimension coke grains used in the manufacture of this graphite which have a preferred direction of orientation. Since the coke

grains are aligned with the long axis parallel to the extrusion direction (specimen axis) and the crystallites themselves are aligned with the a-axis parallel to the long axis of the grains, the circumferential strains of this graphite are consequently larger than the longitudinal ones. Again the variations in e_m were significant in both directions. For a sample of four specimens investigated, the longitudinal strains varied from 85 to 118×10^{-6} with a mean value of 102×10^{-6}. The circumferential strains varied from 210 to 250×10^{-6} with a mean value of 235×10^{-6}. The longitudinal strains under pressure were also smaller than the compressive strains of 550×10^{-6} in the longitudinal direction at a stress of 4.14 MPa (see fig.6.4). The mean bulk modulus for this material was found to be 7.3 GPa. Typical pressure-strain curves are shown in fig.6.9.

The variations in e_m for different specimens of the isotropic graphites are not significant (6-7%) while the anisotropic graphites show larger variations in e_m in both directions. For instance the maximun variations $(e_m(max)-e_m(min))/((e_m(mean))$ are 17% and 33% in the longitudinal direction, 15% and 17% in the circumferential direction for graphites C and D respectively. The pressure-strain results for all the specimens tested are summarised in table 6.3.

6.2.2 Coated specimens

The coated specimens of all the graphites investigated in this work showed an increase in deformation in both directions when tested under hydrostatic pressures up to 600 psi. The magnitude of the increase was different for different graphites. Generally the anisotropic graphites showed a greater increase in deformation than the isotropic ones. For instance, graphite D produced a circumferential strain of over 600×10^{-6} as opposed to about 200×10^{-6} for graphite B (see later). The pressure-strain curves for the coated specimens were also linear with the unloading curves slightly on the

right of the loading ones. Hence, permanent sets were also observed when the pressure was released to atmospheric condition (zero gauge pressure). Subsequent pressure loading and unloading tests on the same specimen produced the same results as long as the layer of flexible coating remained unbroken. Once the coating was broken the pressure-strain curves changed back to those of the uncoated specimen (see fig.6.10) since the presure fluid was then able to penetrate the pores of the material through the opening on the coating. To investigate the cause of failure, a specimen was removed from the pressure vessel after the initial test. It was found that part of the coating had swollen up to form a small "bubble". This was explained by the fact that air was trapped in the open pores when the coating was applied on the specimen. On application of pressure the open pores were squeezed (analogy to the squeezing of a sponge) and the trapped air was forced to escape and pressurize a weaker part of the coating thereby forming the small bubble. Subsequent pressure cycling tests on the same specimen caused the bubble to grow and eventually burst. The coated specimens that failed after a few pressure cycles produced blisters on the coatings due to the collapse of these bubbles.

The two coated specimens of graphite A showed a longitudinal strain (e_m) of about 280×10^{-6} and a circumferential strain of about 200×10^{-6} as opposed to the uncoated strains of 130 and 120×10^{-6} respectively (see fig.6.11). The effective bulk modulus for coated specimen, K_{expt}(coat), was found to be 6.2 GPa. The two coated specimens of graphite B, on the other hand, showed approximately equal strains of about 200×10^{-6} in both directions (see fig.6.12) as opposed to the uncoated strains of about 130×10^{-6}. The K_{expt}(coat) was found to be 6.7 GPa. For coated specimens of the anisotropic graphites the circumferential strains are generally greater than the longitudinal ones. For instance, the coated specimen of graphite C produced a circumferential strain of 275×10^{-6} and a longitudinal strain of

$165x10^{-6}$ as opposed to the uncoated values of 155 and $110x10^{-6}$ respectively (see fig.6.13). Consequently the effective bulk modulus decreased to 5.8 GPa. The coated specimen of graphite D produced a huge circumferential strain of about $650x10^{-6}$ and a longitudinal strain of $350x10^{-6}$ as opposed to the uncoated values of 225 and $100x10^{-6}$ respectively (see fig.6.14). Due to the large dilatation of the coated material, K_{expt}(coat) had the lowest value of 2.5 GPa. The results for all the coated specimens are summarised in table 6.4. Additional results for hydrostatic testing of coated and uncoated specimens can be seen in section 6.5.

6.2.3 Effect of gauge cement

The aim of this test was to investigate whether the application of gauge cement to part of a specimen surface affected the open porosity. The open pore volume (o.p.v.) of two specimnens of graphite A, as determined by helium displacement method, were found to be 11.61 and 10.7%. After application of the cement during strain gauge installations, the open pore volumes of both specimens were found to change by less than 1%. Since the percentage change in o.p.v. was insignificant, it should not affect the dimensional changes of graphites as measured by strain gauges which involved application of cement on the porous material.

6.3 Effects of pre-stressing

6.3.1 Initial investigation

The early work on the effects of pre-stressing was on graphite A as described below:

Test (1) : In this test the compressive pre-stressing was performed on two specimens with strain gauges installed in the longitudinal and circumferential directions respectively. Before the specimens were subjected to a series of longitudinal compressive loads F of 300, 600, 900, 1200 and 1500 kg (100 kg produces a stress of 3.02 MPa on the specimen), they were hydrostatically

tested to 600 psi (ie at F=0) to obtain the initial pressure deformation characteristics for comparison with those obtained after the pre-stressing tests. For the first specimen with the longitudinal gauge, the initial hydrostatic deformation had the usual characteristics (see section 6.2.1) with linear pressure-strain curve and a small positive permanent set. The pressure unloading curve fell slightly on the right of the loading one (see fig.6.15). After the specimen was subjected to a compressive load (F) of 300 kg (9.18 MPa), hydrostatic testing produced no change in the pressure loading curve but the unloading curve was coincident with the loading one showing no permanent set. As F was increased to 600 kg, again there was no change in the pressure loading curve while the unloading curve fell slightly on the left of the loading one producing a negative (tensile) permanent set when the pressure was released to atmospheric condition. This implied that the specimen was slightly elongated. For F of 900, 1200 and 1500 kg, the hydrostatic behaviour was the same as above except that the unloading curves were further away from the loading ones. The permanent sets also increased slightly. The pressure-strain curves for F of 0, 300 and 1500 kg are shown in fig.6.15.

For the second specimen with a circumferential gauge, there was no observable difference between the loading and unloading curves in the initial hydrostatic deformation (F=0) as shown in fig.6.16. However, after a longitudinal compressive load of 300 kg, there was a slight increase in e_m (strain at 600 psi). The unloading curve fell slightly on the right of the loading one indicating the usual permanent set (compressive). For F of 600, 900, 1200 and 1500 kg, the behaviour was the same as above with permanent sets slowly increasing in that order. At F=1500 kg (45 MPa), e_m increased from 140 to 155×10^{-6} and the permanent set increased from nothing to about 15×10^{-6} (see fig.6.16). This implied that the specimen had actually shrunk in the circumferential direction.

Apart from these characteristics, compressive pre-stressing did not seem to affect the linear deformation of graphite under hydrostatic pressures up to 600 psi and only insignificant changes in e_m were observed. The bulk modulus (K_{expt}(uncoat)) was found to decrease only slightly after each level of pre-stressing. For instance, the bulk modulus initially had a value of 10.0 GPa (at F=0, unstressed condition) which decreased to 9.9,9.8,9.7,9.7 and 9.5 GPa at each level of F=300, 600, 900, 1200 and 1500 kg. At a pre-stress load of 1500 kg (45 MPa) which was approximately 60% of the fracture stress of graphite A, the decrease in K_{expt} was only 5% which was very insignificant considering the high level of pre-stressing. On the other hand, the decrease in Young's modulus could be as high as 35% after pre-stressing. For instance, Hall [49] reported that after pre-stressing to 3000 psi (21 MPa) the Young's modulus was only 65% of its original value.

Test (2) : In this test three specimens were first compressed directly to 1500 kg and strain gauges were then installed in the longitudinal, circumferential and transverse directions respectively. Hydrostatic testing of the pre-compressed specimens produced similar results as reported earlier (i.e. at F=1500 kg in test (1)). For instance, the longitudinal unloading curve was on the left of the loading one and a negative permanent set (tensile) was subsequently produced at atmospheric pressure. On the other hand, the unloading curves in both the circumferential and transverse directions were on the right of the loading ones giving the usual permanent sets (compressive). The pressure-strain curves for F of 1500 kg are shown in fig.6.17. The similarity in the results of both tests indicated that compression up to 1500 kg (in test (1)) did not affect the performance of the strain gauges. These results also showed that compressive pre-stressing did not affect significantly the hydrostatic deformation of graphite with little or no change in e_m. However, the permanent sets were different in the longitudinal direction as opposed to those in the circumferential and transverse

directions. For the second test the bulk modulus, after pre-stressing to 1500 kg which was approximately 60% of the fracture stress, was found to be 9.6 GPa which was in good agreement with the value obtained in the first test.

6.3.2 Later investigation

In the later work on the effects of pre-stressing, all four graphites were investigated following the method of test (2) as described earlier (see also section 5.3). For specimens of the isotropic graphites (A and B) longitudinally compressed to 2000 kg (60.4 MPa), hydrostatic testing produced little changes in the longitudinal strain (e_m) but there was an increase in the circumferential strain. The form of the unloading curves was as reported in section 6.3.1 (see fig.6.18 and 6.19). For the subsequent pressure cycling tests both the maximum strains and permanent sets increased slightly. For instance the strains for graphite B were 120 and 143×10^{-6} in the longitudinal and circumferential directions in the first test. These changed to 120 and 160×10^{-6} respectively in the 5th test. After these tests, the bridge meters were reset by adjusting the deflection needle to indicate zero strain (origin of pressure-strain curve). The specimen was then tested hydrostatically and the strains at 600 psi were smaller than those observed in the initial test by the amount of the residual strains produced. The strains were roughly equal in both the longitudinal and circumferential directions and values of 130 and 133×10^{-6} were obtained. Hence pre-stressing had the effect of introducing slight anisotropy in the isotropic graphites during the initial test and this disappeared when the specimens were retested to 600 psi. The pre-compressed specimens of the anisotropic graphites (C and D) also produced similar results under hydrostatic testing (see fig.6.20 and 6.21). For graphite C, the initial test produced strains of 100 and 170×10^{-6} in the longitudinal and circumferential directions. These changed to 108 and 155×10^{-6} when the

specimen was retested to 600 psi. For graphite D, the initial test produced strains of 84 and 220×10^{-6} in the longitudinal and circumferential directions. These changed to 90 and 196×10^{-6} respectively when the specimen was retested to 600 psi.

Despite the large decrease in E of over 35% after pre-stressing, the decrease in K_{expt}(uncoat) was again found to be very small. In the later work where the specimens were pre-stressed to over 60 MPa the bulk moduli were either similar to those of the unstressed specimens (A and B) or within the sample's variation of the unstressed specimens (C and D). The results for the pre-stressed specimens are summarised in table 6.5 (see also table 6.3).

6.4 Irradiated sleeve graphites

Neutron irradiated sleeve graphites of the type similar to graphite C were employed. In the early work the irradiated material had been subjected to a dose of 6.8 n/cm^2. In the later work irradiated sleeve graphites similar to type C but of higher doses were also investigated. The doses were 11.0 and 17.0×10^{20} n/cm^2 respectively. The results are presented as follows.

6.4.1 Neutron dose of 6.8×10^{20} n/cm^2

A total of eight specimens were tested under hydrostatic pressures of loading and unloading. The pressure-strain curves obtained were not linear, contrary to those observed for the unirradiated materials. The non-linear pressure-strain curves were in a way similar to the stress-strain curves obtained for the unirradiated materials. Because of this non-linearity, big pressure-strain loops were formed after a pressure cycle of loading and unloading. The circumferential loops were generally bigger than those observed in the longitudinal direction (see fig.6.22). However, linear pressure-strain curves were also observed in a few specimens in the longitudinal direction with insignificant hysteresis effects; the circumferential ones,

however, were always non-linear with big pressure-strain loops (see fig.6.23). Other than the above characteristics there was a drop in deformation in both directions for the irradiated material as opposed to the unirradiated specimens of graphite C. For the eight specimens tested, the circumferential strains varied from 100 to 124×10^{-6} whereas the longitudinal ones varied from 54 to 70×10^{-6} (as opposed to 160 and 100×10^{-6} respectively for graphite C). The bulk moduli varied from 13.3 to 15.7 GPa while the bulk modulus was about 9.0 GPa for unirradiated graphite C. The increase in bulk modulus after neutron irradiation is similar to the increase in Young's modulus observed after the irradiation.

When the irradiated specimens were coated with M-coat C, there was an increase in deformation under pressure in both directions (see fig.6.24 and 6.25), a trend similarly observed for the coated specimens of other unirradiated materials. The strains at 600 psi were almost double those of the uncoated specimens. For instance the circumferential strains for the coated specimens varied from 210 to 230×10^{-6} while the longitudinal ones varied from 82 to 95×10^{-6}. Consequently the bulk modulus decreased due to the increase in dilatation with values ranging from 7.6 to 8.1 GPa. The overall results are summarised in table 6.6.

Compression stress-strain curves were also obtained for the irradiated specimens and are shown in fig.6.26. The static Young's modulus was found to be 19.6 GPa which was higher than 12.3 GPa for the unirradiated material of graphite C.

6.4.2 Neutron dose of 11.0×10^{20} n/cm^2

A total of four specimens were tested, two in the circumferential direction and two in the longitudinal direction. The pressure loading curves were slightly non-linear and the unloading curves produced big pressure-strain loops after a pressure cycle. The loops were bigger in the circumferential

direction (see fig.6.27 and 6.28) as at the lower dose. The strains were 102 and 120×10^{-6} in the longitudinal direction, and 90 and 85×10^{-6} in the circumferential direction. The longitudinal strains were slightly bigger due to the fact that the specimens were machined in the circumferential from the sleeve material. These strains were quite similar to those obtained for the specimens irradiated to a dose of 6.8×10^{20} n/cm^2. The bulk modulus was found to be 14.7 GPa.

Coated specimens of this material also showed some increase in deformation under pressure. For instance the longitudinal strain was 125×10^{-6} (an increase of over 20%) while the circumferential strain was 120×10^{-6} (an increase of over 30%).

6.4.3 Neutron dose of 17.0×10^{20} n/cm^2

This was the highest dose investigated. Again four specimens were tested as in section 6.4.2. The pressure loading curves were also non-linear in both directions. The pressure-strain loops were quite large in both cases. Since the specimens were machined in the axial direction from the sleeve material, the circumferential strains were bigger than the longitudinal ones (see fig.6.29 and 6.30). The decrease in deformation was quite substantial for this irradiated material. For the two specimens tested in the longitudinal direction, the strain was found to be 55×10^{-6} for both specimens while the circumferential specimens produced strains of 102 and 85×10^{-6} respectively. The bulk modulus was found to be 16.9 GPa which is some 1.8 times bigger than that of the unirradiated material (see section 6.2.2).

The coated specimens also showed an increase of deformation under pressure. The longitudinal strain was 92×10^{-6} which showed an increase of over 60% compared with the uncoated one. The circumferential strain was 136×10^{-6} which showed an increase of over 40%. Consequently the bulk modulus decreased to 11.3 GPa.

The results for all the irradiated materials are summarised in table 6.7. When a graph of (K/Ko - 1) versus neutron dose is plotted where Ko is the unirradiated value of K, it shows that the bulk modulus increased with neutron dose and the increase appeared to be saturated for dose greater than 17.0×10^{20} n/cm² (see fig.6.31).

6.4.4 Effect of annealing

Three irradiated specimens of dose 6.8×10^{20} n/cm² were sent to SNPDL for annealing at 2350°C for one hour in an argon atmosphere. One specimen (106) had been previously tested under pressure while the other two were untested (109 and 110). After the annealing, all the specimens showed linear pressure loading and unloading curves in the longitudinal direction. The circumferential pressure-strain curves were slightly non-linear with small pressure-strain loops (see fig.6.32 to 6.34). All the annealed specimens showed increases in strains in both directions as compared to the irradiated unannealed specimens (see fig.6.35 for specimen 106 prior to annealing). The maximum strains (e_m) were 125 and 230×10^{-6} in the longitudinal and circumferential directions respectively. These strains were also considerably higher than those of the unirradiated specimens of graphite C. Since the average strains were 110 and 170×10^{-6} for graphite C in the longitudinal and circumferential directions, thermal annealing of the irradiated specimens increased the strains by 13% and 34% respectively. The bulk modulus after the annealing was 7.1 GPa which was some 22% lower than for the pre-irradiation material.

6.5 Porosity measurements

6.5.1 Unirradiated materials

Two specimens each of the graphites were studied. The closed and

open pore volumes were determined as the percentage fraction of the bulk volume. The porosity measurements of graphite A were taken at the early stage of this work during an investigation to determine whether the application of gauge cement on part of the specimen surface affected the open pore volumes (see section 6.2 for details). The porosity measurements for graphite B, C and D were undertaken to study the effect of increasing the closed porosity (achieved by coating the specimens prior to hydrostatic testing) on the hydrostatic deformation of graphite.

The total porosity (closed + open porosity) varied considerably from graphite to graphite and ranged from 25.96% (average over two specimens) for graphite D to 18.28% for graphite C (see table 6.8). The isotropic graphites of A and B have an average total porosity 20.12 and 19.14% respectively. Graphite D is extremely porous with over 85% of the total porosity open to a gas. For instance the open pore volume is over 22% as compared to the closed pore volume of only 3.8%. For graphite C the closed pore volume is 9.34% which is only slightly higher than the open pore volume of 8.93%. For the isotropic materials, the open pore volume is higher than the closed pore volume in graphite A (11.17% for o.p.v. as opposed to 9.01% for c.p.v.) whereas the reverse is true for graphite B (8.93% for o.p.v. as opposed to 10.21% for c.p.v.). The porosity values for individual specimens are summarised in table 6.8.

Having determined the open and closed pore volumes of all the graphite specimens, they were then hydrostically tested to 600 psi under two conditions: when uncoated and when coated with M-coat C as described earlier in this work. The results obtained were compatible with those described earlier in secion 6.2. The pressure-strain curves were generally linear in both pressure loading and unloading with the exception that the strains at 600 psi were slightly different. Graphite B is fairly isotropic with an average strain of 125×10^{-6} in both directions. Graphite D is extremely

anisotropic in which the average circumferential strain of $195x10^{-6}$ is almost double the longitudinal strain of $100x10^{-6}$. Graphite C is intermediate between the two with average strains of 164 and $108x10^{-6}$ in the directions tested.

The coated specimens also showed linear pressure-strain curves and substantial increases in deformations as opposed to the uncoated ones, a trend similarly observed for the coated specimens tested earlier (see section 6.3). The increase in strain was about 50% in both directions for graphite B, the maximum strain being $185x10^{-6}$ in both directions. For graphite C there was an average incraese of over 40% in the longitudinal strain of $150x10^{-6}$ and about 50% in the circumferential strain of $245x10^{-6}$ (see table 6.9). Graphite D which had the highest total porosity of which 85% were open pores showed huge increases in strains, over 150% in the longitudinal direction and over 250% in the circumferential direction. The average strains measured were 255 and $700x10^{-6}$ respectively. The results are summarised in table 6.9.

6.5.2 Irradiated materials

Two specimens of the neutron irradiated sleeve graphite of dose $6.8x10^{20}$ n/cm^2 were studied. The open and closed porosity were also determined as the percentage fraction of the bulk volume and are shown in table 6.10 together with values of bulk and helium density. The average open pore volume was 10.91% which was slightly higher than the average closed pore volume of 8.78%.

Since the irradiated specimens were machined from the fuel sleeve material of a reactor (see chapter 5), there was no virgin material of the same type for further investigation. However, the pre-irradiation data such as the porosity measurements of this type of graphite was available from UKAEA (SNPDL) for comparison. The porosity measurements of the virgin

sleeve graphite obtained from UKAEA (P. Schofield, private communication) were the mean value of nine and are shown in table 6.11 together with the range. The mean open porosity was 8.9% which was roughly the same as the closed porosity of 8.7%. By comparing the irradiation and pre-irradiation data (table 6.10 and 6.11), it can be seen that there was no significant change in the closed porosity (less than 1%) after the irradiation but the open porosity increased from 8.9% to 10.91%, an increase of over 20%.

6.6 Elevated temperature tests

In the elevated temperature tests, graphite specimens were subjected to a constant pressure of 600 psi while the temperature was raised from 20 to 300°C. By using the accurate apparent strain correction data (see section 5.3), the change in deformation of the test specimens under constant pressure as the temperature varies can be evaluated.

For two specimens of graphite B investigated, the variation in e_m with temperature was found to be relatively small. The longitudinal strain (e_m) only increased slightly over the temperature range investigated. For instance, at 20°C the strains were 126 and 132×10^{-6} for the two specimens tested. These increased slightly with temperature and reached values of 142 and 146×10^{-6} respectively at 300°C, increases of 13% and 11% (see fig.6.36 and 6.37). On the other hand there was no observable increase of e_m in the circumferential direction. At 20°C the circumferential strain was 127×10^{-6} and this remained quite constant over the entire range. The bulk modulus was 10.7 GPa at 20°C and this decreased to 10.4 GPa at 300°C, a decrease of less than 3%.

For graphite C, the elevated temperature test produced a large deformation in the circumferential direction. For a specimen investigated, the circumferential strain increased from 150×10^{-6} at 20°C to 172×10^{-6} at 300°C, an increase of 15%. However the longitudinal strain changed only

slightly from 120 to 130×10^{-6} at 300°C, an increase of 8% (see fig.6.38). The room temperature bulk modulus was 9.9 GPa. This decreased to 8.7 GPa at 300°C, a decrease of 10%.

Graphite D also produced a small change in deformation in the longitudinal direction for the elevated temperature test. For a specimen investigated, the longitudinal strain at 20°C was 90×10^{-6}. This increased slowly with temperature and reached a value of 106×10^{-6} at 300°C, an increase of 18%. The circumferential strain was 214×10^{-6} at 20°C which dropped to below 200×10^{-6} before increased again and reached a value 216×10^{-6} at 300°C (see fig.6.39). The bulk modulus decreased from 8.0 to 7.7 GPa, a decrease of less than 4%.

The overall results for the elevated temperature tests showed only relatively small increase in strain for the temperature range under investigation. The decrease in bulk modulus with temperature was also small, from less than 3% for graphite B to 10% for graphite C.

6.7 Four-point bend tests

The aim of the bend tests was to investigate whether the bend strength of polycrystalline graphite changes when the tests were performed under a constant pressure of 600 psi. Initially a sample of graphite specimens were loaded under 4-point bending at atmospheric pressure to obtain the mean bend strength. This was followed by a second batch of specimens in which the tests were performed under 600 psi. Three graphites were employed, one was isotropic moderator material (similar to graphite B) of block SI2 IJ while the other two were sleeve material (similar to graphite C) of block 392 and 398.

The bend strength was taken to be the maximum tensile stress on the extreme fibre of the specimen when fracture occurred. This was calculated from the elastic beam theory and the fracture strain was

calculated by considering the geometry of a bend specimen prior to fracture. Due to the scattering of bend strengths among different specimens in a batch, a mean value was taken from a sample of fifteen specimens and the bend strength of a particular graphite was quoted as the mean strength ± 1 standard deviation. The results are presented as follows.

Isotropic graphite (Blk.SI2,IJ)

For the isotropic material, there was a large variation of bend strengths within the batch of fifteen specimens under investigation. For instance, at atmospheric pressure the bend strengths varied from 24.46 to 34.60 MPa while the fracture strains varied from 1720 to 2700x10^{-6}. The bend strengths and fracture strains for all the specimens tested are summarised in table 6.12. The mean bend strength of the batch was found to be (31.08 ± 2.81) MPa while the mean fracture strain was found to be (2190 ± 230) x10^{-6}. At 600 psi, again the variation of bend strengths within the batch was significant, from 27.02 to 34.82 MPa (see table 6.12). The fracture strains varied from 1560 to 205ox10^{-6} (see table 6.12). The mean bend strength was found to be (30.41 ± 3.12) MPa and the mean fracture strain was found to be (1910 ± 150) x10^{-6}. From a sample of fifteen specimens tested in both conditions, it was found that the mean bend strength of the isotropic graphite decreased only slightly when the tests were performed under 600 psi. Although the decrease in the mean bend strength was small, the decrease of the mean fracture strain was quite substantial and a decrease of over 13% was observed. This signifies the fact that the bend specimens were actually more brittle when the tests were performed under 600 psi.

Sleeve graphite (Blk. 392)

The sleeve graphite also showed some variations in bend strengths

under atmospheric pressure. For a sample of fifteen bend specimens tested, the bend strengths of the block 392 material at atmospheric pressure varied from 29.49 to 35.14 MPa while the fracture strains varied from 2500 to 3100×10^{-6}. The mean bend strength was found to be (32.21 ± 1.67) MPa and the mean fracture strain was $(2710 \pm 170) \times 10^{-6}$ (see table 6.13). Under a pressure of 600 psi, the bend strengths varied from 29.05 to 33.22 MPa while the fracture strains varied from 1980 to 2560×10^{-6}. The mean fracture strength was found to be (29.87 ± 1.68) MPa and the mean fracture strain was $(2230 \pm 150) \times 10^{-6}$ (see table 6.13). These results also showed that the mean bend strength of the block 392 material decreased when the bend specimens were tested under a pressure of 600 psi. The decrease was over 7% which was higher than the decrease found in the isotropic material of over 2%. The decrease in the fracture strain was even greater for the bend specimens at 600 psi. The decrease was found to be 18% and implied that this material also became more brittle when tested at 600 psi.

Sleeve graphite (Blk. 398)

For a sample of fifteen specimens tested at atmospheric pressure, the bend strengths of the block 398 material varied from 25.52 to 30.65 MPa with a mean bend strength of (27.16 ± 1.55) MPa. The fracture strains varied from 2340 to 2890×10^{-6} with a mean value of $(2510 \pm 180) \times 10^{-6}$ (see table 6.14). For another fifteen specimens tested at 600 psi, the bend strengths varied from 23.83 to 29.26 MPa with a mean bend strength of (26.24 ± 1.44) MPa. The fracture strains varied from 1820 to 2300×10^{-6} with a mean value of $(2060 \pm 185) \times 10^{-6}$ (see table 6.14). The bend specimens of the block 398 material also showed a small drop in the mean bend strength under a pressure of 600 psi. The decrease was only 4% which was higher than that observed for the isotropic material. However, the decrease of the fracture strain under pressure was quite substantial and a drop of 18% was observed.

Although the bend tests produced results which scattered significantly for different specimens within a batch, the overall results implied that the mean strengths of all the graphites investigated dropped when the bend tests were performed under 600 psi. The drop in the mean bend strengths ranged from just over 2% for the isotropic graph ite to over 7% for the sleeve material from block 392. The drop in the mean strain to failure was, on the other hand, quite substantial with values ranging from 13 to 18% for the graphites investigated.

CHAPTER 7

DISCUSSION

7.1 Introduction

Commercial graphites are usually made from coke or filler particles mixed with pitch binder which are then shaped, baked and graphitized by high temperature heat treatment. Because of the variety of raw materials and processing methods, the manufactured artefacts often show a wide range of properties and micro-structures. In addition there exists a complicated network of pores interlaced with the micro-structures of coke grains in the graphite matrix. Hence, the properties of polycrystalline graphites are not expected to follow directly those of either the single crystals or homogenous isotropic bodies. They should be dependent on the properties of the coke particles and their crystallites, their interaction with each other and with porosity. Before analysing the experimental results obtained in this work, it is essential to discuss briefly the properties and deformation behaviour of graphite single crystals as well as the polycrystalline aggregates.

Single crystals of graphite consist of layers of hexagonally-arranged atoms of carbon. The bonds between the carbon atoms within the layer planes are strong covalent bonds while the bonds between the layer planes are of the weaker van der Waals type of long range forces. The elastic deformation of a single crystal can generally be described in terms of two sets of elastic constants, ie:

$$\text{stress component} = C_{ij} \times \text{strain components}$$

where C_{ij} are the elastic moduli or stiffnesses, or

$$\text{strain components} = S_{ij} \times \text{stress components}$$

where S_{ij} are the elastic compliances. For a graphite crystal which has hexagonal symmetry, there are five independent elastic stiffnesses which are

C_{11}, C_{12}, C_{13}, C_{33} and C_{44}. Alternatively, the five elastic compliances are S_{11}, S_{12}, S_{13}, S_{33} and S_{44}. These elastic constants, as quoted from Kelly [4], are shown in table 7.1. The Young's modulus is $1/S_{11}$ in the basal planes and has a very high value of 10^{12} N/m². The Young's modulus perpendicular to the basal planes is $1/S_{33}$ and has a value of 36 GN/m². The shear modulus related to interlayer shear ($C_{44} = S_{44}^{-1}$) has a very low value which shows the ease with which a single crystal deforms by relative motion of the layer planes (shear in the a-axis direction). This is associated with the movement of dislocations lying in the basal planes. Neutron irradiation of single crystal has been shown [48] to pin the basal plane dislocations and increase the shear modulus to a true value of about 4 GN/m² [4]. The bulk or volume compressibility of a single crystal is given by

$$1/K_c = 2S_{11} + S_{33} + 2S_{12} + 4S_{13} \qquad \text{eqn.7.1}$$

where K_c is the bulk modulus of a single crystal. The volume compressibility has a value of 29.4×10^{-12} m²/N using the values of elastic compliances quoted in table 7.1. The experimental value of the volume compressibility as determined by Bridgeman [39] has a value of 29.8×10^{-12} m²/N which is in good agreement with the calculated value. The compressibility of graphite crystal is known to change with pressure. Kabalkina et al. [59] measured the changes in c-spacing with x-rays of ceylon graphite crystals subjected to high pressures of up to 1.6 GPa and obtained expression of the form

$$\delta c/c = 2.85 \times 10^{-11} p - 94 \times 10^{-22} p^2 \qquad \text{eqn. 7.2}$$

where p is in N/m². This is essentially the c-axis compressibility (strain per unit pressure), which is at low pressure equal to $S_{33} + 2S_{13}$ and has a value of 2.85×10^{-11} m²/N. The a-axis to c-axis compressibility ratio for single crystals has been found to be 0.06 by Drickamer et al. [60] while the results of Blaslee et al. [61] indicate a value of 0.018 (quoted from Green et al. [62]). Theoretically, it is ($S_{11} + S_{12} + S_{13}$), which from table 7.1 is 0.018.

The deformation behaviour of polycrystalline graphite differs from

that of a single crystal on a macroscopic scale due to the existence of numerous cracks and voids which effectively reduce the load carrying area of the porous material. The presence of microporosity in the coke particles has the effect of reducing the restraint on the plastic flow of one crystallite which might be exerted by neighbouring crystallites of different orientation. On the other hand the presence of macropores in the binder phase provides free surfaces to accommodate the bending and buckling deformation of individual coke particles. The fact that impregnation by relatively soft materials [63] or even by sugar solution [64] can increase significantly the modulus of polycrystalline graphite shows that the impregnant can seal the pores and resist shear deformation of individual grains. The external stresses within the individual crystallites can lead, as suggested by Seldin [16], to a combination of (1) elastic deformation, (2) irreversible shear or plastic deformation, (3) relief of internal stresses and (4) local stresses greater than the breaking strength which can cause microcracks. The first two processes are used to describe the general stress-strain behaviour of graphite while the last three processes are used to describe the differences between the stress-strain curves in different directions. The Young's moduli of polycrystalline graphite are generally much lower than $1/S_{11}$ or $1/S_{33}$ for a single crystal. Assuming that the stress-strain behaviour of polycrystalline graphite is related to that of individual crystallites, Simmons [48] and Kelly [65] both suggested that the elastic moduli of polycrystalline graphite depend primarily on the single crystal shear modulus; since the easy mode of deformation in a crystal is shear due to movement of dislocations along basal planes. The highly non-linear stress-strain behaviour of polycrystalline graphite is very similar to that of a Ticonderoga graphite crystal obtained by Baker and Kelly [66] and reflects the behaviour of single crystals in shear.

7.2 Hydrostatic deformation

The deformation behaviour of polycrystalline graphite under hydrostatic deformation is in a way different from that under uniaxial loading. The polycrystalline material contains a wide spectrum of pores. Some of these pores are open and accessible to a gas whereas others are closed and inaccessible. Both type of pores will have different effects on the way the bulk material deforms under different modes of loading. Before discussing these effects, it is useful to examine the micro-structures of the polycrystalline aggregate consisting of a few particles as shown schematically in fig.7.1. As suggested by Mrozowski [7], the coke particles support each other during baking until the binder is solidified. As a result, the particles are always in direct contact with each other in the baked artefact and they are linked by bridges of coke binder (fig.7.1). The binder in baking does not produce a dense shell around each particle due to shrinkage. Hence the binder layer is full of minute cracks as the shrinking binder decreases its volume by way of opening cracks perpendicular to the surface of the particles. Macropores of size comparable to the particle size appear in between the particles as well as through out the binder phase. The crystallites within the coke particles are nearly all parallel. Due to differential thermal contraction of these crystallites, microcracks are formed parallel to the basal planes. Other microporosity also arises due to the slight misorientation of these crystallites. In a way, the coke grains are full of voids and cracks but of a microscopic scale. Under uniaxial loading, both the open and closed pores behave in the same way by providing free surfaces to accommodate the shear deformation of the coke particles and contribute to the overall deformation of the porous aggregate. This is further demonstrated schematically by an arrangement of four such particles (from Mrozowski [7]) under uniaxial compression as shown in fig.7.2. It can be seen that shear and compression occur at the same time. The shear

deformation of the coke grains into the available voids is also responsible for the apparent low value of Poisson's ratio for the polycrystalline material. However, the situation changes when the porous material is under hydrostatic pressure. With the existence of open pores in the binder phase as well as the numerous cracks in the binder layer that surrounds the coke particles (fig7.1), there is no doubt that individual particles are accessible to the pressure fluid. As a result, shear deformation of individual grains into the open pores (as in the case of uniaxial loading) is greatly restricted due to internal pressure present in these pores. This is again demonstrated by the same four particles under hydrostatic pressure as shown schematically in fig.7.3. It can be seen that the hydrostatic deformation of the porous material comes mainly from the dilatation of individual particles. The presence of some closed porosity between the grains, on the other hand, can also contribute to the overall deformation by accommodating some of the internal strains in the particles. However, with the absence of major shearing of the particles into the open voidage, the strains observed under hydrostatic pressures should be considerably lower than the strains observed for uniaxial loading. In the present work, hydrostatic testing to 600 psi produced longitudinal strains of about 130×10^{-6} for graphites A and B and about 100×10^{-6} for graphites C and D. These strains are considerably lower than those obtained under a compressive stress of 4.14 MPa, which were over 500×10^{-6} for graphites A, B and D and 350×10^{-6} for graphite C. Thus polycrystalline graphite becomes stiffer when tested under pressure. The Poisson's ratio v, for a homogenous and isotropic body can be determine from the ratio of the strain under hydrostatic pressure p (equal to $p/3K = p(1 - 2v)/E$) over the compressive strain (equal to s/E, where s is the stress). For p=s, the ratio has the value of $(1 - 2v)$. The value of v calculated in this way are 0.37 for the isotropic graphites, 0.35 and 0.4 for graphites C and D respectively. The experimental values from the ratio of lateral to longitudinal strain under uniaxial loading

(section 6.1.1) are, however, smaller than the calculated values by a factor of over three. Even when the strain for a coated specimen under pressure (see later) is used in the numerator, the effective v values found (0.3, 0.26 and 0.18 for the four graphites) are much larger than those measured experimentally by uniaxial loading. These comparisons emphasize the difference in the nature between hydrostatic and uniaxial loading for porous bodies.

The hydrostatic deformation of the coke particles comes mainly from the crystallites and their interaction with each other and with the microporosity present in the particles. The extremely low shear modulus of graphite crystals is associated with the movement of dislocations lying in the basal planes. In polycrystalline graphites, the population of mobile basal-plane dislocations is believed to be significantly greater than in large single crystals due to the greater population of tilt and twist boundaries (within and between crystallites) which can be fertile sources of mobile dislocations [41]. Hydrostatic pressurisation of a non-porous body does not produce shear stresses which can induce plastic flow. However, the coke grains contain pores and the crystallites are themselves full of cracks running parallel to the basal planes. Hence, under hydrostatic pressure, the crystallites deform by shear motion of the layer planes. The plastic flow of crystallites of different orientation is made possible with the presence of microporosity. The fact that hydrostatic testing of graphite specimens also produces small positive residual strains indicates the irreversible shear deformation of the crystallites. The results of the neutron irradiated specimens provide additional evidence for the dislocation contribution towards the hydrostatic strain (see later). The bulk modulus of the irradiated specimens increases with increasing neutron dose, a trend similarly observed for the increase in Young's modulus which has been attributed to dislocation pinning by the irradiation-induced defects. Hence, the increase in K is most certainly due to

the dislocation pinning effect which resists the shear deformation of the crystallites within the particles.

Other than the shearing of crystallites, the high compressibility of the crystallites in the c-axis direction can also contribute to the overall deformation of the coke grains under pressure. For the low pressure work described here, it is believed that the hydrostatic strain of polycrystalline graphite is due to a combination of crystallite shear into the microporosity and the compression of crystallites in the c-axis direction. As the pressure increases, it is believed that the microvoids and cracks in the particles become exhausted and the compression term becomes predominant at pressures higher than that investigated here. Since the c-axis compressibility of single crystal is known to decrease with increasing pressure, it is reasonable to expect that the deformation of the polycrystalline aggregate also decreases with increasing pressure. Although the maximum pressure reached in this work is only 600 psi, the high pressure work of Kmetko et al. [38] and Jortner [41] indicates the stiffening behaviour of polycrystalline graphite at higher pressures. This stiffening behaviour of the porous aggregate clearly comes from the stiffening of the coke grains due to elimination of the microporosity and the subsequent decrease of the crystallite compressibility at higher pressures. The crystal bulk modulus (K_c), from the inverse of the volume compressibility, has a value of about 33 GPa. This is greater than that for the polycrystalline material (by a factor of over three) due to the existence of minute cracks and voids in the coke grains.

Jortner [41] in his work on ATJ-S graphite reported that below 2000 psi, the deformation behaviour of both coated and uncoated specimens follow the predicted elastic pressure deformation which is essentially

$$e = (1 - 2v)p/E \qquad \text{eqn.7.3}$$

where E and v are Young's modulus and Poisson's ratio and are obtained from uniaxial compression tests. The behaviour of both specimens only depart from

the elastic theory of deformation at pressure higher than 2000 psi where the hydrostatic behaviour of both specimens diverge increasingly from each other and from the elastic theory. In other words, the coated specimens become more compressible while the uncoated specimens become increasingly stiffer as pressure increases. The data for the elastic theory of deformation were calculated for graphite A based on the values of E and ν obtained from the uniaxial compression tests. However, it is found that the deformation behaviour of the isotropic graphite does not follow the behaviour as predicted by the elastic theory of deformation (see fig.7.4). It can be seen that the isotropic graphite is actually stiffer than the theory predicted. This stiffer behaviour of the actual material signifies the inadequacy of the conventional elastic theory of homogeneous bodies to predict the hydrostatic deformation of polycrystalline graphite. The elastic theory employs E and ν whose values are obtained from uniaxial tests where both the open and closed porosity can contribute to the overall deformation. However, only the closed porosity of graphite can contribute to the deformation under hydrostatic pressure, it is inevitable that the discrepancy will arise. Consequently the theoretical bulk modulus K_t, as determined from the elastic theory where

$$K_t = E/3(1-2\nu) \qquad \text{eqn.7.4}$$

is considerable lower than the bulk modulus of the actual materials as determined from the pressure tests. The values of K_t were found to be 3·8 and 3·5 GPa for graphite A and B as opposed to the experimental value of about 10 GPa for both graphites.

7.3 Hydrostatic behaviour of coated specimens

Booy and Bacon [67] reported that the closed porosity of polycrystalline graphite can contribute to its bulk deformation under pressure. The effects of closed porosity is to increase the compressibility of the porous material by providing free surfaces to accommodate the

deformation of the coke particles under pressure. Coating the porous material provides a simple way of increasing the closed porosity since the total porosity becomes effectively sealed from the pressure fluid. As expected, the hydrostatic deformation of the coated specimens increases considerably in both directions. This behaviour resembles the uniaxial loading of the uncoated specimens where major shearing of the coke grains into the available pores occurred. In other words, when the open pores are free from the pressure fluid, individual coke grains are no longer under a multiaxial stress field and the rigid network of grains and pores can be compressed as a whole. Consequently the compressibility of the coated materials increases as observed by Kmetko et al. [38] and Jortner [41]. The high pressure work of Kmetko et al. on coated specimens of AUC graphite indicates that above a pressure of 600 MPa (6 kbars) virtually all of the porosity has been eliminated and the volume compressibility is found to be 30.3×10^{-12} m²/N. This is very close to Bridgeman's value for single crystal of ceylon graphite which is 29.6×10^{-12} m²/N. Although Jortner reported that the deformation of the coated specimens only departs from that of the uncoated ones at pressure above 2000 psi, the results on all four graphites employed here show that even at low pressures of up to 600 psi, all the coated specimens show a significant increase in deformation over the uncoated ones. The increase in strain ranged from 50% for graphite B to over 200% for graphite D in the circumferential direction. The extremely large deformation of graphite D is attributed to the large fraction of open pores which are probably distributed between the long dimension coke particles. When these pores become closed upon coating the material, an exceptionally large deformation will occur in the circumferential direction. Since the total porosity can contribute to the bulk deformation under pressure, the pressure-strain response of the coated specimens should move closer towards the elastic theory of deformation than the uncoated ones. This is demonstrated for graphite A in fig.7.4. Due to the

increase in dilatation, the bulk moduli of the coated specimen, K_{expt}(coat), are lower than those of the uncoated ones (K_{expt}(uncoat)). For the isotropic graphites, K_{expt}(coat) should be closer to the theoretical modulus (K_t) than K_{expt}(uncoat). For instance the values of K_t for graphites A and B are 3.8 and 3.5 GPA whereas K_{expt}(coat) has values of 6.2 and 6.7 GPa respectively. On the other hand, K_{expt}(uncoat) has a value of about 10 GPa for both graphites.

7.4 Effect of closed porosity

In order to investigate how the hydrostatic deformation of polycrystalline graphite depended upon the closed porosity, specimens of known porosity values (o.p.v. and c.p.v.) were employed. The results for these specimens are presented in section 6.5.1. (see also table 6.8 and 6.9). If the closed porosity contributes to the overall dilatation of the uncoated specimens, then it is reasonable to assume that the open porosity will also be responsible for the increase in dilatation of the coated specimens, since the increase in closed porosity is entirely from the open porosity. The fractional increase in dilatation together with the fraction of open porosity are calculated for the specimens tested and are shown in table 7.2. It is seen that the two sets of data are in good agreement with each other for graphites B and C, i.e. the increase in dilatation of the coated specimens is actually proportional to the increase in closed porosity, which is essentially the open porosity in the uncoated specimens. However, for graphite D which has a higher fraction of open porosity, the two values differ significantly (see table 7.1).

The relationships between the elastic modulus E, and total porosity (voidage) V, that have been proposed in the literature are as follows:

1) $E = E_0 (1 - kV)$ .....eqn.7.5 , due to Mackenzie[26],

2) $E = E_0 (1 - V)/(1 - bV)$ .....eqn.7.6, due to Hasselman [27],

3) $E = E_o \exp(-cV)$ .....eqn.7.7, due to Spriggs [28].

All these are empirical expressions where E_o is the modulus at zero porosity and k, b and c are constants. Mackenzie [26] originally developed an expression for the effective bulk modulus k of a material containing small spherical holes distributed at random throughout the volume of the material. This has the form of

$$1/k = 1/k_o + 3(1 - d)/4\mu_o d \qquad \text{eqn.7.8}$$

where k_o and μ_o are the bulk and shear moduli of the real material while d is the density of the actual material. The expression due to Hasselman was based on solutions given by Hashin [68] where a continuous phase contains a dispersed phase of spherical voids. The one due to Spriggs is a simple exponential equation which appears to be valid for aluminium oxide and other refractory materials [28]. Although all the expressions yield E equal to E_o when the voidage is set to zero, only the one due to Hasselman satisfies the condition that E is equal to zero when the voidage is set to unity. Due to the significance of the closed porosity of polycrystalline graphite under pressure, these expressions can be modified to represent the empirical relations between the bulk modulus K and the closed porosity U, as follows:

1) $K = K_o (1 - kU)$ eqn.7.9

2) $K = K_o (1 - U)/(1 - bU)$ eqn.7.10

3) $K = K_o \exp(-cU)$ eqn.7.11

where K_o is the bulk modulus at zero porosity while k, b and c are empirical constants. It can be shown that eqn.7.9 can be derived from eqn.7.8 and is not therefore simply an empirical relation. Kmetko et al. showed that above 500 MPa, all the porosity of the polycrystalline material is eliminated and the volume compressibility is very close to that for graphite single crystals. Hence, it is reasonable to assume that K_o of polycrystalline graphite is equivalent to the bulk modulus of single crystals (K_c), i.e. K_o has a value of 33 GPa. To investigate the applicability of these expressions, the results for

the graphite specimens with known porosity values are again employed (see table 6.8 and 6.9). There are two ways of testing the applicability. First, the constants k, b and c for each graphite can be evaluated in each case by substituting the experimental value of K for the uncoated specimens (K_{expt}(uncoat)) and the volume fraction of closed porosity for U in the expressions. The bulk modulus from the porosity expression (K_{thy}) is then calculated for the coated specimens (K_{thy}(coat)) by substituting the volume fraction of total porosity for U and putting the appropriate constant and K_o into the expressions. The calculated K from the three expressions are then compared with the experimentally determined values (K_{expt}(coat)). Second, the whole procedure may be repeated the other way round by evaluating the constants k, b and c using experimental data (i.e K_{expt}(coat) and total porosity) from the coated specimens and calculating K_{thy}(uncoat) using data from the uncoated specimens (i.e. closed porosity) and the new constants. The calculated K values are also compared with the experimentally determined values (K_{expt}(uncoat)). The results are shown in table 7.3 and 7.4. It can be seen that the calculated values of K based on the Hasselman expression are in approximate aggrement with the experimental values. The calculated values of K_{thy}(coat) give differences of 27, 18 ad 48% for graphites B, C and D respectively. The calculated values of K_{thy}(uncoat), on the other hand, give differences of 26, 20 and 63% for the graphites investigated. The exponential expression due to Spriggs only gives a rough, but not so good, agreement with the experimental values for graphites B and C. For instance the variations in K_{thy}(coat) are 43 and 54% while the variations in K_{thy}(uncoat) are 35 and 50% respectively for graphites B and C. The linear expression due to Mackenzie is entirely inapplicable due to the negative values obtained for K_{thy}(coat) and the large variations in K_{thy}(uncoat) from 74 to over 200%. However, when the average values of the empirical constants k, b and c are used for the porosity expressions, there is a significant improvement in the

calculated values of K_{thy}(uncoat) and K_{thy}(coat), see table 7.5. In this case, the expression due to Hasselman gives a reasonably good agreement with the experimental values with variations of only about 5, 8 and 23% for the calculated values of K_{thy}(uncoat) and 8, 11 and 32% for the calculated values of K_{thy}(coat) for graphites B, C and D respectively. In view of the limited amount of porosity data available for different graphites, it can be said that the expression due to Hasselman (eqn.7.10) gives a reasonably accurate relationship between the bulk modulus K and the closed porosity for the graphites investigated in this work. It is not clear that this observation has more general significance.

With the average empirical constant from the Hasselman's expression, the Young's modulus at zero porosity (E_o) can be determined from eqn.7.6 by using the experimentally determined values of E and the total porosity V. Values of E_o obtained are 36, 69 and 155 GPa for graphites B, C and D. The values of E_o from other investigations are as follows.

1) E_o = 8.4 GPa ... due to Hutcheon et al.[25];

2) E_o = 22 GPa ... due to Hong, quoted from Hutcheon et al. [25];

3) E_o = 25.5 GPa ... due to Cost et al.[69].

Unfortunately, the true value of E_o is not known, for theoretical estimates obtained by using the single crystal elastic constants to calculate the Reuss and Voigt average for a non-porous polycrystalline aggregate are 2 GN/m^2 and 500 GN/m^2 respectively [8]. Although all the values of E_o fall within this range, the discrepancy between the values suggests that the empirical constant b derived from the bulk modulus - porosity expression cannot be used in the equivalent Young's modulus - porosity expression, since there are differences between the uni$\overset{a}{\underset{\wedge}{x}}$ial and hydrostatic deformation behaviour of polycrystalline graphites.

7.5 Effect of pre-stressing

Compressive pre-stressing of graphite specimens results in an increase in dislocation density and the introduction of additional cracks. Microscopic examinations have revealed that cracks appear to initiate preferentially at the boundaries of existing pores and spread along particle-binder boundaries [31-34]. Secondary cracking is prevalent in regions of high pore density where crack extension occurs by joining up with the main crack. Hence, the immediate effect of pre-stressing is to lower the Young's modulus of polycrystalline graphite due to the increase in dislocation and crack densities. Hall's results [36] showed that at a pre-stress level of 21 MPa, the Young's modulus decreased by 35% of its unstressed value. However, the annealing results indicated that for the high level of pre-stressing, the drop in the modulus is only partially recovered. On the other hand, the recovery is almost complete for the specimens subjected to a lower level of pre-stressing, i.e. 7 MPa. From these results, it is concluded that at low pre-stress levels, the decrease in Young's modulus is entirely due to an increase in dislocation density, since the decrease can be completely recovered following a thermal anneal. However, the decrease in E at high level of pre-stressing is probably due to a combination of an increase in dislocation density and the generation of new cracks. Since the drop in E is only partially recovered in this case, it is postulated that only the dislocation contribution to the fall in E is recoverable; the crack contribution to the fall in E is entirely non-recoverable, since recovery would require rebonding of the crack surfaces.

For the effect of the pre-stressing on the hydrostatic deformation investigated in this work, all the graphite specimens were subjected to a very high level of pre-stressing. In the early investigation, specimens of graphite A were subjected to an increasing level of pre-stressing from 9 to 45.3 MPa which was over 50% of the compressive fracture stress of this material. In the later investigation, specimens of graphites A, B and C were subjected to

a compressive stress of 60.4 MPa which were 76, 66 and 68% of the respective fracture stress of these graphites. A specimen of graphite D was subjected to a compressive stress of 22.7 MPa which was about 82% of the fracture stress. It has been reported that above 50% of the fracture stress, optical resolvable cracks are formed in the graphite matrix. Hence, it is reasonable to believe that cracks were also produced in all the pre-compressed specimens employed here.

Despite the high level of pre-stressing carried out in this investigation, the change in properties of polycrystalline graphite under subsequent hydrostatic testing was found to be insignificant. For instance, the strain at 600 psi only changed slightly in the circumferential direction. The change in bulk modulus is also insignificant as compared to the change in Young's modulus under the same level of pre-stressing. For the specimens of graphite A subjected to an increasing level of compressive stress from 0 to 45.3 MPa at 9 MPa per level, the bulk modulus only decreased by about 1% after each level of pre-stressing (see section 6.3.1). Hence, after a pre-stress of 45.3 MPa, the bulk modulus was found to have dropped by only about 5% of the original unstressed value. The small decrease in K following this high level of pre-stressing can be explained in relation to the deformation behaviour of polycrystalline graphite as discussed in sections 7.1 to 7.3.

The hydrostatic deformation of polycrystalline graphite is generally small due to the absence of major shearing of the coke particles into the open voidage as a result of internal pressure acting in the pores. The strain of the bulk material originates from individual coke particles with a combination of shearing and compression of the crystallites within these particles. Since the effect of pre-stressing is to increase the dislocation and crack densities in the graphite matrix, it is believed that only those occurring within the coke particles would affect the hydrostatic deformation of graphite under pressure. The cracks occurring around the pores and those

running along the coke-binder boundaries have little or no effects since they are open to a gas and are in a way similar to the open pores already existing in the material. The small decrease in K observed is thus explained by the increase in dislocation density after the pre-stressing. For the later investigation on the other graphites, it was found that the decrease in K was either small or within the specimen variation from a batch. Hence, the dislocation contribution to the hydrostatic strain is probably small. The small increase in the circumferential strain and the slight anisotropy effect for the isotropic graphites after pre-stressing are probably due to the deformation of pores and cracks on the basal planes of the crystallites as suggested by Eto and Oku [70]. Their porosimetry results indicated that the pore volume increased in the with-grain specimens while the across-grain specimens showed a decrease in pore volume following compressive pre-stressing. They then proposed a model whereby the deformation of cracks and pores in the the basal planes accounts for the difference in the behaviour of resistivity change between the with-grain and across-grain specimens and between tensile and compressive pre-stressing. The deformation of cracks and pores occur in the manner shown in fig.7.5. Hence, it can be seen that compressive pre-stressing increases the size of the cracks and pores in the crystallites with basal planes lying in the direction of the applied stress. However, for crystallites with basal planes perpendicular to the direction of the applied stress, the cracks and pores decrease in size. The reverse is true for the case of tensile pre-stressing. Due to the low compressibility of the crystallites in the a-axis direction, the hydrostatic strain in any direction will then be influenced by those crystallites perpendicular to that direction. Hence, the longitudinal strain is predominantly influenced by the crystallites with basal planes parallel to the circumferential direction. Since there is a decrease of pore volume of these crystallites after pre-stressing, the change in the longitudinal strain (e_m) is thus found to be small. On the other hand, the

circumferential strain is predominantly influenced by the crystallites with basal planes parallel to the longitudial direction. Since there is an increase in pore volume of these crystallites after pre-stressing, the increase in the circumferential strain is thus explained. The slight anisotropy of the isotropic graphites is also due to the increase in pore volume of the crystallites which affected the circumferential strain. However, the decrease in the circumferential strain after the initial tests indicates that the cracks and pores deform back to their original shapes after pressurisation. As a result, additional testing under pressure on the same specimen produces no further change in the strains at 600 psi.

7.6 Neutron irradiated specimens

Fast neutron-induced changes are complex, consisting of within-crystal effects and changes resulting from the presence of porosity. In addition there are changes due to radiolytic oxidation by the coolant under nuclear reactor environments. The within-crystal effects arise from the irradiation-defects within graphite crystals which effectively pin down glissile basal plane dislocations and increase the shear modulus of the crystals. Under low dose low temperature irradiation, these effects predominate and are responsible for the initial increase in the Young's modulus with neutron dose. The structural changes arise from the irradiation-induced volume changes which are shrinkage at low doses and expansion at higher doses. The initial shrinkage is a direct result of crystal dimensional changes which are a combination of c-axis growth and a-axis shrinkage. The initial effect on the structure is a closure of fine pores which causes the Young's modulus to increase steadily during volume shrinkage as the porosity decreases. At higher doses, unrestrained crystals will continue to change dimensions and intercrystalline reactions in the polycrystalline material result in a large-scale generation of new porosity. This explained the fall in E at higher doses

due to a net growth in the material. The decline of the modulus of polycrystalline graphites, according to Brocklehurst [10], occurs at doses greater than $2x10^{22}$ n/cm² for irradiation temperatures from 360 to 440°C. For irradiation temperatures from 560 to 790°C, the decline in the modulus occurs at a slightly lower dose of $1.5x10^{22}$ n/cm². This decline in E signifies the expansion phase of polycrystalline graphite under high neutron doses.

The highest neutron dose investigated in this work is $17x10^{20}$ n/cm² which is below the dose where the decline in E occurs. Hydrostatic testing of the irradiated specimens produced smaller strains in both directions and a subsequent rise in the bulk modulus (section 6.4.1 to 6.4.3). From specimens of different doses investigated in this work, the results indicate that the increase in K appears to saturate for doses greater than $17x10^{20}$ n/cm². This increase in K with neutron dose is in a way similar to that observed for the Young's modulus. This is attributed to the pinning of glissile plane dislocations by irradiation-induced defects within the crystallites. However, the non-linear pressure-strain curves and the large pressure-strain loops observed for the irradiated specimens are in contrast to those observed for uniaxial testing. The precise reason for this phenomenon is not known but a possible explanation is that the c-layer growth of the crystallites due to irradiation could be responsible for changing the linear c-axis strain-response under pressure.

Although thermal annealing of neutron irradiated specimens is known to restore the pre-irradiation properties of polycrystalline graphite, the results on the three annealed specimens (section 6.4.4) produced strains greater than those of the irradiated unannealed material as well as the unirradiated unannealed material. Subsequently the bulk modulus fallsbelow that for unirradiated specimens. This behaviour is also observed by Kelly et al. [51] who showed that for annealing temperatures above 1500°C, the modulus falls below that of the virgin material, the decrease continuing

steadily right up to the highest annealing temperature of 2800°C. They attributed this behaviour to the abnormal c-axis expansion which closes the micro-cracks in the basal planes of the crystallites as the temperature is raised. As a result, the thermal expansion of the aggregate will increase. The structure of graphite will yield to accommodate this increased expansion and an irreversible dilatation will occur. This stretching effect probably occurs by crystal shear in the aggregate and will certainly produce a re-arrangement of the basal plane dislocations or even cracking which eventually results in the fall of the modulus.

The bulk modulus of an isotropic non-porous body is related to the aggregate compliances by

$$K = 1 / 3(3\bar{S}_{11} - \bar{S}_{44}) \qquad \text{eqn.7.14}$$

where $1/\bar{S}_{11}$ and $1/\bar{S}_{44}$ are the aggregate Young's modulus and shear modulus respectively. If $\bar{S}_{11}$ and $\bar{S}_{44}$ are estimated from the single-crystal constants, the two extreme theoretical estimates are K_R for the uniform stress (Reuss) model and K_V for the uniform strain (Voigt) model. Using the values of $\bar{S}_{11}$ and $\bar{S}_{44}$ for these two models quoted in Birch [8], the values of K_R and K_V can be determined. For the dislocations-unpinned model, K_R has a value of 35.5 GPa while K_V has a value of 288 GPa. For the dislocations-pinned model (i.e. after irradiation), values of 36.6 and 288 GPa are obtained for K_R and K_V respectively. Although there are significant changes with irradiation in $\bar{S}_{11}$ and $\bar{S}_{44}$ for both models, the changes in K_R and K_V are small. It can be seen that K_R for both the dislocations-unpinned and dislocations-pinned models are quite close to the single crystal bulk modulus of 33 GPa. As a result, K_o in the porosity expressions (eqn.7.9 to 7.11) may be assumed to remain unchanged for the irradiated specimens. It can be concluded that the empirical constant b for Hasselman's expression will change due to changes in the porosity values with irradiation.

7.7 Elevated temperature tests

The elevated temperature tests in this work showed a small increase in strain and a subsequent small or insignificant drop in the bulk modulus of polycrystalline graphite tested in the temperature range from 20 to 300°C. The results will be discussed in relation to the change in Young's modulus with temperature. Mason and Knibbs [70] investigated the change in Young's modulus over the temperature range from -196 to 1000°C for a British nuclear-grade graphite. They found that generally there is a fall in the modulus from -196°C until a minimum is reached at about 300°C, which is then followed by a rise as the temperature is increased to 1000°C. The minima in the modulus-temperature curves occur at about 200 to 300°C. They explained the tempearature dependence of modulus in terms of a dislocation unpinning model and a void-filling mechanism. In view of the negative temperature dependence of pyrolytic graphite up to about 2000°C [71], they suggested that basically the individual crystallites have a negative temperature dependence on modulus. The positive temperature dependence observed at higher temperature is attributed to a process of void-filling which is determined by the difference between the volume thermal expansion coefficients of artefact and constituent crystallites. Below room temperature the negative temperature dependence arises from a thermally dependent dislocation unpinning process in which the dislocations are pulled free of the pinning points by some thermally generated force. This continues into the temperature region where the temperature dependence of the modulus becomes positive. Above room temperature, there becomes superimposed on the unpinning process another one, thought to be the closing of microvoids, which causes the modulus to rise with temperature. Above about 300°C, the void-filling mechanism predominates and results in the increase in modulus with increasing temperature up to 1000°C.

The temperature range investigated in this work is from 20 to

300°C which coincides with the temperature range where the Young's modulus is still decreasing with temperature but approaching a minimum before increasing again. As the hydrostatic deformation of polycrystalline graphite depends primarily on the properties of the constituent crystallites, the slight drop in the bulk modulus with temperature is consistent with the reduction in crystal stiffness with increasing temperature. The void-filling mechanism is, however, unimportant for the temperature range investigated here. The small decrease in the bulk modulus observed here is, therefore, due to dislocation unpinning which is a thermally activated process.

7.8 Four point bend tests

The results of the 4-point bend tests indicate that both the mean bend strength and the strain to failure of all the graphites drop when the tests were performed under 600 psi (section 6.7). To investigate the stress-strain behaviour of the bend specimens, five specimens were employed and the values of bend stress and strain were recorded during the bend tests before fracture occurred. The sample mean and standard deviation were then calculated which enabled a mean stress-strain curve to be plotted. This procedure was carried out for the bend tests at atmospheric pressure and at 600 psi. All three graphites were investigated and the stress-strain curves of the bend specimens are shown in fig.7.6 to 7.8. The results showed that all the bend specimens were stiffer when tested under a pressure of 600 psi. The bend strengths were further analysed following the approach of Weil et al. [72] which was also employed bt Brocklehurst et al. [73]. The probability of fracture S, corresponding to a particular stress level s_n are calculated from the expression

$$S = n/(N+1)$$

where N is the total number of specimens tested in the series, and n is the specimen serial number listing the fracture stress in an increasing order from

1 to N, with s_n being the nth fracture stress. In this way, the probability of fracture S at a particular fracture stress can be calculated for all the specimens tested in a batch. The graphs of S versus bend strengths of individual specimens are then plotted for the graphites investigated and are shown in fig.7.9 to 7.11. From these figures it can be seen that the bend strength distribution curves at 600 psi are clearly shifted from those at atmospheric pressure in a direction closer to the stress axis. This implies that at the same probability of fracture, the bend strengths at 600 psi are lower than those at atmospheric pressure. For the sleeve material which showed a drop of mean strength by over 7%, the two curves are well separated.

The stiffer behaviour of the bend specimens under pressure can be explained by the internal pressure presence in the accessible pores which has the effect of resisting the bending deformation of the specimens. This also accounts for the brittle behaviour of the bend specimens when tested under 600 psi. In order to account for the decrease in bend strength, the fracture behaviour of polycrystalline graphite must be resolved. There is a number of research publications regarding the fracture mechanics of nuclear graphites [76-79] either using finite element approach or statistical and computer modelling of crack initiation and propagation. The theoretical model of graphite on the basis of its micro-structure by Buch [78] is considered here. In this model, fracture is considered as a progressive phenomenon that involves the initiation of microcracks within individual crystallites. These microcracks increase in density as stress is increased and interlinking occurs between suitably oriented neighbours. This crack growth proceeds until the grain is regarded as the fundamental unit, and further interlinking occurs between suitably oriented grains when sufficient strain energy is available to fracture the misoriented region at the grain boundaries. Eventually this leads to macro-fracture due to coincident alignment of arrays of cracked grains. This is shown schematically in fig.7.12.

The effect of pressure on the fracture behaviour of graphite is to enhance the crack initiation and propagation and the eventual alignment of suitably oriented cracked grains due to the internal pressure acting in the accessible pores. This postulation is not unreasonable in view of the work of Diefendorf [80] who showed that the bend strength of a commercial graphite at 1000°C in vacuum was about 20% greater than that at room temperature in air, and about half this strength increase was retained on cooling to room temperature while maintaining the vacuum. However, re-admission of air reduced the strength to the original value. Rowe [81] and Gillin [82] also reported that the strength of graphite is higher in vacuum than in air. Logsdail [83] investigated the effect of water vapour on flexure strength of graphite and reported that the room temperature strength and strain to failure were reduced by the physical absorption of water vapour, removal of which increased these parameters by up to 40%. The decrease in strength was attributed to the decrease in surface energy (γ) of graphite which affected the weak van der Waals bonding between the basal planes. The work of Diefendorf [84] on pyrolytic graphite supported this view since it was shown that only the strength between the basal planes was reduced by exposure to air. Gillin [82], on the other hand, commented that the effects of the atmosphere are to attack the weak bonding between layers (a corrosive effect) and possibly influence the yield shear stress in the basal planes. He suggested that since the coefficient of friction is higher in vacuum (based on the work of Rowe et al. [85]) the yield shear stress will be higher and plastic deformation will be more difficult along the basal planes.

From these observations, the decrease in strength when the test environment changes from a vacuum to atmospheric condition is similar to the decrease in bend strength from atmospheric condition to a pressure of 600 psi, since both cases involve an increase of pressure in the test environment. However, there is not sufficient evidence in this work to

support the views that the decrease is due either to a corrosive effect which attacks the weak bonding between layer planes, or a decrease in the coefficient of friction between layer planes which reduces the yield shear stress. The influence of pressure on the bend strength of graphite is believed to be mainly a mechanical effect. Since pressure can penetrate and open up the pores and cracks within the particles, it is envisaged that crack initiation and growth along basal planes will be enhanced with the presence of internal pressure in the bend specimens. This aspects can further be demonstrated by considering the Griffith equation for fracture, i.e.

$$s_f = ((2E\gamma)/(\pi c))^{0.5} \qquad \text{eqn.7.12}$$

where s_f is the fracture stress, c is the maximum crack length and γ is an effective surface energy. In the absence of significant plastic deformation, the fracture strain e_f is given approximately by Hooke's law where

$$e_f = s_f/E = ((2\gamma)/(\pi Ec))^{0.5} \qquad \text{eqn.7.13}$$

Since it has been shown that the bend specimens were actually stiffer under a pressure of 600 psi, it is reasonable to believe E increases. The increase in E is, however, offset by the increase in c due to pressure which opens up the cracks. From eqn. 7.12, the change (decrease) in s_f is , therefore, not very significant as observed in this work. However, from eqn.7.13, the decrease in e_f will be significant. This is in agreement with the substantial drop in the fracture strain of the bend specimens observed under pressure.

CHAPTER 8

CONCLUSIONS

8.1 Hydrostatic behaviour

Under hydrostatic pressures, individual coke grains in the graphite matrix are directly compressed by the pressure fluid due to the presence of open pores and cracks throughout the binder phase. It is the deformation of these grains that contributes to the overall dilatation of the bulk material. The shearing of the grains into the open pores, a common feature under uniaxial compression, is restricted due to internal pressure acting in these pores. The closed pores, however, can contribute to the dilatation of the aggregrate under pressure by accommodating the internal strain of the coke grains. For the low pressure work conducted here, it is believed that the deformation of the coke grains is due mainly to a combination of shear and compression of the constituent crystallites. The shearing of the crystallites into the microporosity is attributed to the low shear modulus along the basal planes due to mobile dislocations. For graphite specimens coated with a flexible rubber layer, the total porosity becomes closed. This has the effect of increasing the compressibility of the porous aggregrate under pressure since the rigid network of grains and pores can be compressed as a whole. As a result, the effective bulk moduli for the coated specimens are significantly lower than those for uncoated specimens. The conventional elastic theory is found to be inadequate to predict the hydrostatic behaviour of polycrystalline graphite, which shows a stiffer behaviour under pressure. Consequently the theoretical bulk modulus K_t where K_t is $E/3(1 - 2v)$ for an isotropic continum, is some 50% lower than the experimental values of K for uncoated specimens of the isotropic graphites. This exposes the error in using K_t for K, for it only applies to material for which both the open and closed pores contribute to the bulk modulus, i.e. a sealed sample.

8.2 Effect of closed porosity

In view of the significance of the closed porosity upon the hydrostatic deformation of polycrystalline graphite, the closed and open pore volumes of three graphites (B, C and D) were determined. The results from these specimens indicate that the increase in dilatation of the coated specimens is proportional to the increase in closed porosity due to sealing of the open porosity. The effect of the closed porosity is further investigated following the different empirical expressions due to Mackenzie [26], Hasselman [27] and Spriggs [28] which relate the porosity with modulus for porous materials. The calculated values of both K_{thy}(uncoat) and K_{thy}(coat) based on Hasselman's expression (see section 7.4) are found to be in good agreement with the experimental values. Since the porosity data are limited for different graphites, it may be concluded that the Hasselman's expression (eqn.7.10) gives a fairly accurate relationship between the closed porosity and the bulk modulus for the graphites investigated here.

8.3 Effect of pre-stressing

Despite the large fall in the Young's modulus of polycrystalline graphite subjected to a high level pre-stressing, hydrostatic testing of the pre-compressed specimens only produced a small and insignificant decrease in the bulk modulus. Since compressive pre-stressing of graphite specimens increases the dislocation and crack densities of the graphite matrix, it is concluded that the slight drop in K is a dislocation contribution effect. The generation of new cracks which accounts for the large fall in E, has little effect since it resembles the open porosity already existing in the material. The slight increase in strain in the circumferential direction is attributed to the deformation of cracks and pores within the crystallites following pre-stressing.

8.4 Irradiated specimens

For the three sleeve graphites with different irradiation doses investigated, it is found that the bulk modulus increases with increasing neutron dose and the increase appears to saturate for doses greater than those employed here. The increase in K is attributed to a dislocation-pinning effect which effectively increases the shear modulus of graphite crystallites. For the annealed specimens, The bulk modulus is found to fall below that of the unirradiated material. This is explained by a stretching effect due to closure of micropores which causes an irreversible dilatation in the graphite structure as it is forced to accommodate the large c-axis expansion of the crystallites.

8.5 Elevated temperature tests

The elevated temperature tests produced only small decrease in the bulk modulus for the temperature range investigated (20 to 300°C). This is similar to the decrease in E over the same temperature range as observed by Mason and Knibbs. The slight fall in K is, therefore, attributed to a dislocation-unpinning effect which is a thermally activated process.

8.6 Four point bend tests

The results of the 4-point bend tests indicate a drop in both the mean bend strength and the strain to failure when the tests are performed under a pressure of 600 psi. The stress-strain curves of the bend specimens show a stiffer behaviour at 600 psi. The bend strength distribution curves at 600 psi reveal that at a particular probability of fracture, the bend strength at 600 psi is clearly lower than that at atmospheric pressure. The stiffer behaviour of the bend specimens under pressure is due to the internal pressure in the open pores which restricts the bending deformation. The decrease in bend strength is similar to the decrease in strength reported in

the literature when a test specimen is exposed to atmospheric air as exposed to a vacuum. It is concluded that the drop in bend strength under pressure is due to gas which penetrates and opens up the pores and cracks within the coke particles. Hence, the crack initiation and growth along the basal planes will be enhanced with the presence of internal pressure in the bend specimens. This feature, together with an increase in stiffness, leads to the observed reduction in strain to failure.

REFERENCES

1. Kelly B T, Bacon D J and Boey S Y, Carbon, 20, 355, 1982.
2. Kelly B T and Brocklehurst J E, Proc. 3rd Conf. on Carbon and Graphite, SCI, London, 363, 1971.
3. Losty H H W, Bell I P and Jenkins G M, Proc. 5th Carbon Conf., Pergamon Press, New York, 266, 1963.
4. Kelly B T, Physics of graphite, Applied Science Publishers, London and New York, 1981.
5. Davidson H W and Losty H H W, Proc. 4th Carbon Conf., Pergamon Press, Oxford, 585,1960.
6. White E S, Proc. 4th Carbon Conf., Pergamon Press, Oxford, 675, 1960.
7. Mrozowski S, Proc. 1st and 2nd Carbon Conf., Univ. of Buffalo, 195, 1956.
8. Birch M, PhD Thesis, Liverpool University, 1980.
9. Mrozowski S, Proc. 1st and 2nd Carbon Conf., Univ. of Buffalo, 31, 1956.
10. Brocklehurst J E, A Review, UKAEA Report 2731 (S), Feb., 1976.
11. Blackman L F C, Modern Aspects of Graphite Technology, Academic Press, London and New York, 1970.
12. Mastrom C, Keen R and Green L J, J. Appl. Phys., 22, 593, 1951.
13. Green L,Jr., J. Appl. Mech., 20, 289, 1953.
14. Losty H H W and Orchard J S, Proc. 5th Carbon Conf., Pergamon Press, Oxford, 1, 519, 1962.
15. Tsuzuko T and Saito M H, Chemistry and Physics of Carbon, Vol 4 (Ed. P L Walker, Jr), Marcel Dekker, New York, 185, 1968.
16. Seldin E J, Carbon, 4, 177, 1966.
17. Andrew J F, Okada J and Wobschall D C, Proc. 4th Carbon Conf., Pergamon Press, Oxford, 599, 1960.
18. Davidson H W and Losty H H W, Proc. 2nd Int. Conf. on Peaceful Uses of Atomic Energy, paper p/128, United Nations, Geneva.

19. Greenstreet W L, Smith J E and Yahr G T, Carbon, 7, 15, 1969.

20. Jenkins G M, J. Appl. Phys., 13, 30, 1962.

21. Hesketh R V, J. Appl. Phys., 35, 3604, 1964.

22. Wooley R L, Phil. Mag., 11, 799, 1965.

23. Jenkins G M, Williamson G K and Barret J T, Carbon, 3, 1, 1965.

24. Jenkins G M, J. Nucl. Mater., 29, 322, 1969.

25. Hutcheon J M and Price M S T, Proc. 4th Carbon Conf., Pergamon Press, Oxford, London, 645, 1960.

26. Mackenzie J K, Proc. Phys. Soc., 62, 2,1950.

27. Hasselman D P H, J. Amer. Ceram. Soc., 45, 1962.

28. Spriggs R M, J. Amer. Ceram. Soc., 44, 628, 1961.

29. Brocklehurst J E, Brown R E, Gilchrist K E and Labaton V Y, J. Nucl. Mater., 35, 183, 1970.

30. Jenkins G M and Williamson G K, J. Appl. Phys., 34, 2837, 1967.

31. Jenkins G M, J. Nucl. Mater., 5, 280, 1962.

32. Slagle O D, J. Amer. Ceram. Soc., 50, 495, 1967.

33. Knibbs R H, J. Nucl. Mater., 24, 174, 1967.

34. Oku T and Eto M, Carbon, 11, 639, 1973.

35. Eto M and Oku T, J. Nucl. Mater., 46, 315, 1973.

36. Hall E, J. Nucl. Mater., 15, 137, 1965.

37. Oku T and Eto M, Carbon, 2, 103, 1964.

38. Kmetko E A, Morgan J R and Andrew J F, Carbon, 6, 571, 1968.

39. Bridgeman P W, Proc. Amer. Acad. Arts. Sci., 76, 9, 1945.

40. Paterson M S and Edmon J M, Carbon, 10, 29, 1971.

41. Jortner J, Technical Report AFML-TR-71-253, Dec., 1971.

42. Reynolds W N, Physical Properties of Graphite, Elsevier Pub. Co. Ltd., 1968.

43. Thrower P A, Carbon, 9, 265, 1971.

44. Kelly B T, Progress in Nuclear Energy, Pergamon Press Ltd., 2, 219, 1978.

45. Engle G B, Carbon, 9, 539, 1971.

46. Pitner A L, Carbon, 9, 637, 1971.

47. Henson R W, Perks A J and Simmons J H W, Carbon, 6, 789, 1968.

48. Simmons J H W, Proc. 3rd Carbon Conf., Pergamon Press, 559, 1957.

49. Simmons J H W, Proc. SCI Conf. on Carbon and Graphite, 511, 1957.

50. Reynolds W N and Simmons J H W, Proc. 5th Carbon Conf., 1, 255, 1961.

51. Kelly B T, Jones D and James A, J. Nucl. Mater., 7, 279, 1962.

52. Birch M and Bacon D J, Carbon, 21, 491, 1983.

53. Milligan R V, Expt. Mech., 4, 25, 1964.

54. Milligan R V, Ibid., 5, 59, 1965.

55. Milligan R V, Ibid., 7, 67, 1967.

56. Gerdeen J C, Ibid., 3, 73, 1963.

57. Brace W F, Ibid., 4, 212, 1964.

58. Steele M C and Eichberger L C, SESA Proc. 13, 151, 1955.

59. Kabalkina S S and Vereschagin L F, Soviet Physics, Doklady, 5, 373, 1960.

60. Drickamer H G, Lynch R W, Clendenen R L and Perez-Albuerne E A, Solid State Phys., 19, 135, 1966.

61. Blaslee O L, Proctor D G, Seldine J, Spence G B and Weng T, J. Appl. Phys., 41, 3373, 1970.

62. Green J F, Bolsaitis P and Spain I L, J. Phys. Chem. Solids, 34, 1927, 1973.

63. Jenkins G M, Chemistry and Physics of graphite (P.L. Walker, Jr. and P A Thrower, ed.) Vol 2, Dekker, New York, 189, 1973.

64. Boyland D A, G E C Atomic Energy Review, 2, 244, 1959.

65. Kelly B T, Phil. Mag., 9, 721, 1964.

66. Baker C and Kelly A, Phil. Mag., 9, 927, 1964.

67. Boey S Y and Bacon D J, 6th Int. Conf. on Carbon and Graphite, SCI, London, 40, 1982.

68. Hashin Z, J. Appl. Mech., 29, 143, 1962.

69. Cost J R, Janowski K R and Rossi R C, Phil. Mag., 17, 851, 1968.

70. Eto M and Oku T, J. Nucl. Mater., 54, 245, 1974.

71. Mason I B and Knibbs R H, Carbon, 5, 493, 1967.

72. Barrachin A M, Jouquet G, Miccaud G and Pattau F, J. Nucl. Mater., 20, 294, 1966.

73. Weil N A, Bortz S A and Firestone R F, Mater. Sci. Res., 1, 291, 1963.

74. Brocklehurst J E and Darby M I, Mater. Sci. Eng., 16, 91, 1974.

75. Arai T and Oku T, J. Nucl. Mater., 79, 227, 1979.

76. Matthews R, J. Amer. Ceram. Soc., 57, 225, 1974.

77. Price M S T, 6th Int. Conf. on Carbon and Graphite, SCI, London, Sept, 1982.

78. Buch J D, Mechanical behaviour for graphites, Properties related to fracture t' oughness, ASTM STP, 605, 124, 1976.

79. Rose A P G and Tucker M O, J. Nucl. Mater., 110, 186, 1982.

80. Diefendorf R J, Proc. 4th Carbon Conf., Pergamon Press, 489, 1959.

81. Rowe G W, Nuc. Eng., 7, 102, 1962.

82. Gillin L M, J. Nucl. Mater., 23, 280, 1967.

83. Logsdail D H, AERE Report 5721.

84. Diefendorf R J, Proc. 4th Carbon Conf., Pergamon Press, 483, 1959.

85. Rowe G W and Baldwin D J, Tube Investment Research Report No. 62.

TABLES AND FIGURES

GRAPHITE TYPE	SPECIMEN NO.	YOUNG'S MOD. (GPa)	POISSON'S RATIO , ν
A	8	7·6	0·17
A	1	8·2	–
B	25	8·1	0·13
B	28	7·6	0·13
C	24	11·9	0·15
C	27	12·6	0·15
D	23	7·6	0·13
D	26	8·0	0·10

Table 6·1 Compressive stress-strain data

GRAPHITE TYPE s_f (MPa), e_f (%)	SPECIMEN 1	SPECIMEN 2	SPECIMEN 3	SPECIMEN 4
A , s_f	86·1	87·6	83·1	60·4
e_f	3·0	3·2	3·0	2·2
B , s_f	92·1	90·6	92·1	90·6
e_f	3·2	3·2	3·3	3·4
C , s_f	89·1	87·6	89·1	87·6
e_f	2·9	2·8	2·8	2·8
D , s_f	27·2	30·2	26·6	25·7
e	1·8	1·5	1·7	1·8

Table 6·2 Compressive strengths (s_f) and strain to failure (e_f)

Graphite Type	Specimen No	$e_m \times 10^6$		$K_{expt.}$ (GPa)
		long.	circum.	
A	3	135	140	10.0
"	9	130	132	10.5
"	51	130	120	11.2
"	52	130	120	11.2
B	25	132	140	10.0
"	28	135	140	10.0
"	36	138	140	9.9
"	37	135	140	10.0
C	24	108	155	9.9
"	27	102	154	10.0
"	34	120	180	8.6
"	35	126	174	8.7
D	23	100	233	7.3
"	26	85	210	8.2
"	31	105	240	7.1
"	32	118	250	6.7

Table 6.3 Pressure-strain data for the uncoated specimens

Graphite Type	Specimen No	$e_m \times 10^6$		$K_{expt.}$ (GPa)
		long.	circum	
A	2	310	—	—
"	51	280	195	6·2
B	28	200	210	6·7
C	24	165	275	5·8
D	23	350	650	2·5

Table 6·4 Pressure-strain data for the coated specimens

Graphite Type	Specimen No	$e_m \times 10^6$		K_{expt} (GPa)
		long.	circum.	
A	44	125	128	10·9
"	49	120	138	10·5
B	45	130	140	10·0
"	48	130	133	10·5
C	46	100	170	9·4
D	47	84	222	7·8

Table 6·5 Pressure-strain data for the pre-compressed specimens

Graphite A, B, C - prestressed to 60·4 MPa
" D " " 22·7 "

Specimen No	uncoated			coated		
	$e_m \times 10^6$		K_{expt} (GPa)	$e_m \times 10^6$		K_{expt} (GPa)
	long.	circum.		long.	circum.	
101	64	100	15.7	90	210	8.1
102	56	118	14.0	90	—	12.9
103	56	124	13.6	82	235	7.5
104	54	115	14.6	86	216	8.0
105	70	106	14.7	95	220	7.7
106	64	124	13.3	85	230	7.6
107	68	105	14.9	—	—	—
108	60	106	15.2	—	—	—

Table 6.6 Pressure-strain data for irradiated sleeve graphite (6.8×10^{20} n/cm^2)

Neutron dose (10^{20} n/cm^2)	$e_m \times 10^6$		K_{expt} (GPa)
	long.	circum.	
6·8	60	120	14·5
11·0	110	90	14·7
17·0	55	95	16·9

(a)

Neutron dose (10^{20} n/cm^2)	$e_m \times 10^6$		K_{expt} (GPa)
	long.	circum.	
6·8	90	220	7·8
11·0	125	120	11·3
17·0	92	135	11·4

(b)

Table 6·7 Pressure-strain data for irradiated graphites with different dose
(a) : uncoated specimens
(b) : coated specimens

Graphite Type	Specimen No.	Bulk density (g/cm3)	Helium density (g/cm3)	Total porosity vol. %	C.P.V. vol. %	O.P.V. vol. %
A	5	1·772	2·005	21·08	9·47	11·61
"	6	1·787	2·002	19·26	8·54	10·72
B	40	1·829	2·008	19·16	10·26	8·90
"	43	1·830	2·010	19·12	10·16	8·96
C	38	1·854	2·032	18·05	9·31	8·74
"	41	1·844	2·029	18·50	9·37	9·13
D	39	1·674	2·154	26·01	3·72	22·29
"	42	1·676	2·151	25·91	3·83	22·08

Table 6·8 Porosity measurements of graphites

Graphite Type Specimen No.	Uncoated specimens			Coated specimens		
	$e_m \times 10^6$		K_{expt} (GPa)	$e_m \times 10^6$		K_{expt} (GPa)
	long.	circum.		long.	circum.	
B, 40	127	120	11·28	180	180	7·67
" , 43	122	127	11·01	190	178	7·58
C, 38	110	168	9·28	145	250	6·42
" , 41	107	162	9·61	160	240	6·46
D, 39	103	205	8·07	270	740	2·36
" , 42	95	185	8·90	240	660	2·65

Table 6·9 Pressure-strain data of specimens with known porosity values

Specimen No.	Bulk density (g/cm^3)	Helium density (g/cm^3)	O.P.V. vol. %	C.P.V. vol. %
111	1·819	2·039	10·80	8·82
112	1·815	2·040	11·02	8·75

Table 6·10 Porosity values of irradiated sleeve graphite ($6·8 \times 10^{20}$ n/cm^2)

	Mean value of 9	Range
Bulk density, g/cm^3	1·86	1·81 – 1·89
O.P.V., vol. %	8·9	6·7 – 10·1
C.P.V., vol. %	8·7	7·7 – 11·6

Table 6·11 Porosity values of virgin sleeve graphite (from P. Schofield)

No.	Atmospheric pressure		p = 600 psi (4.14 MPa)	
	s_f (bend) (MPa)	e_f (bend) (%)	s_f (bend) (MPa)	e_f (bend) (%)
1	30·3	0·23	32·9	0-21
2	29·0	0·22	27·9	0-18
3	32·9	0·22	32·4	0·20
4	29·0	0·21	29·5	0·19
5	29·1	0·21	35·0	0·21
6	34·9	0·27	30·8	0·19
7	31·4	0·23	28·1	0·18
8	31·9	0·22	30·0	0·19
9	24·5	0·17	32·3	0·18
10	28·4	0·18	34·1	0·22
11	31·8	0·21	34·8	0·21
12	32·8	0·22	35·6	0·19
13	34·5	0·24	31·0	0·20
14	34·6	0·23	24·9	0·16
15	—	—	27·02	0·19

Table 6·12 4-point bend strengths of graphite : Blk. SI2, IJ

No.	Atmospheric pressure		p = 600 psi	
	s_f (bend) (MPa)	e_f (bend) (%)	s_f (bend) (MPa)	e_f (bend) (%)
1	35.1	0.31	31.0	0.21
2	29.5	0.25	29.7	0.23
3	31.6	0.26	33.2	0.24
4	32.9	0.27	29.3	0.22
5	29.8	0.25	29.8	0.23
6	32.5	0.27	28.7	0.21
7	34.3	0.29	26.7	0.21
8	32.1	0.27	29.1	0.20
9	31.4	0.26	32.1	0.23
10	32.9	0.27	29.2	0.20
11	34.0	0.27	29.9	0.21
12	34.1	0.29	32.7	0.23
13	35.1	0.29	32.8	0.23
14	31.9	0.27	33.2	0.26
15	31.9	0.26	30.5	0.21

Table 6.13 4-point bend strengths of graphite : Blk.392

No.	Atmospheric pressure		p = 600 psi	
	s_f (bend) (MPa)	e_f (bend) (%)	s_f (bend) (MPa)	e_f (bend) (%)
1	30·0	0·27	30·0	0·21
2	25·5	0·24	23·8	0·19
3	27·1	0·24	27·8	0·22
4	28·0	0·26	25·9	0·21
5	26·2	0·23	26·0	0·18
6	25·9	0·23	28·0	0·22
7	27·0	0·24	26·5	0·21
8	27·0	0·25	24·7	0·19
9	28·1	0·26	24·1	0·18
10	26·7	0·24	28·0	0·23
11	28·0	0·27	26·81	0·21
12	25·4	0·23	26·0	0·20
13	30·7	0·29	26·3	0·20
14	27·2	0·28	29·3	0·25
15	24·8	0·23	25·2	0·20

Table 6·14 4-point bend strengths of graphite : Blk.398

GN/m^2	$10^{-12}\ m^2/N$
$C_{11} = 1060$	$S_{11} = 0.98$
$C_{12} = 180$	$S_{12} = -0.16$
$C_{13} = 15$	$S_{13} = -0.33$
$C_{33} = 36.5$	$S_{33} = 27.5$
$C_{44} = 4.5$	$S_{44} = 240$

Table 7.1 Elastic constants of a single crystal from Kelly [4]

Graphite Type	Specimen No	$\frac{\delta\Delta}{\Delta}$	$\frac{O.P.V.}{\text{Total porosity}}$
B	40	0.47	0.47
"	43	0.45	0.47
C	38	0.45	0.48
"	41	0.49	0.49
D	39	2.41	0.86
"	32	2.35	0.85

Table 7.2 Fractional increase dilatation with fraction of o.p.v.

$$\frac{\delta\Delta}{\Delta} = \frac{\text{dilatation (coated)} - \text{dilatation (uncoated)}}{\text{dilatation (uncoated)}}$$

Graphite Type	K_{expt} (coat), GPa	K_{thy} (coat), GPa			Constants		
		$K_o(1-kU)$	$\frac{K_o(1-U)}{(1-bU)}$	$K_o \exp(-cU)$	k	b	c
B	7·6	-8	6·5	4·3	6·5	-16·3	10·6
C	6·4	-13	5·2	2·9	7·7	-23·3	13·5
D	2·5	-13·5	1·3	·003	19·5	-72·1	35·7

Table 7·3 Comparison of experimental and calculated values of K for coated specimens using data from uncoated specimens

Graphite Type	K_{expt} (uncoat), GPa	K_{thy} (uncoat), GPa			Constants		
		$K_0(1-kU)$	$\frac{K_0(1-U)}{(1-bU)}$	$K_0 \exp(-cU)$	k	b	c
B	11·2	19·5	14·1	15·1	4·0	-13·1	7·7
C	9·5	19·5	11·4	14·3	4·4	-17·5	9·0
D	8·5	28·4	13·9	22·6	3·6	-33·6	10·0

Table 7.4 Comparison of experimental and calculated values of K for uncoated specimens using data from coated specimens

Graphite Type	K_{expt} (GPa)		K_{thy}, GPa						Average constants		
			$K_o(1-kU)$		$K_o\frac{(1-U)}{(1-bU)}$		$K'_o\exp(-cU)$		k	b	c
	uncoat	coat	uncoat	coat	uncoat	coat	uncoat	coat			
B	11·2	7·6	15·3	-0·09	11·8	7·0	12·9	5·7	5·3	-14·7	9·2
C	9·5	6·4	14·6	-3	10·3	5·7	11·6	4·3	6·0	-20·4	11·2
D	8·5	2·5	18·5	-66	10·5	1·7	13·9	0·1	11·6	-52·9	22·8

Table 7·5 Comparison of experimental and calculated values of K using average constants evaluated in tables 7·3 and 7·4

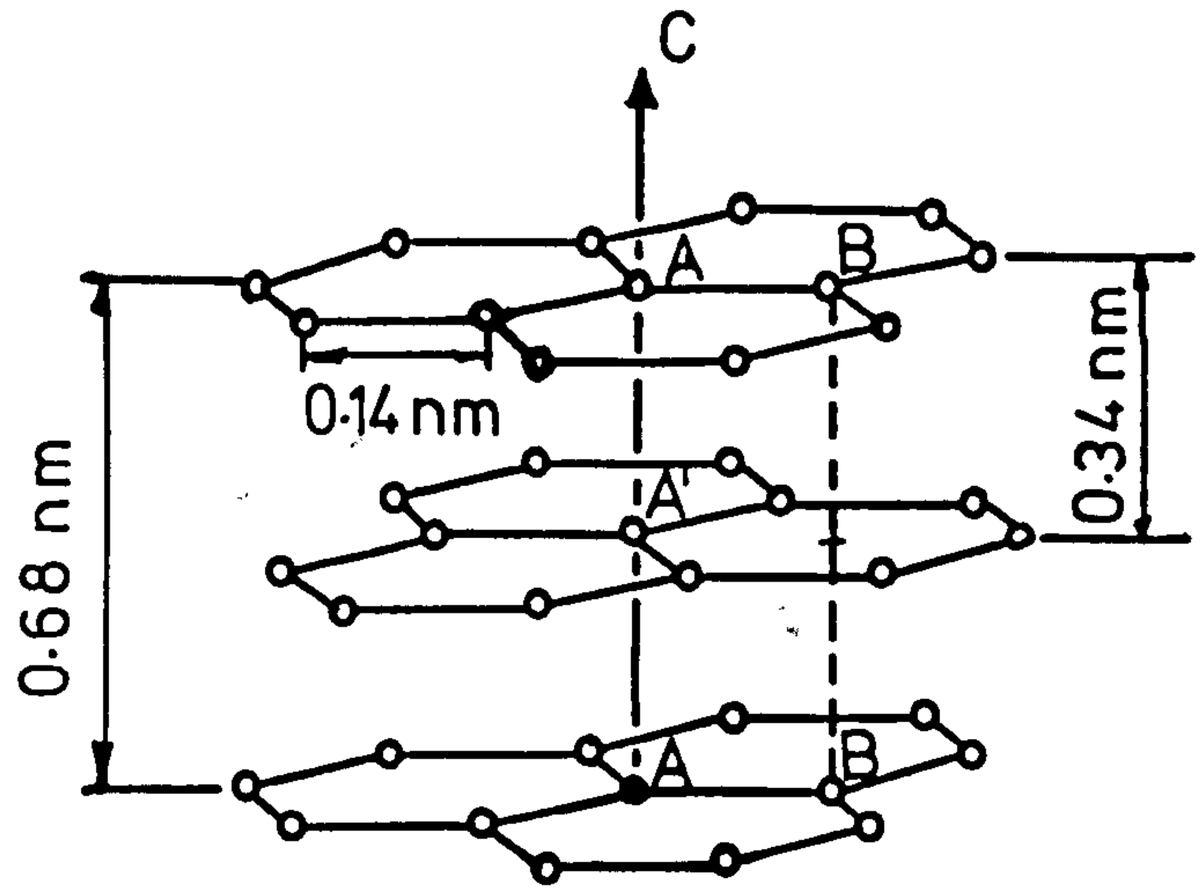

Fig 2.1 Structure of graphite

from Blackman [11]

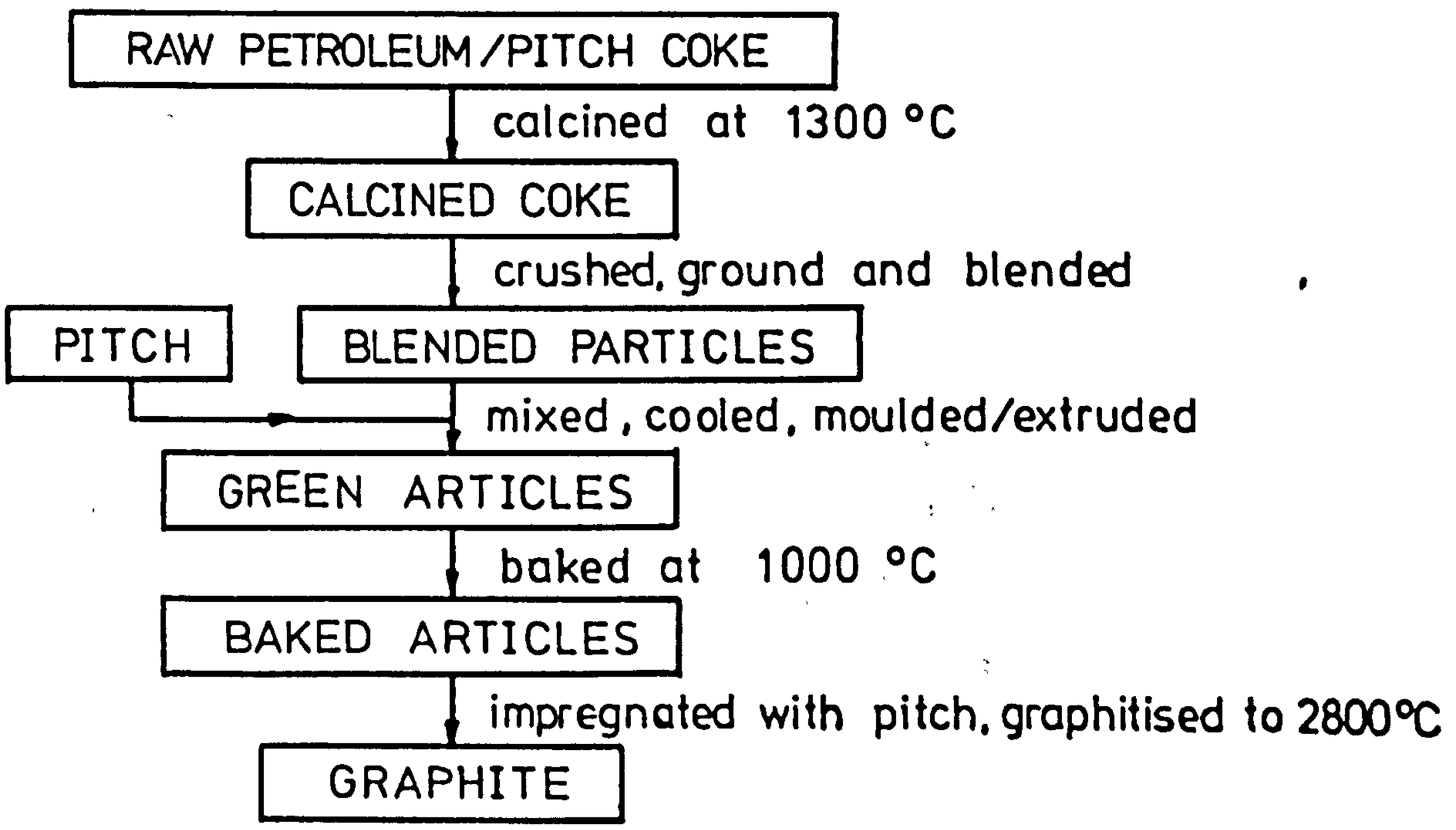

Fig 2.2 Materials and process in graphite manufacture

from Kelly [4]

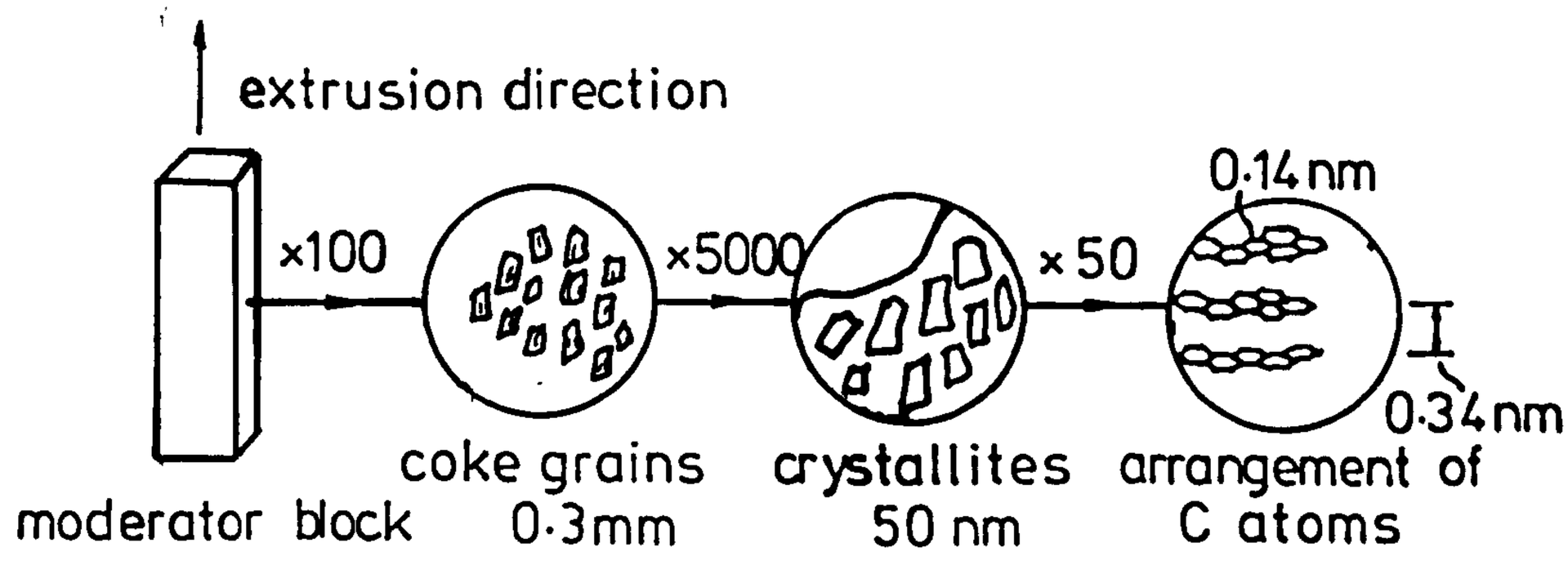

Fig 2.3 Schematic illustration of structure of graphite

from Davidson et al.[5]

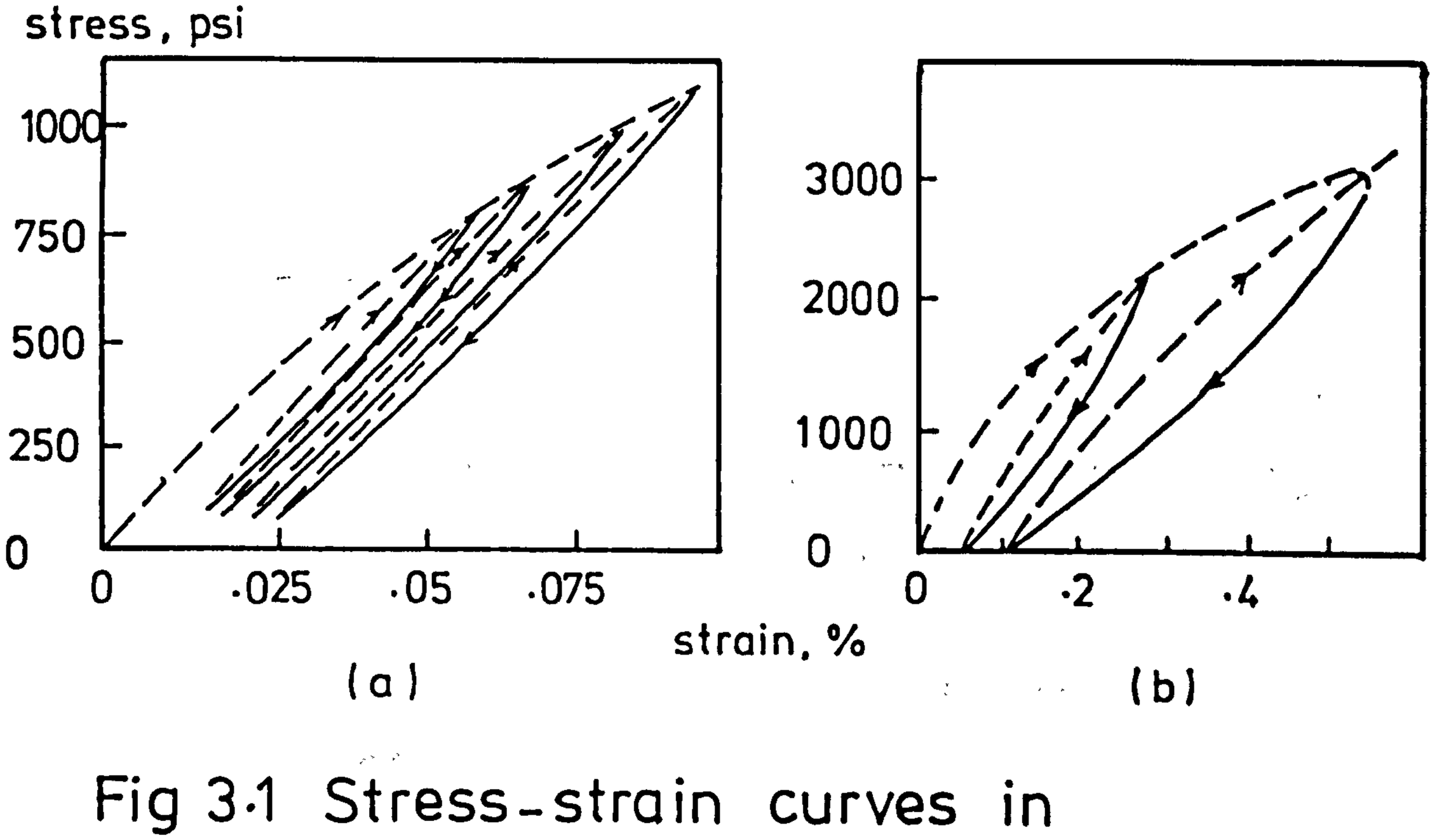

Fig 3.1 Stress-strain curves in (a) tension and (b) compression

from Losty et al.[14]

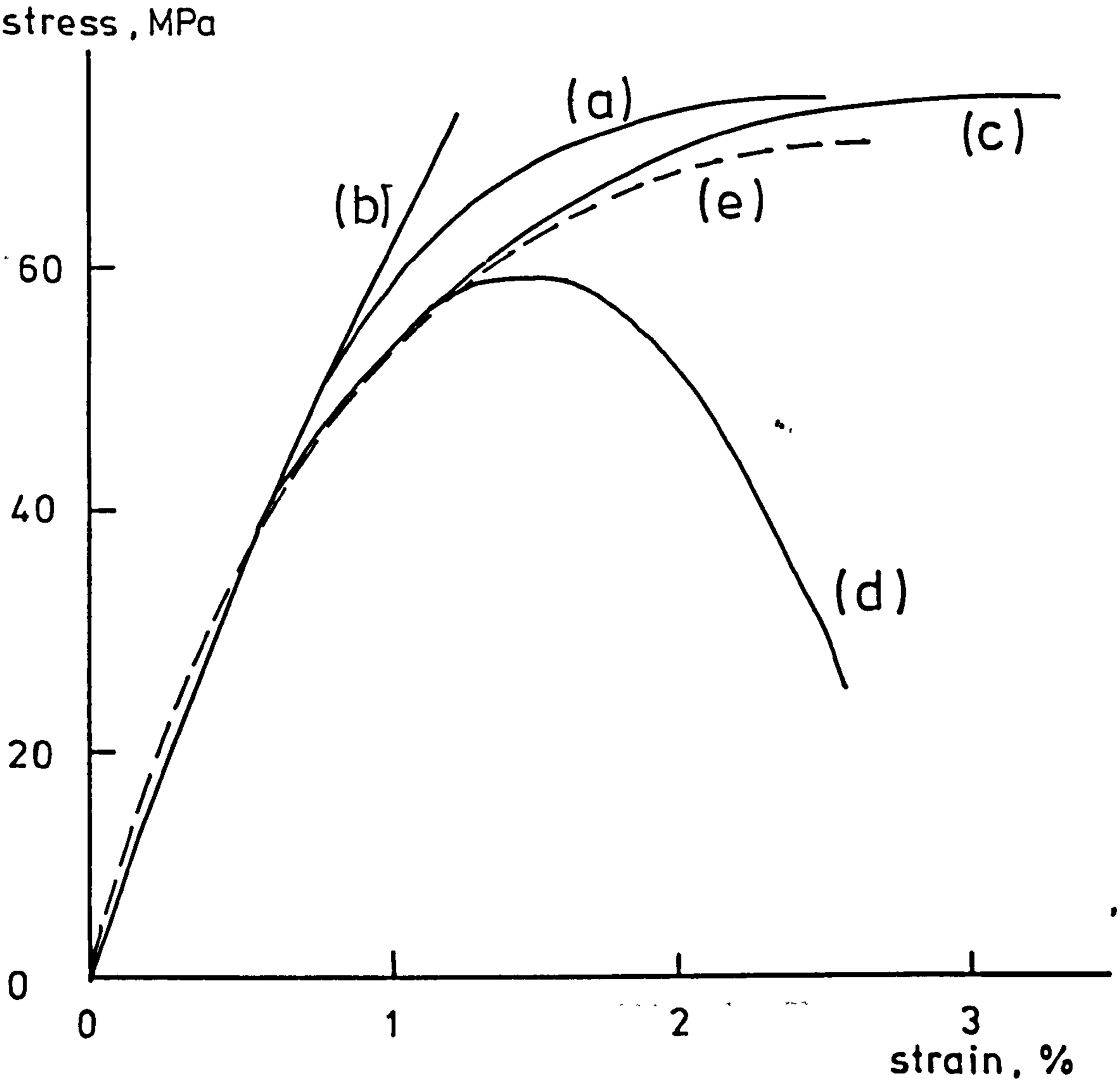

Fig 3·2 Comparison of theoretical models
from Birch [8]

(a) Experimental curve for unirradiated material

(b) Jenkins's initial eqn. [20]

(c) Jenkins's modified eqn. [24]

(d) Hesketh's eqn. [21]

(e) Wooley's eqn. [22]

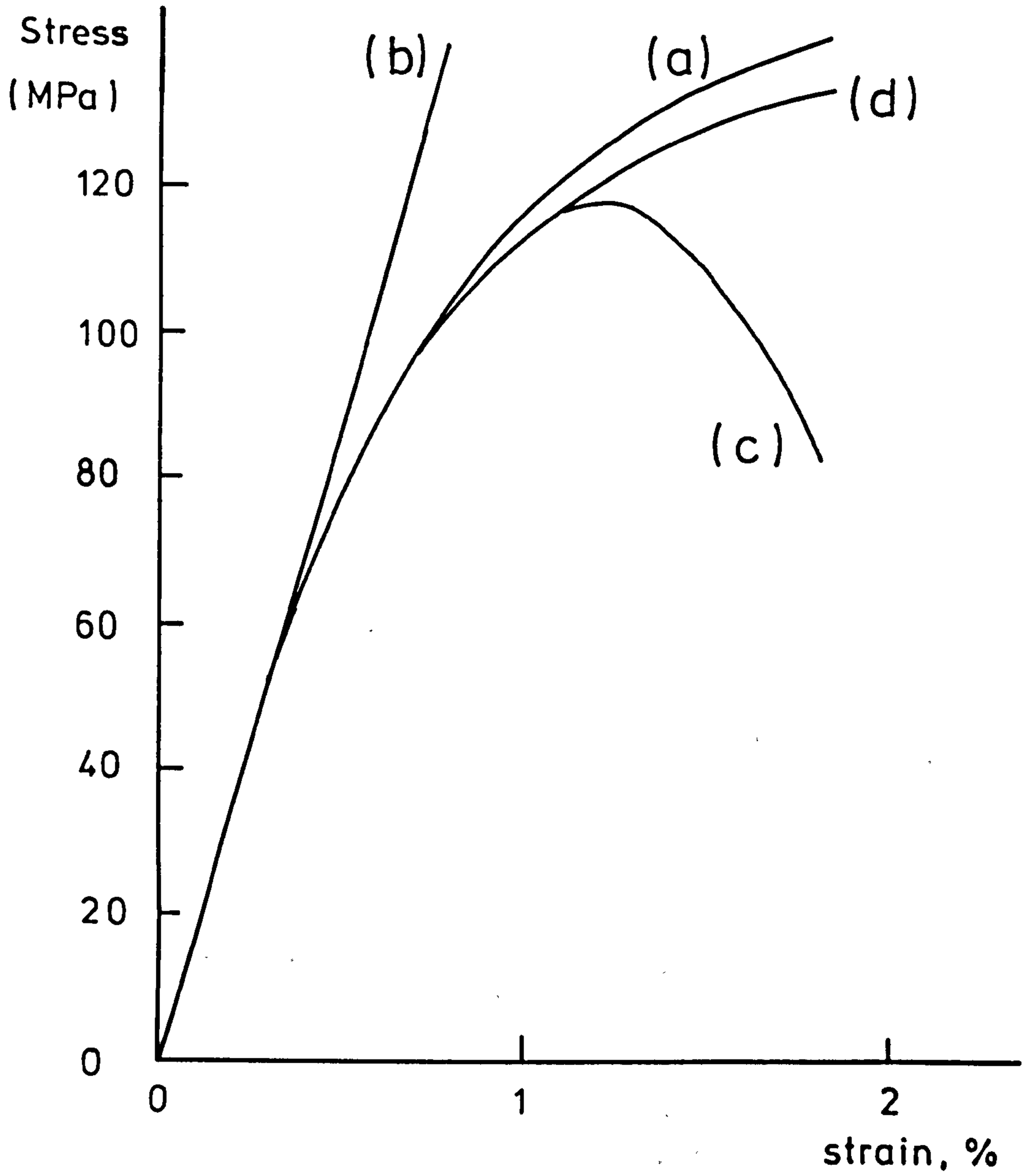

Fig 3.3 Comparison of various models on irradiated graphite from Birch [8]

(a) Experimental curve (6×10^{18} n/cm^2)

(b) Jenkins's eqn. [20]

(c) Hesketh's eqn. [21]

(d) Wooley's eqn. [22]

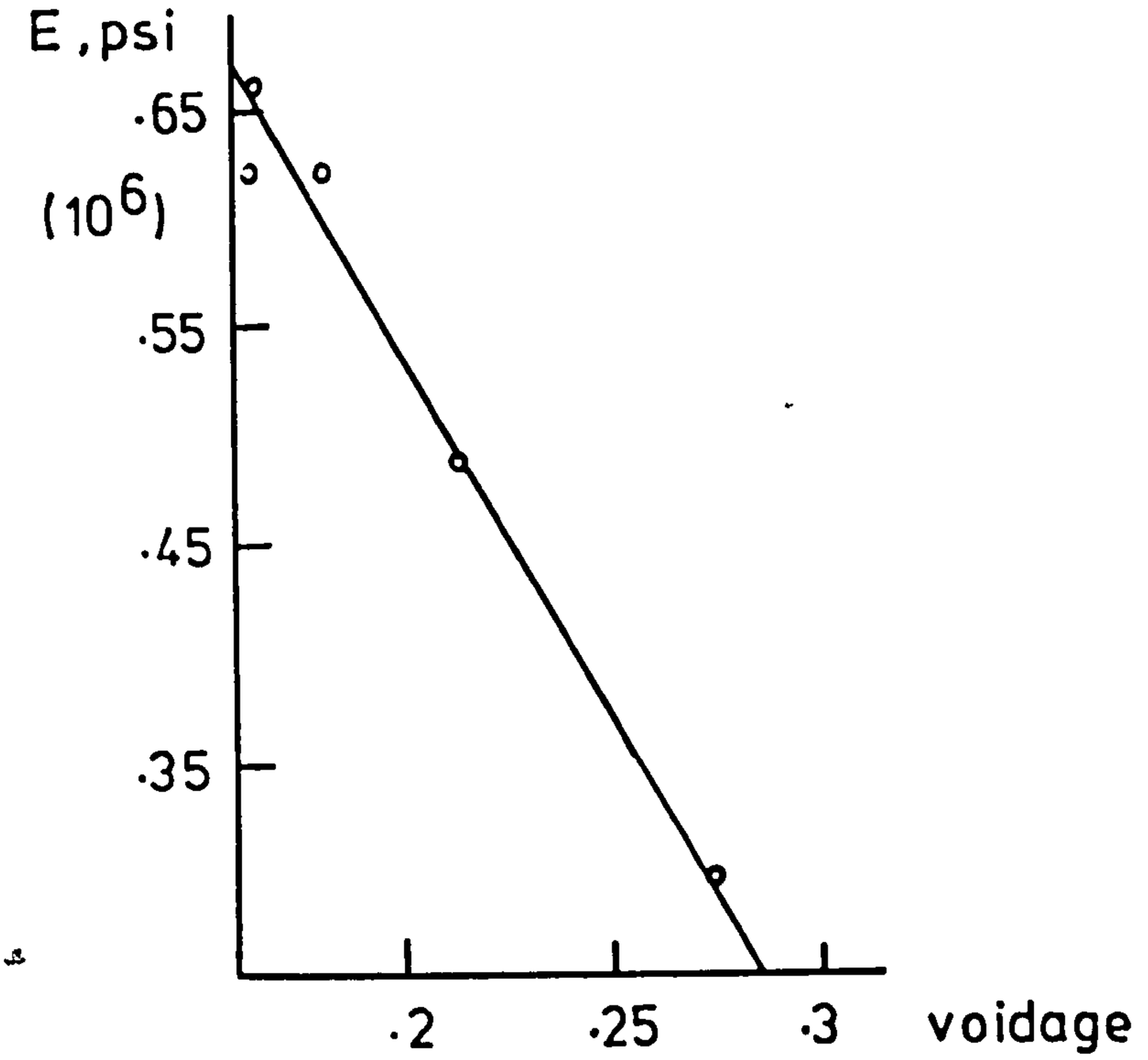

Fig 3.4 Graph of E versus total voidage
from Hutcheon et al [25]

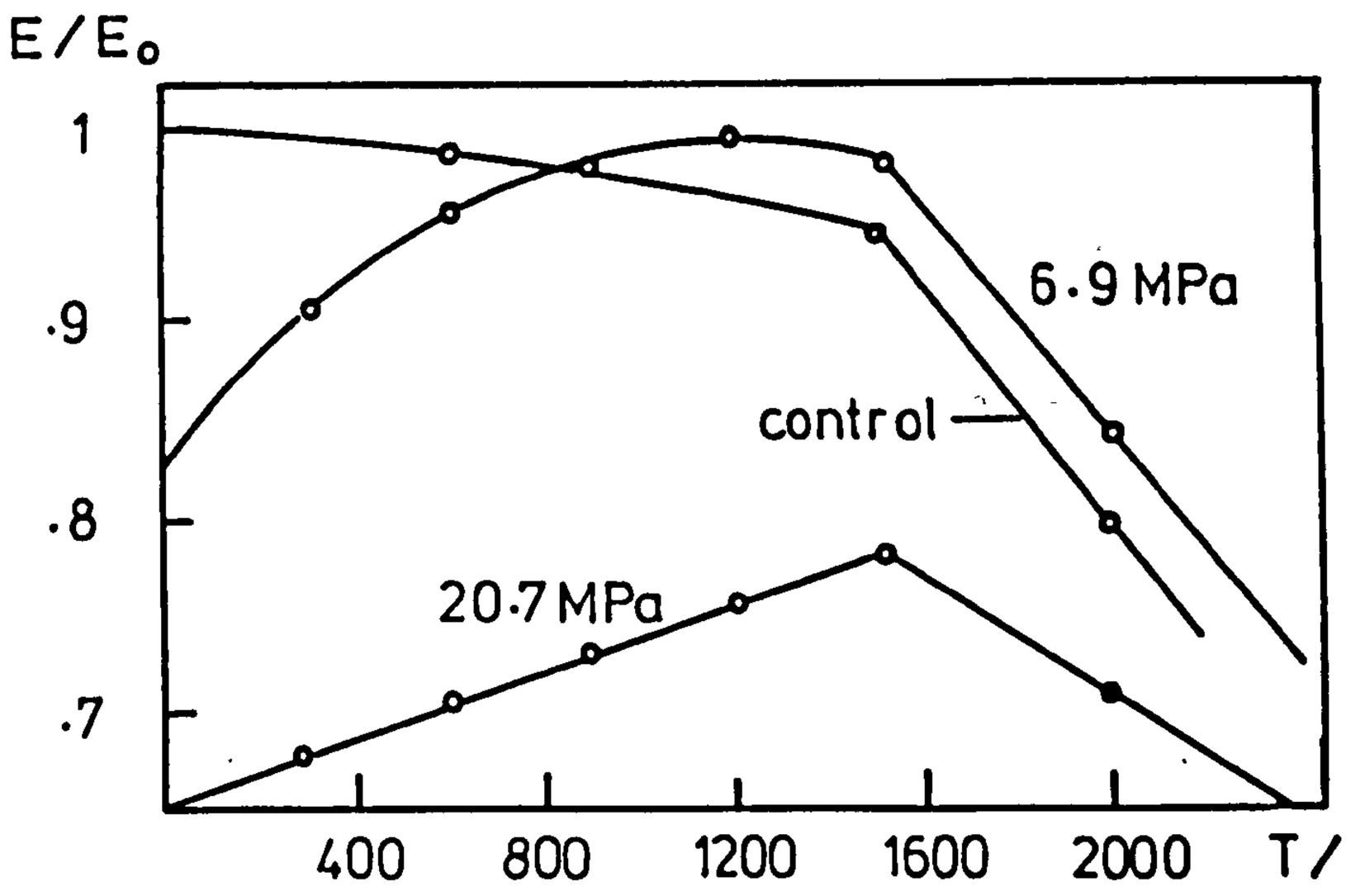

Fig 3.5 Annealing of pre-stressed reactor graphite from Hall [36]

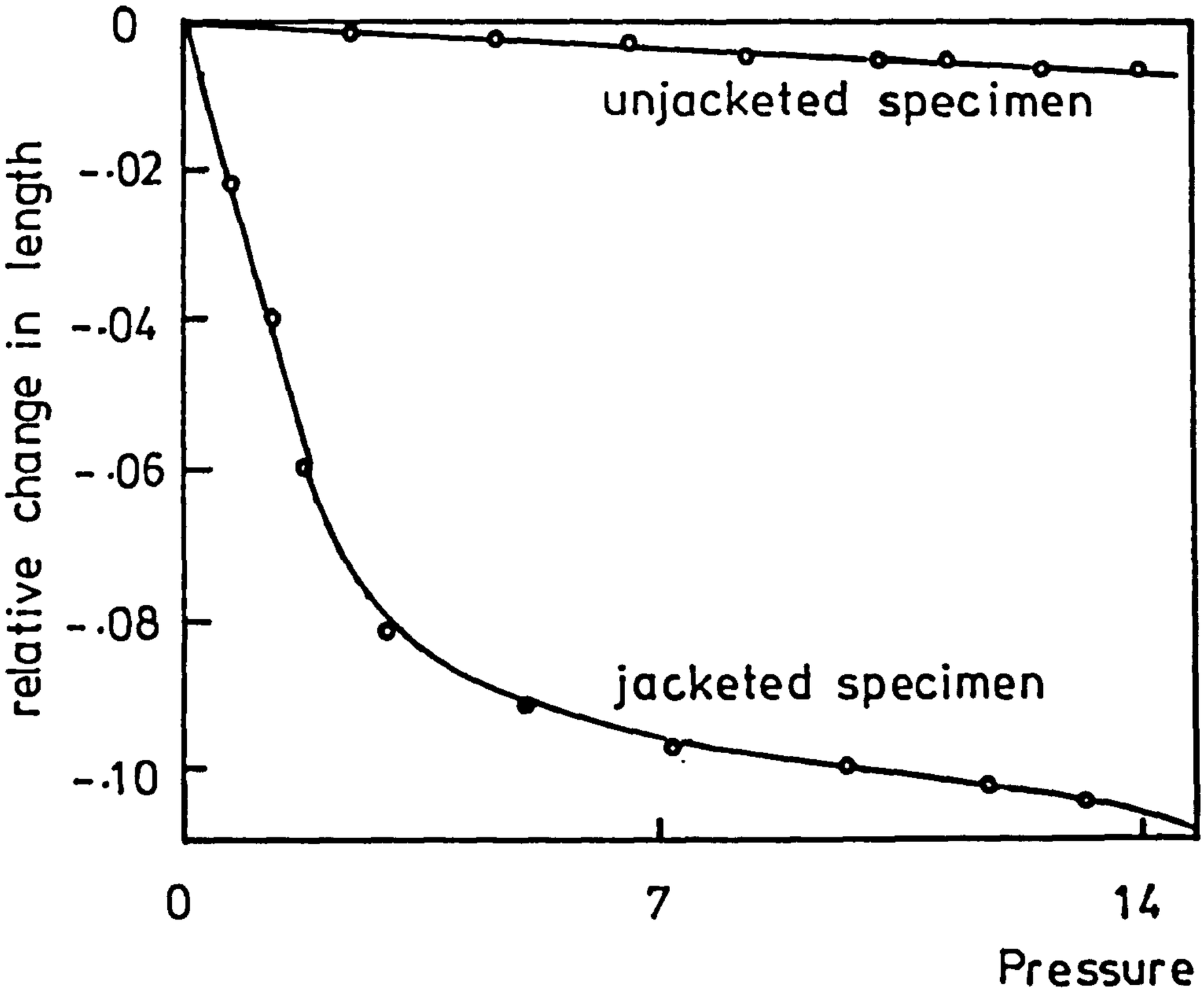

Fig 3.6 Pressure-strain behaviour of AUC graphite from Kmetko et al.[38]

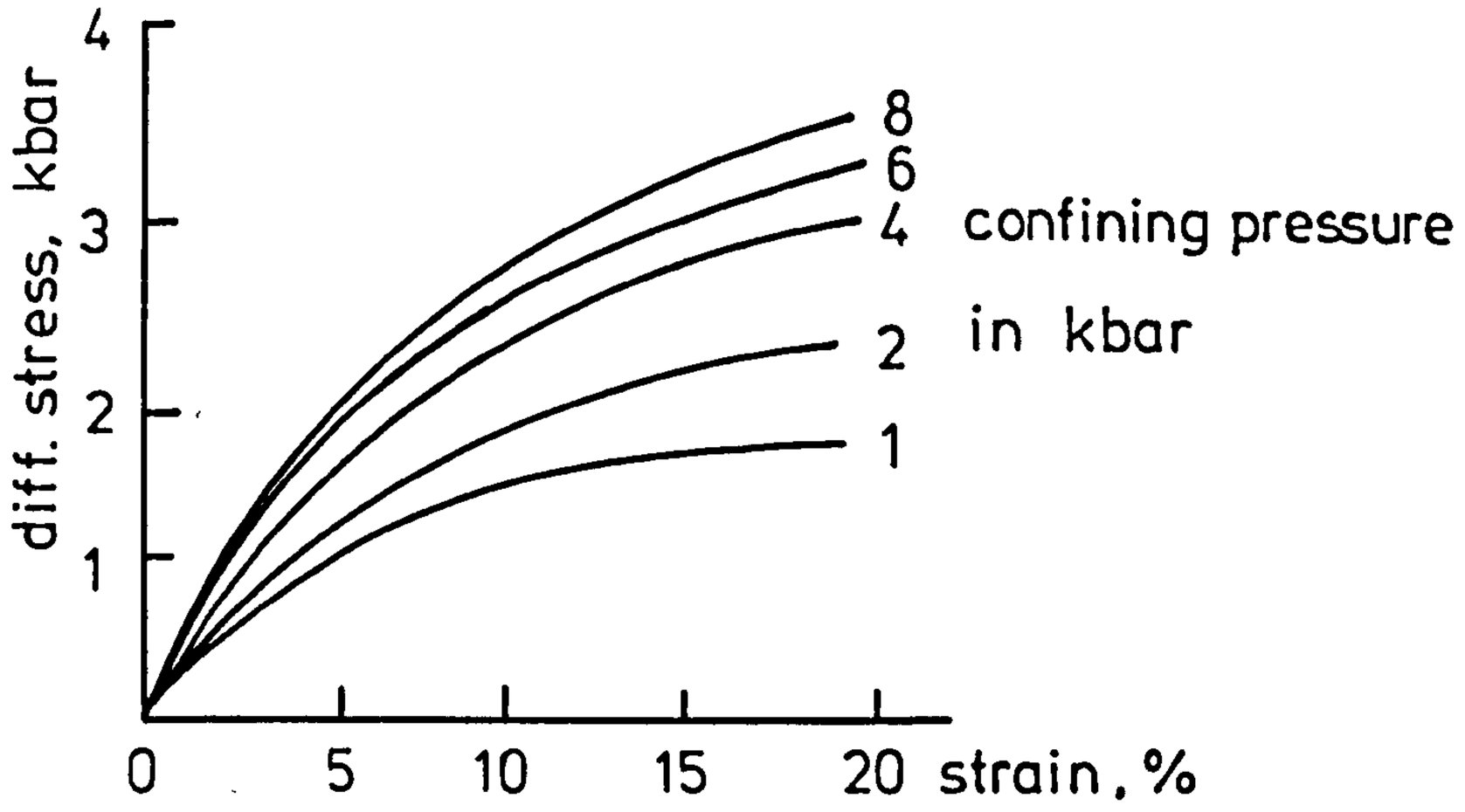

Fig 3·7 Graph of diff. stress versus strain

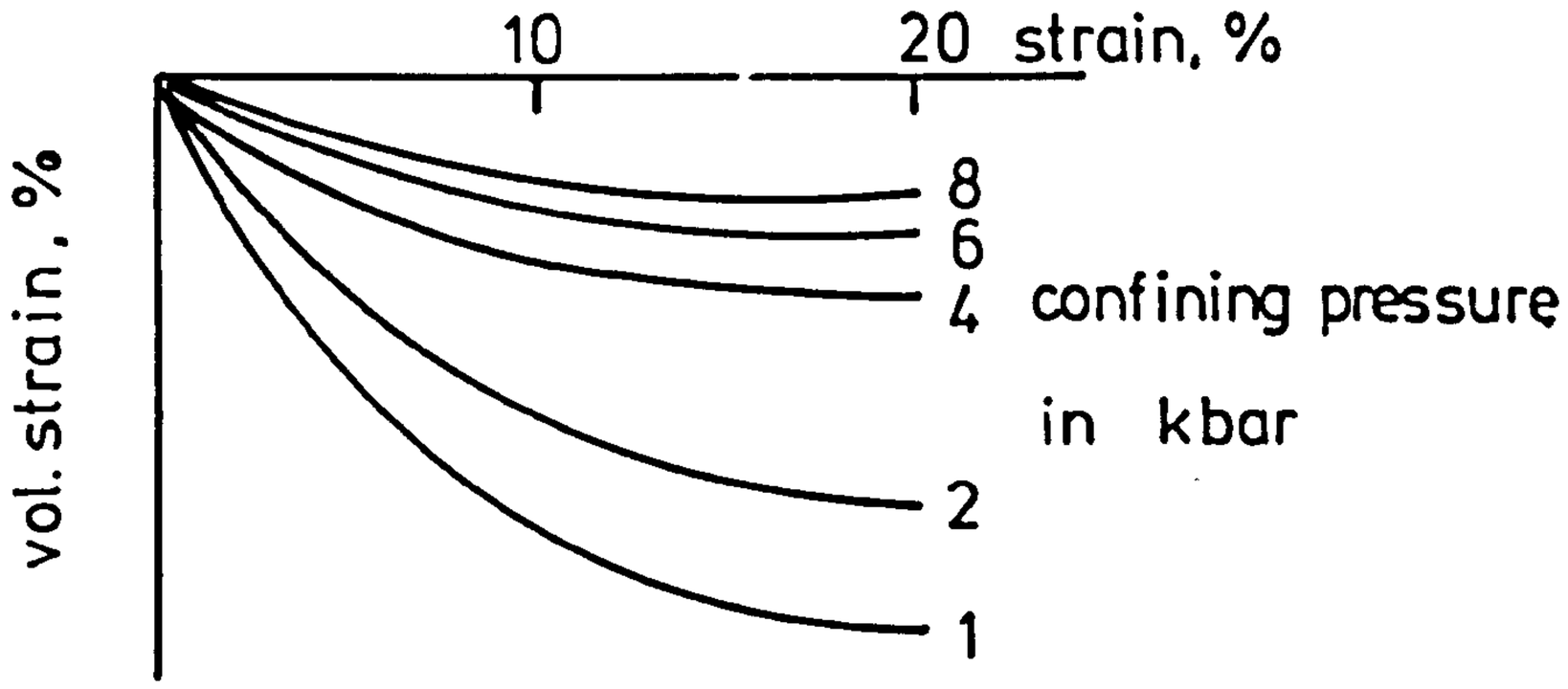

Fig 3·8 Graph of vol. strain versus strain

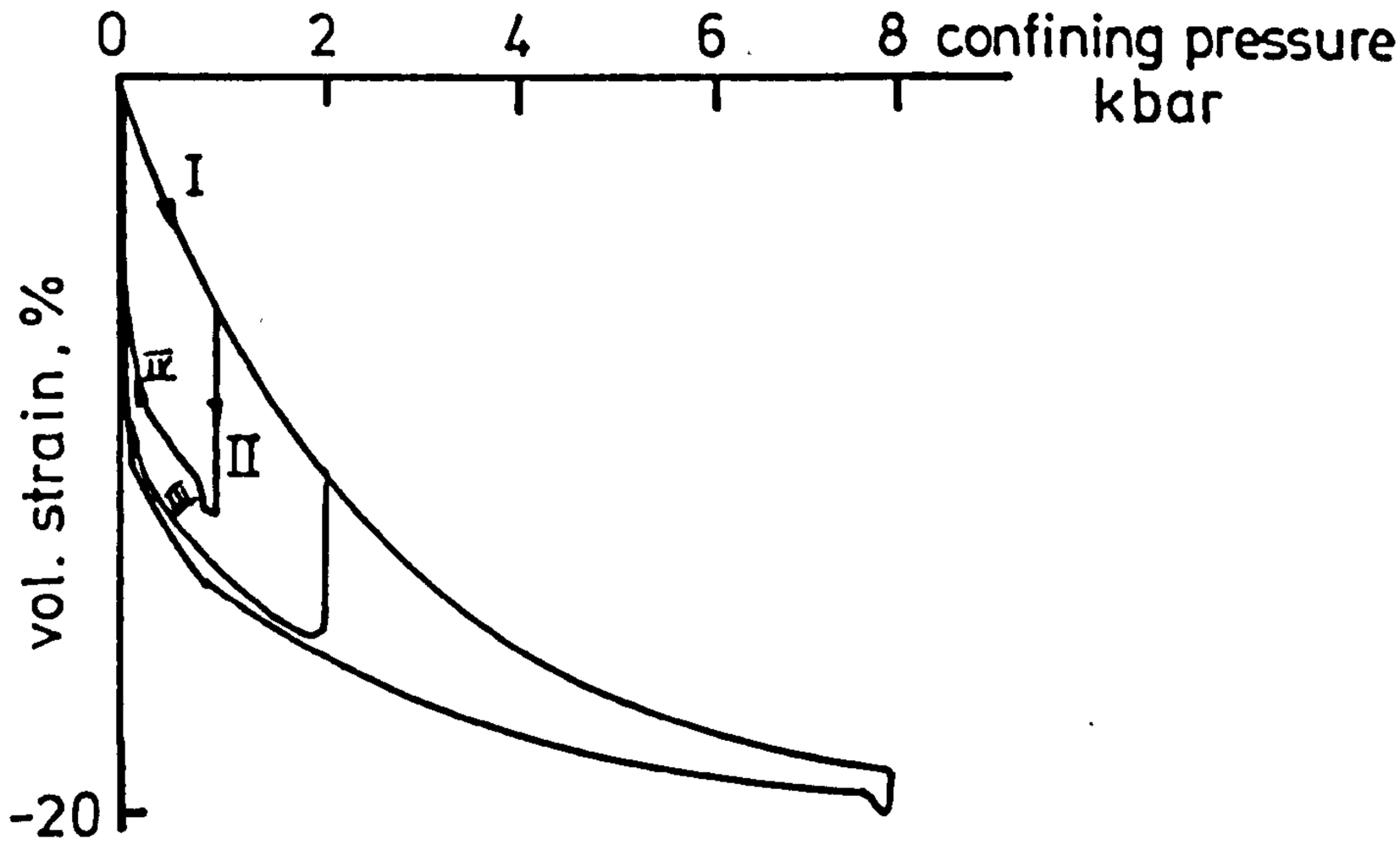

Fig 3·9 Graph of vol. strain versus confining pressure from Paterson et al. [40]

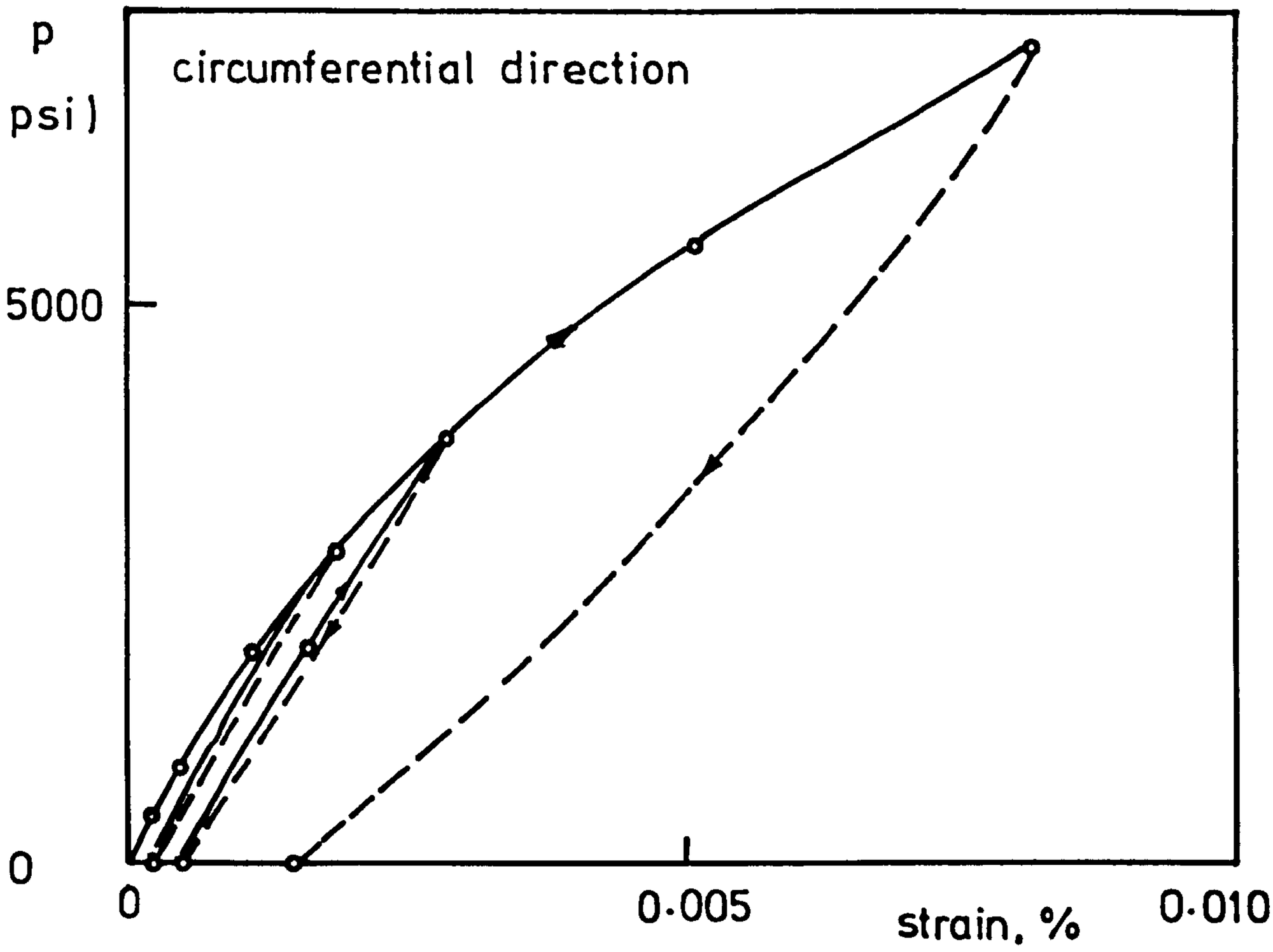

Fig 3·10 Pressure-strain curve of graphite
from Jortner [41]

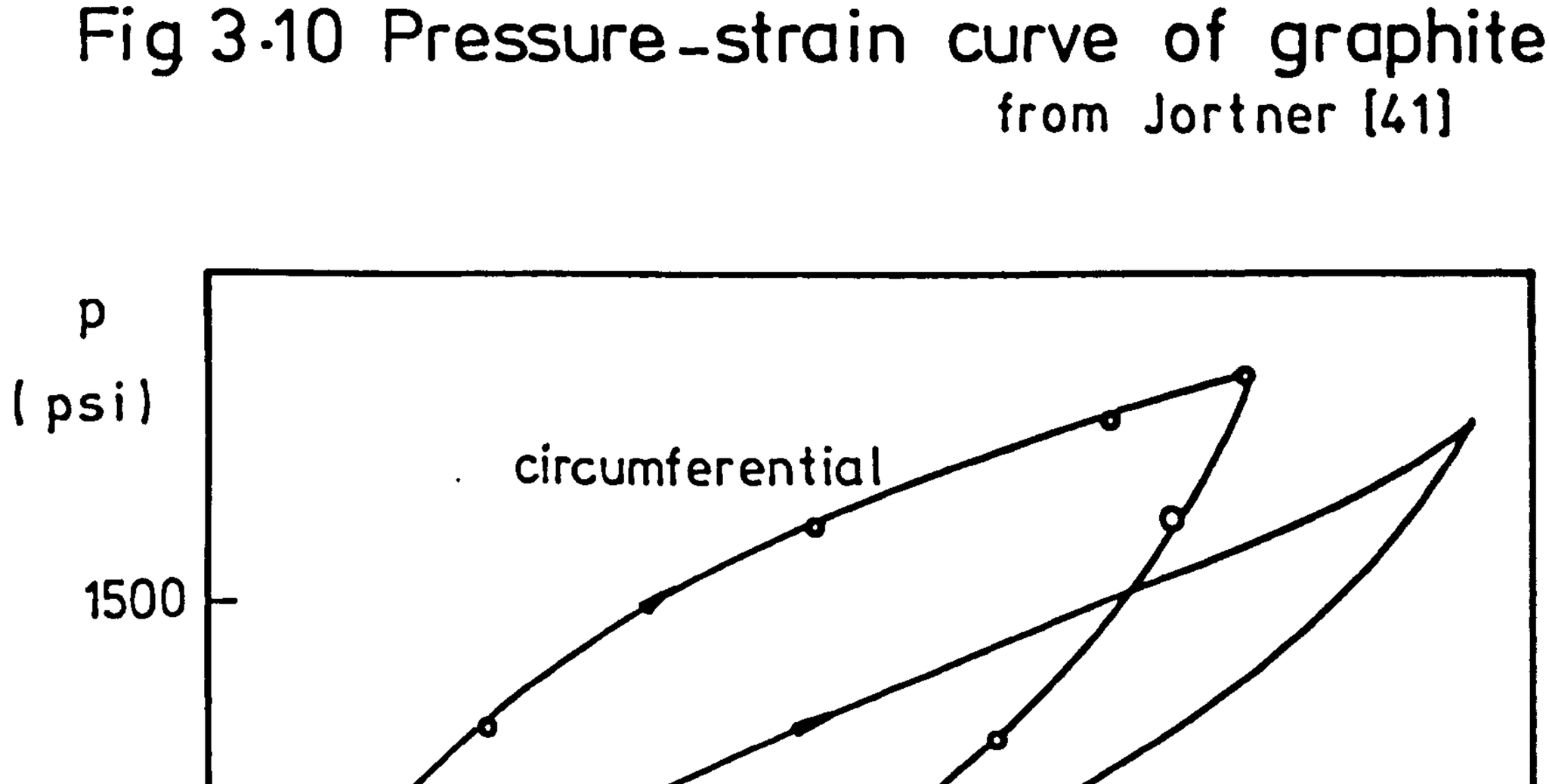

Fig 3·11 Pressure-strain curve of graphite
from Jortner [41]

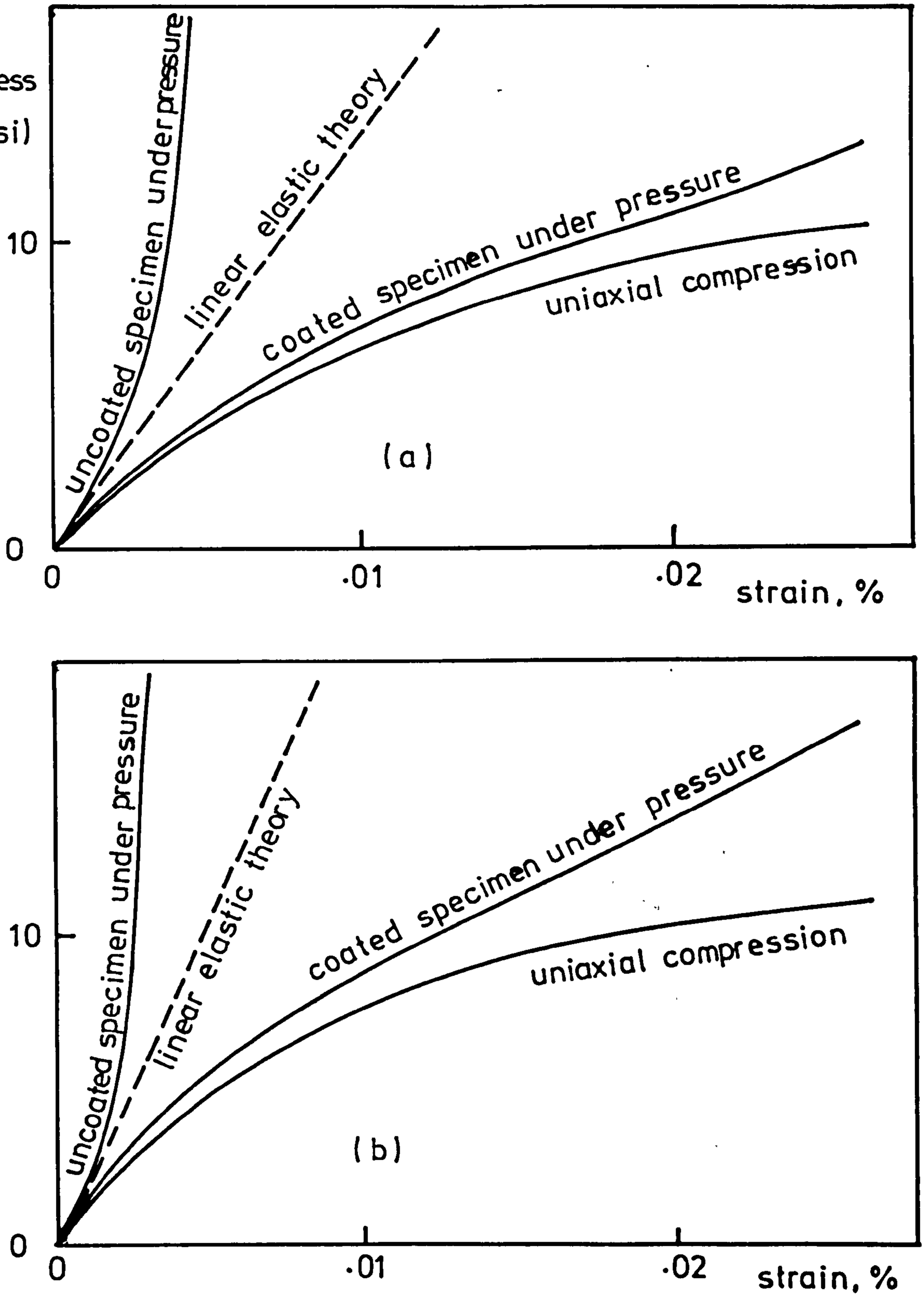

Fig 3.12 Summary of results for ATJ-S graphite: (a) across-grain strains, (b) with-grain strains

from Jortner [41]

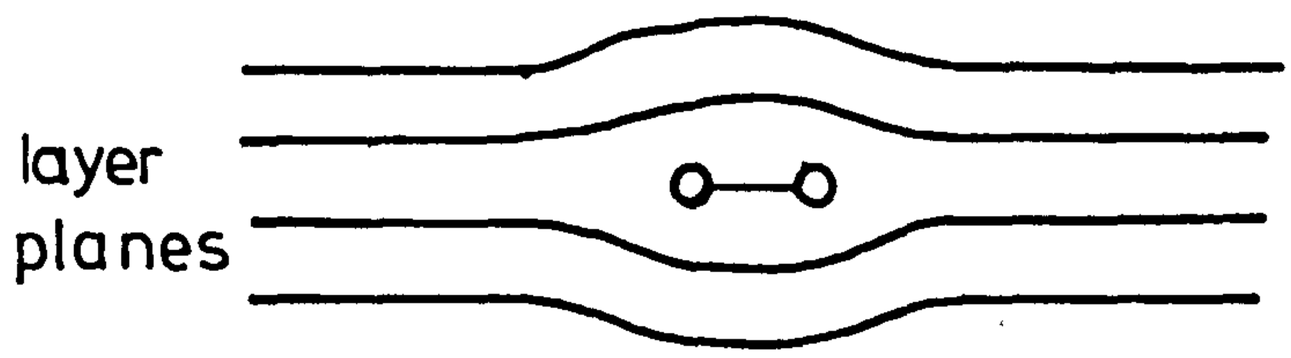

Sub-microscopic cluster of a few atoms

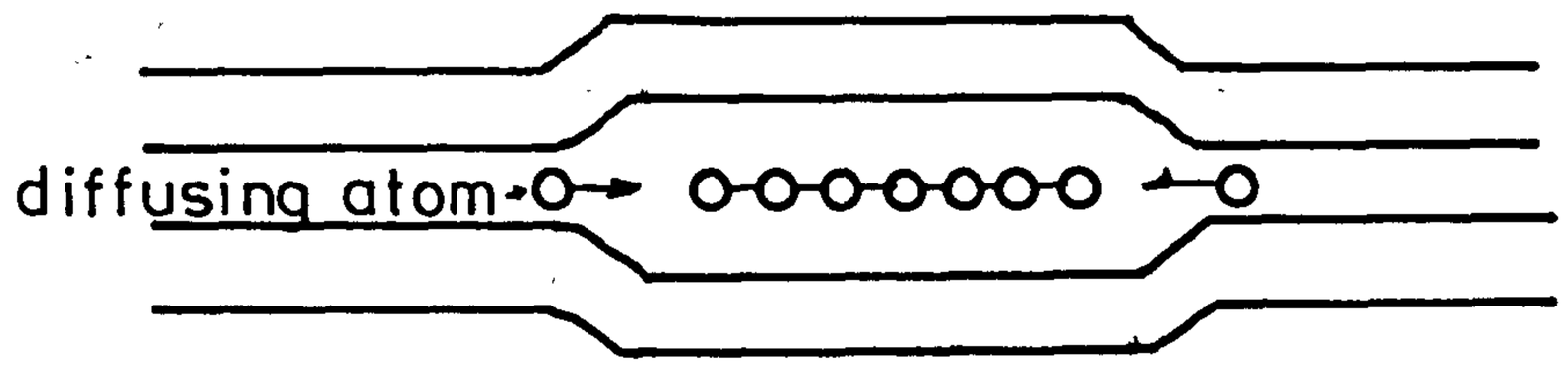

Interstitial loop

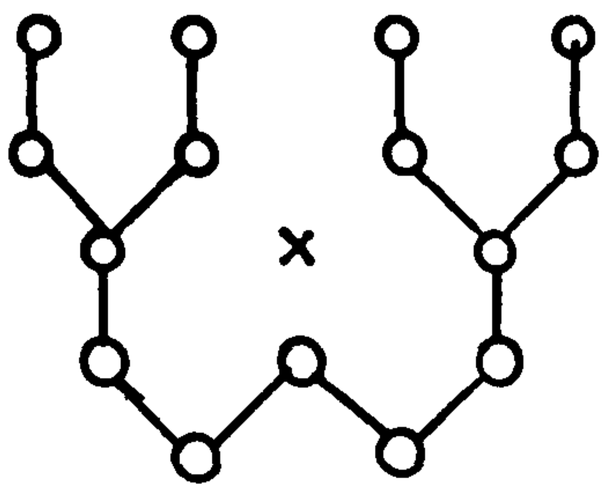

Single vacancy

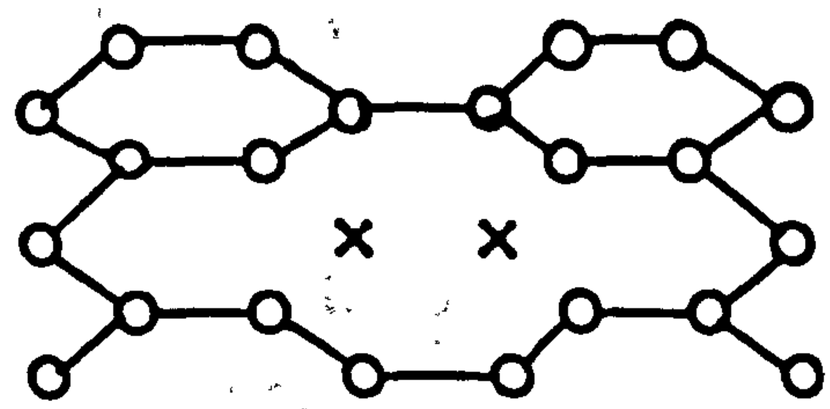

Di vacancies

Fig 3.13 Lattice defects in graphite produced by radiation from Kelly [44]

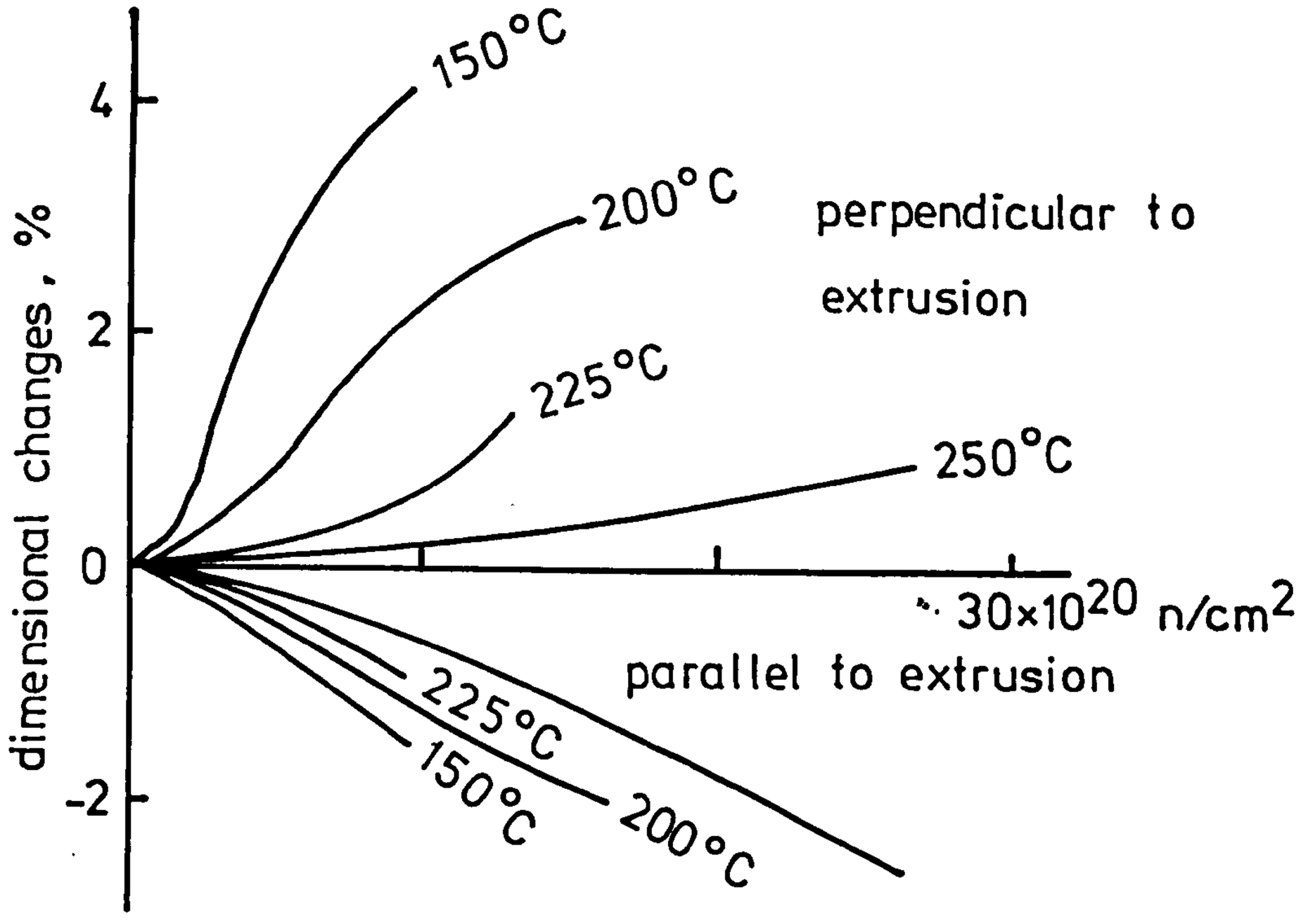

Fig 3.14 Dimensional changes in PGA graphite, 150-250 °C from Kelly [44]

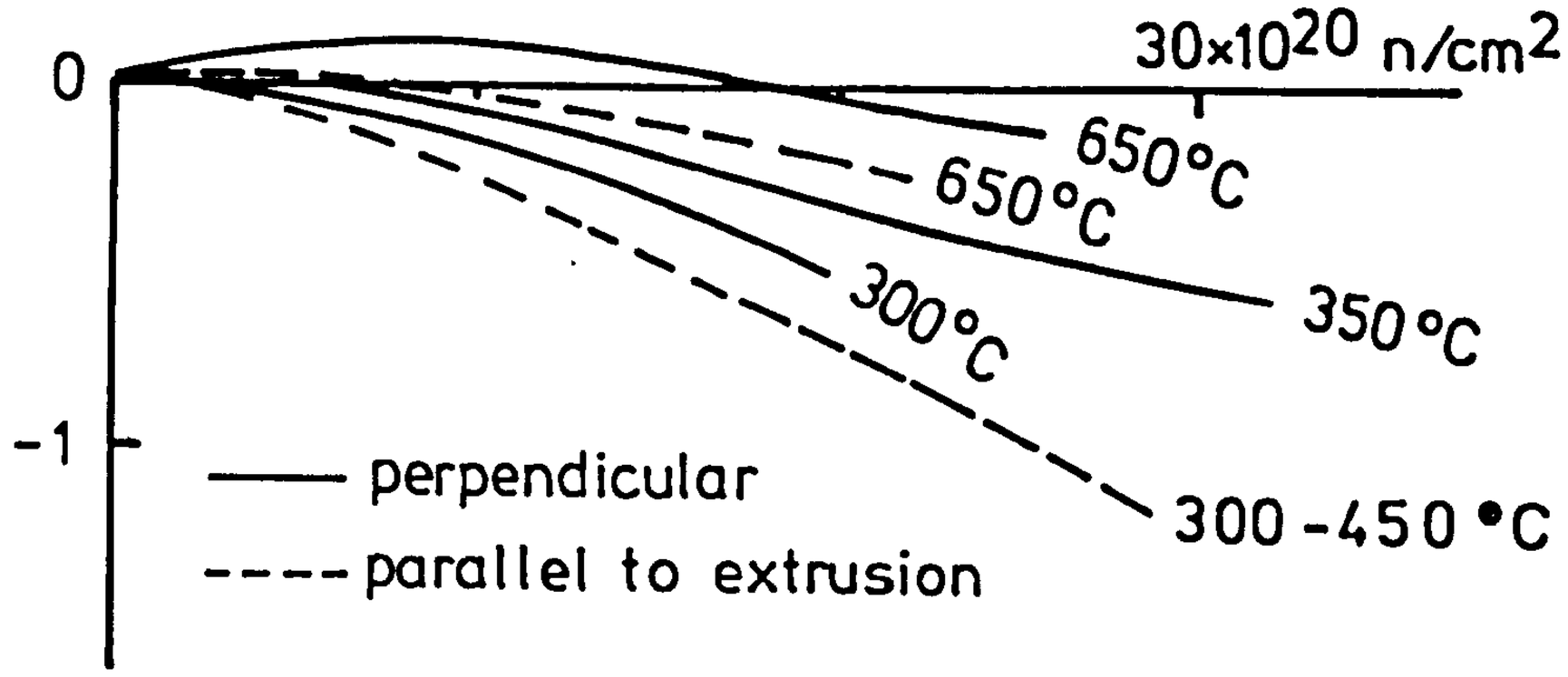

Fig 3.15 Dimensional changes in PGA graphite, 300-650°C from Kelly [44]

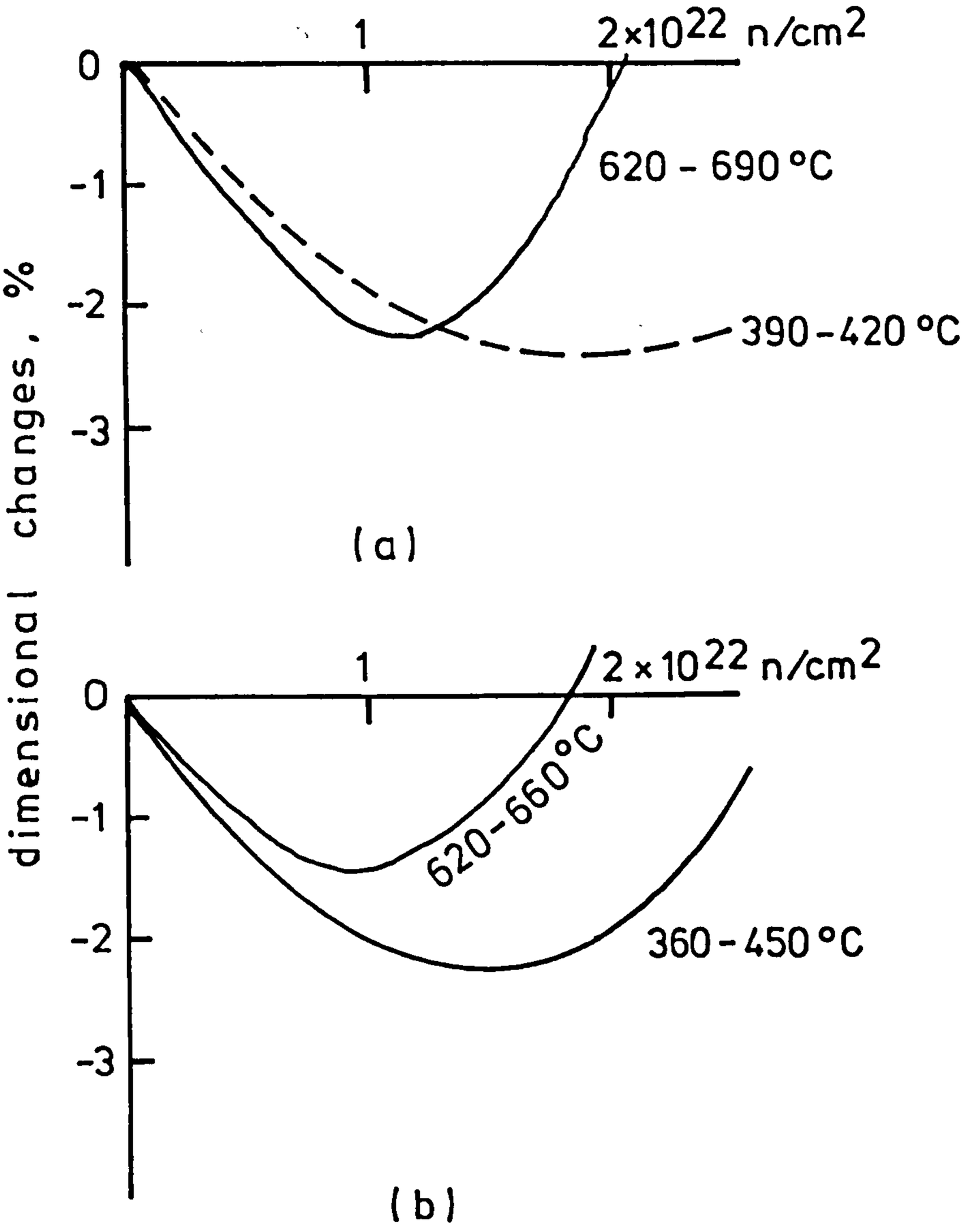

Fig 3.16 Irradiation behaviour of

(a) Gilsocarbon and

(b) pitchcoke graphites

from Kelly [44]

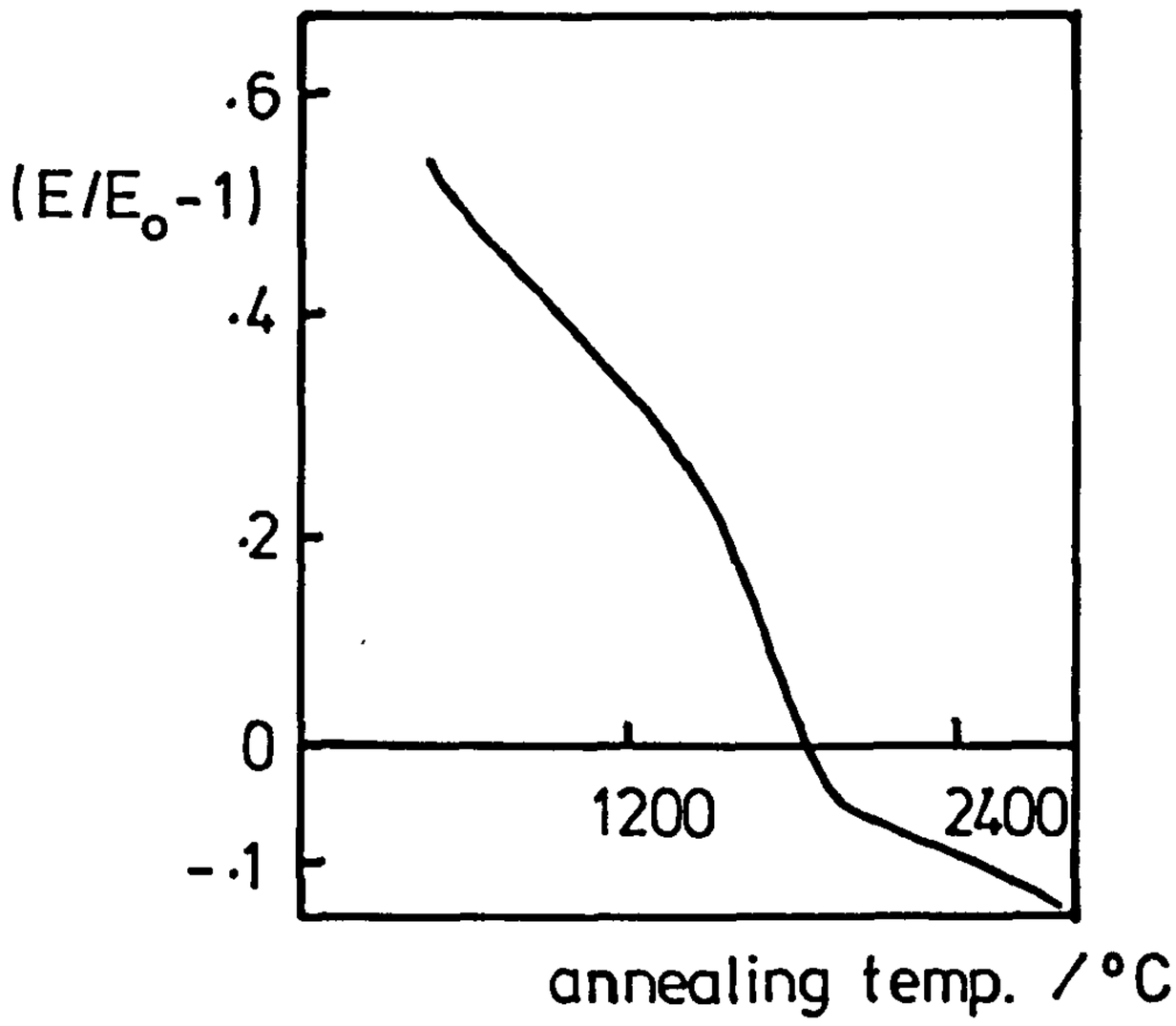

Fig 3.17 Annealing of modulus changes

from Kelly et al. [51]

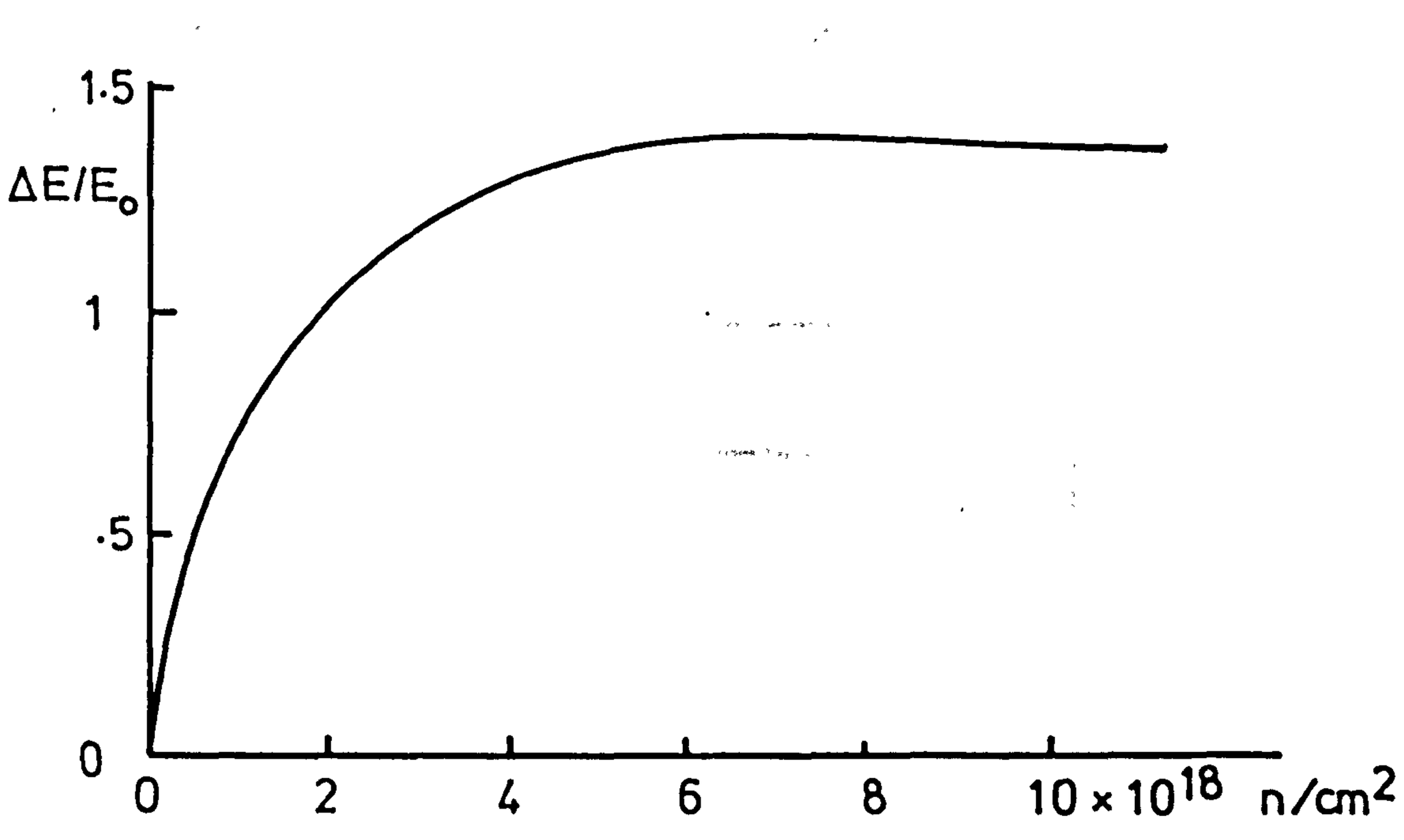

Fig 3.18 Change of dynamic modulus with neutron dose from Birch et al. [52]

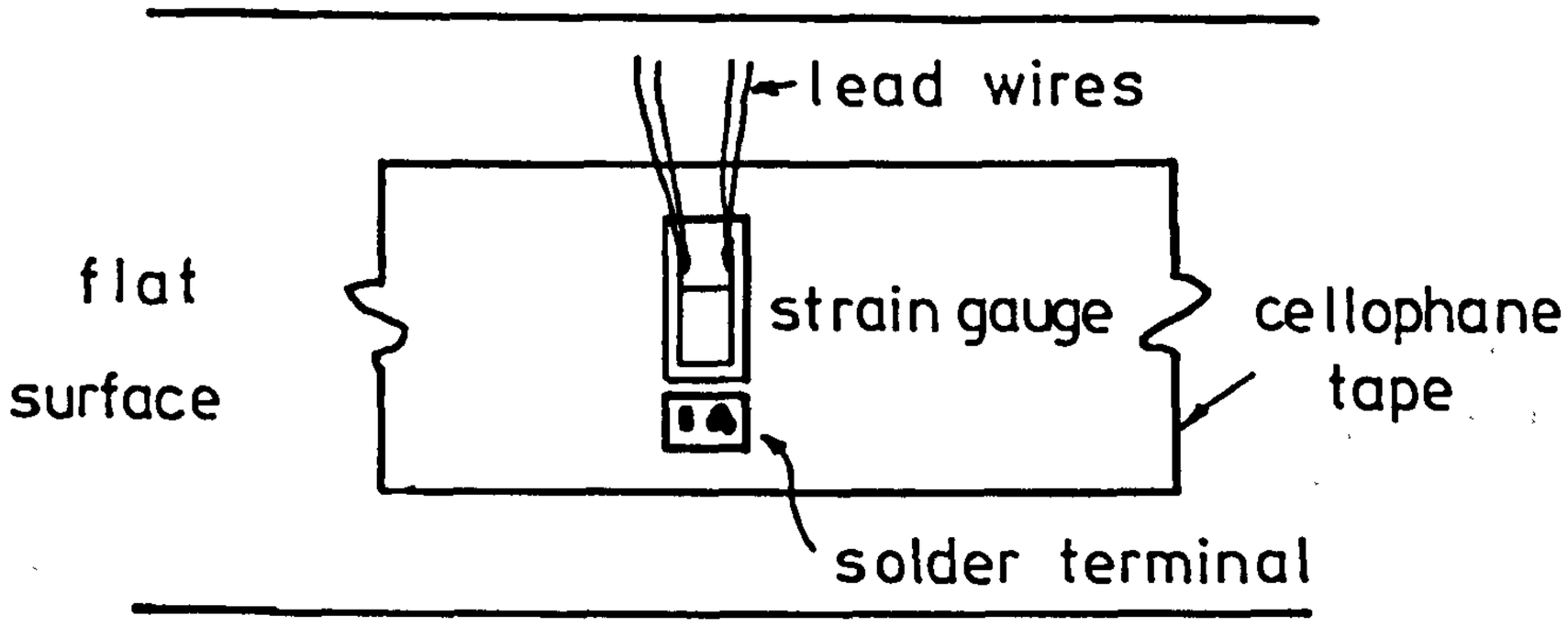

Fig 4.1 Gauge-tape assembly

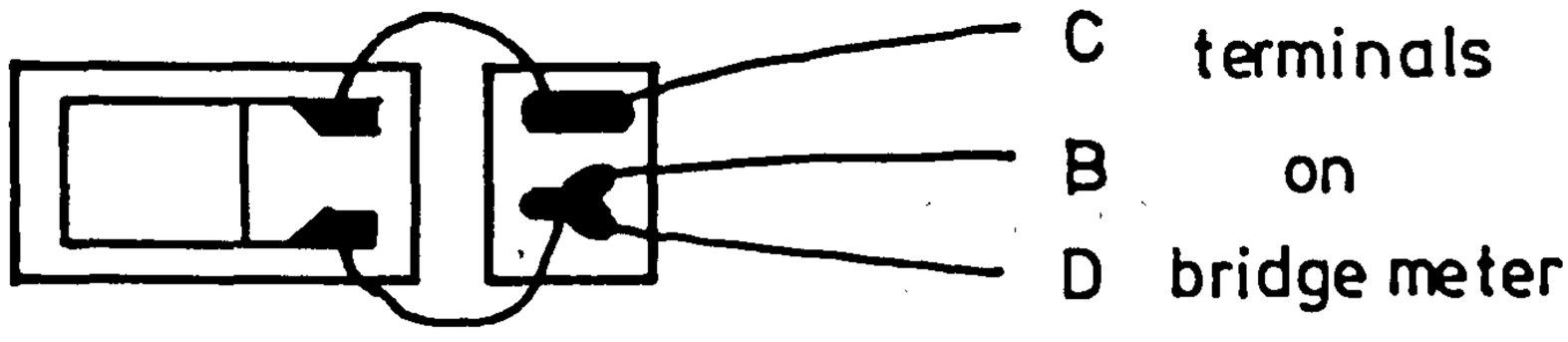

Fig 4.2 3-wire configuration

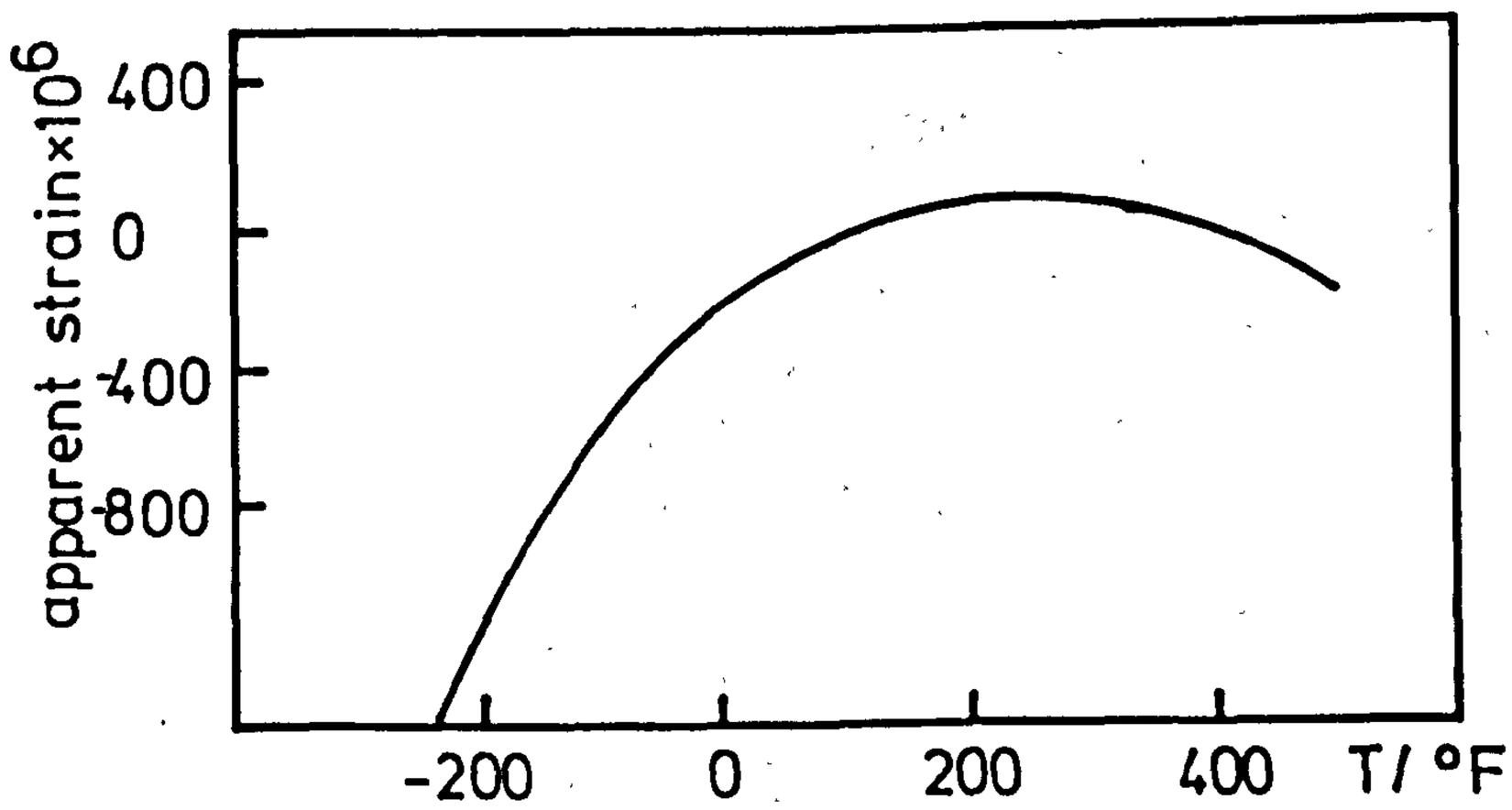

Fig 4.3 Apparent strain data from manufacturer for WK-03-250BG-350 gauge

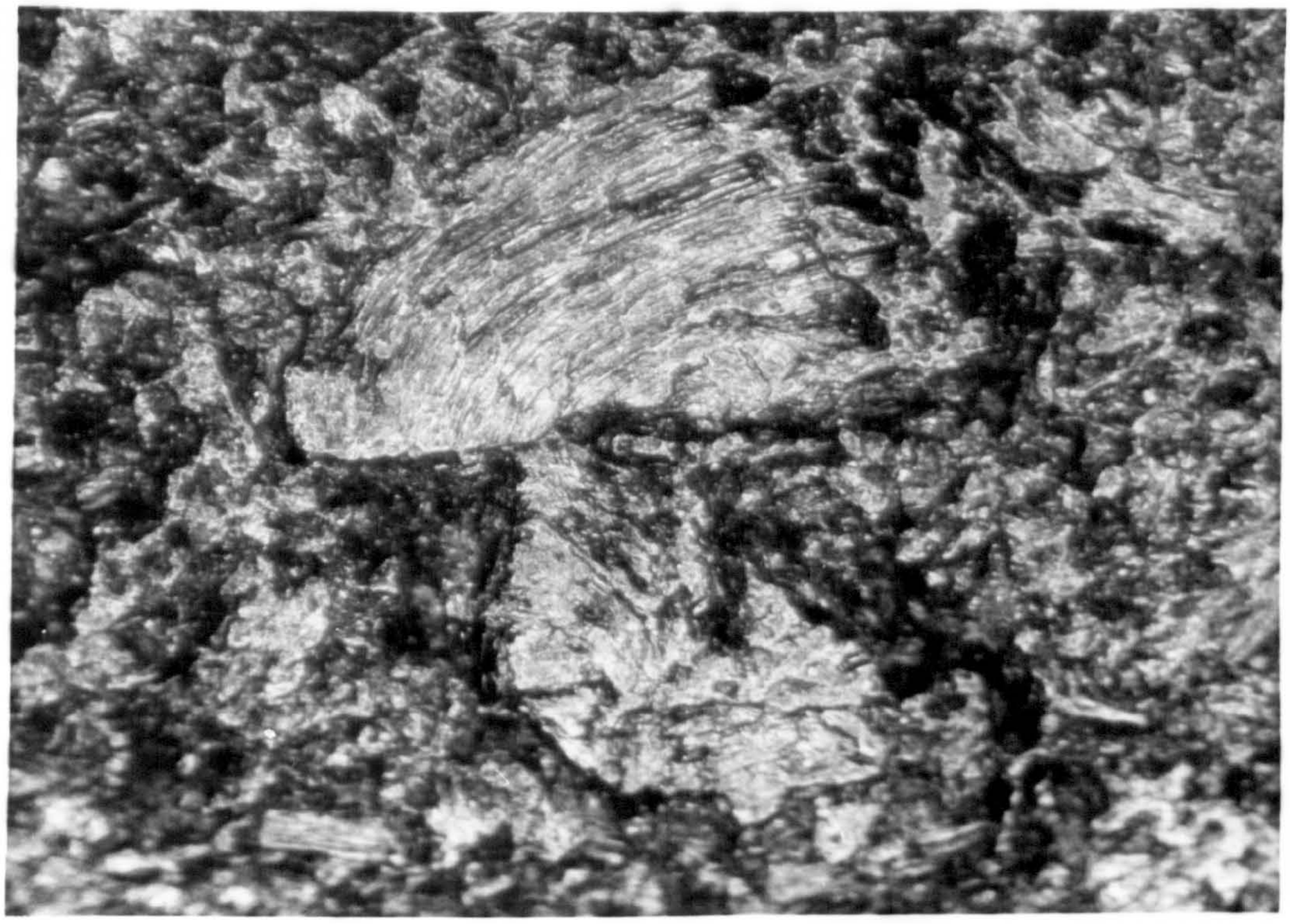

Fig 5.1 Microstructure of graphite D (× 50)

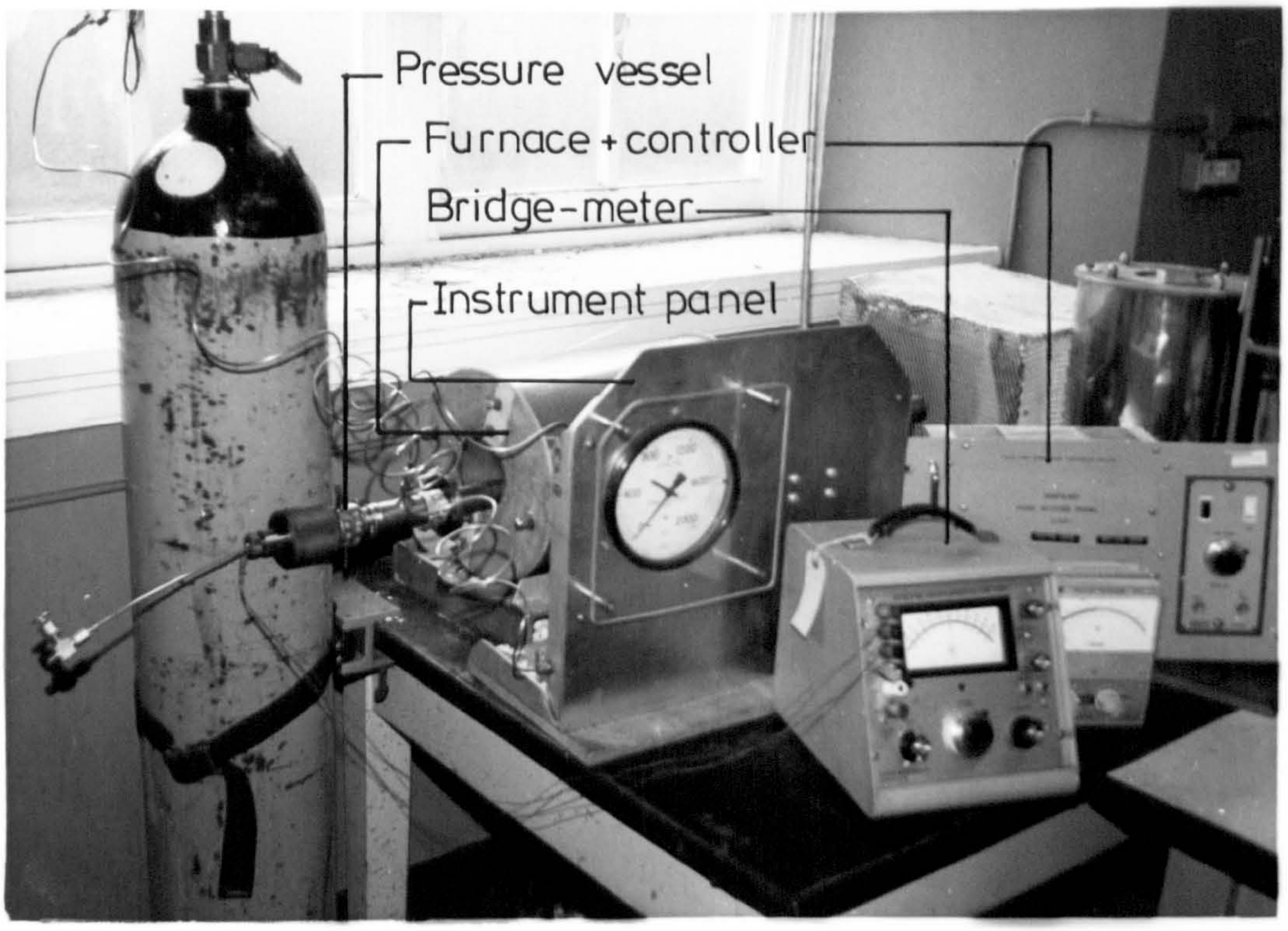

Fig 5.2 Pressure equipment

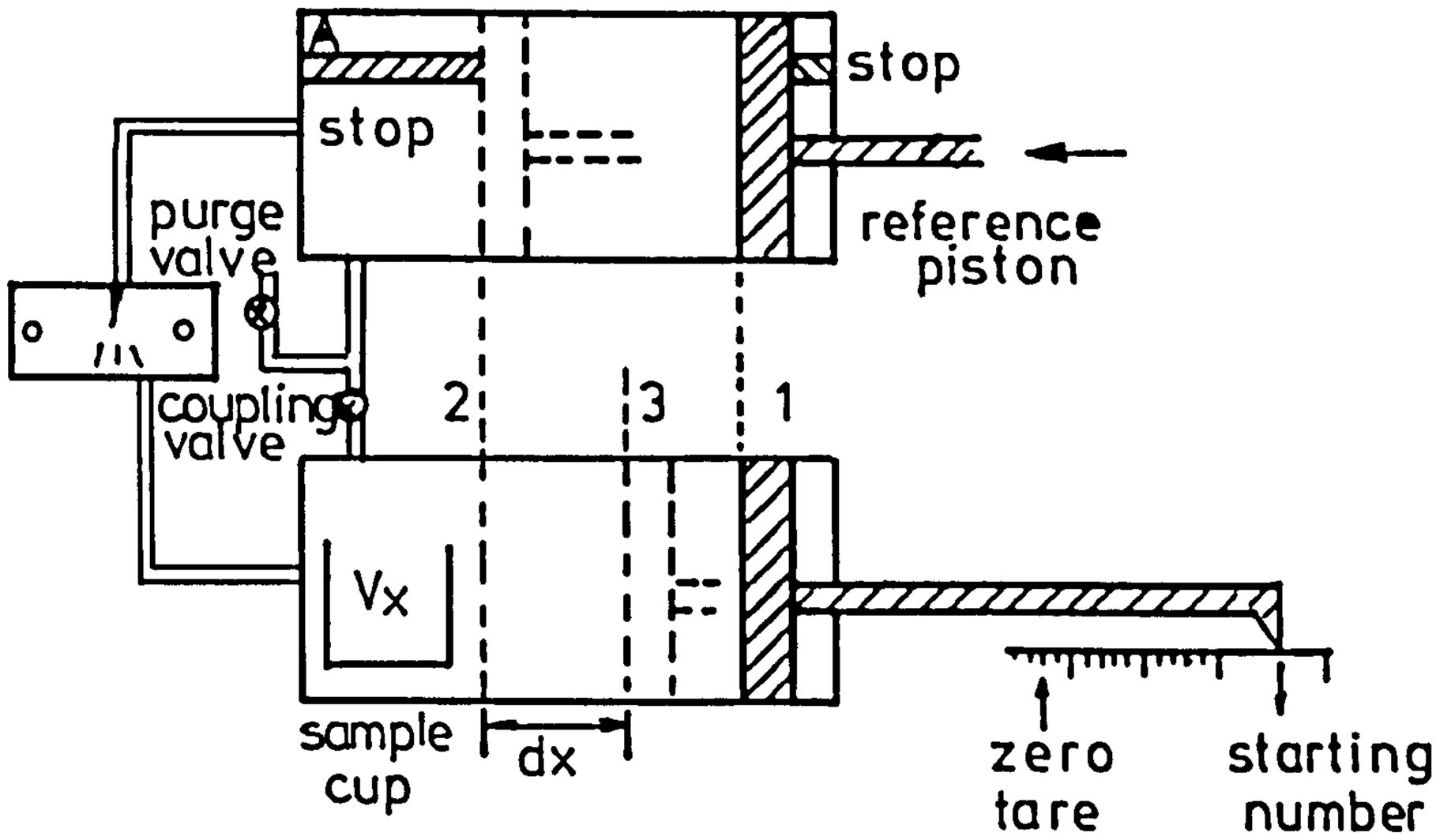

Fig 5.3 Beckman Pycnometer

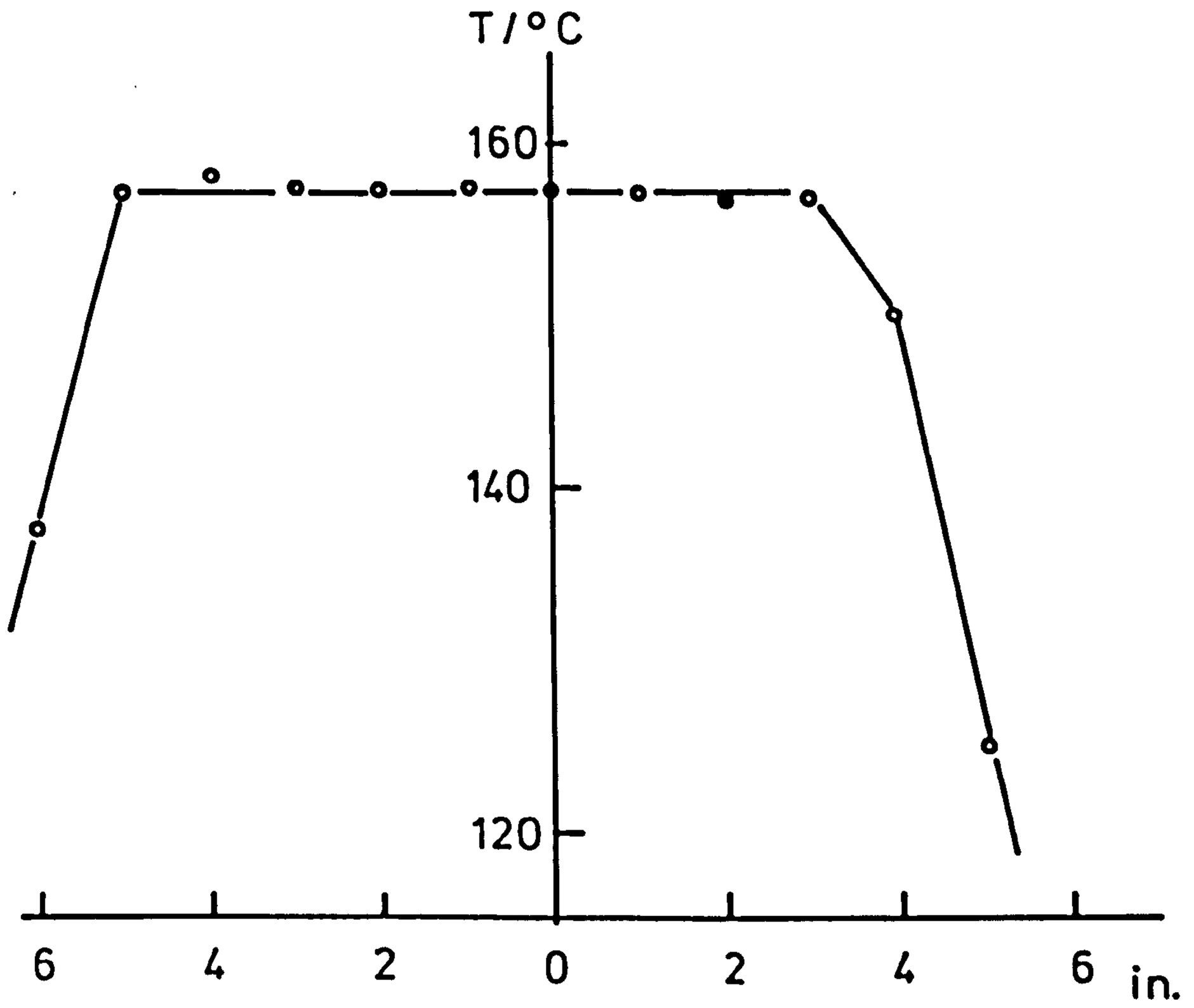

Fig 5.4 Temperature distribution curve from centre of furnace tube

Fig 5.5 4-point bend test equipment

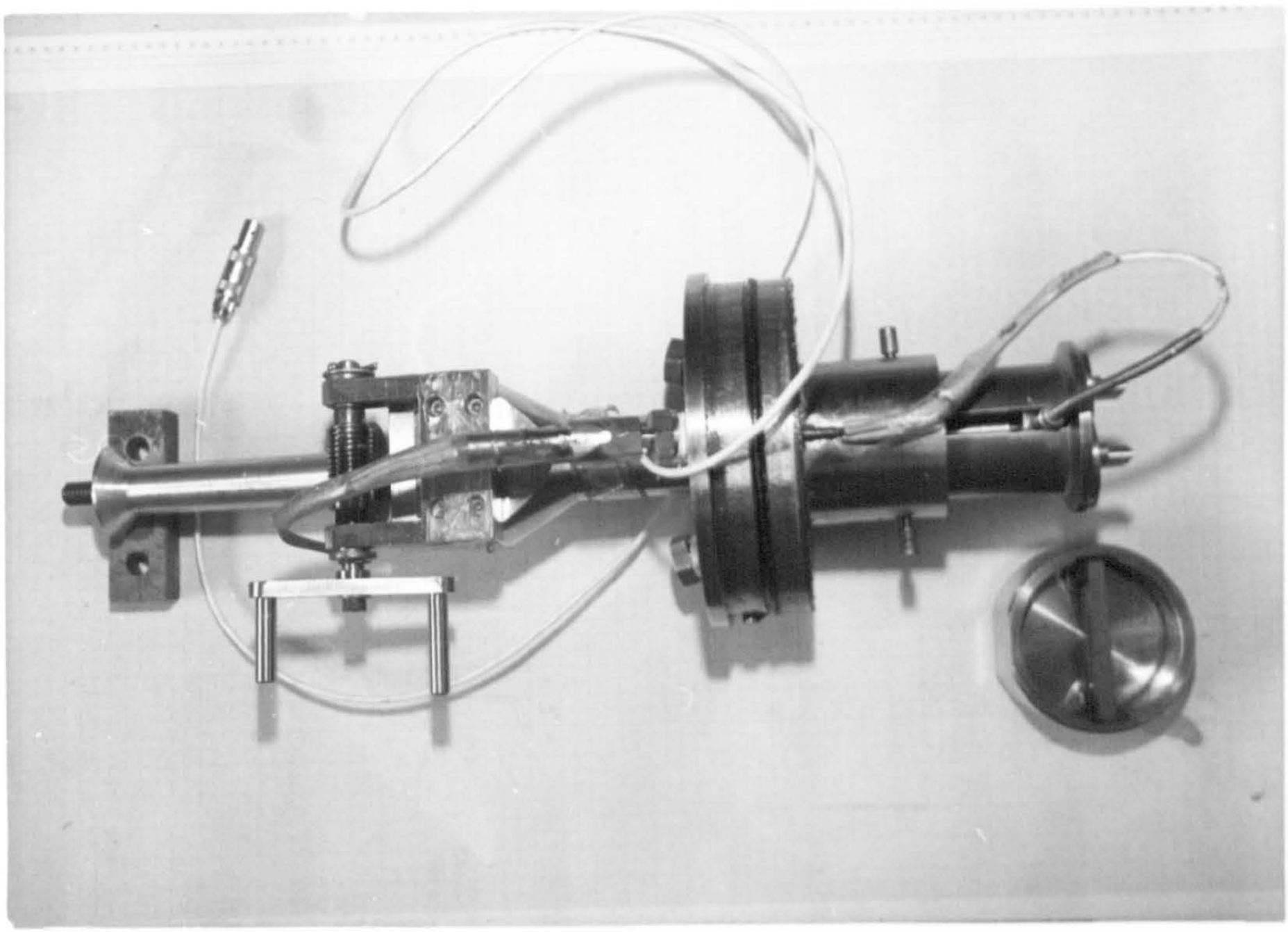

Fig 5.6 Load column assembly

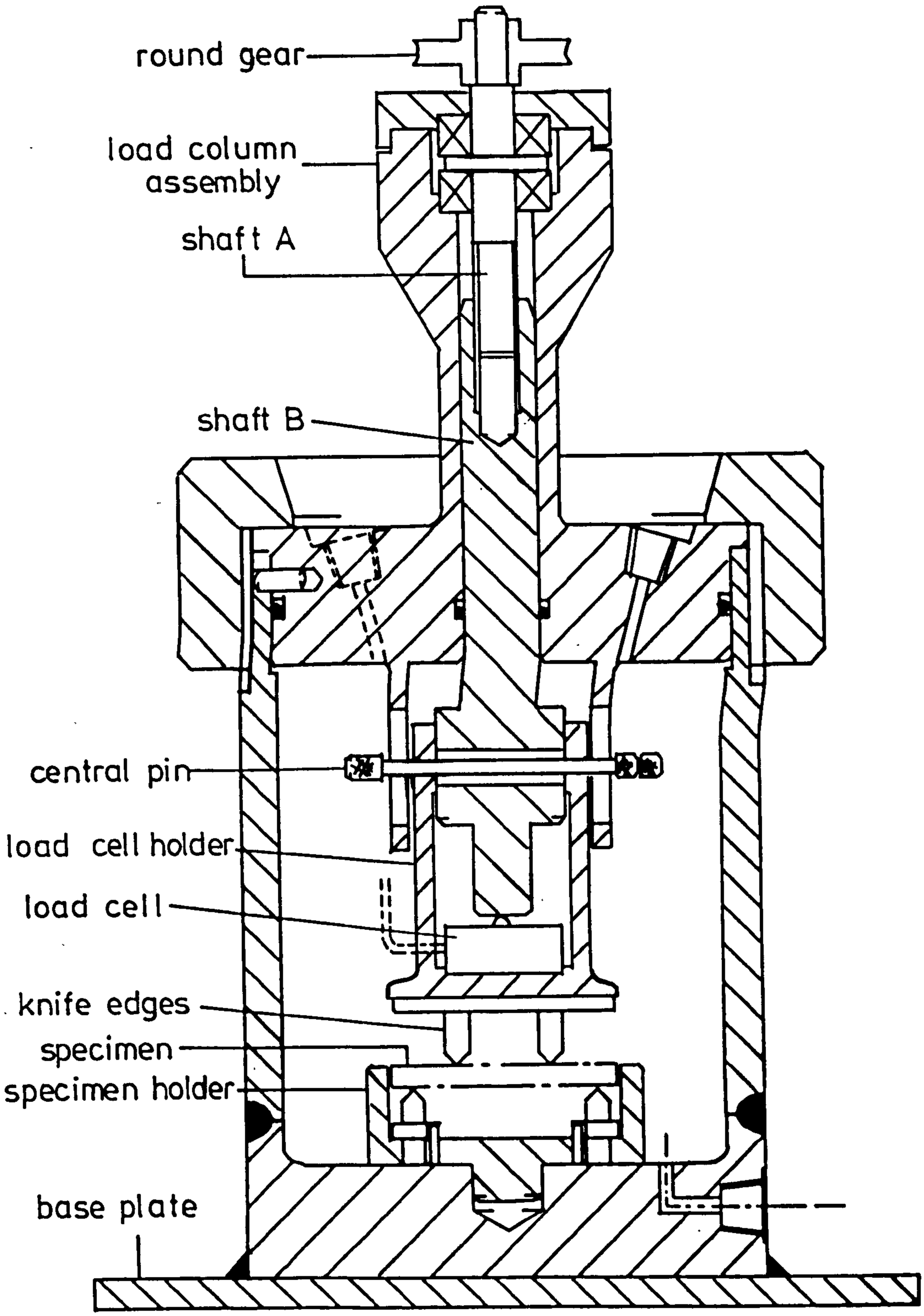

Fig 5.7 4-point bend test equipment

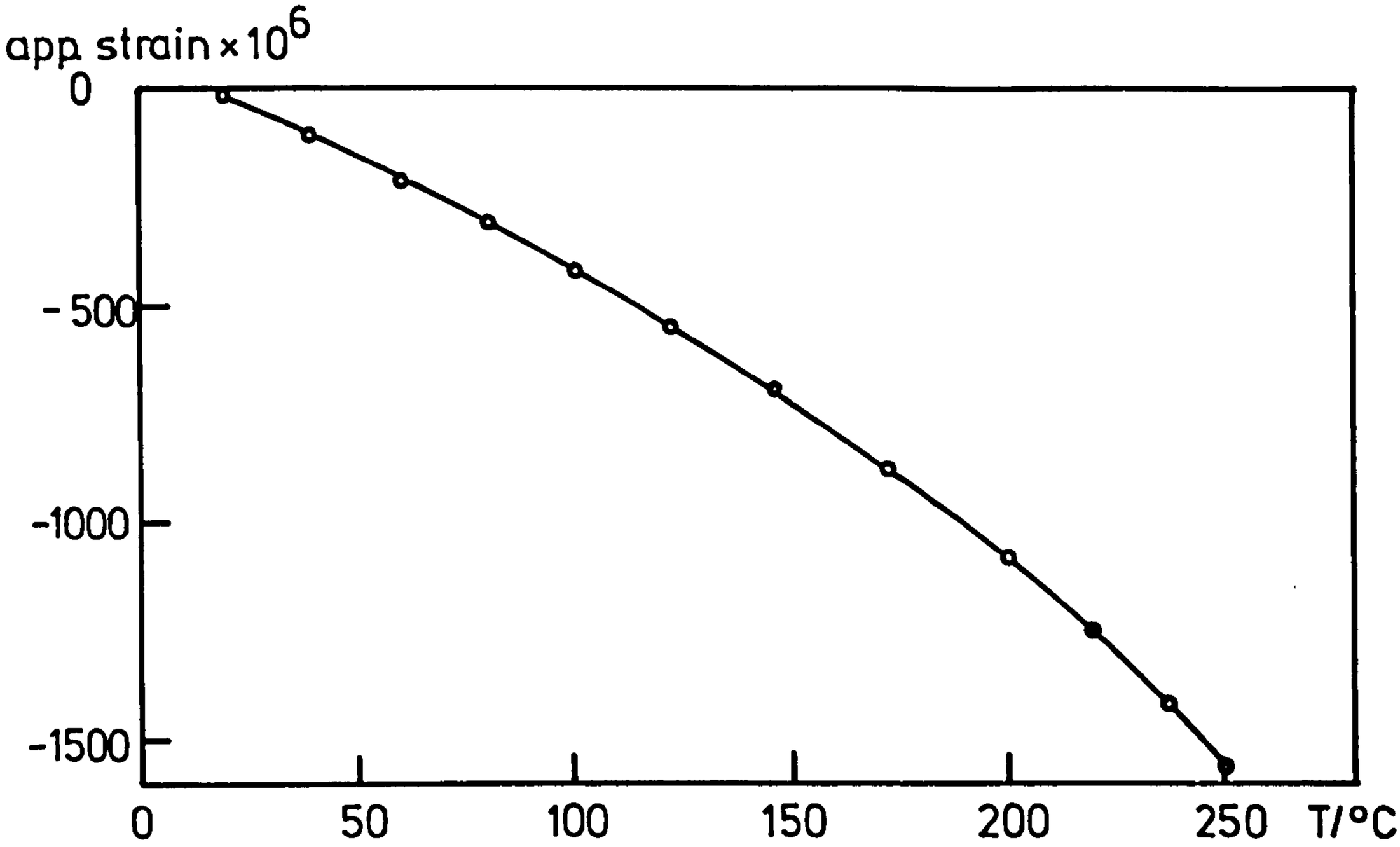

Fig 5.8 Apparent strain data: 06 S.T.C. gauge

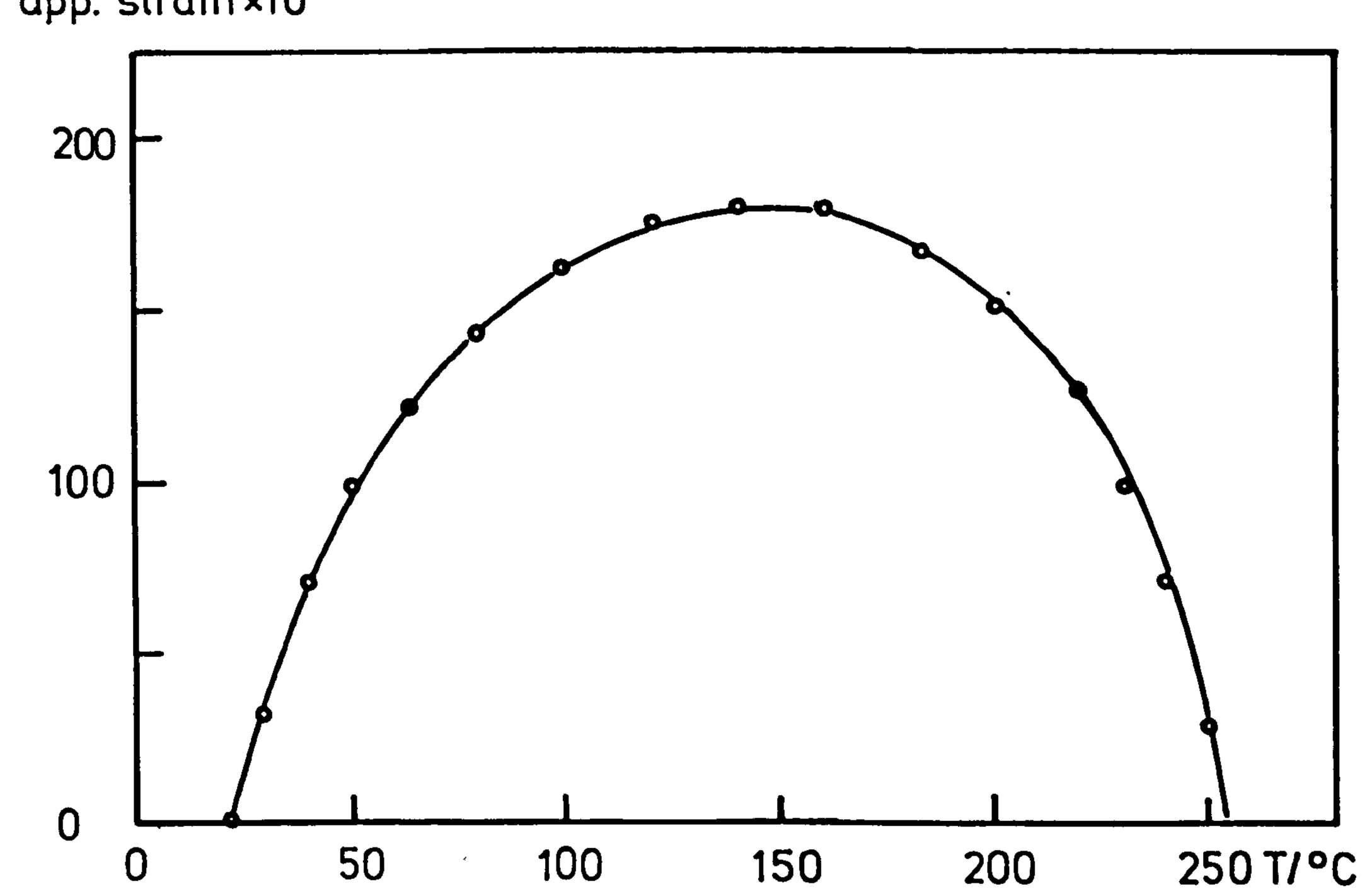

Fig 5.9 Apparenf strain data: 03 S.T.C. gauge

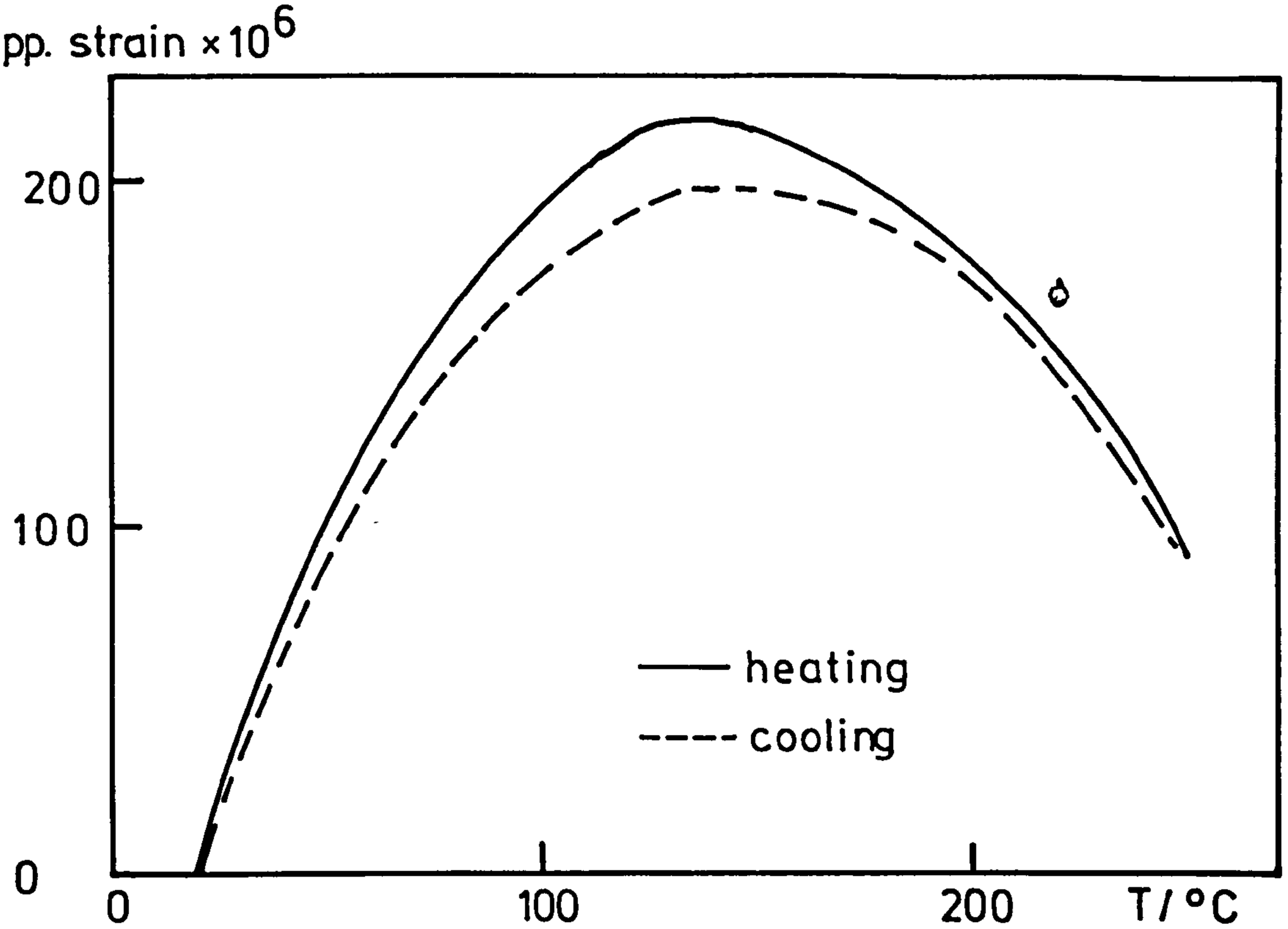

Fig 5.10 Continuous heating and cooling apparent strains : graphite A

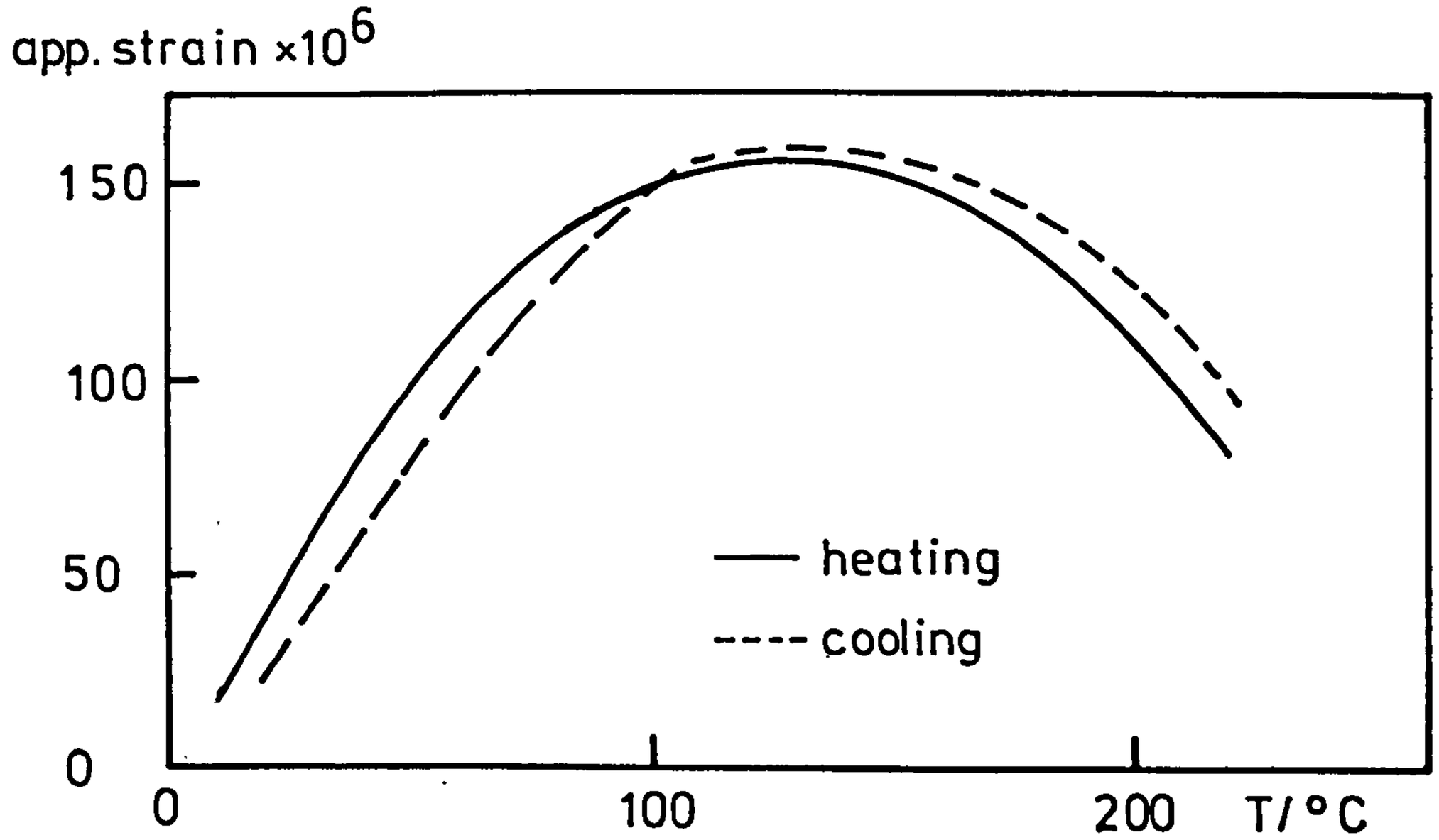

Fig 5.11 Continuous heating and cooling apparent strains : molybdenum

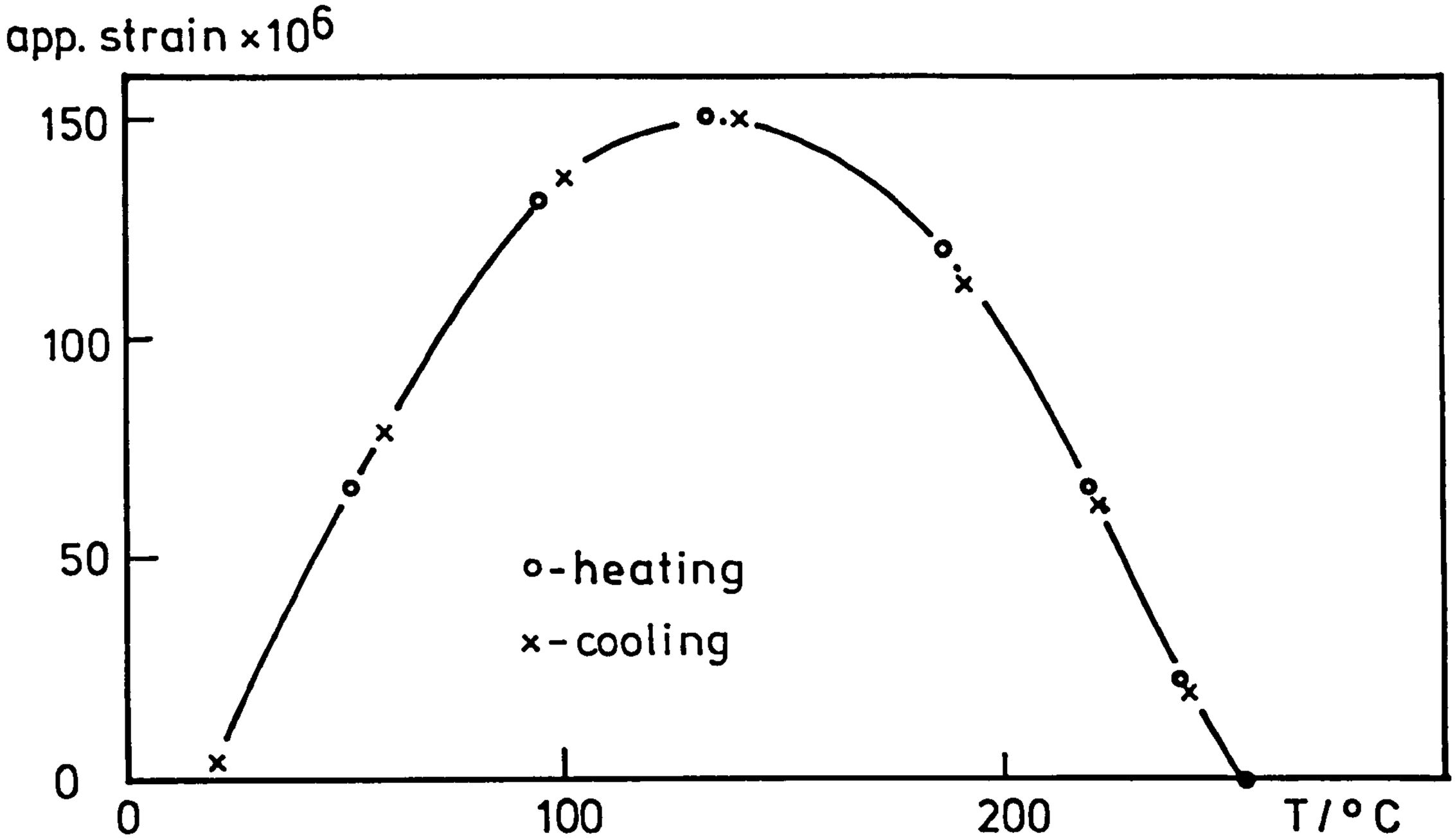

Fig 5.12 Apparent strains from slow temp. increments and decrements : graphite A

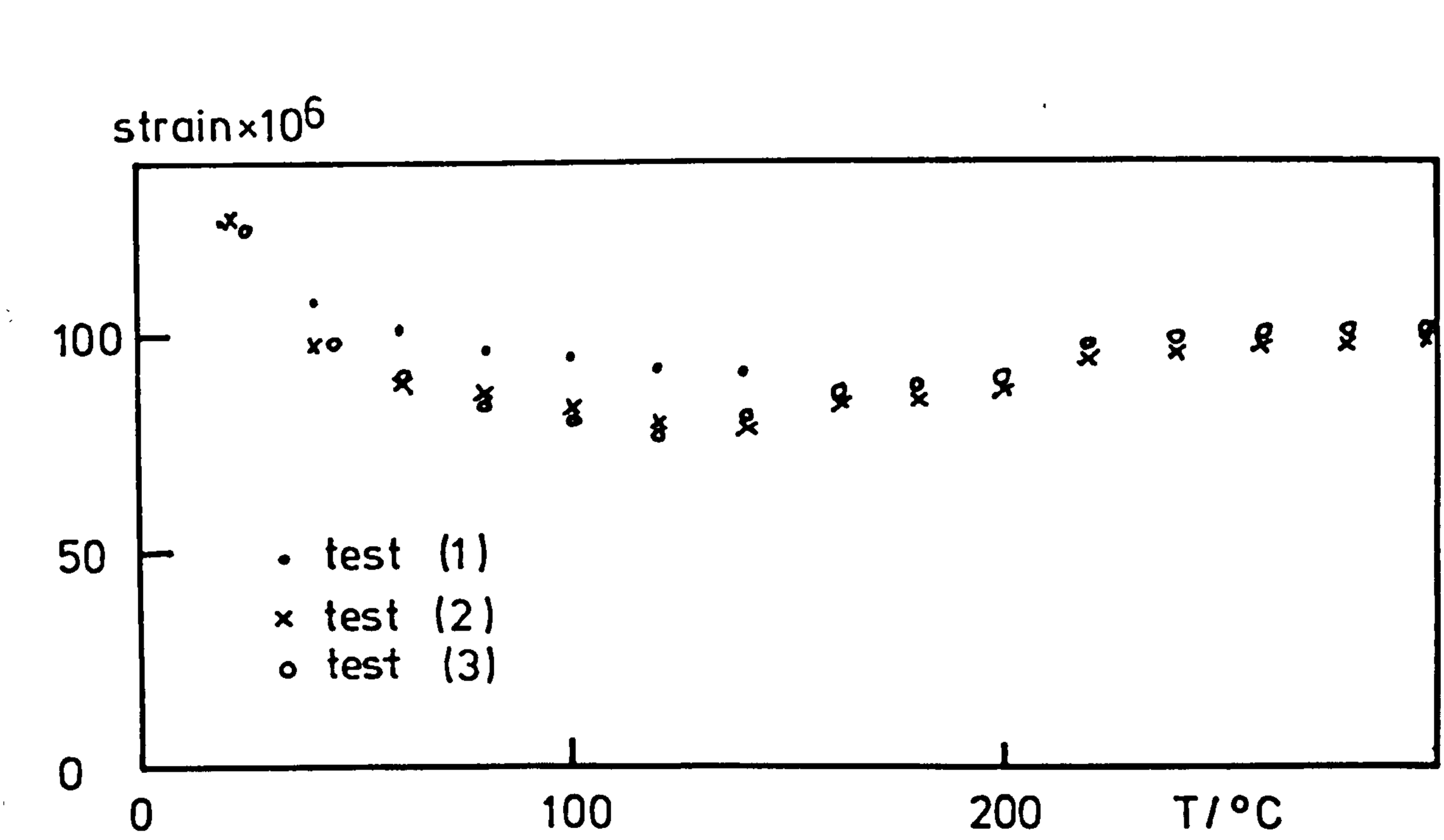

Fig 5.13 Elevated temp. test : graphite A

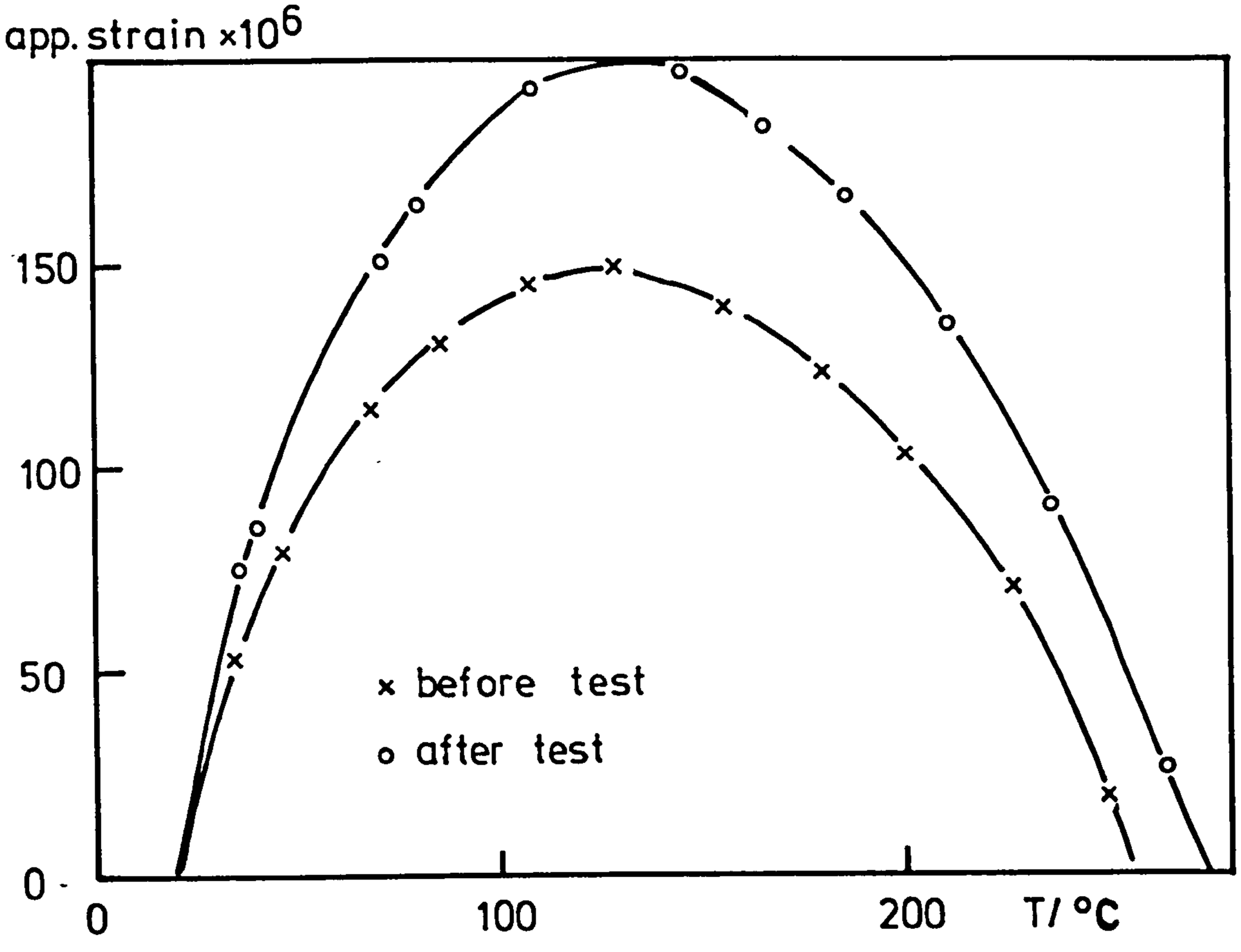

Fig 5.14 Apparent strains before and after elevated temp. test : graphite A

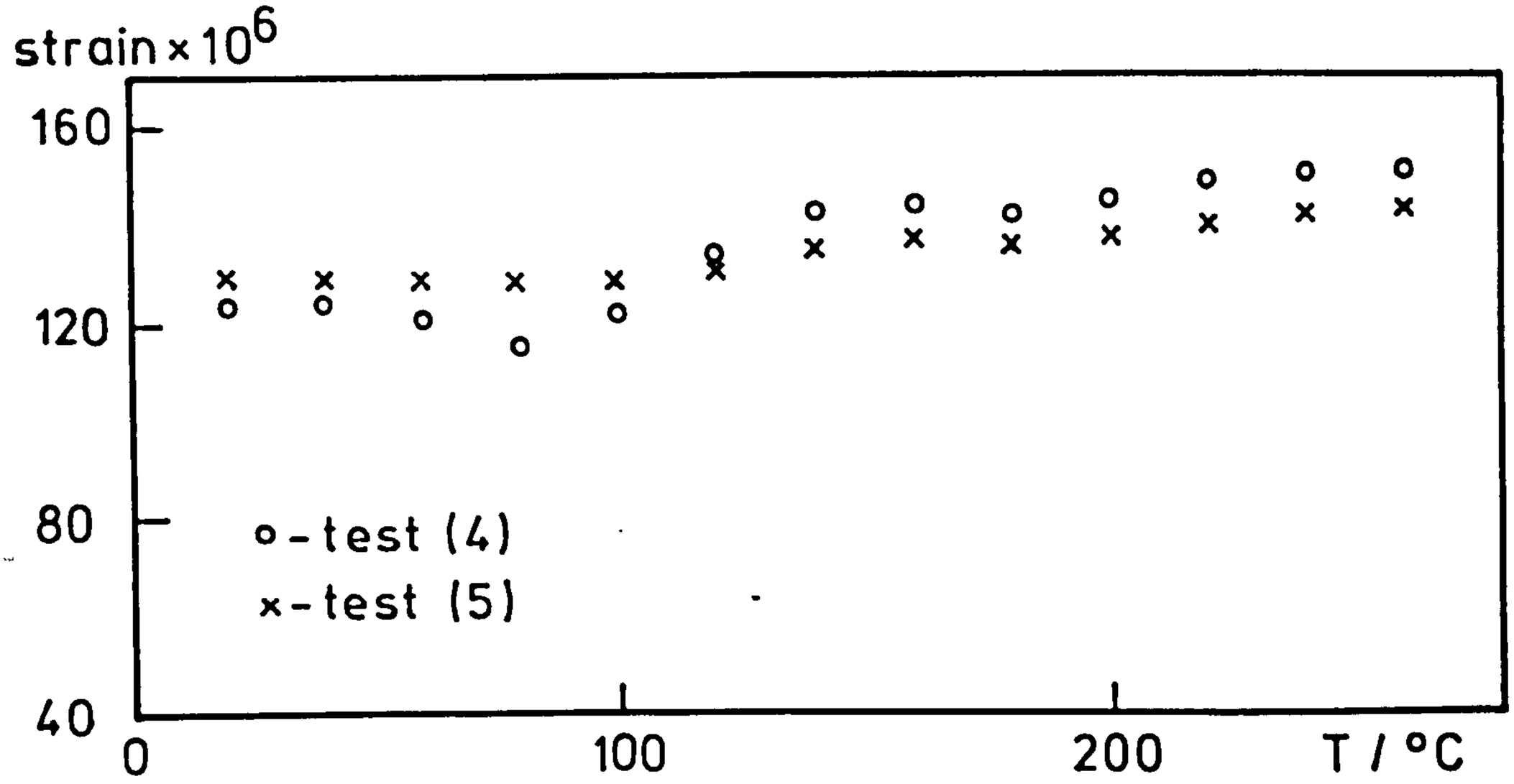

Fig 5.15 Elevated temp. tests of graphite A with new apparent strain data

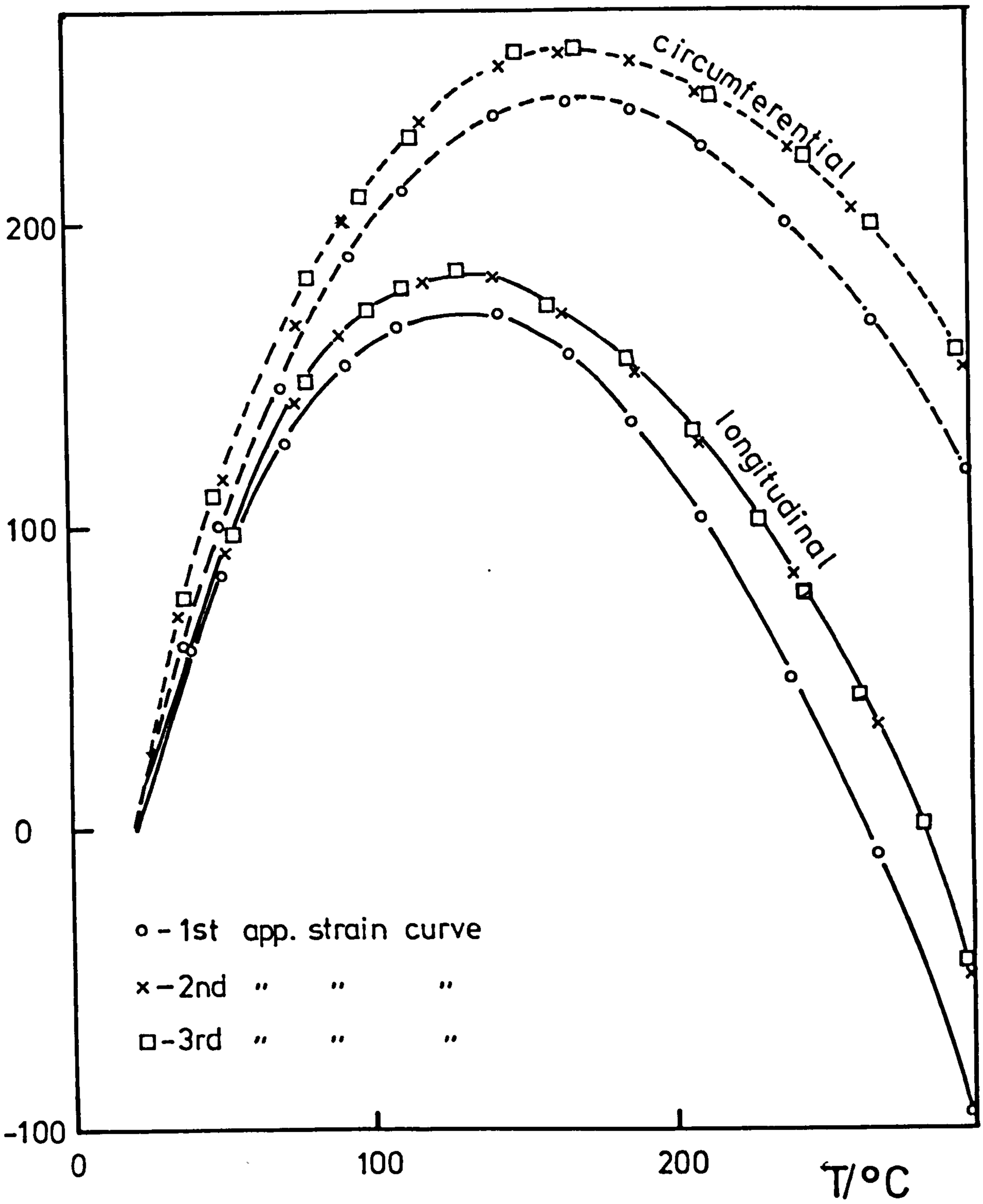

Fig 5.16 Apparent strains before and after elevated temp. tests : graphite B

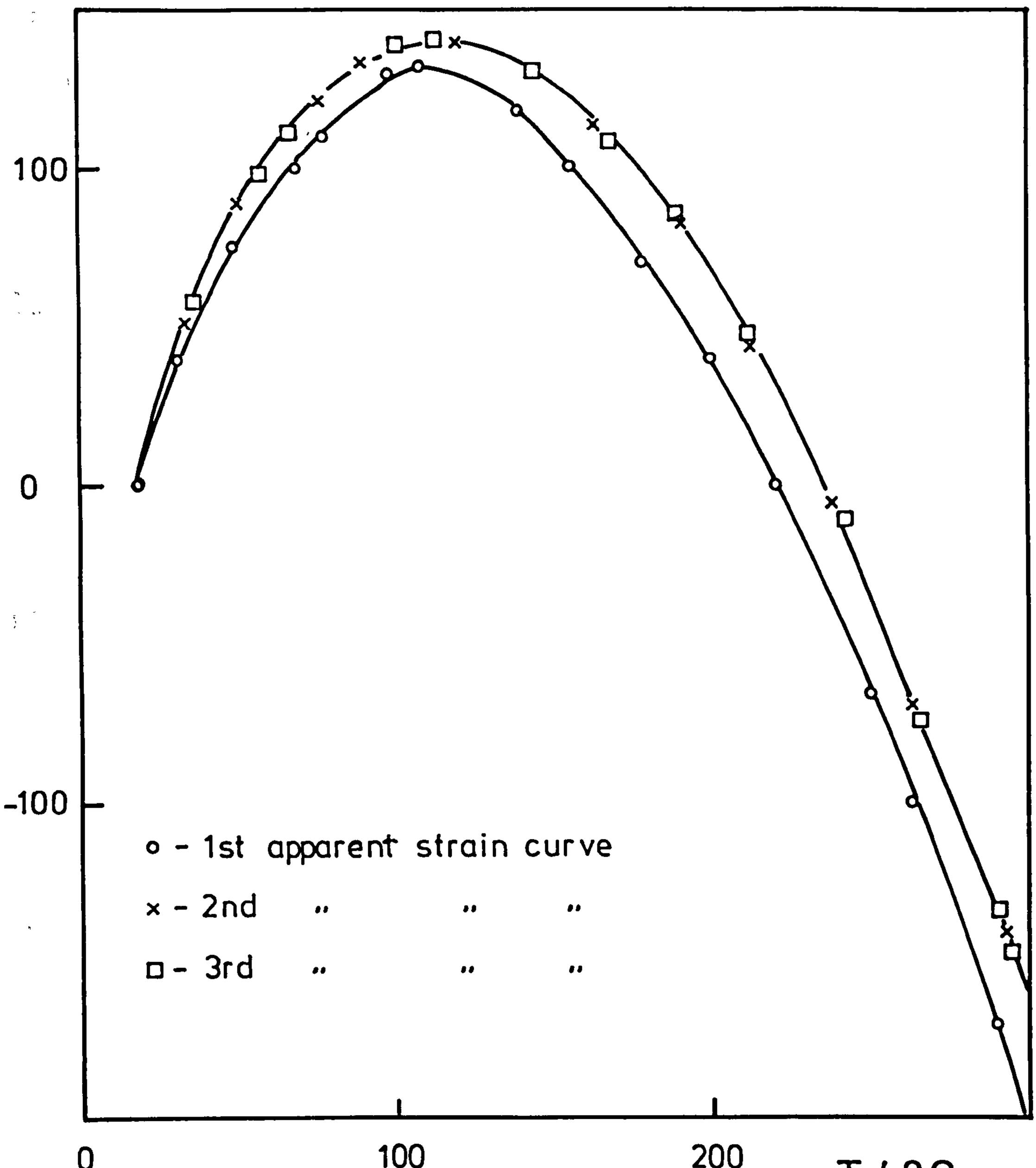

Fig 5·17 Longitudinal app. strains before and after elevated temp. tests : graphite C

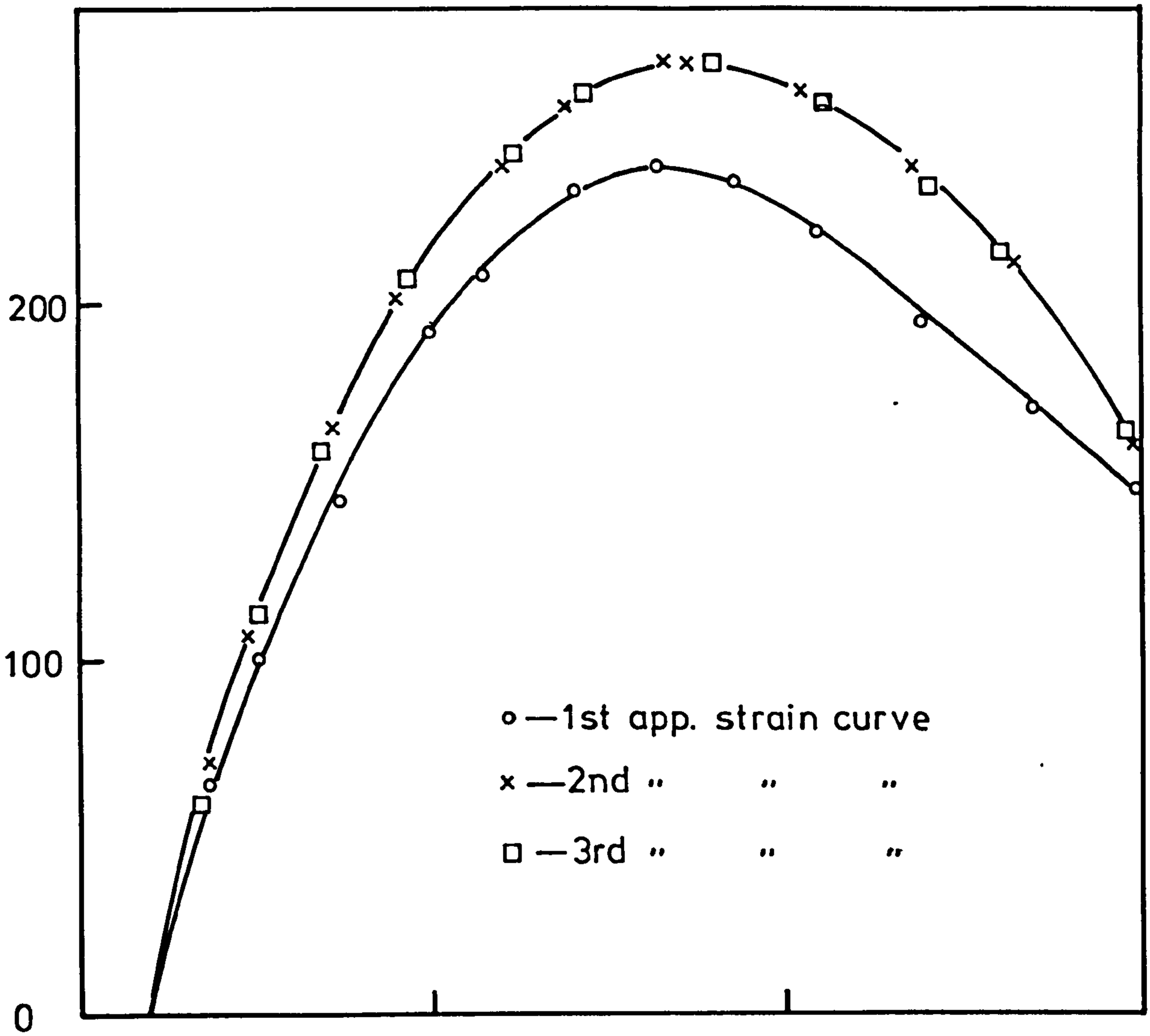

Fig 5.18 Longitudinal app. strains before and after elevated temp. tests : graphite D

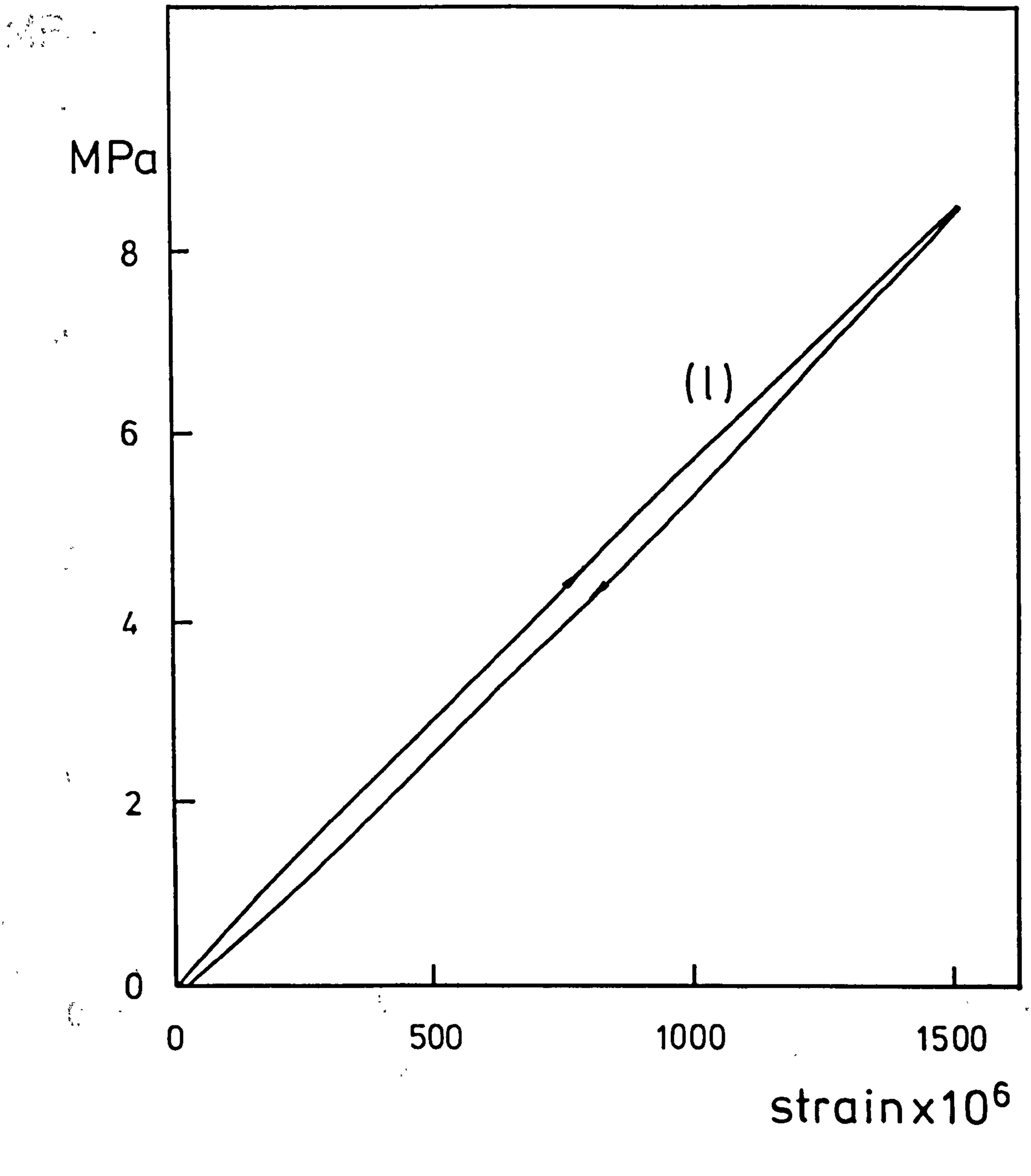

Fig 6.1 Compressive stress-strain curve of graphite A in longitudinal (l) direction

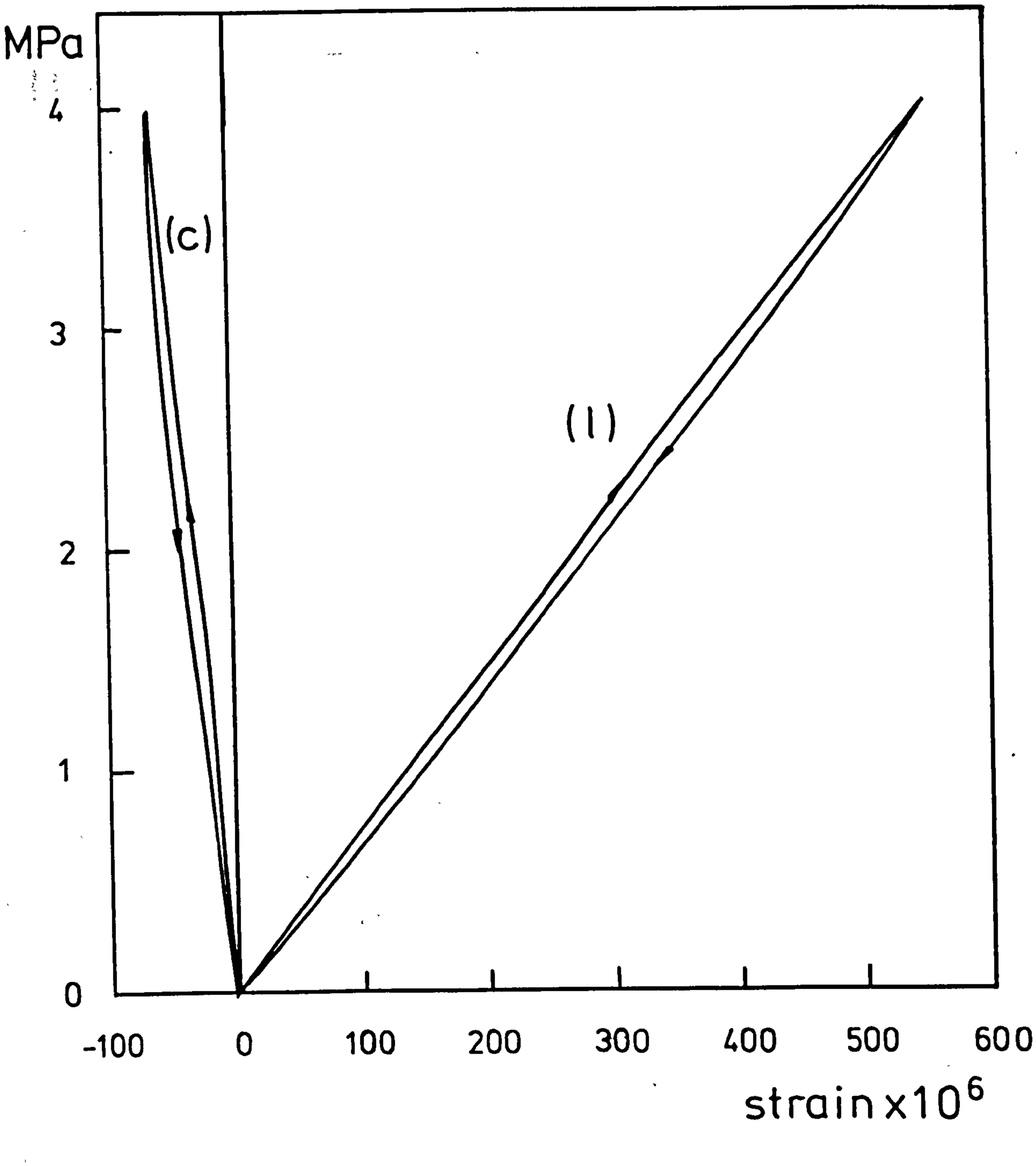

Fig 6.2 Compressive stress-strain curves of graphite B in longitudinal (l) and circumferential (c) directions

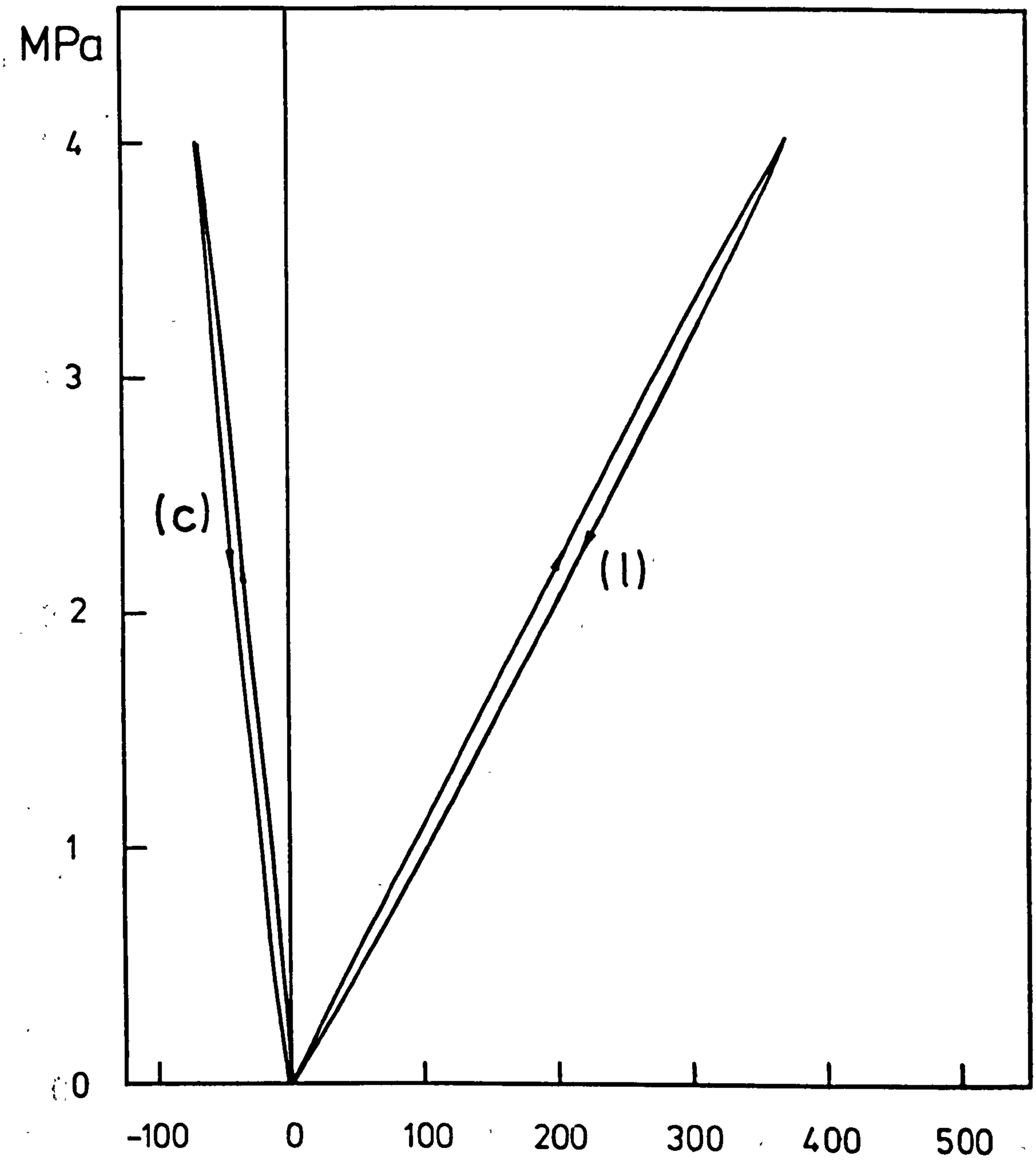

Fig 6.3 Compressive stress-strain curves of graphite C in longitudinal (l) and circumferential (c) directions

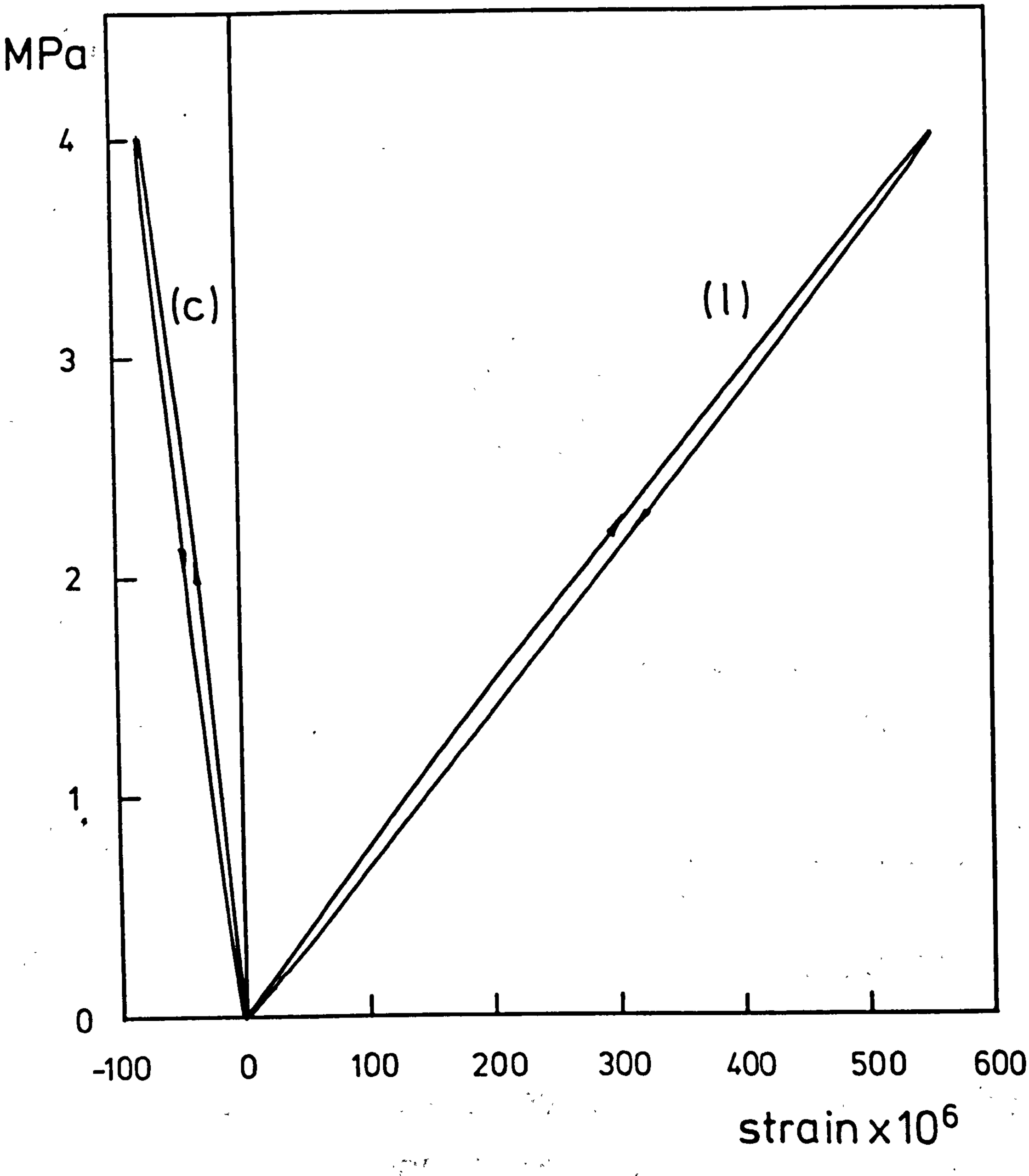

Fig 6.4 Compressive stress-strain curves of graphite D in longitudinal (l) and circumferential (c) directions

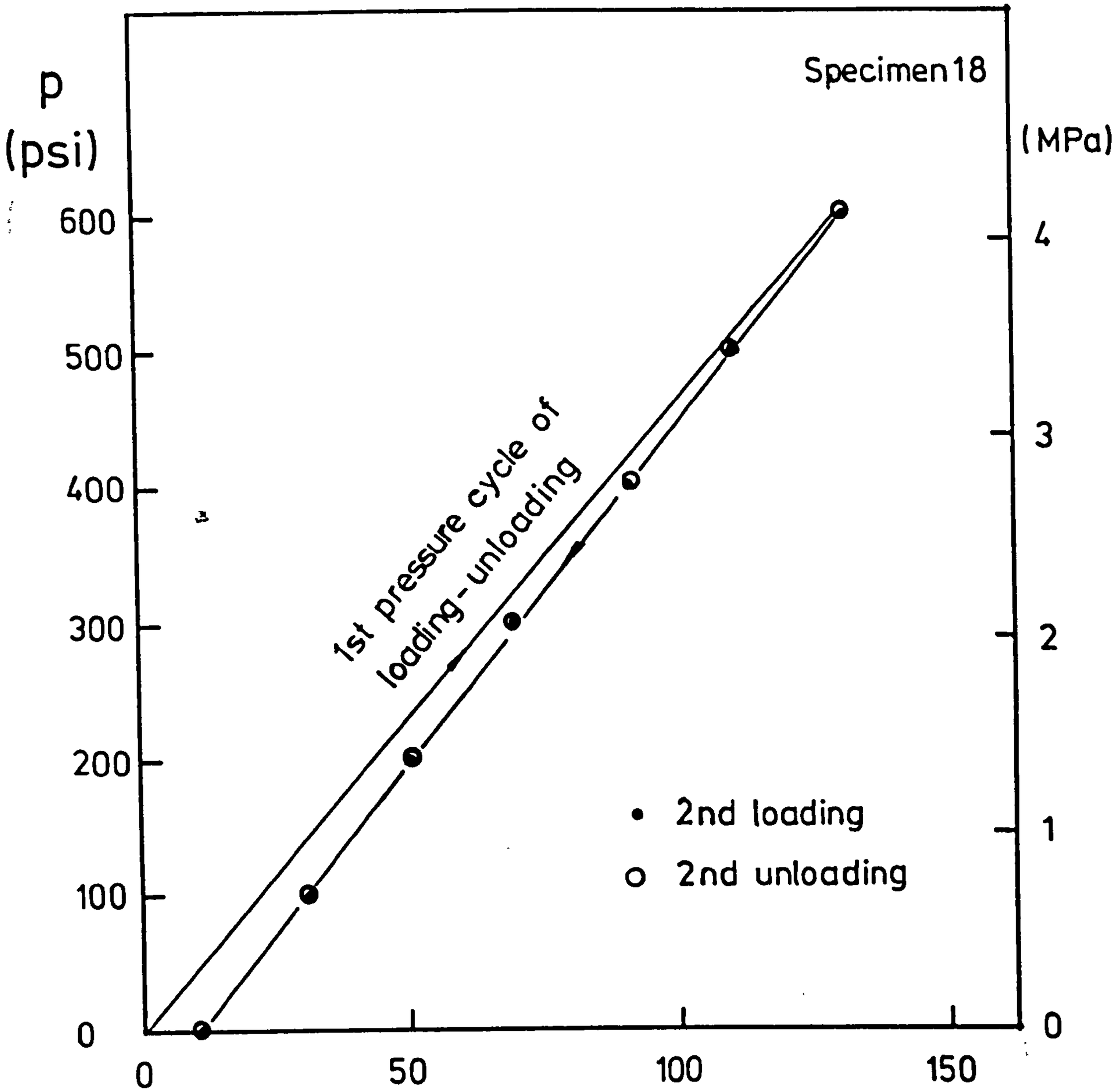

Fig 6.5 General behaviour of polycrystalline graphite under pressure (graphite B)

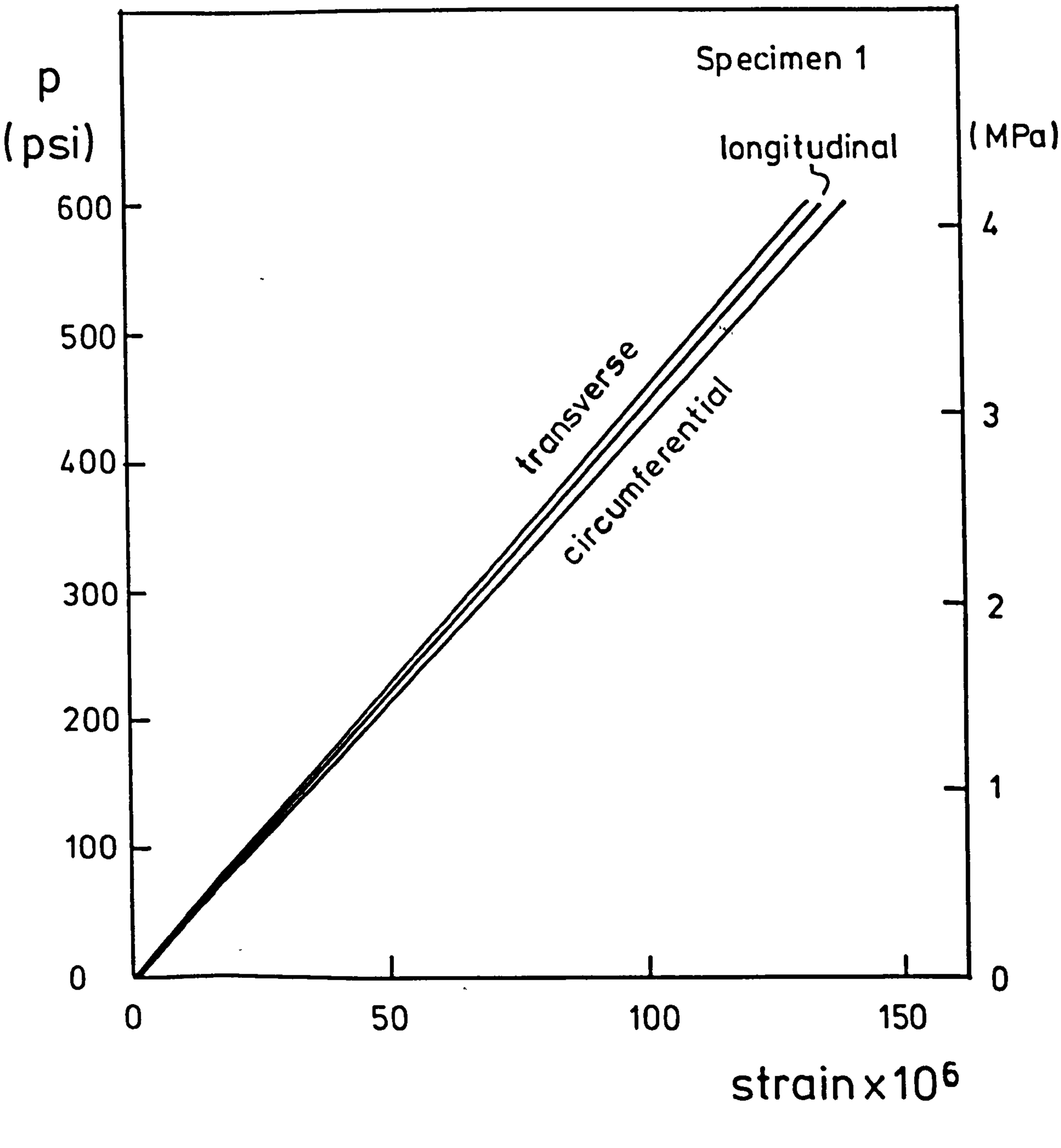

Fig 6·6 Pressure-strain curves of graphite A in 3 directions

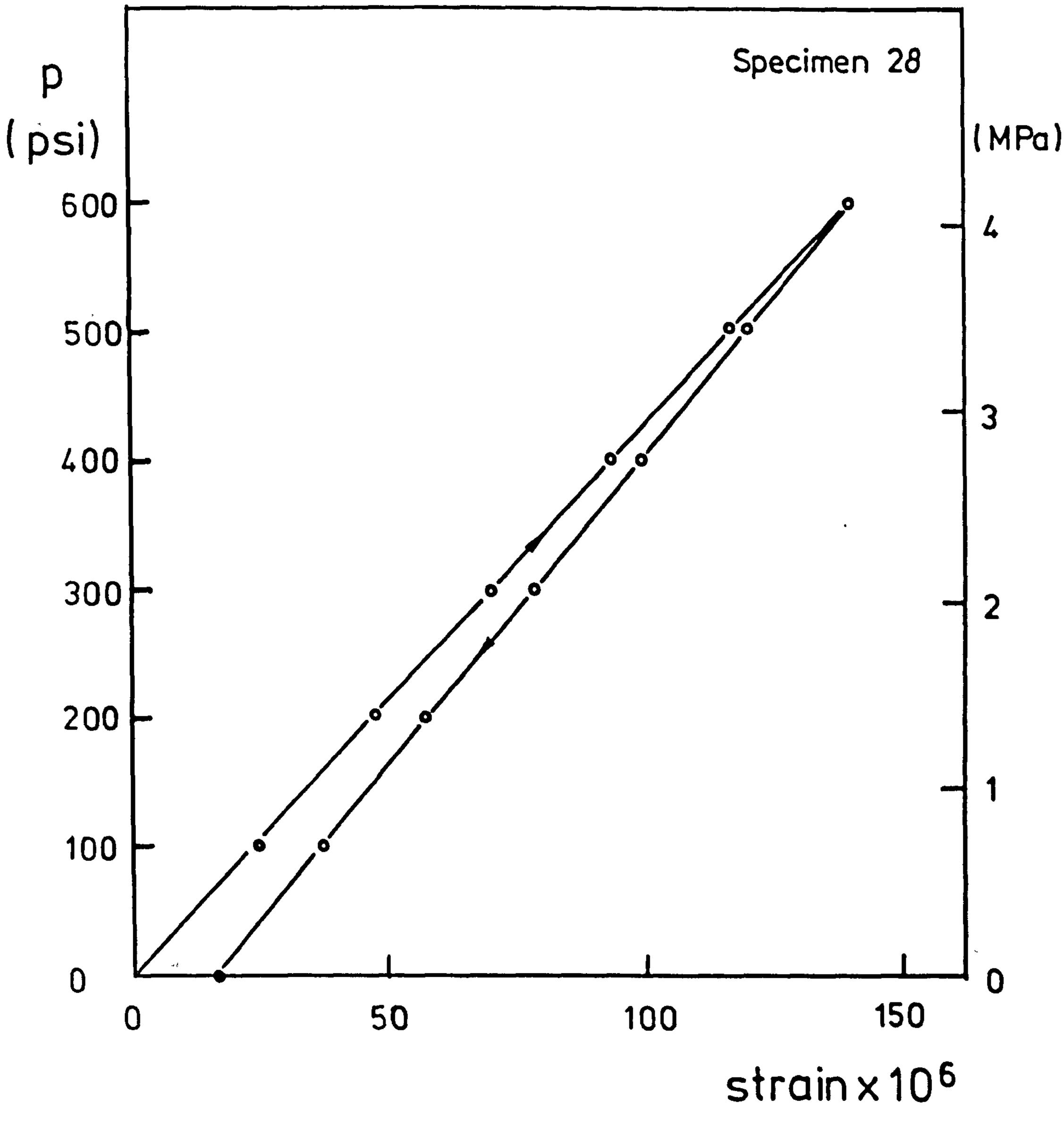

Fig 6.7 Pressure-strain curves of graphite B

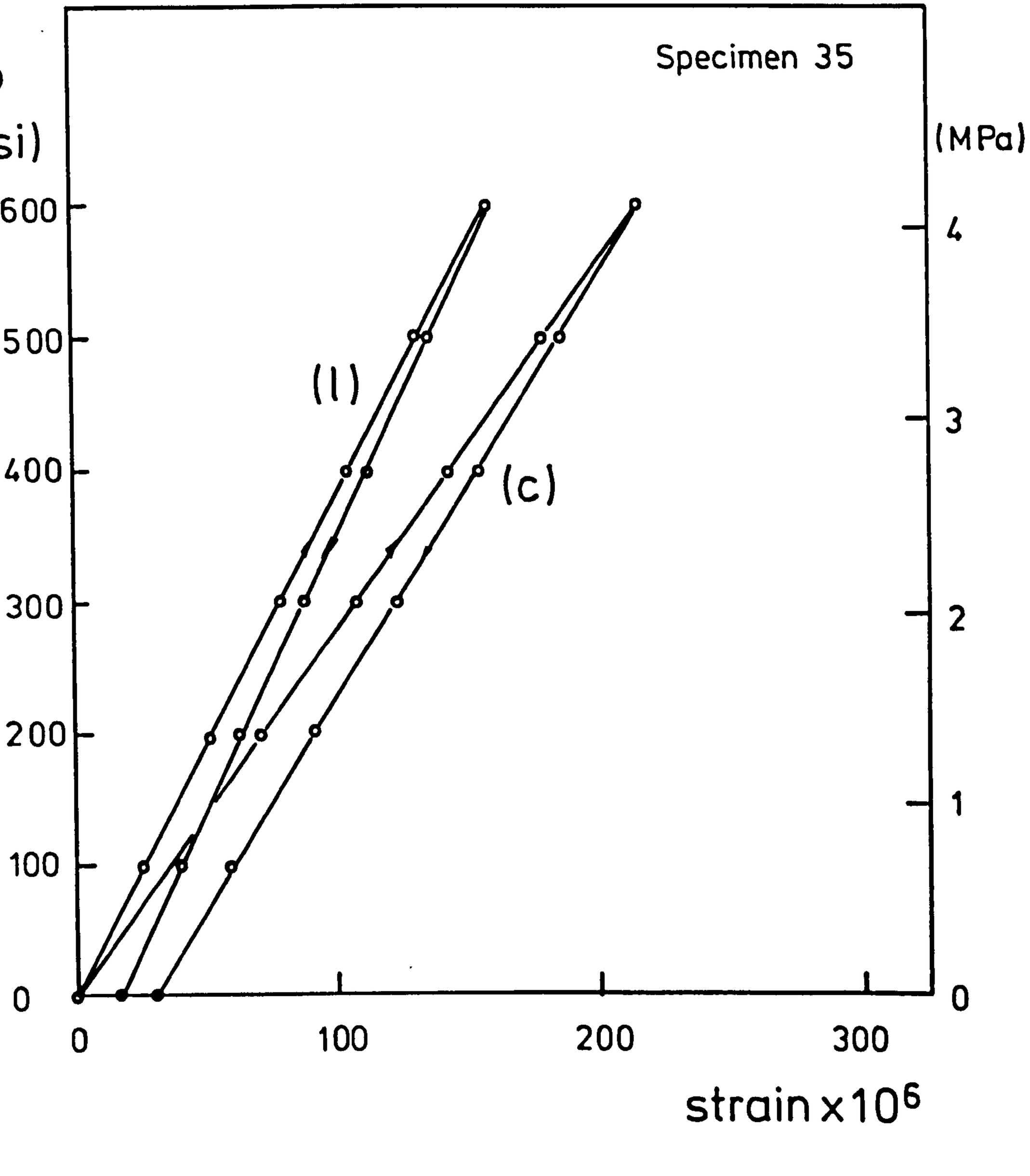

Fig 6.8 Pressure-strain curves of graphite C in longitudinal (l) and circumferential (c) directions

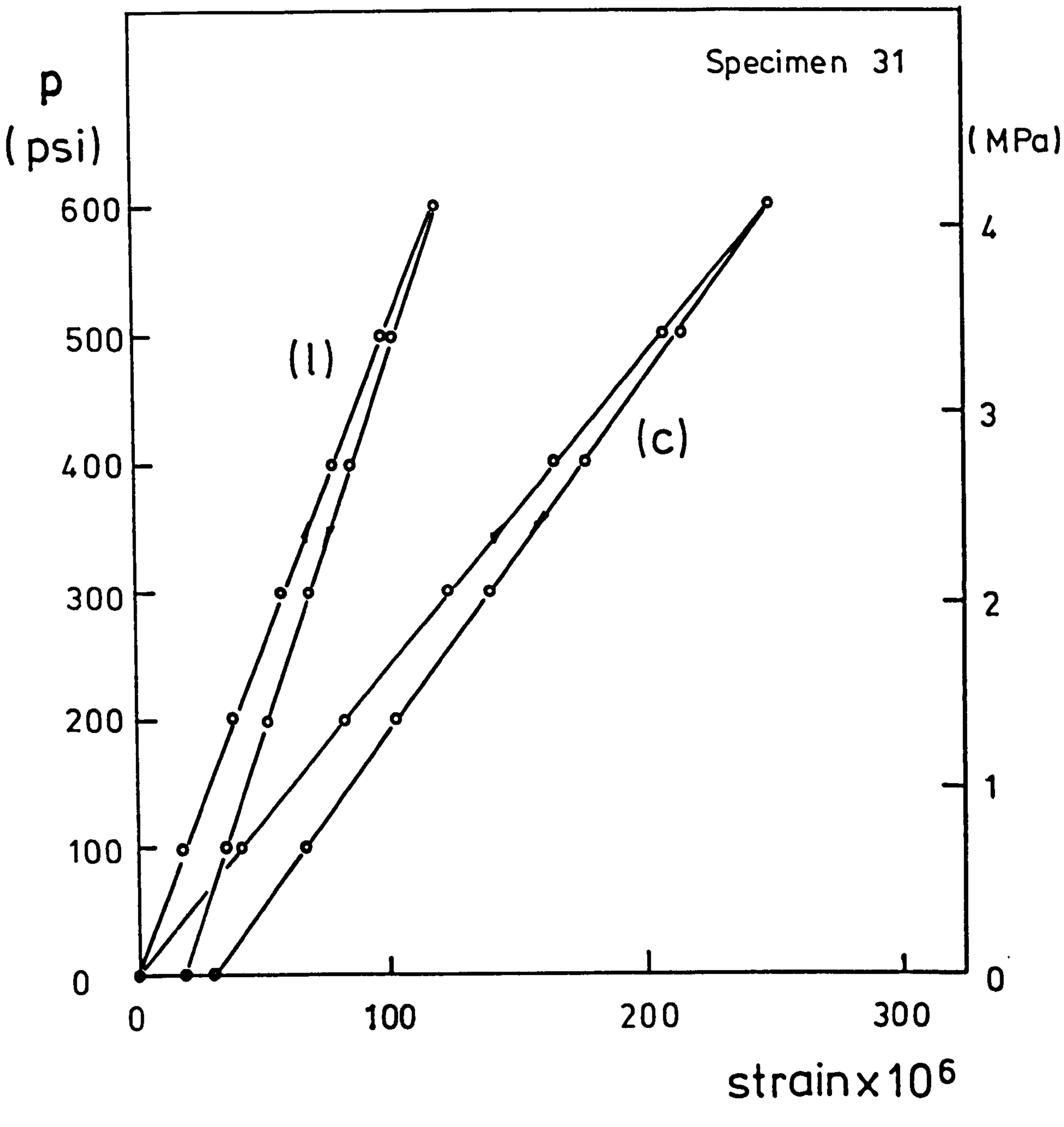

Fig 6.9 Pressure-strain curves of graphite D in longitudinal (l) and circumferential (c) directions

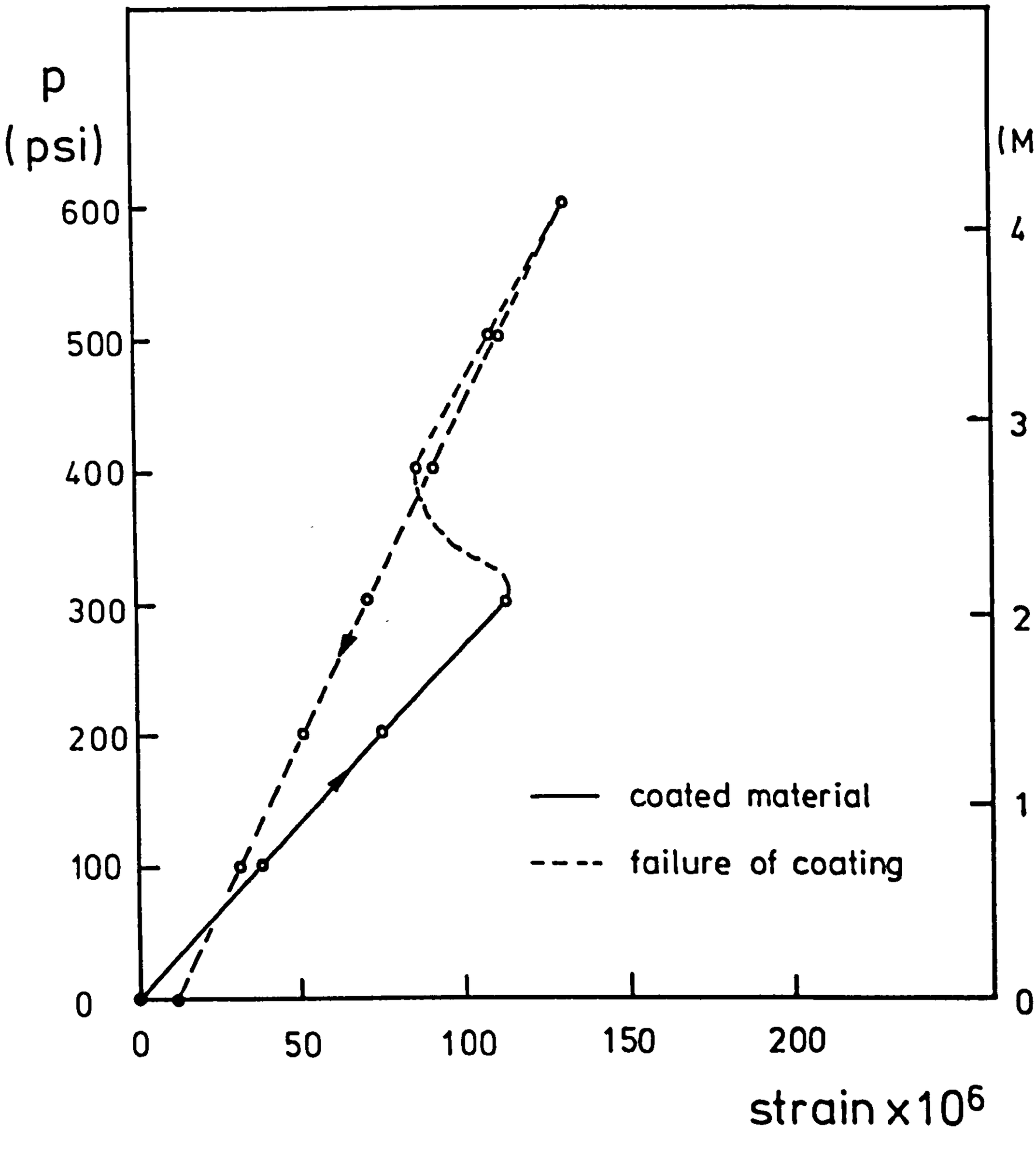

Fig 6·10 Graph showing pressure-strain response before and after failure of coating for a specimen of graphite B

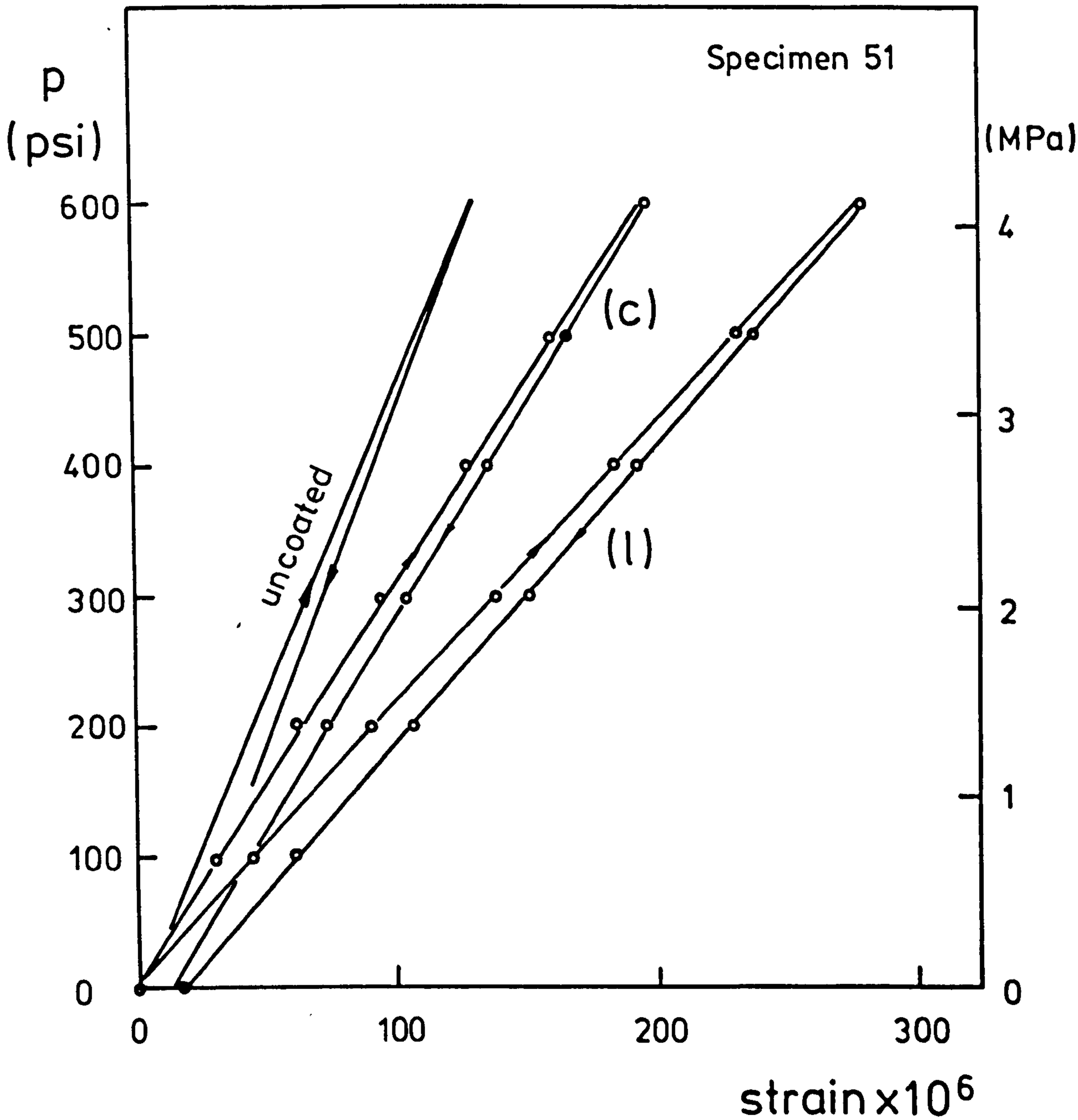

Fig 6.11 Pressure - strain curves for the coated specimen of graphite A in longitudinal (l) and circumferential (c) directions

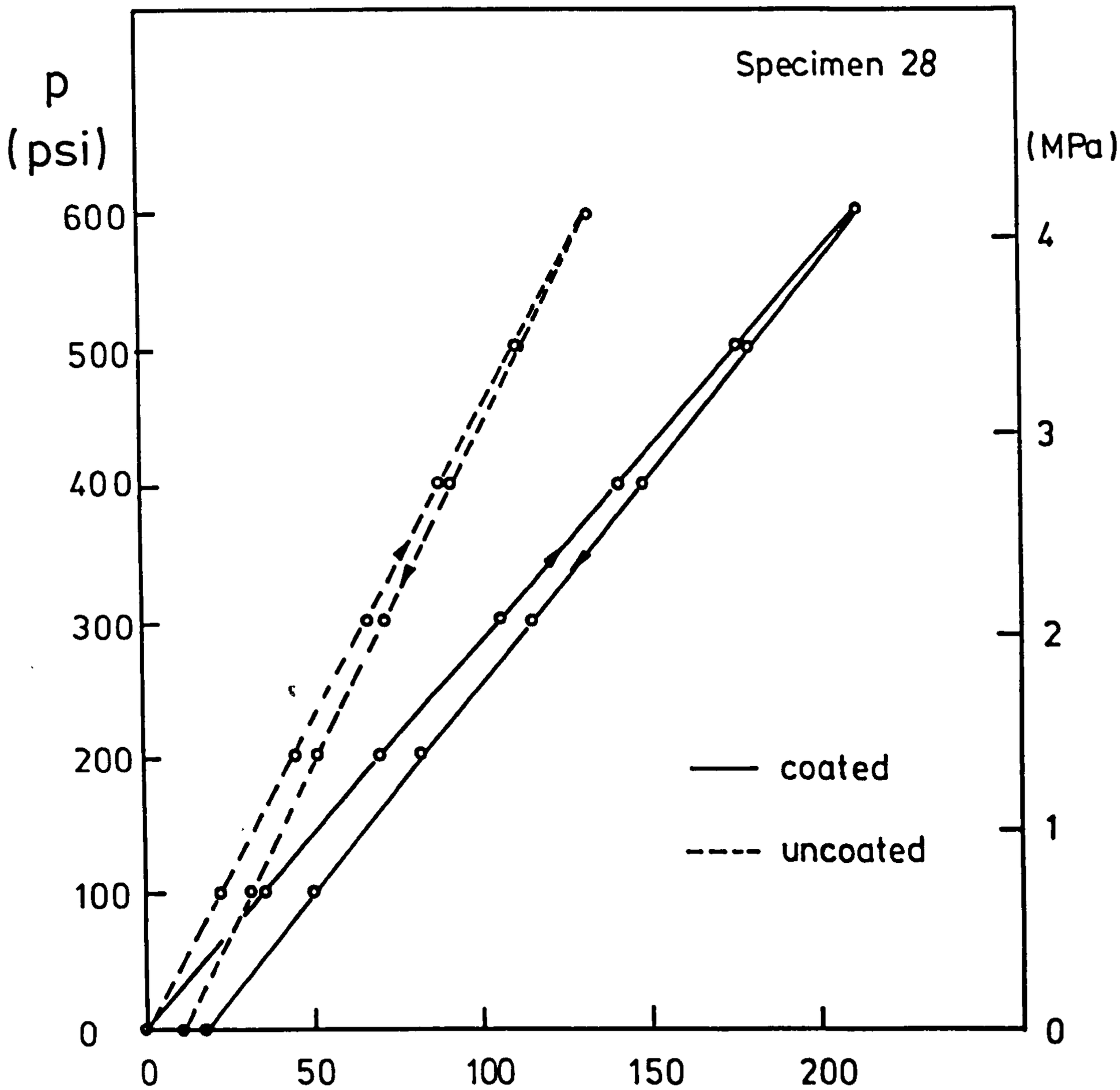

Fig 6.12 Pressure-strain curves of coated and uncoated specimen of graphite B

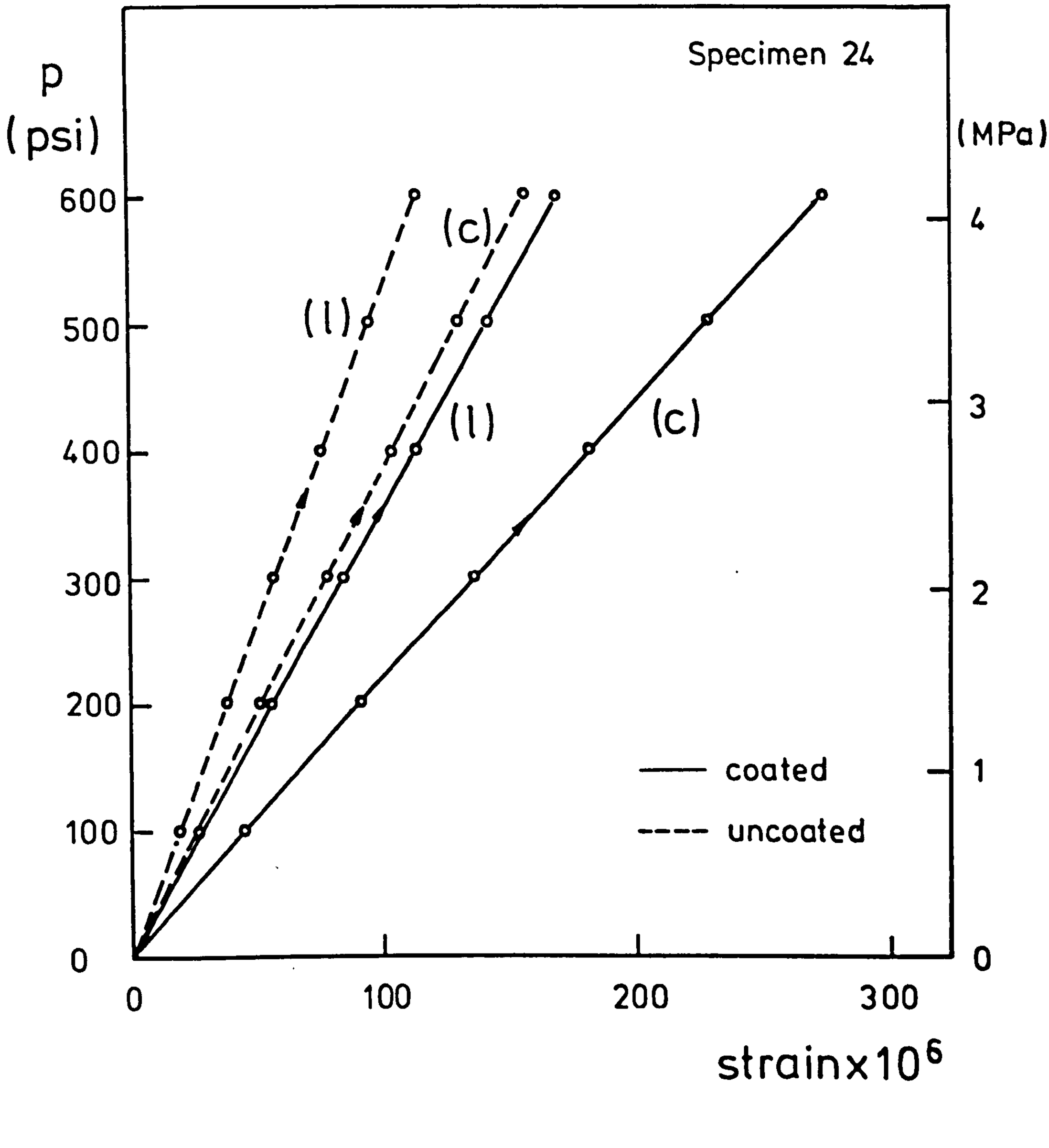

Fig 6.13 Pressure-strain loading curves for the coated and uncoated specimen of graphite C in longitudinal (l) and circumferential (c) directions

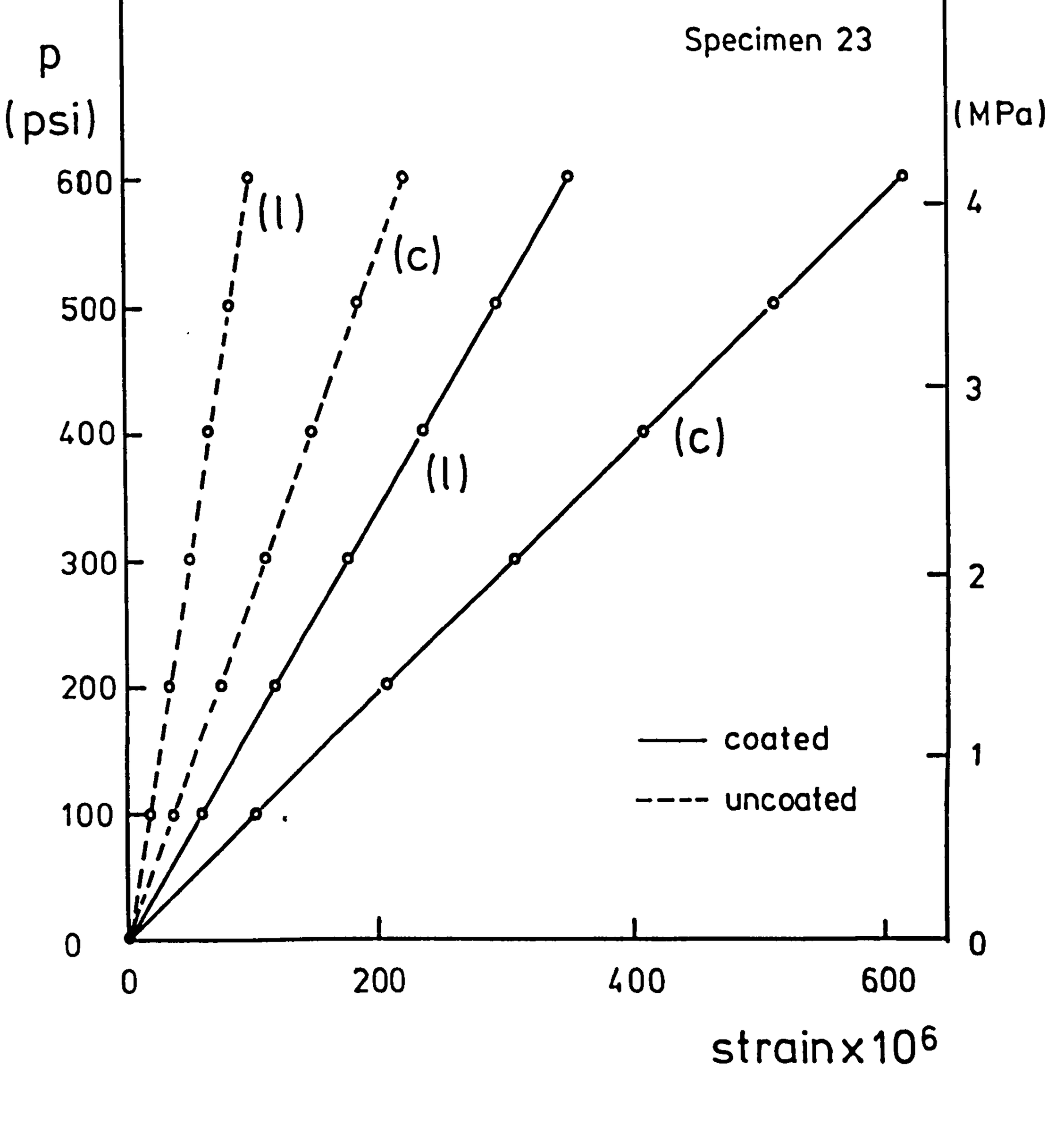

Fig 6.14 Pressure-strain loading curves for the coated and uncoated specimen of graphite D in longitudinal (l) and circumferential (c) directions

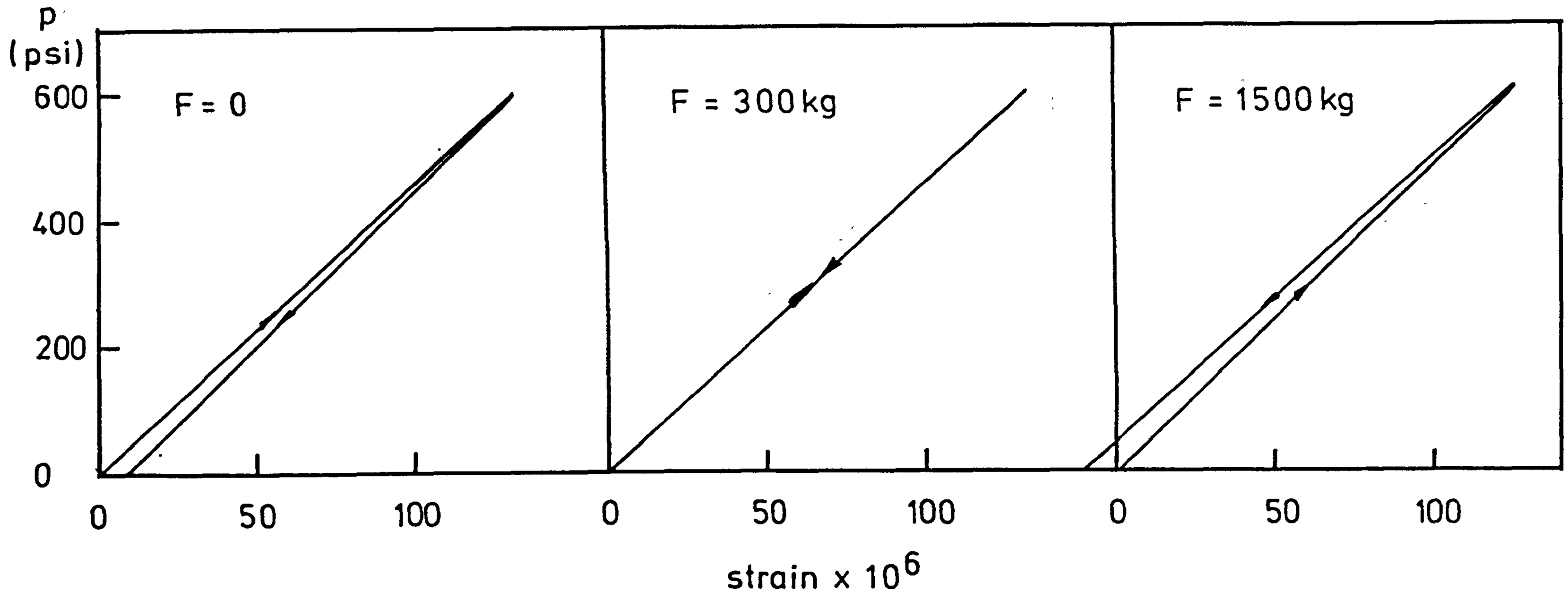

Fig 6.15 Pressure-strain behaviour of graphite A after a series of compressive loads from F=0 to 1500 kg in longitudinal direction : test (1)

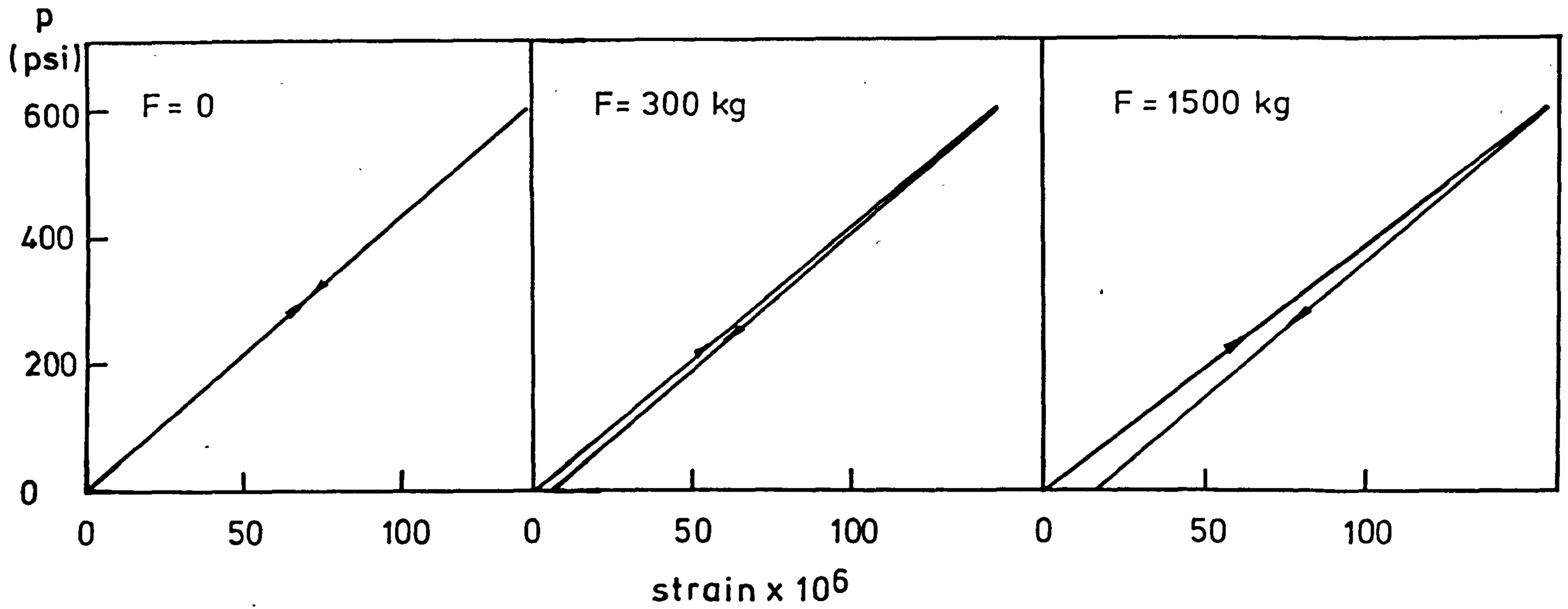

Fig 6.16 Pressure-strain behaviour of graphite A after a series of compressive loads from F=0 to 1500 kg in circumferential direction : test (1)

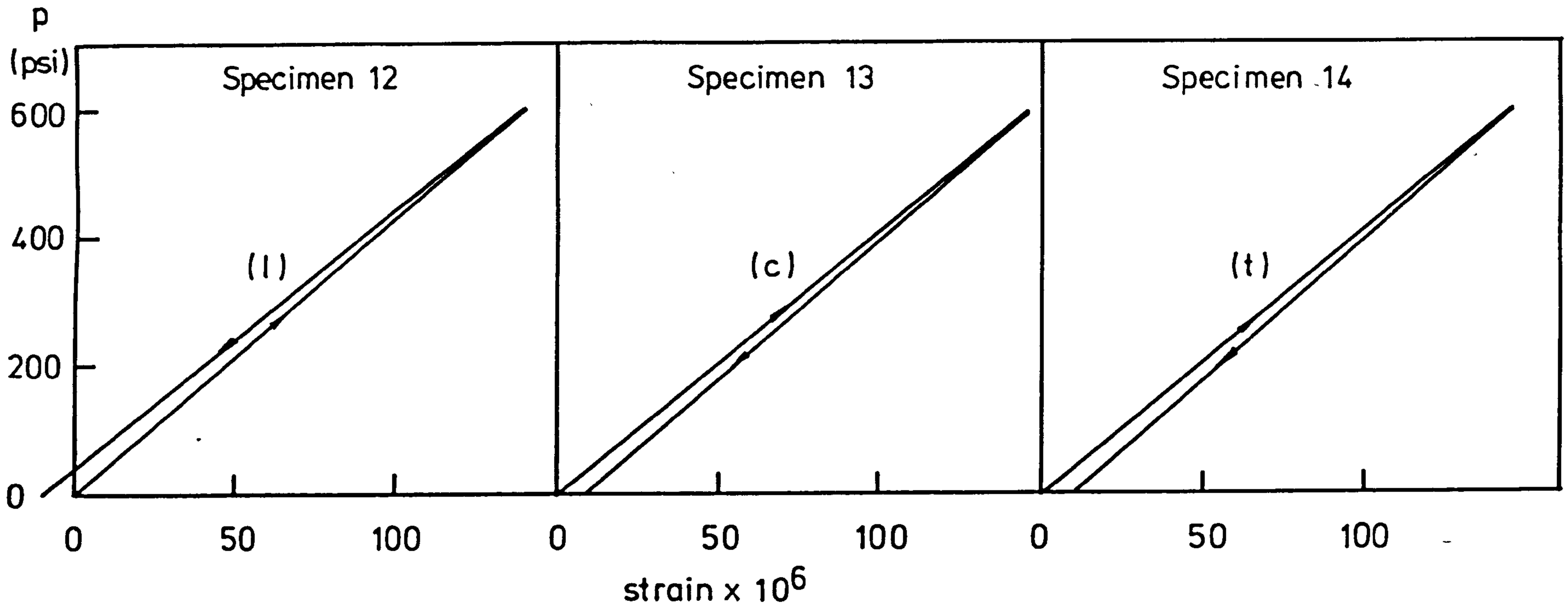

Fig 6.17 Pressure-strain behaviour of graphite A after a compressive load of 1500 kg in longitudinal (l), circumferential (c) and transverse (t) directions : test (2)

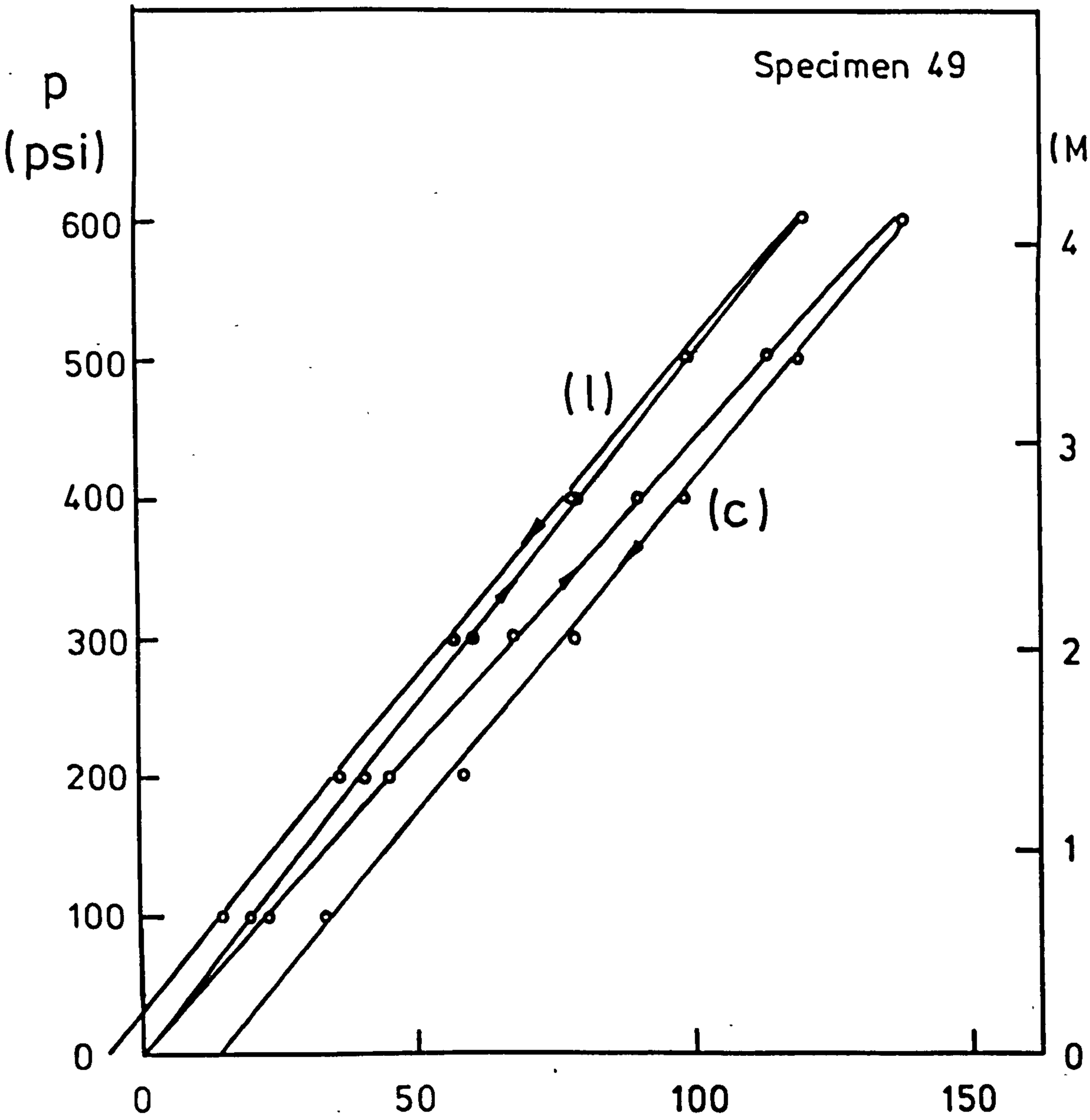

Fig 6.18 Pressure - strain curves of graphite A in longitudinal (l) and circumferential (c) directions after a compressive load of 2000 kg

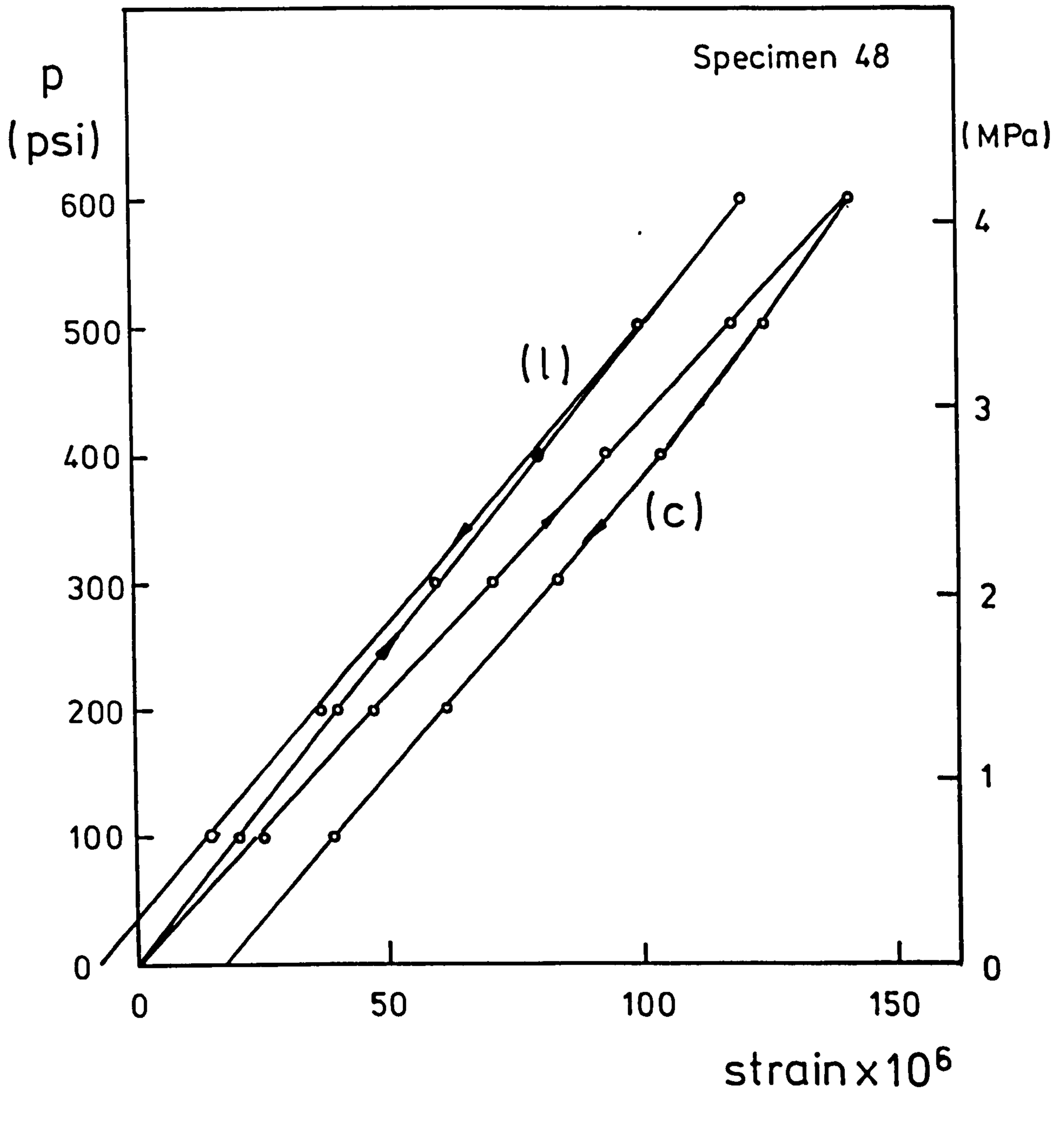

Fig 6.19 Pressure-strain curves of graphte B in longitudinal (l) and circumferential (c) directions after a compressive load of 2000 kg

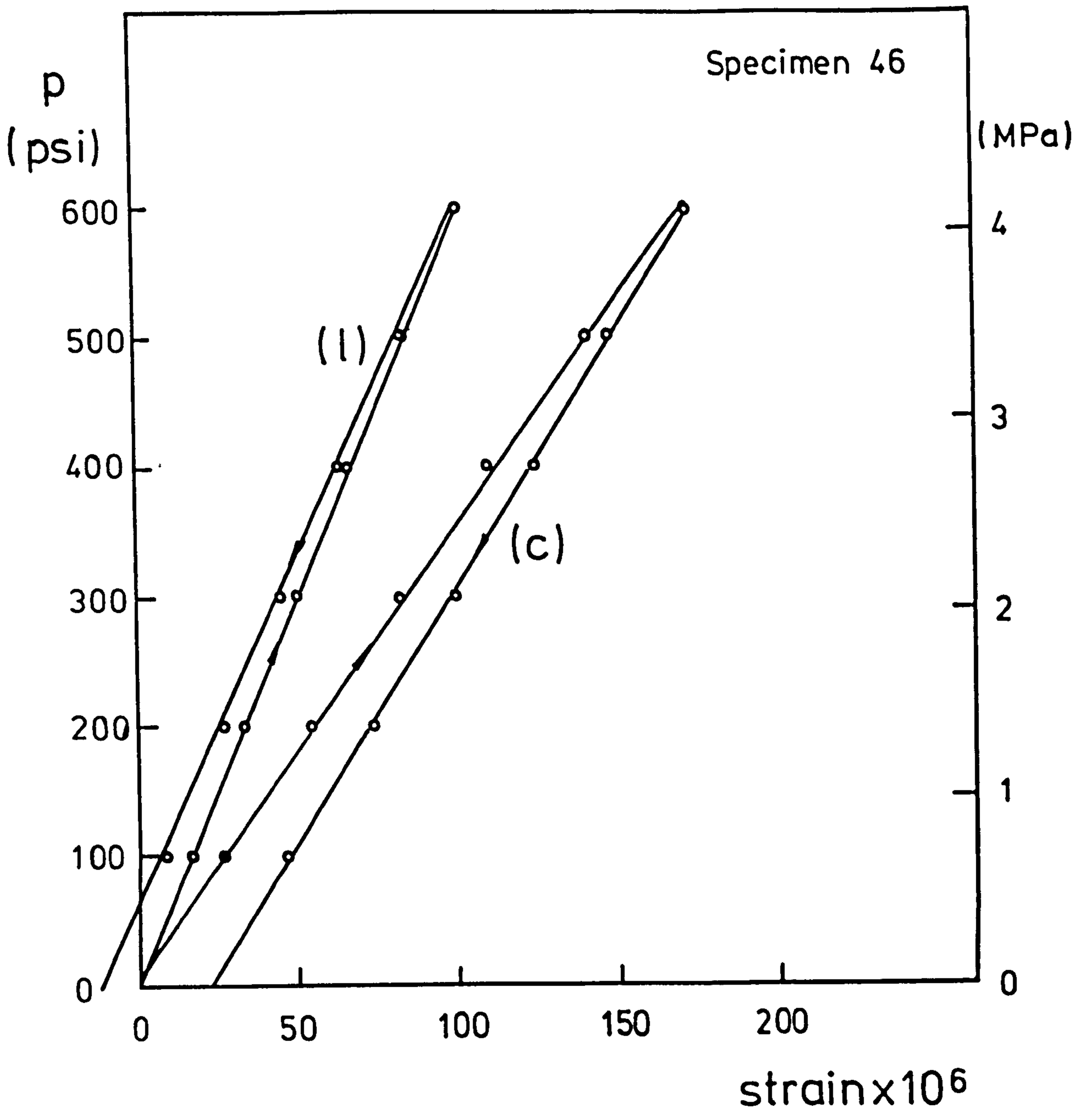

Fig 6.20 Pressure-strain curves of graphite C in longitudinal (l) and circumferential (c) directions after a compressive load of 2000 kg

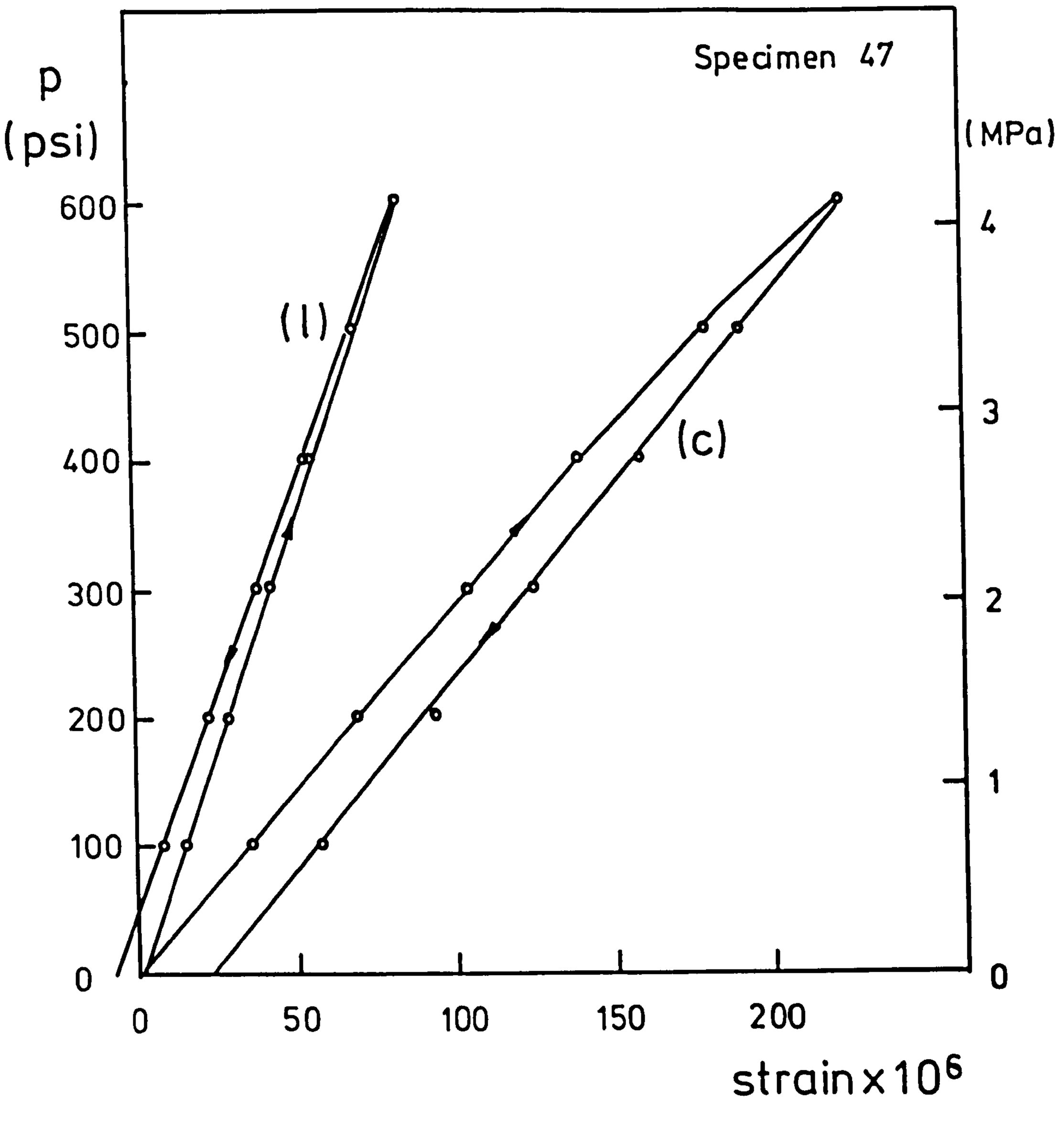

Fig 6.21 Pressure-strain curves of graphite D in longitudinal (l) and circumferential (c) directions after a compressive load of 750 kg

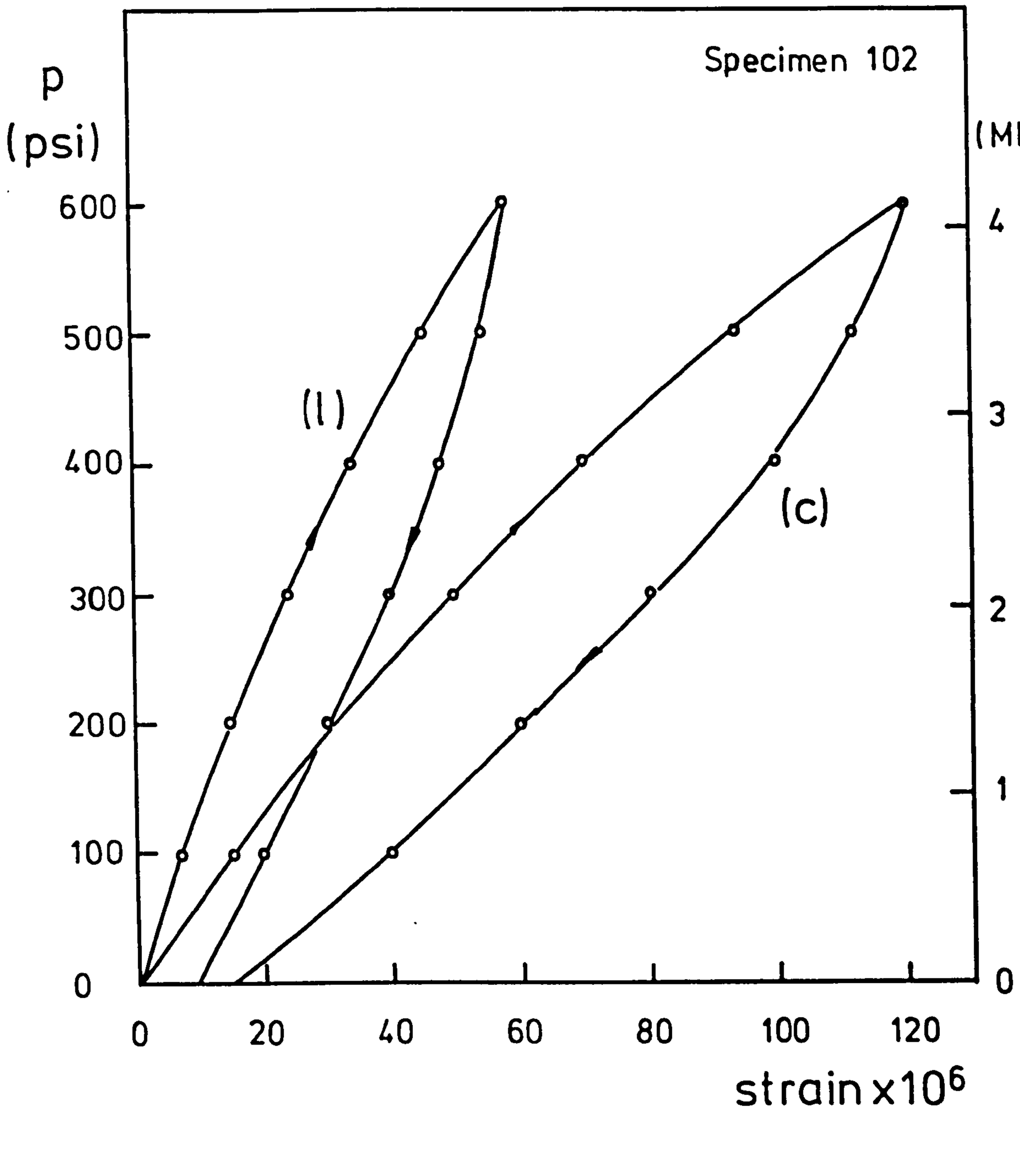

Fig 6.22 Pressure-strain curves of sleeve graphite irradiated to a dose 6.8×10^{20} n/cm^2 in longitudinal (l) and circumferential (c) directions

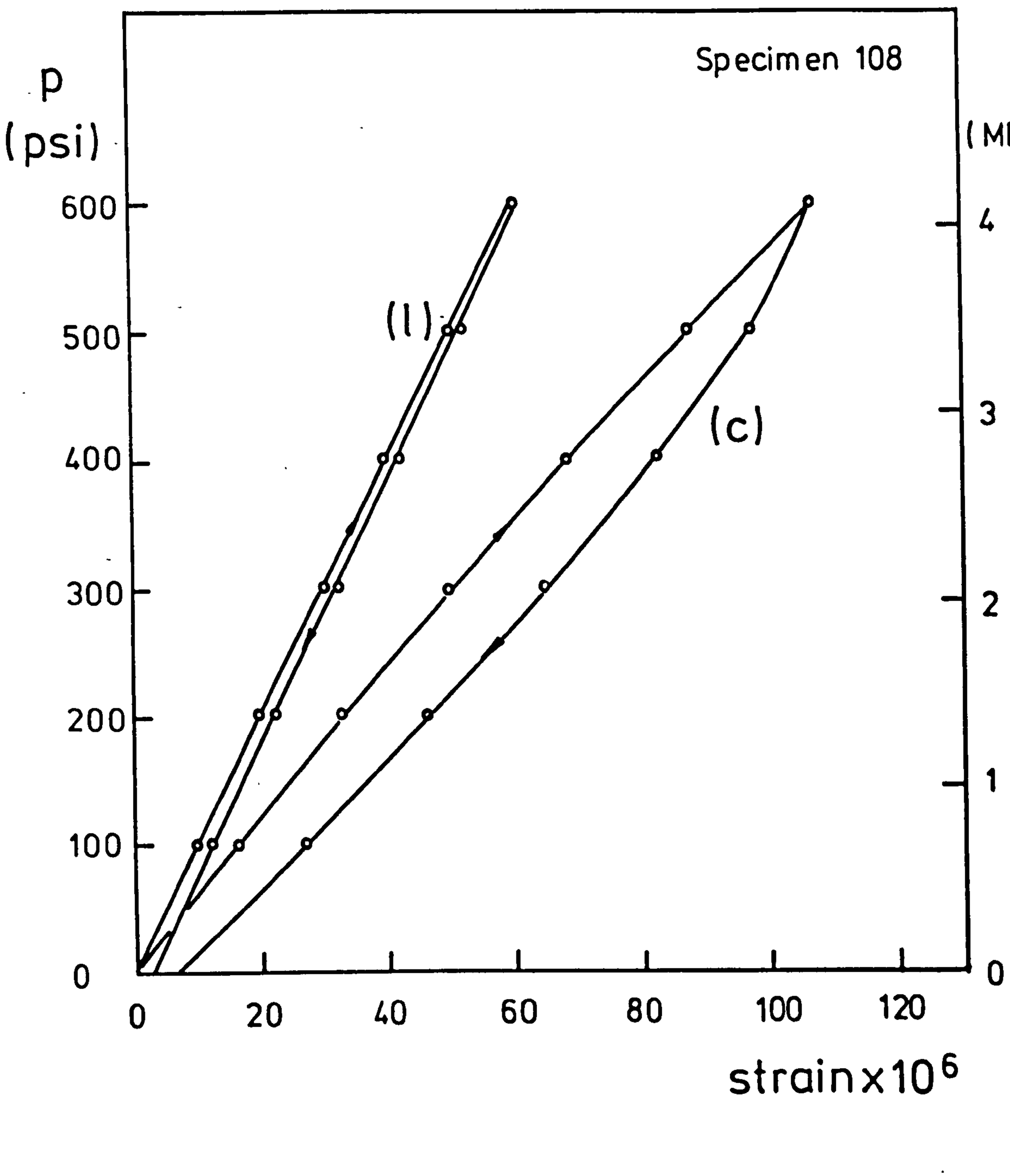

Fig 6.23 Pressure-strain curves of sleeve graphite irradiated to a dose of 6.8×10^{20} n/cm^2 in longitudinal (l) and circumferential (c) directions

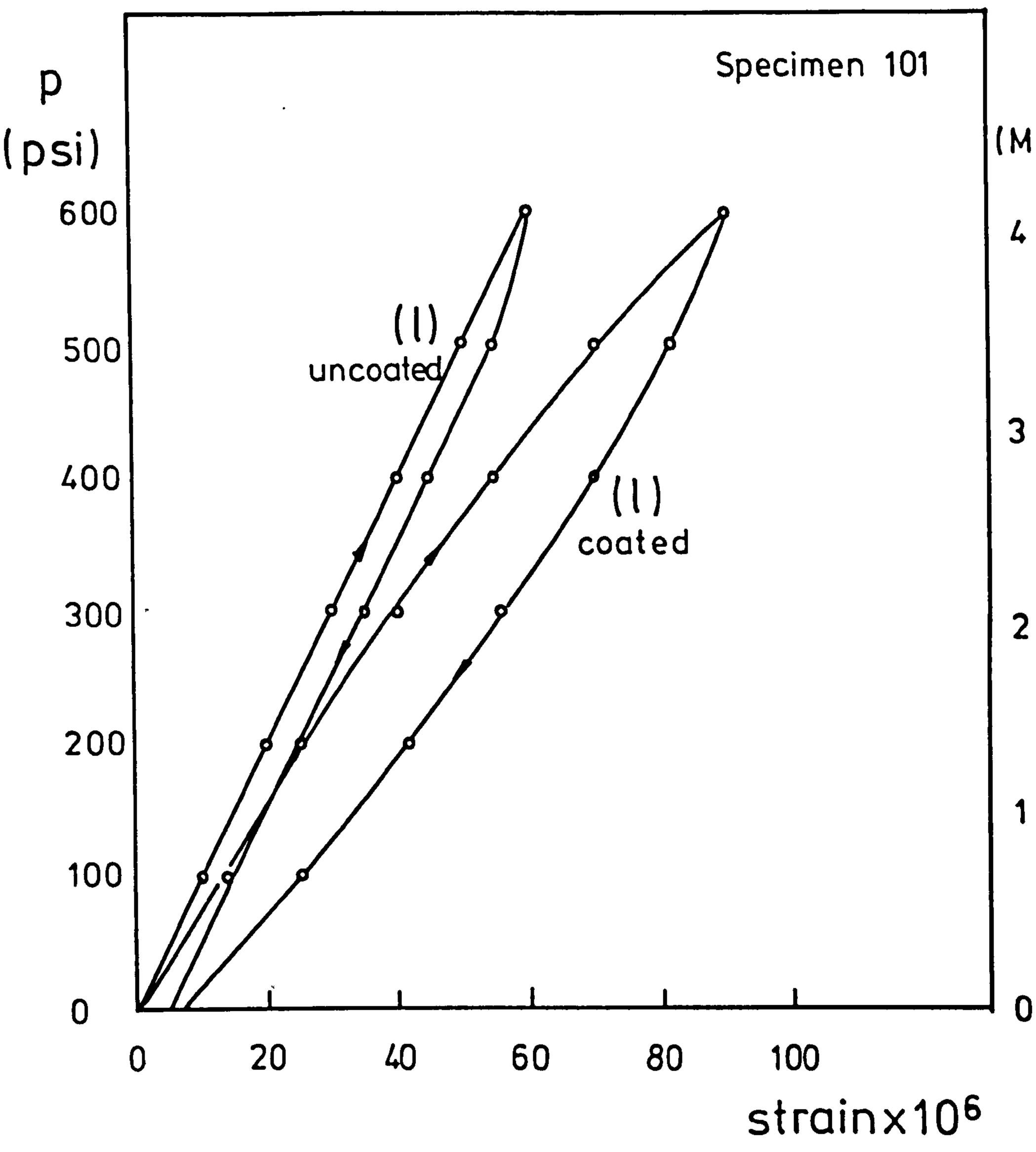

Fig 6.24 Pressure-strain curves of sleeve graphite irradiated to a dose of 6.8×10^{20} n/cm^2 in longitudinal (l) direction for a coated and uncoated specimen

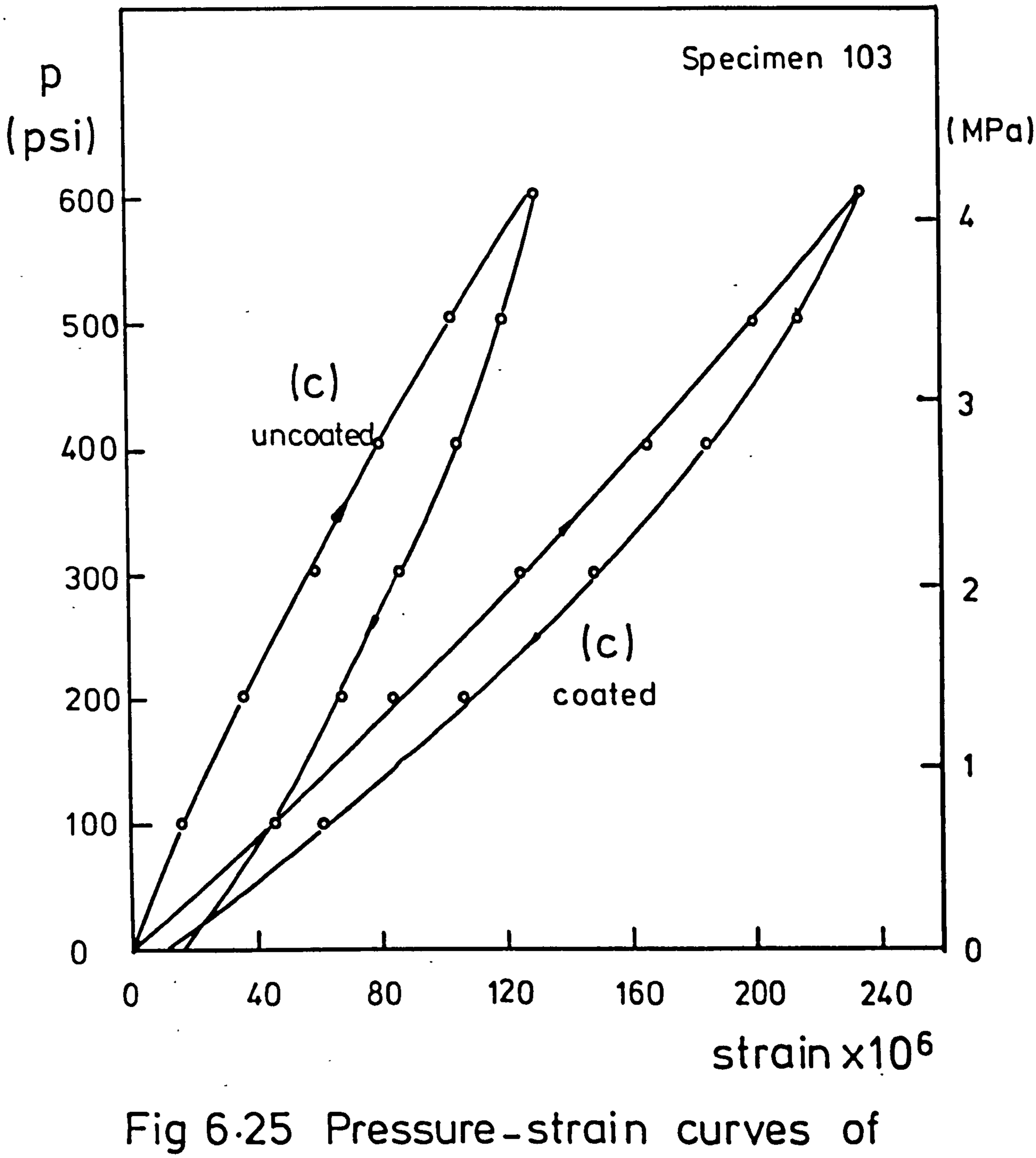

Fig 6·25 Pressure-strain curves of sleeve graphite irradiated to a dose of 6.8×10^{20} n/cm^2 in circumferential (c) direction for a coated and uncoated specimen

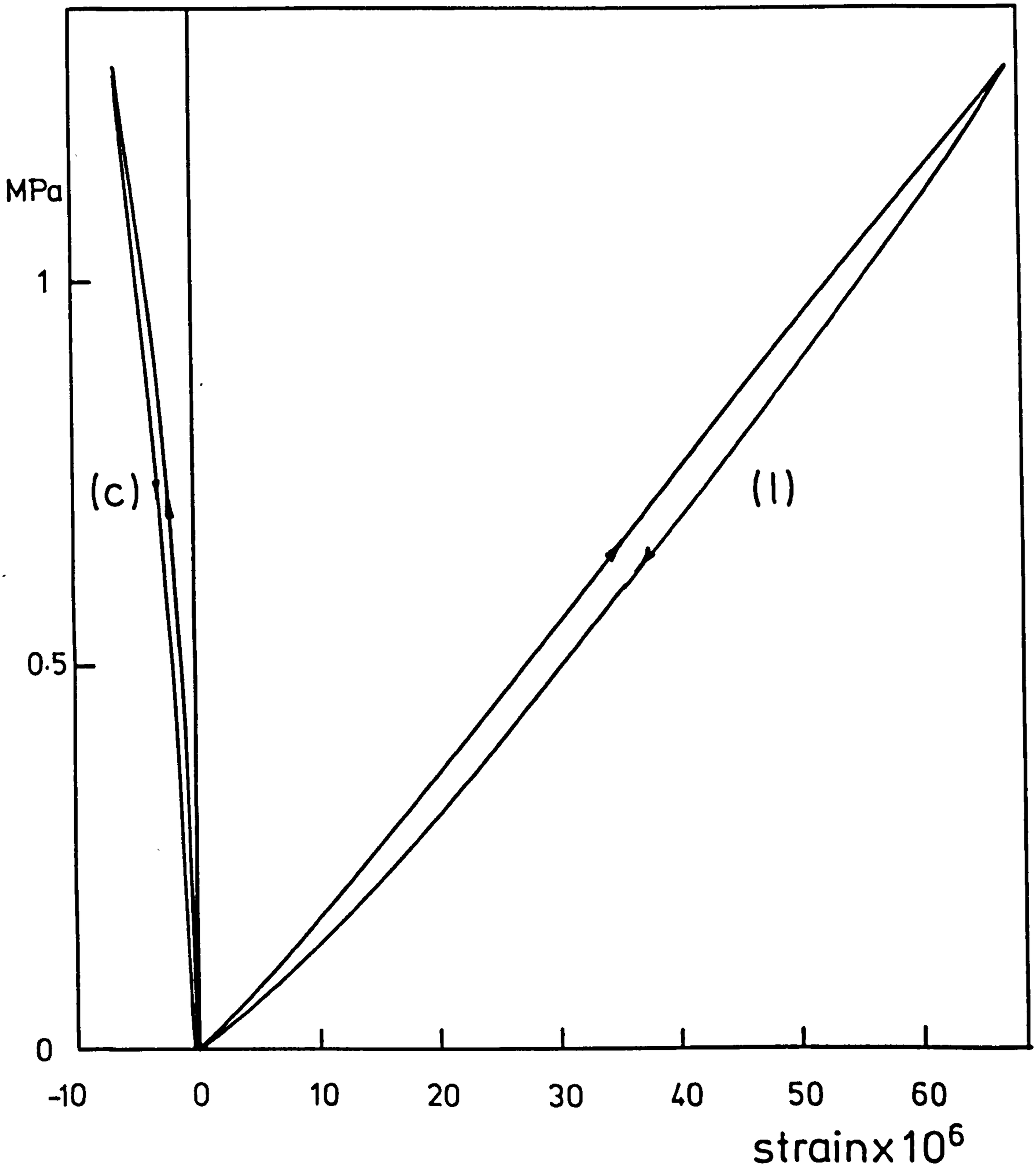

Fig 6.26 Compressive stress-strain curves of irradiated sleeve graphite (6.8x10 n/cm) in longitudinal (l) and circumferential (c) directions

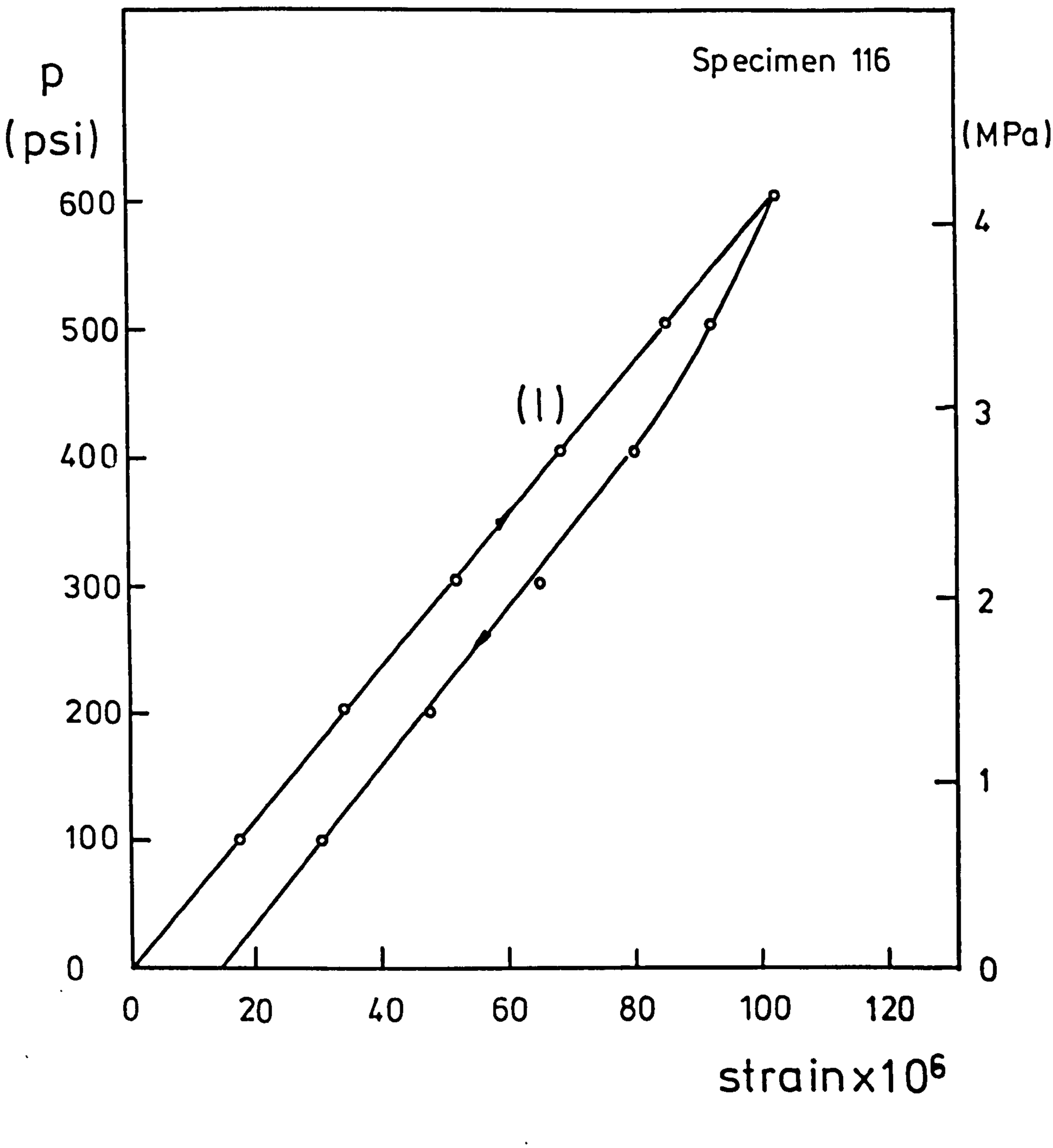

Fig 6.27 Pressure - strain curves of sleeve graphite irradiated to a dose of 11×10^{20} n/cm^2 in longitudinal (l) direction

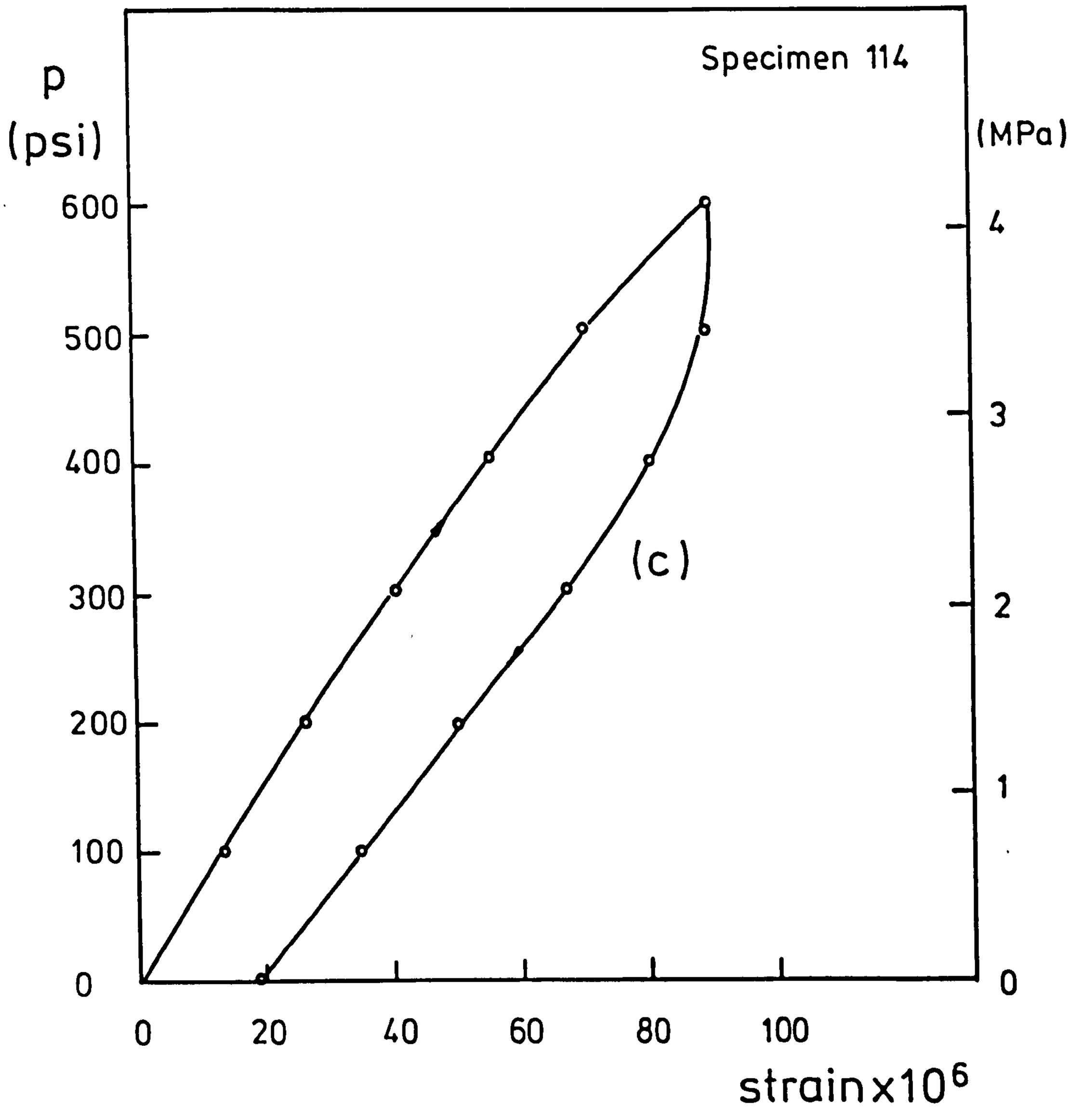

Fig 6.28 Pressure-strain curves of sleeve graphite irradiated to a dose of 11×10^{20} n/cm^2 in circumferential (c) direction

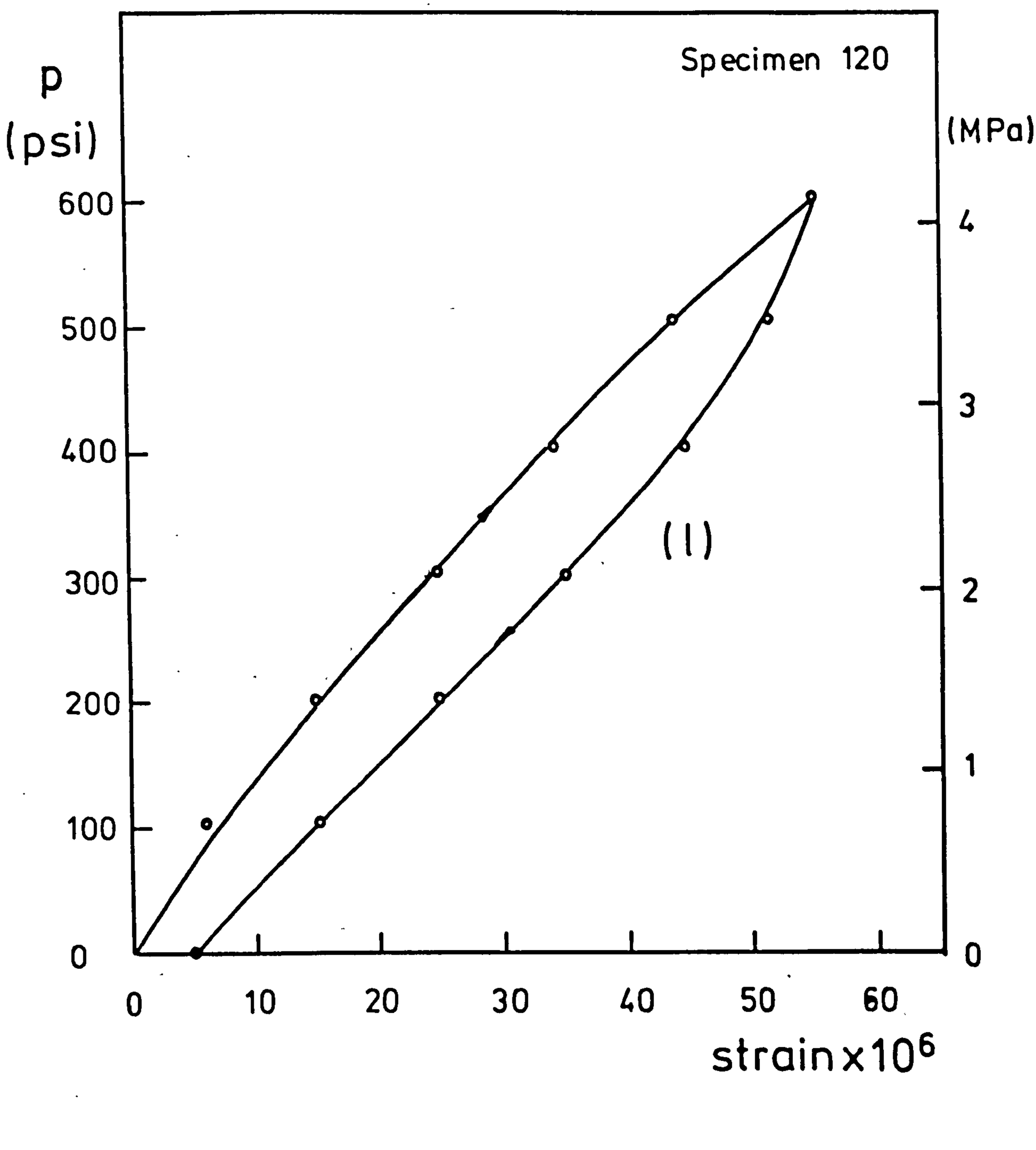

Fig 6.29 Pressure-strain curves of sleeve graphite irradiated to a dose of 17×10^{20} n/cm^2 in longitudinal (l) direction

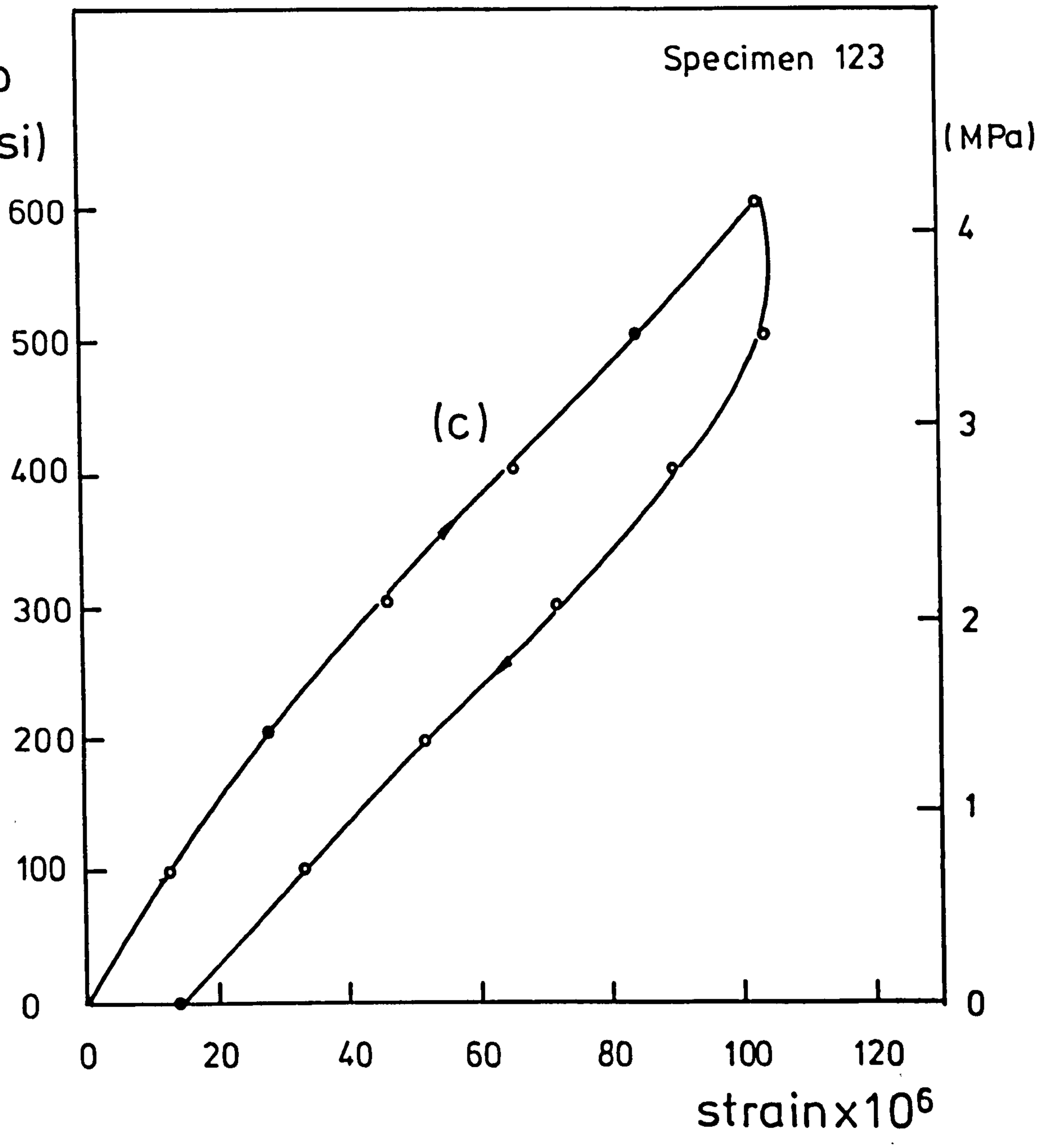

Fig 6.30 Pressure-strain curves of sleeve graphite irradiated to a dose of 17×10^{20} n/cm in circumferential (c) direction

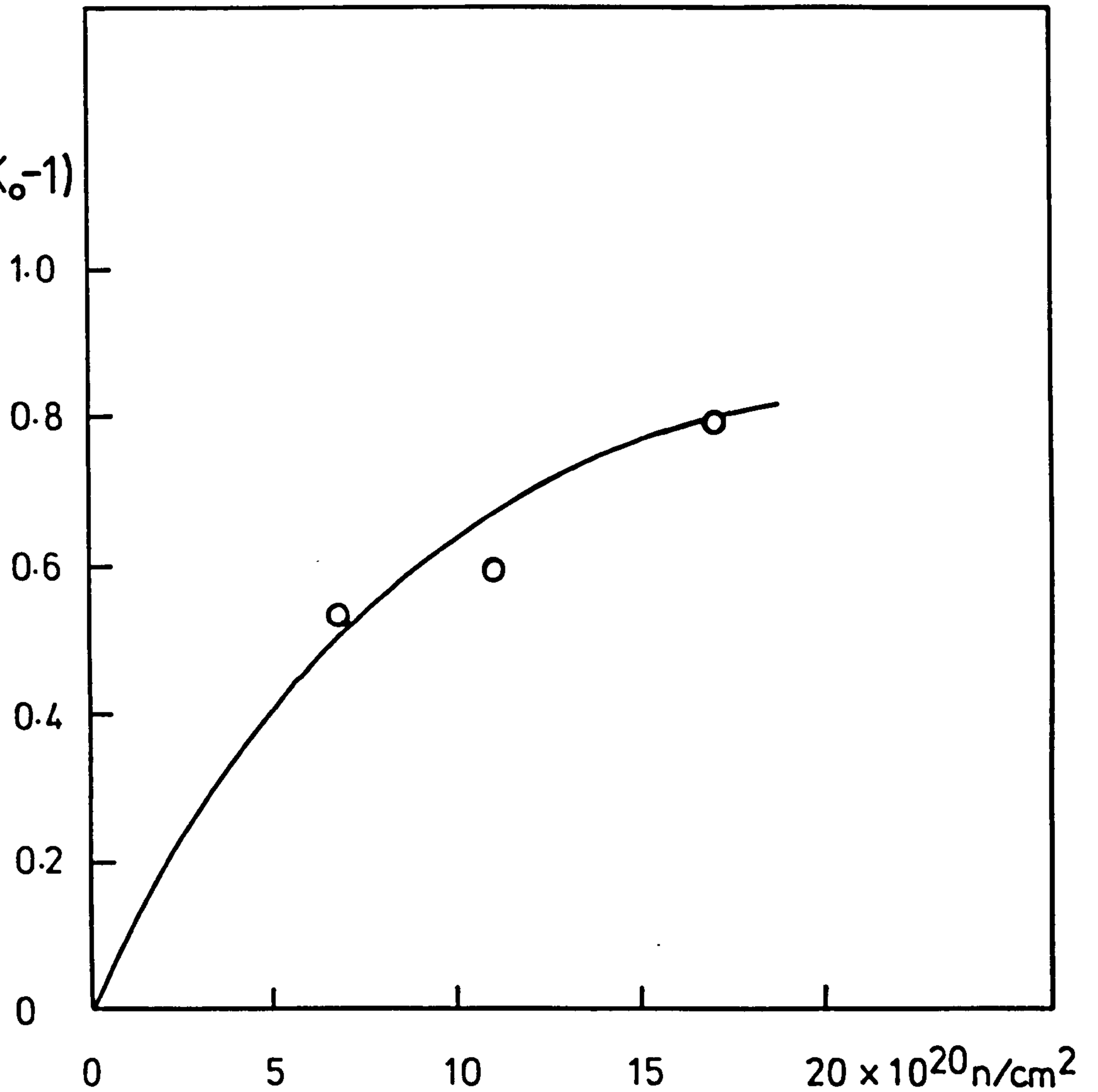

Fig 6.31 Graph of (K/K_o-1) versus neutron dose for the irradiated sleeve graphites

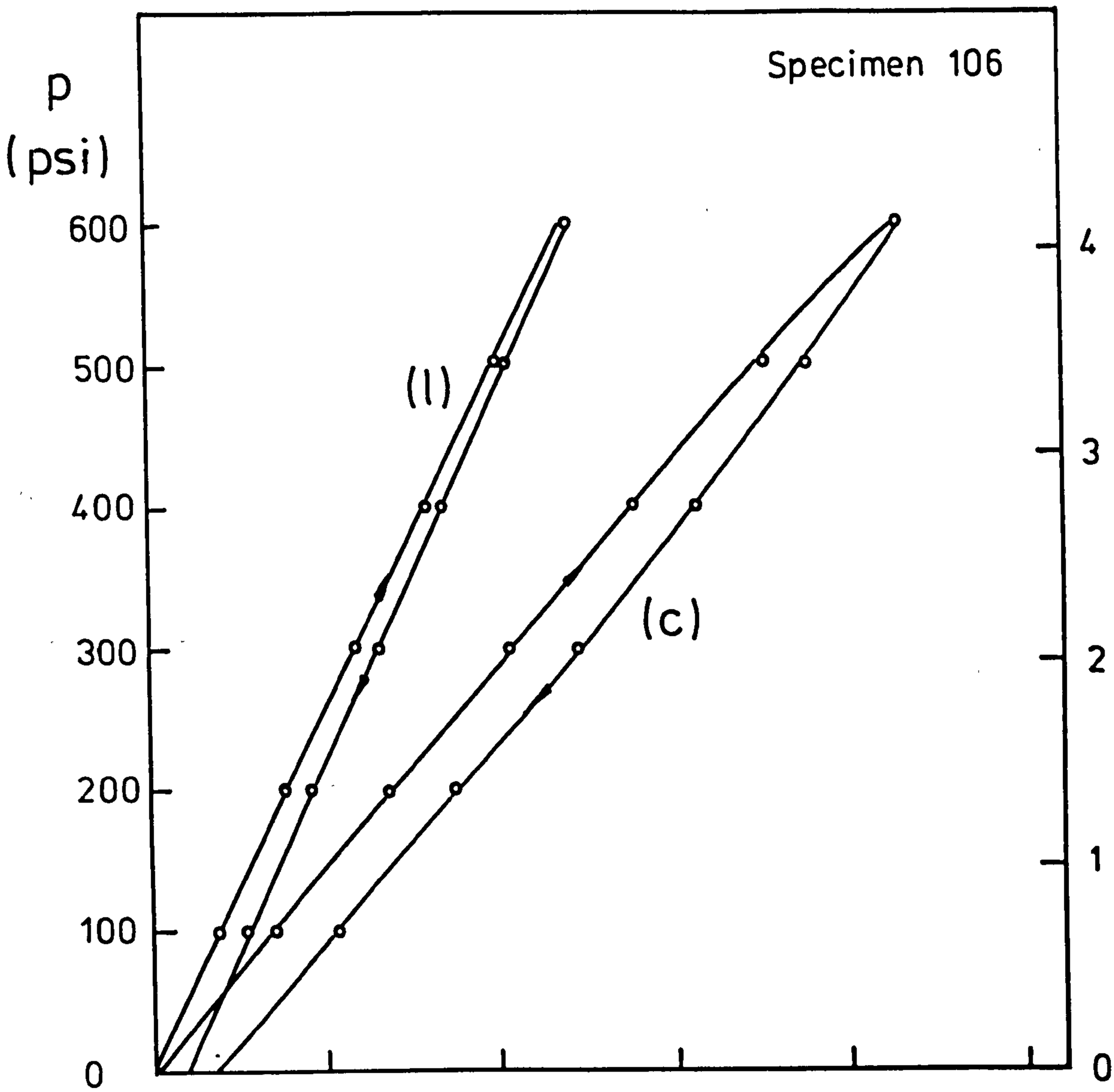

Fig 6.32 Pressure-strain curves of annealed specimen of irradiated sleeve graphite (6.8×10^{20} n/cm^2) in longitudinal (l) and circumferential (c) directions

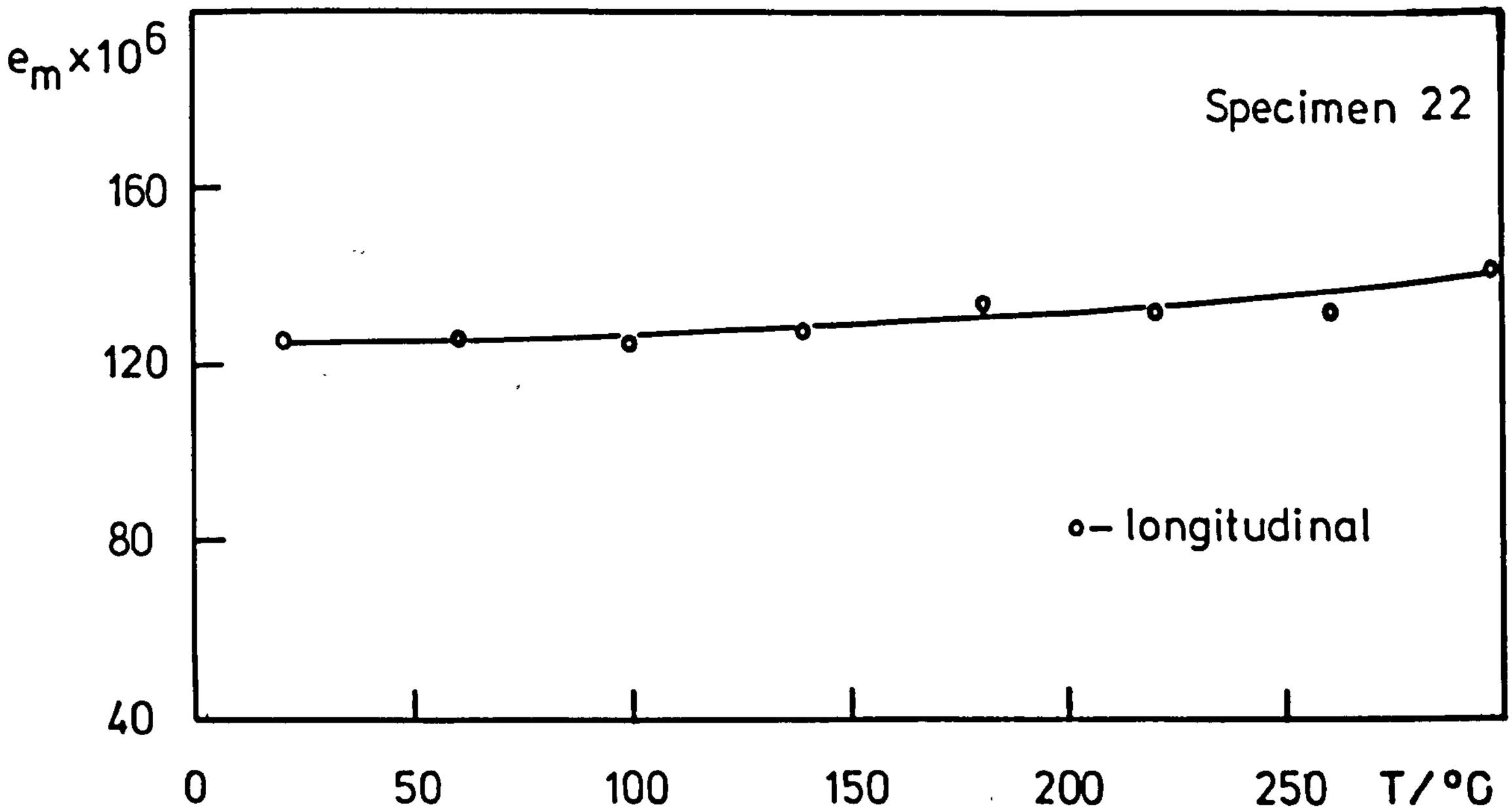

Fig 6.33 Elevated temperature test: graphite B

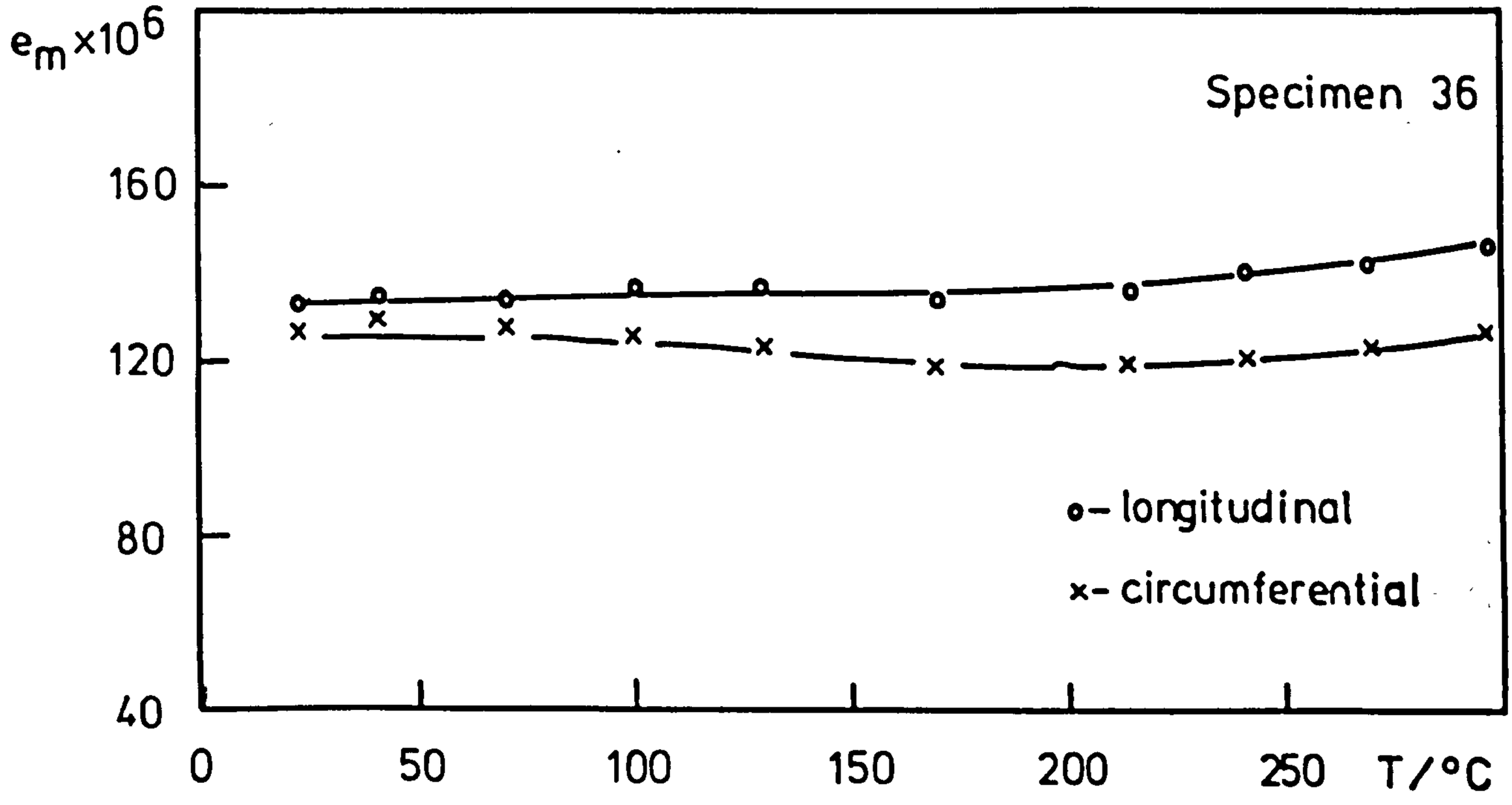

Fig 6.34 Elevated temperature test: graphite B

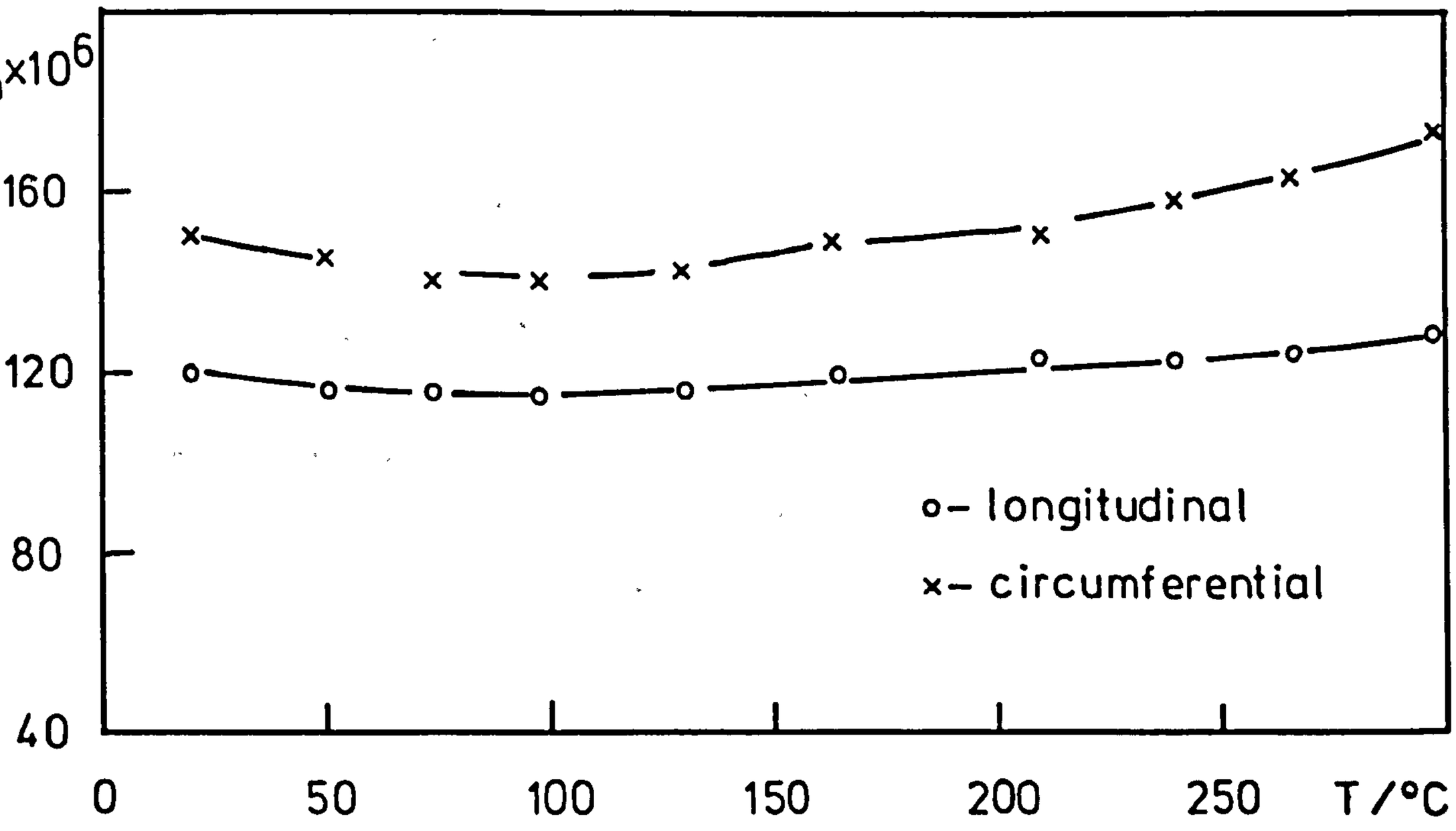

Fig 6.35 Elevated temperature test: graphite C

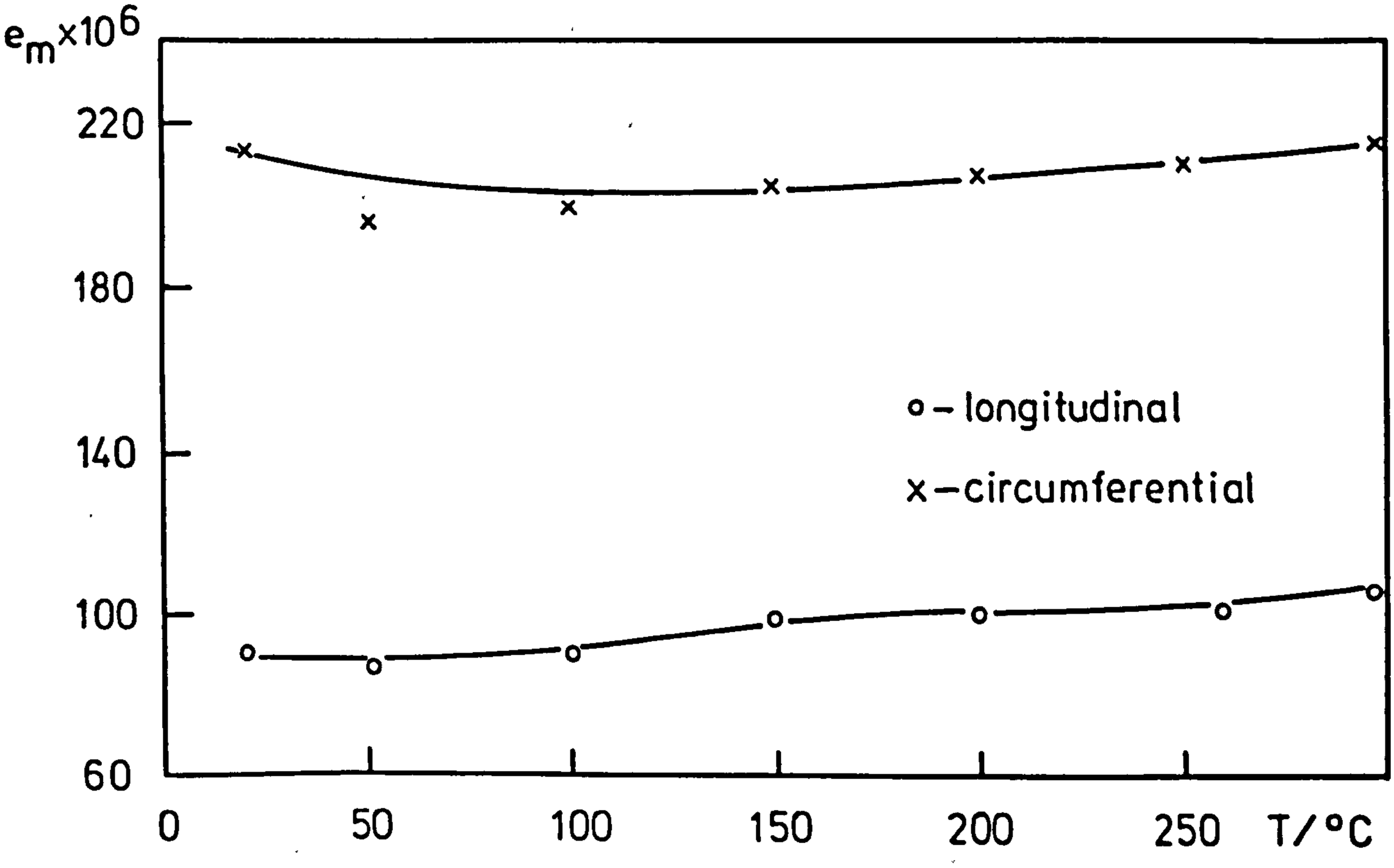

Fig 6.36 Elevated temperature test: graphite D

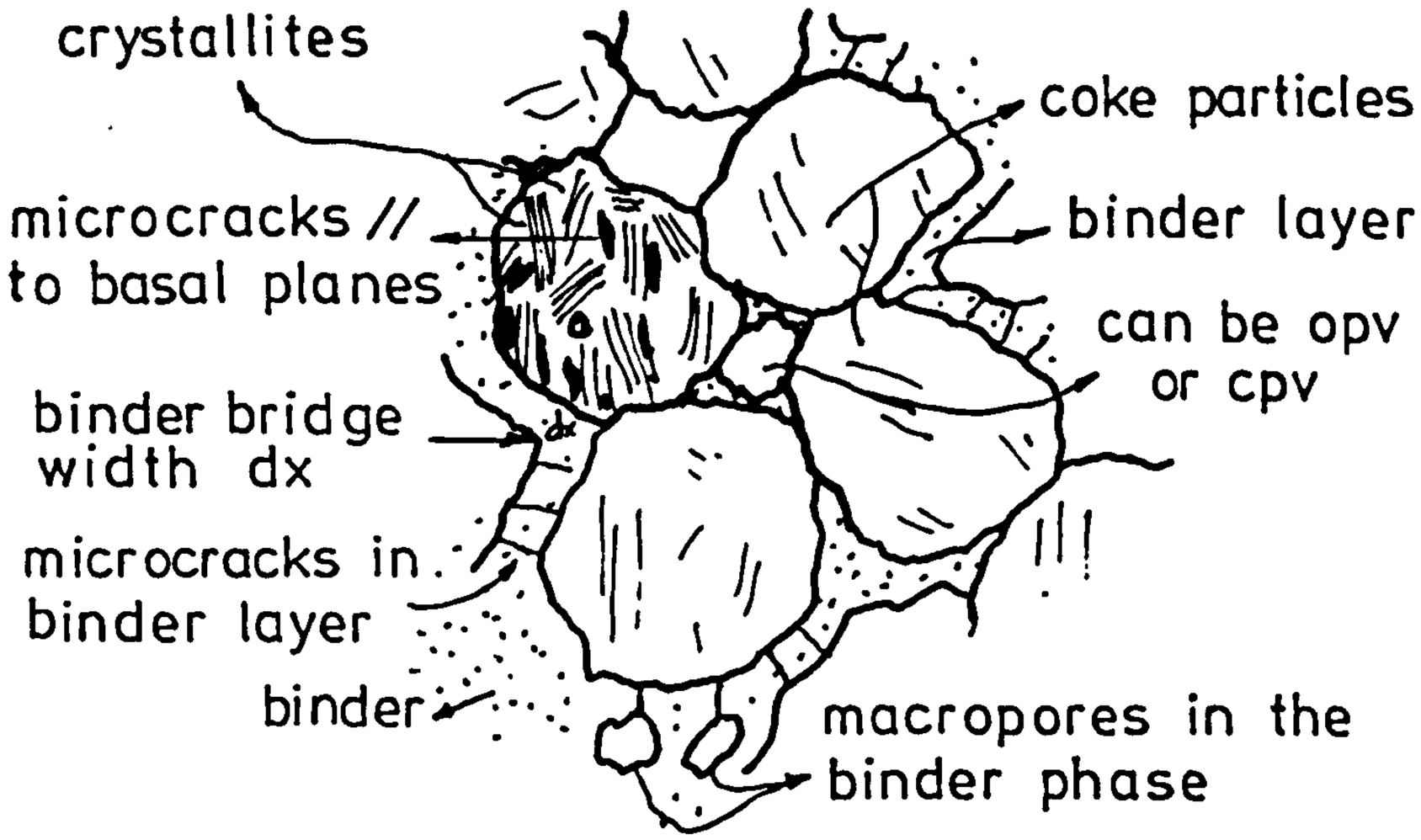

Fig 7.1 Microstructures of graphite

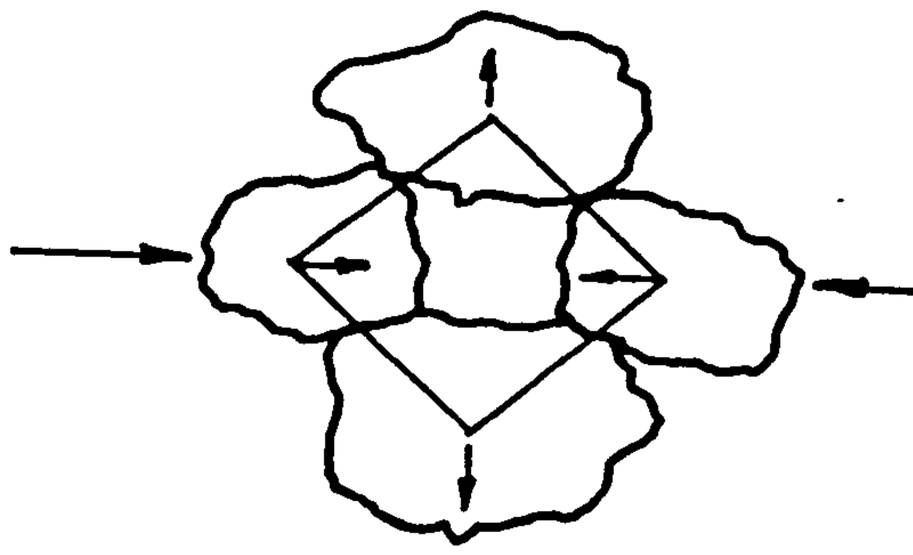

Fig 7.2 Uniaxial compression

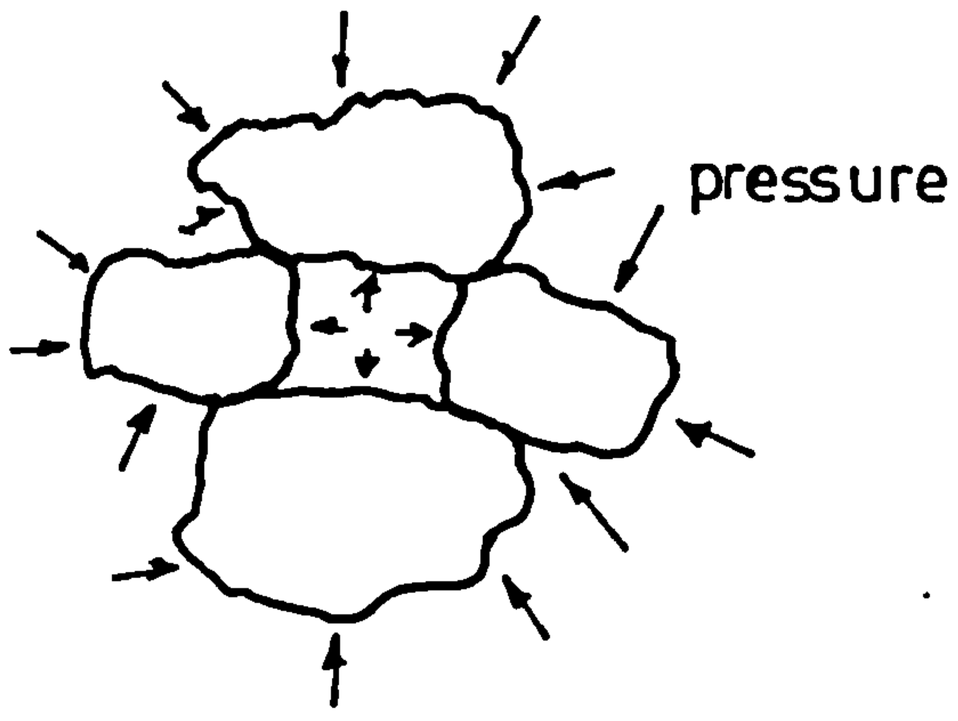

Fig 7.3 Hydrostatic pressurisation

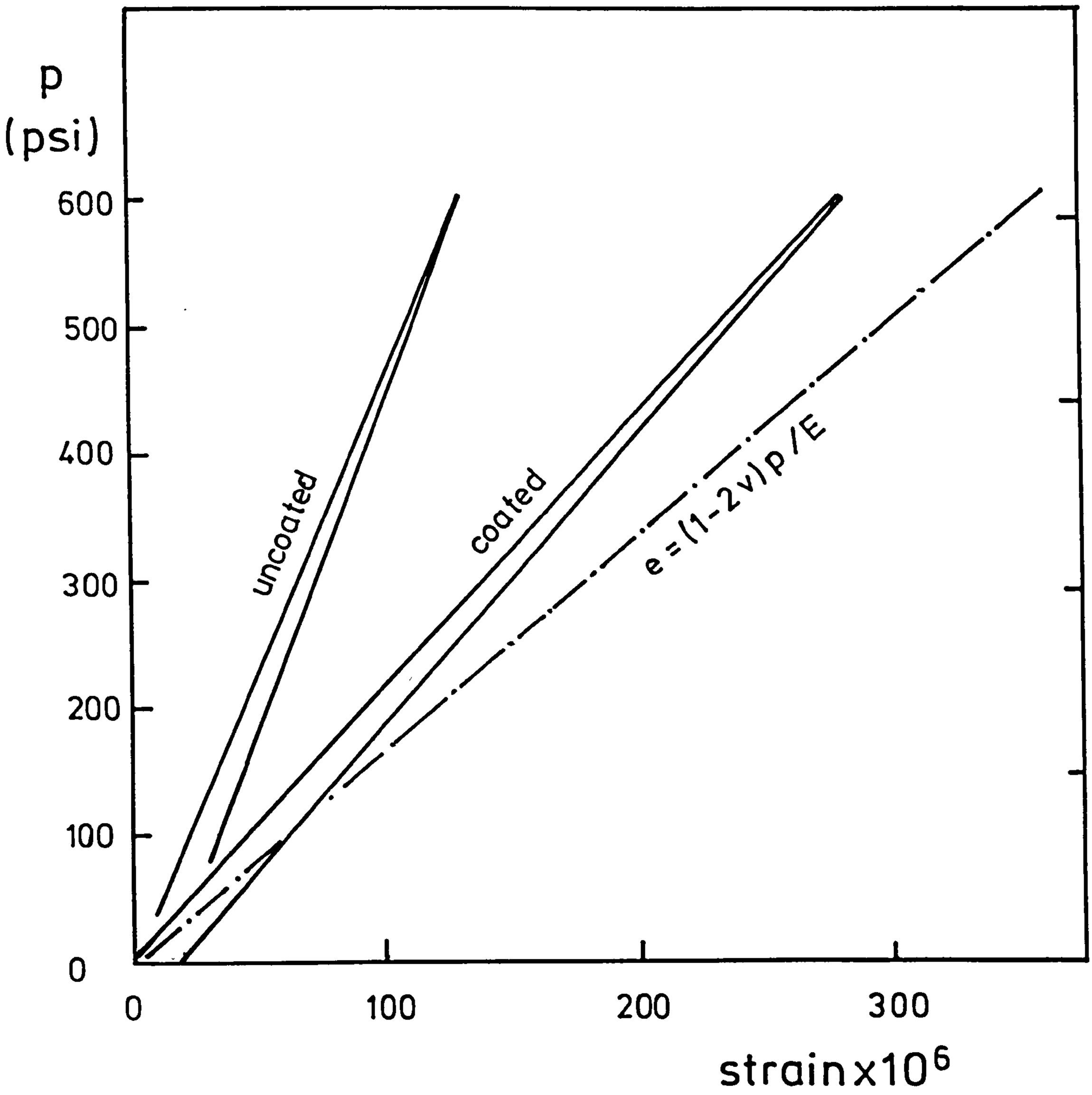

Fig 7.4 Comparison of hydrostatic behaviour with elastic theory for graphite A

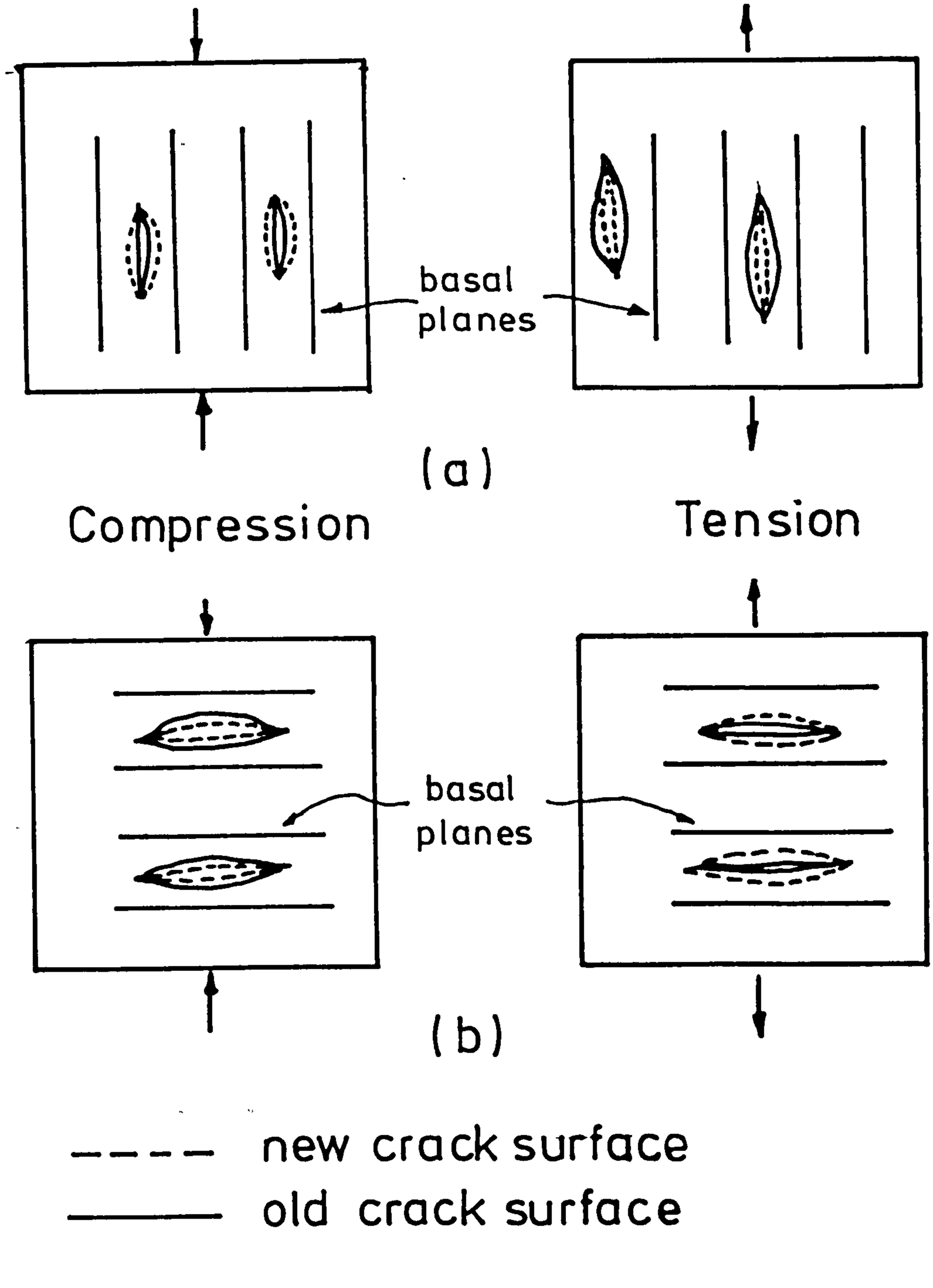

Fig 7.5 Deformation of cracks on the basal planes in the cases of tension and compression for (a) with-grain specimen and (b) across-grain specimen

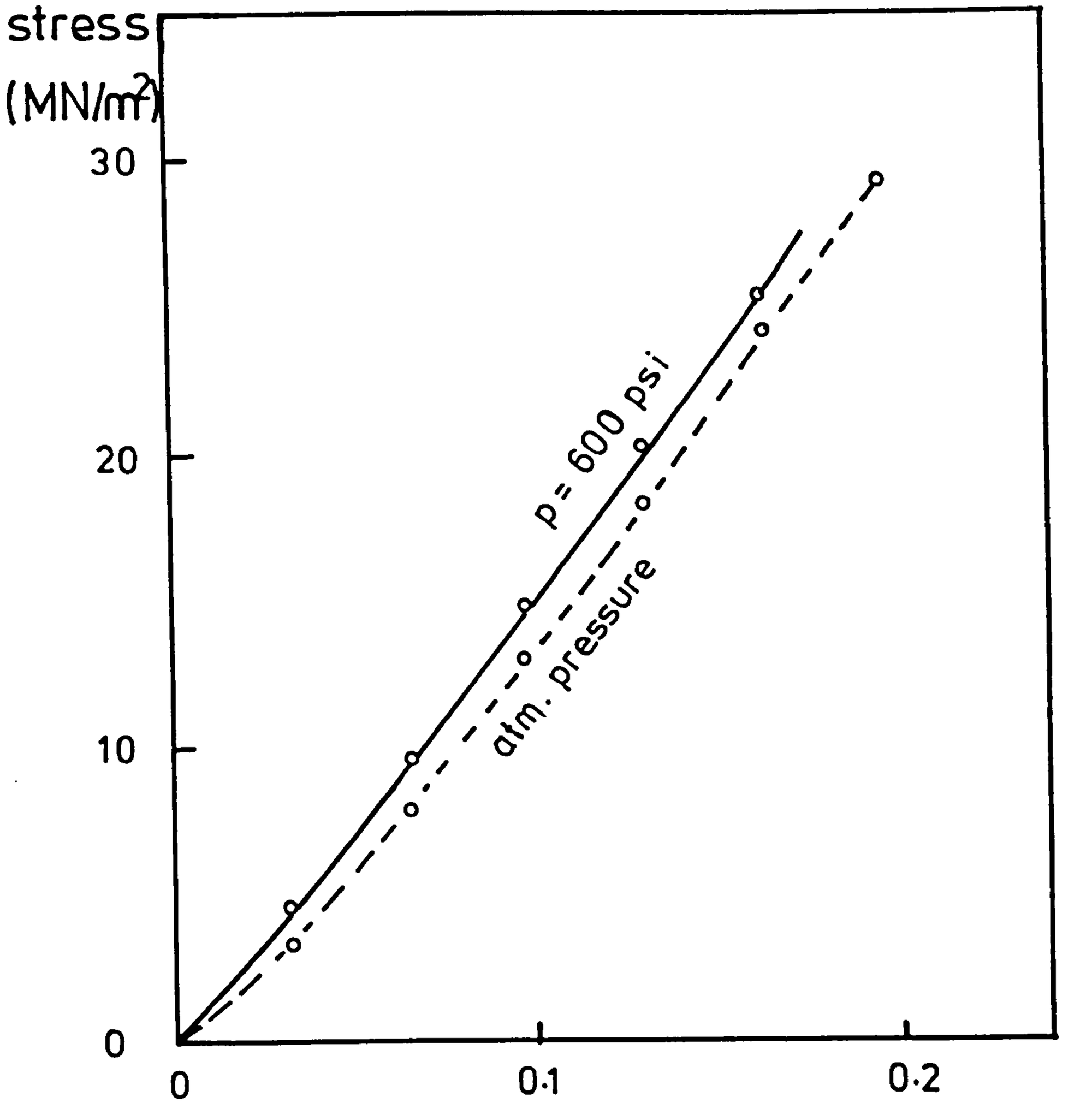

Fig 7·6 Graph of fibre stress versus strain for graphite : Blk. SI2, IJ

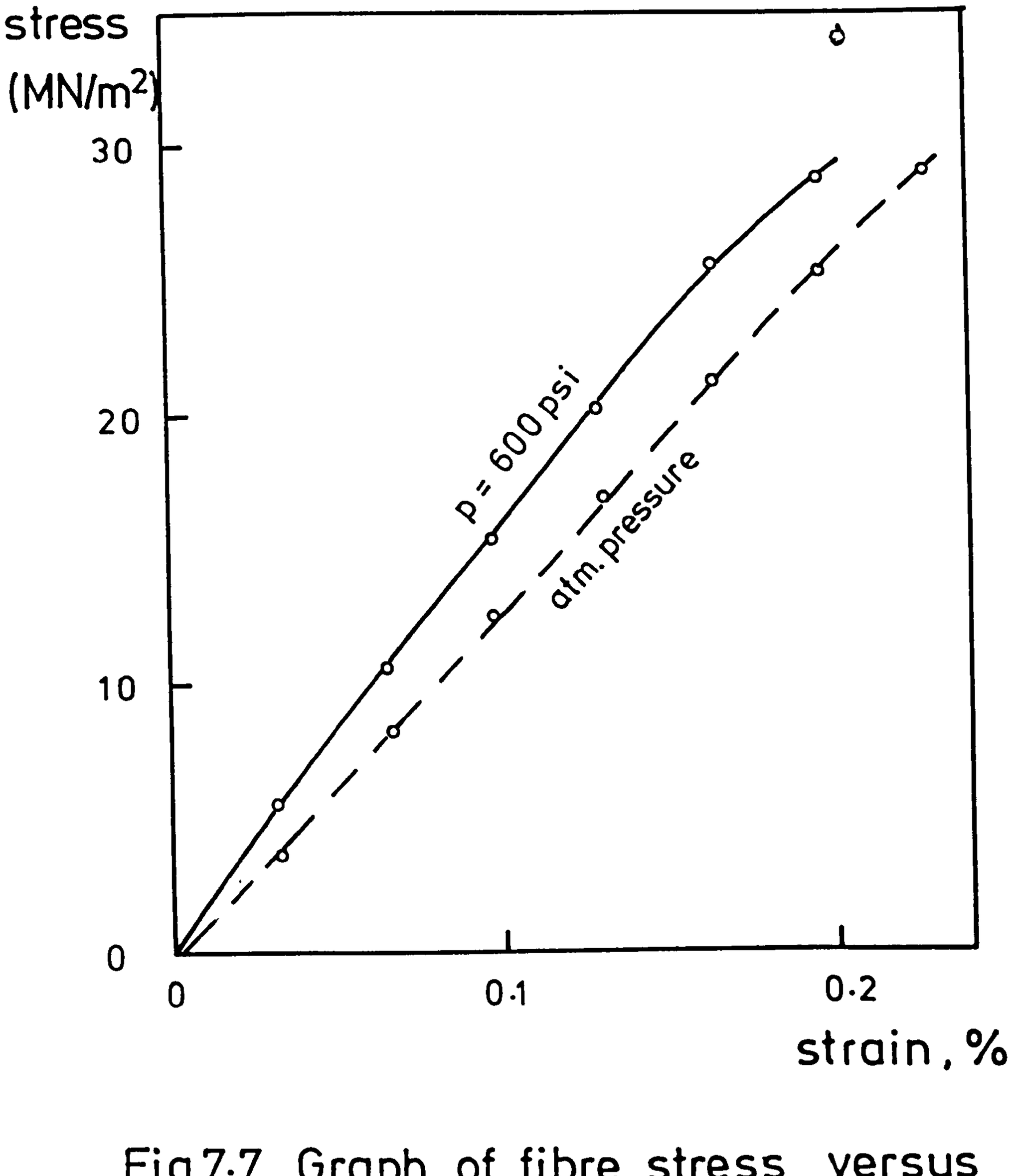

Fig 7·7 Graph of fibre stress versus strain for graphite : Blk. 392

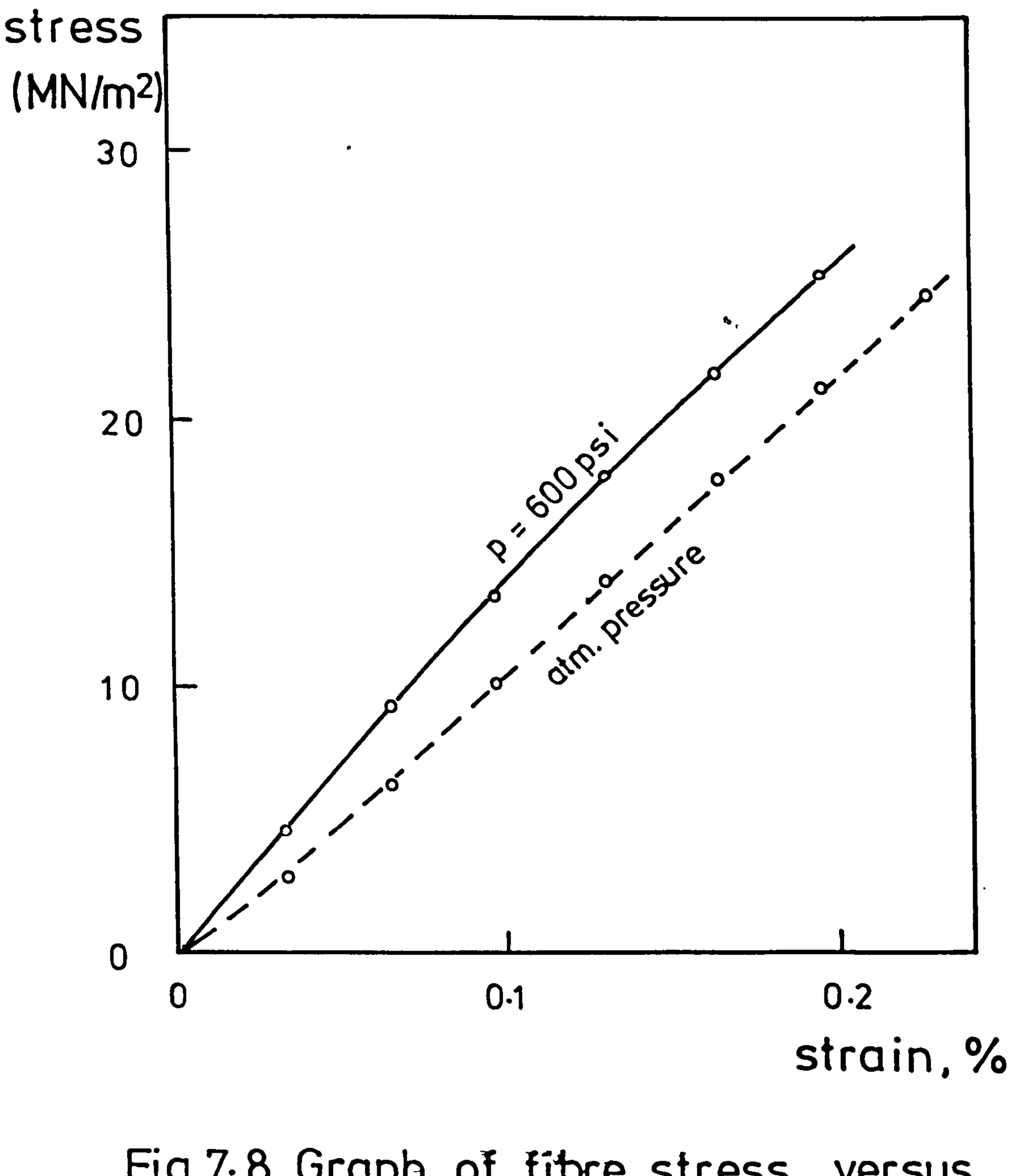

Fig 7.8 Graph of fibre stress versus strain for graphite : Blk. 398

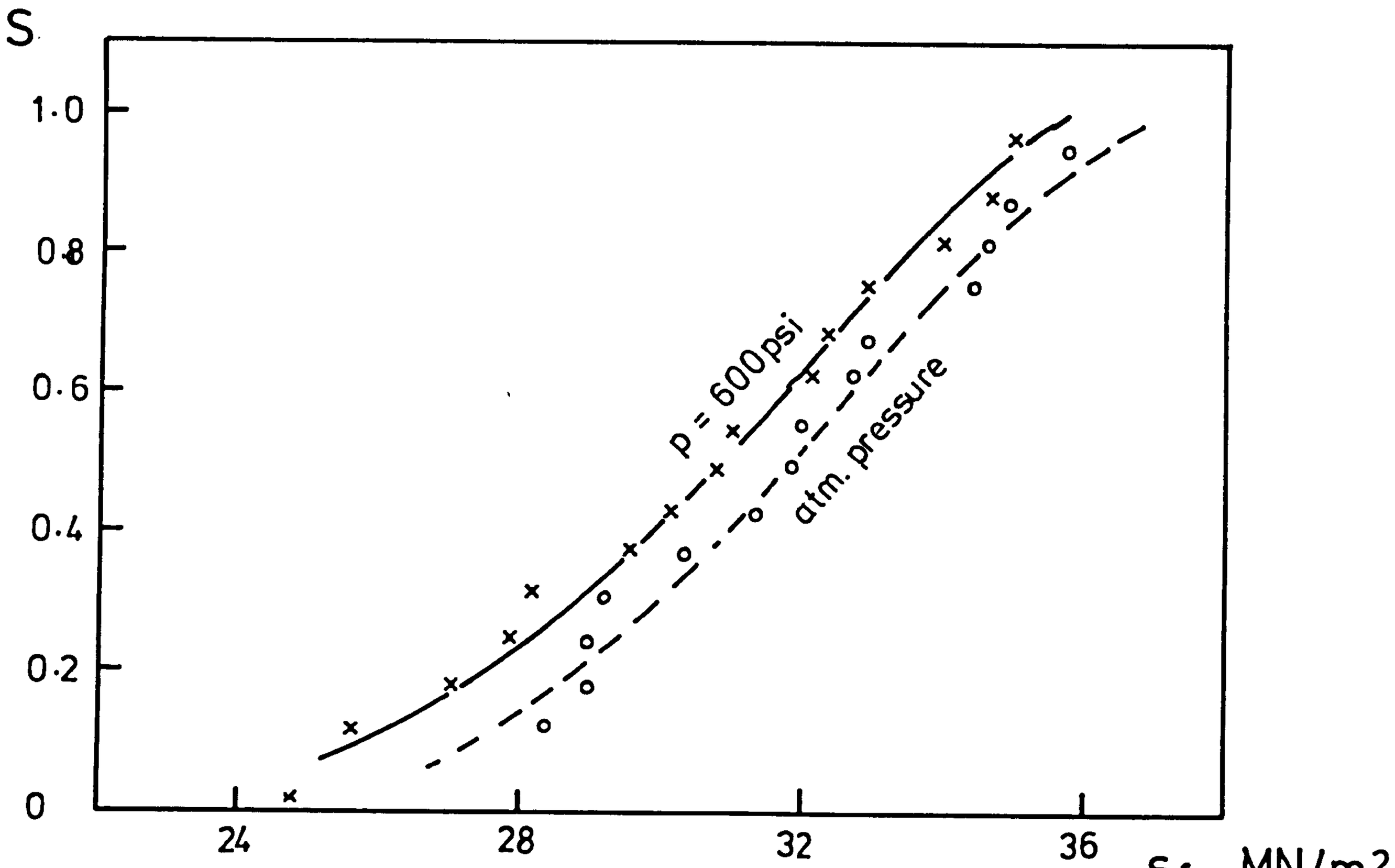

Fig 7.9 Graph of S versus s_f : Blk. SI2, IJ

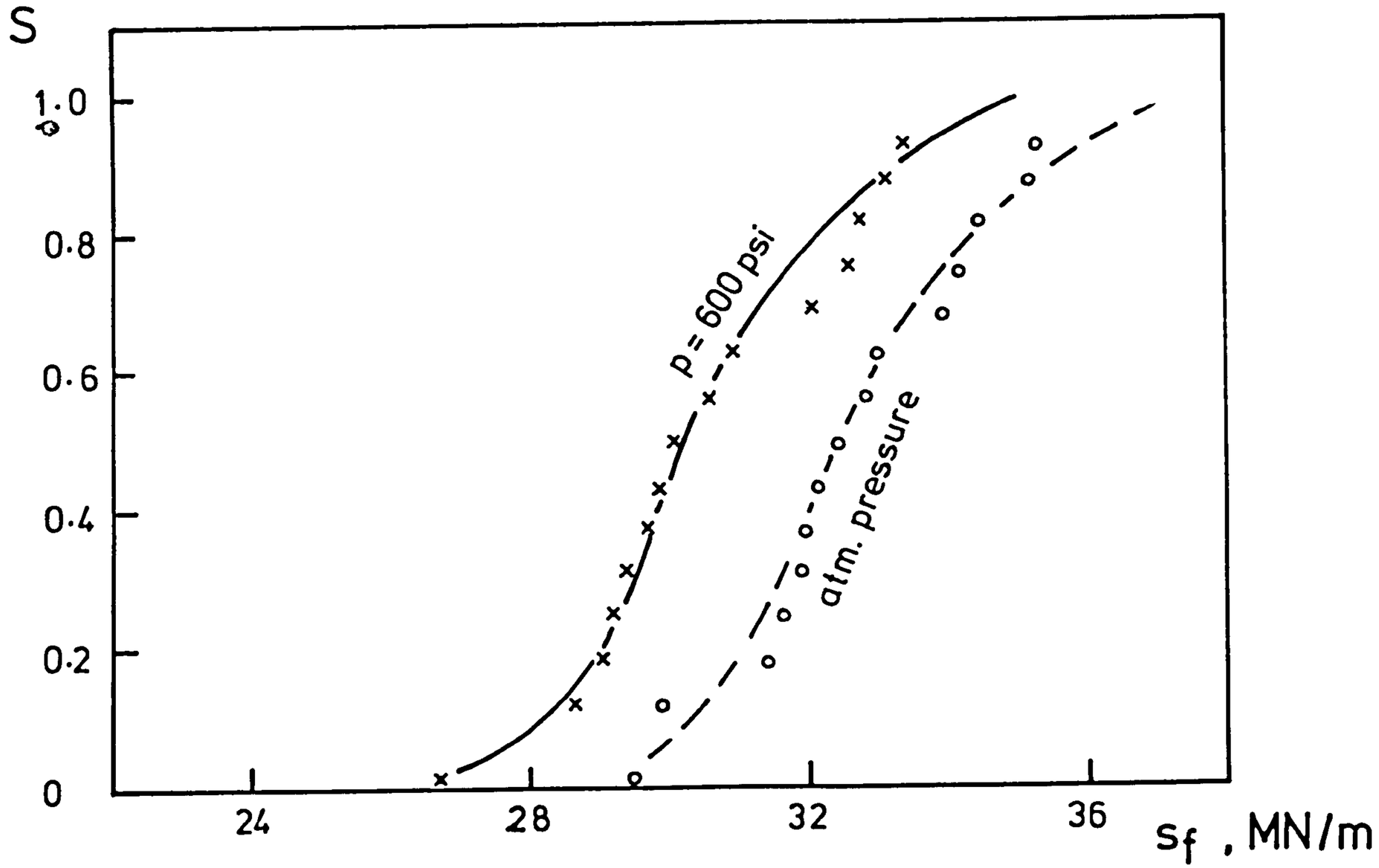

Fig 7·10 Graph of S versus s_f : Blk. 392

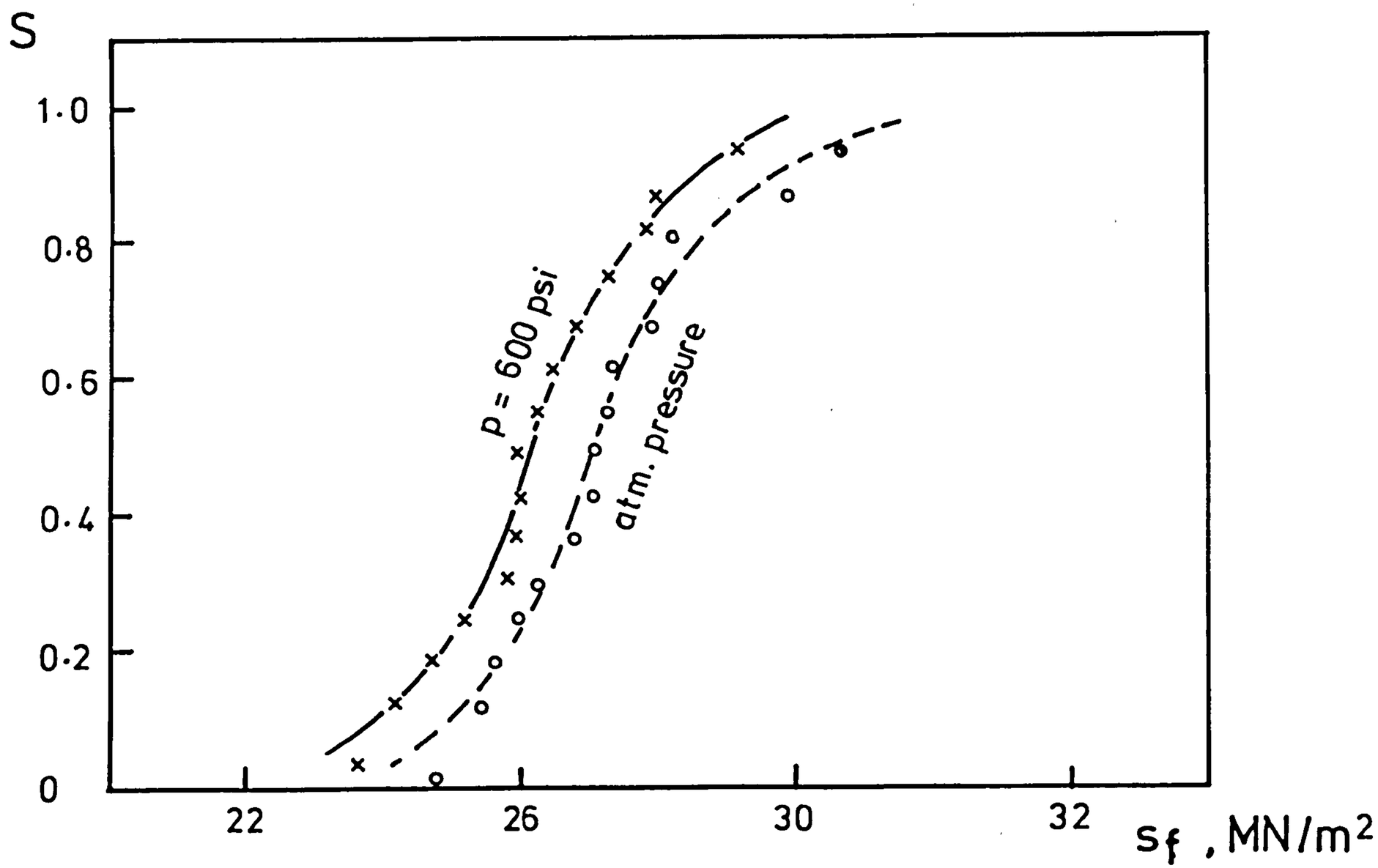

Fig 7·11 Graph of S versus s_f : Blk. 398

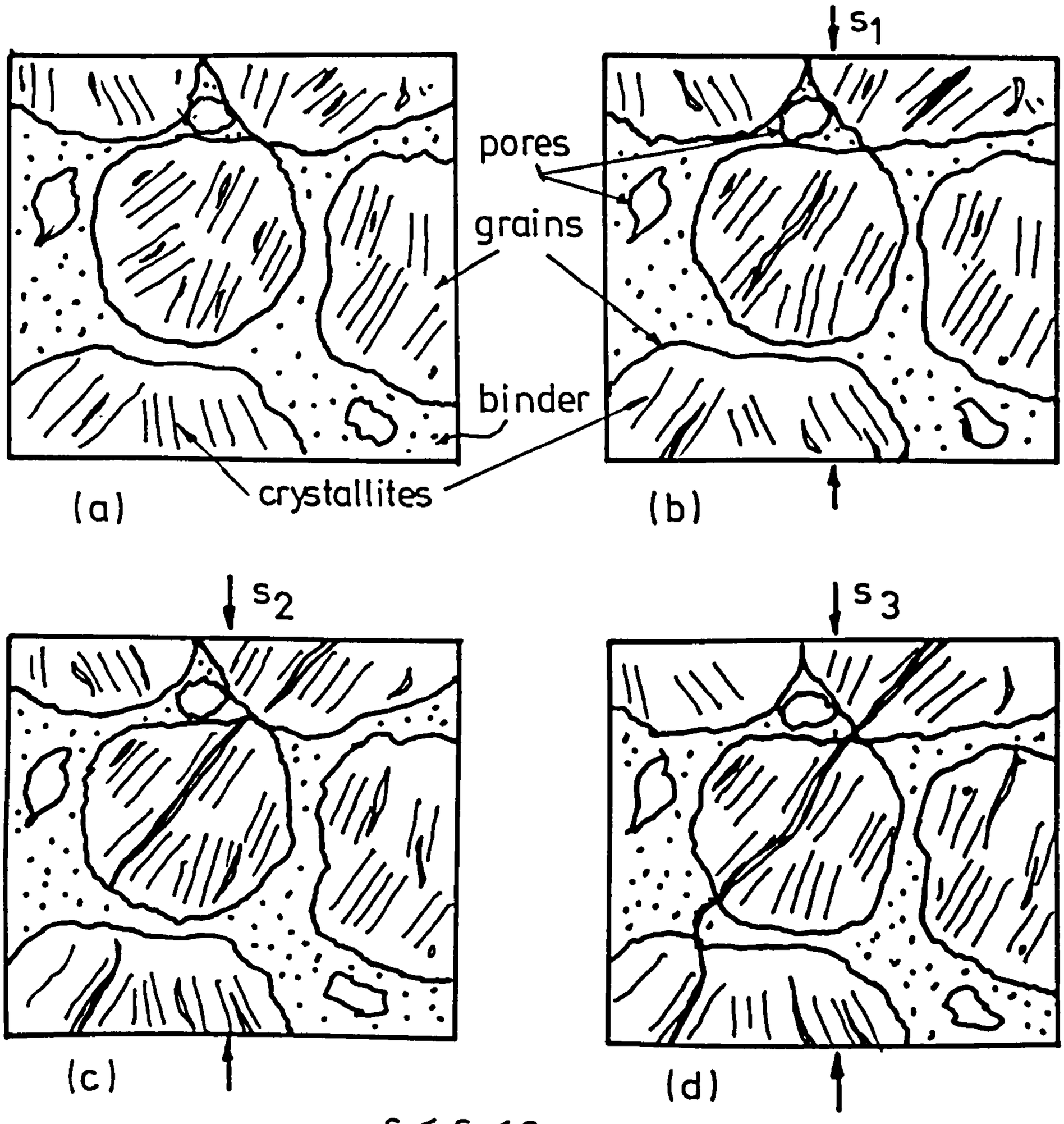

Fig 7.12 Schematic drawings showing the fracture behaviour of graphite

(a) existing cracks in the basal planes

(b) growth of cracks under stress

(c) grain is cracked as stress increases

(d) alignment of cracked grains